Thesis

submitted for the degree of

Doctor of Philosophy in Applied Sciences

Presented by

Anne-Catherine Dieudonné

Hydromechanical behaviour of compacted bentonite: from micro-scale analysis to macro-scale modelling

June 2016

JURY

Prof. Alain DASSARGUES (President)	Université de Liège
Prof. Robert CHARLIER (Supervisor)	Université de Liège
Prof. Frédéric COLLIN	Université de Liège
Prof. Tristan GILET	Université de Liège
Prof. Tomasz HUECKEL	Duke University
Prof. Enrique ROMERO	Universitat Politècnica de Catalunya
Dr. Jean TALANDIER	Andra

This research was funded by:

F.R.I.A. - F.R.S. - FNRS
Fonds pour la formation à la Recherche dans l'Industrie et dans l'Agriculture
Rue d'Egmont 5
1000 Brussels, Belgium

Abstract

Deep geological disposal constitutes one of the most promising solutions for the safe isolation of high-level and intermediate-level radioactive wastes. While the concept of disposal differs from one country to another, the insulation of the radioactive wastes from the biosphere always relies on a multi-barrier concept in which bentonite-based materials play a central role. Indeed, the objective of the bentonite barrier is to form a tight contact with the surrounding geological formation and to create a zone of low permeability able to limit water flow around the excavated galleries, thereby delaying the release of radionuclides to the biosphere. The present PhD work aims at better understanding and modelling the complex hydromechanical behaviour of compacted bentonite-based materials under repository conditions.

In this research work, the problem is analysed in a systematic and progressive manner by considering increasing scales of interest. As a first step, the hydration and swelling mechanisms of bentonite are addressed at a microscopic scale. The effects of hydraulic and mechanical loading on the microstructure of bentonites are thoroughly analysed. Based on the interpretation of experimental data, a new model for the evolution of the microstructure is proposed. It is later used to represent the effects of the microstructure on the macroscopic material behaviour.

The constitutive and numerical modelling of bentonite behaviour is then addressed at a macroscopic scale. A classic hydromechanical framework for partially saturated porous media is progressively enriched to take into account the important multi-scale and multi-physical coupled processes observed in bentonites. More specifically, the contributions of the PhD thesis include:

- The development of a new water retention model accounting for separate retention mechanisms in the micropores and macropores. The model successfully captures the main features of the water retention behaviour of compacted bentonites, including the evolution of the water retention properties upon free swelling.
- The extension of the Barcelona Basic Model developed by Alonso *et al.* (1990) to better reproduce the mechanical behaviour of bentonites, and especially the development of the swelling pressure.
- The extension of the flow model to take into consideration the permeability evolution with the material dry density and microstructure.

The developed models are implemented in the finite element code `LAGAMINE` and validated on different bentonite-based materials. They provide a new and better understanding of

the material behaviour along hydromechanical stress paths.

At the scale of the underground structure, technological gaps and interfaces between materials of the disposal are discontinuities that are likely to affect the hydromechanical behaviour of the engineered barrier. In order to investigate the influence of interfaces on important safety-relevant properties, an experimental study is carried out at the Technical University of Catalonia in Barcelona, Spain. The experimental data evidence a major influence of the interface on the saturation process, which is poorly reproduced with classic numerical models that assume a perfect contact between materials. To get over this limitation, zero-thickness interface elements are adopted to represent interfaces and technological gaps.

Finally, the developed hydromechanical model is used to analyse two experiments, namely the Bentogaz 2 test and the PGZ2 *in situ* test. Numerical results are not only in good agreement with the experimental data, both qualitatively and quantitatively, but the developed hydromechanical model provides a new understanding of the complex material behaviour. In particular, it highlights the important effects of multi-physical and multi-scale processes on the state of the bentonite buffer.

Résumé

Le stockage en couches géologiques profondes apparait comme une solution prometteuse pour assurer l'isolement des déchets radioactifs de haute et moyenne activités. L'isolation des déchets de la biosphère repose sur un concept multi-barrières dans lequel les matériaux à base de bentonite ont un rôle central. En effet, l'objectif de la barrière de bentonite est de former un contact parfait avec la formation géologique environnante, de créer une zone de faible perméabilité capable de limiter les flux d'eau autour des galeries et de retarder ainsi la migration des radionucléides vers la biosphère. Ce travail de thèse vise une meilleure compréhension et une meilleure modélisation du comportement hydromécanique de la bentonite compactée dans les conditions de stockage.

Dans ce travail, le problème est abordé de manière systématique et progressive en considérant des échelles d'intérêt croissantes. Dans un premier temps, les mécanismes d'hydratation et de gonflement de la bentonite sont étudiés à une échelle microscopique. Les effets de chargements hydraulique et mécanique sur la microstructure des bentonites sont analysés en détail. Sur base de l'interprétation de données expérimentales, un nouveau modèle d'évolution de la microstructure est proposé. Il est utilisé par la suite pour représenter les effets de la microstructure sur le comportement macroscopique du matériau.

Les modélisations constitutive et numérique du comportement de la bentonite sont ensuite abordées à une échelle macroscopique. Un cadre de modélisation classique du comportement hydromécanique des matériaux partiellement saturés est progressivement enrichi afin de prendre en compte les importants couplages multi-échelles et multi-physiques observés dans la bentonite. Plus particulièrement, les contributions de cette thèse comprennent:

- Le développement d'un nouveau modèle de courbe de rétention incorporant des mécanismes de rétention distincts dans les micropores et les macropores. Le modèle est capable de représenter les caractéristiques essentielles du comportement de rétention des bentonites compactées, en cela compris l'évolution des propriétés de rétention lors de chemin d'hydratation à volume libre.

- L'extension du Modèle de Barcelone développé par Alonso *et al.* (1990) afin de mieux reproduire le comportement mécanique des bentonites, en particulier le développement de la pression de gonflement.

- L'extension du modèle d'écoulement afin de prendre en compte l'évolution de la perméabilité avec la densité sèche et la microstructure du matériau.

Les modèles développés sont implémentés dans le code éléments finis Lagamine et validés sur différents matériaux à base de bentonite. Ils fournissent une meilleure compréhension

du comportement du matériau en améliorant de manière significative leur modélisation hydromécanique.

A l'échelle de la structure souterraine, les vides technologiques et interfaces entre matériau du dépôt représentent autant de discontinuités susceptibles d'affecter le comportement hydromécanique de la barrière ouvragée. Afin d'étudier l'influence des interfaces sur des propriétés critiques pour la sécurité de l'ouvrage, une campagne expérimentale a été réalisée à l'Université Polytechnique de Catalogne en Espagne. Les données expérimentales mettent en évidence une influence majeure de l'interface sur le processus de saturation, ce qui est mal reproduit par les modèles numériques classiques qui supposent un contact parfait entre matériaux. Pour dépasser cette limite, des éléments d'interface sont adoptés pour représenter les interfaces et vides technologiques.

Finalement, le modèle hydromécanique développé est utilisé pour analyser deux expériences, à savoir l'essai Bentogaz 2 et le test *in situ* PGZ2. Les résultats numériques sont non seulement en accord avec les données expérimentales, à la fois qualitativement et quantitativement, mais le modèle de comportement hydromécanique développé fournit de nouvelles clés de lecture et une meilleure compréhension du comportement des noyaux de bentonite en condition *in situ*.

Publications

Journal papers

1. **Dieudonné, A.C.**, Cerfontaine B., Collin F. & Charlier, R. (2015). Hydromechanical modelling of shaft sealing for CO_2 storage. *Engineering Geology* **193**, 97–105.

2. Della Vecchia, G., **Dieudonné, A.C.**, Jommi, C. & Charlier, R. (2015). Accounting for evolving pore size distribution in water retention models for compacted clays. *International Journal for Numerical and Analytical Methods in Geomechanics* **39**, No. 7, 702–723.

3. Cerfontaine, B., **Dieudonné, A.C.**, Radu, J.P., Collin, F. & Charlier, R. (2015). 3D zero-thickness coupled interface finite element: Formulation and application. *Computers and Geotechnics* **69**, 124–140.

4. Gatabin, C., Talandier, J., Collin, F., Charlier, R. & **Dieudonné, A.C.** (2016). Competing effects of volume change and water uptake on the water retention behaviour of a compacted MX-80 bentonite/sand mixture *Applied Clay Science* **121–122**, 57–62.

5. **Dieudonné, A.C.**, Della Vecchia, G. & Charlier, R. A water retention model for compacted bentonites. *Canadian Geotechnical Journal*, 10.1139/cgj-2016-0297.

6. **Dieudonné, A.C.** *et al.*. Hydromechanical behaviour of compacted bentonite upon water saturation: experimental observations and modelling. In preparation.

Conference papers

1. **Dieudonné, A.C.**, Levasseur, S., Charlier, R., Della Vecchia, G. & Jommi, C. (2013). A water retention model for compacted clayey soils. *Third International Symposium on Computational Geomechanics, ComGeo III*, Krakow, Poland.

2. **Dieudonné, A.C.**, Charlier, R., Levasseur, S., Della Vecchia, G. & Jommi, C. (2014). Evolution of clay fabric and water retention properties along hydromechanical stress paths. *Numerical Methods in Geotechnical Engineering, Proceedings of the 8th European Conference on Numerical Methods in Geotechnical Engineering, NUMGE 2014*, Delft, the Netherlands.

3. **Dieudonné, A.C.**, Charlier, R. & Romero, E. (2014). Hydration kinetics of compacted low-density bentonite. *Unsaturated Soils: Research and Applications, Proceedings of the 6th International Conference on Unsaturated Soils, UNSAT 2014*, Sydney, Australia.

4. **Dieudonné, A.C.**, Della Vecchia, G., Charlier, R. & Jommi, C. (2014). Influence of microfabric evolution on the retention behaviour of compacted clayey soils. *Unsaturated Soils: Research and Applications, Proceedings of the 6th International Conference on Unsaturated Soils, UNSAT 2014*, Sydney, Australia.

5. Cerfontaine, B., **Dieudonné, A.C.**, Radu, J.P., Collin, F. & Charlier, R. (2015). Three-node zero-thickness hydro-mechanical interface finite element for geotechnical applications. *COUPLED PROBLEMS 2015, Proceedings of the 6th International Conference on Coupled Problems in Science and Engineering*, Venice, Italy.

6. **Dieudonné, A.C.**, Gatabin, C., Talandier, J., Collin, F. & Charlier, R. (2016) Water retention behaviour of compacted bentonites: experimental observations and constitutive model. *Third European Conference on Unsaturated Soils, E-UNSAT 2016*, Paris, France.

7. **Dieudonné, A.C.** & Charlier, R. (2017) Evaluation of the instantaneous profile method for the determination of the relative permeability function. *International Workshop on Advances in Laboratory Testing and Modelling of Soils and Shales*, Villars, Switzerland.

Contents

List of Symbols

Throughout the manuscript, boldface letters denote vectors and tensors.

Roman symbols

a	Parameter of Van Eekelen model
A	Parameter of the macrostructural water retention model
b	Parameter of Van Eekelen model
$\boldsymbol{b}$	Vector of body forces
B	Parameter controlling the dependence of the air-entry value on void ratio in Equation (4.4)
$\boldsymbol{B}$	Transformation matrix in Equation (3.100)
$\mathcal{B}$	Deformable porous body in current configuration
$\partial\mathcal{B}$	Boundary of the deformable body $\mathcal{B}$
$\mathcal{B}_0$	Deformable porous body in reference configuration
$\partial\mathcal{B}_c^i$	Boundary of $\mathcal{B}^i$ on which contact is likely to happen
$\mathcal{B}_i$	Deformable porous body in initial configuration
$\partial\mathcal{B}_{q^a}$	Boundary on which the total air flux is imposed
$\partial\mathcal{B}_{q^w}$	Boundary on which the total water flux is imposed
$\partial\mathcal{B}_t$	Boundary on which the total normal stress is imposed
$\partial\mathcal{B}_{\bar{u}_g}$	Boundary on which gas pressure is imposed
$\partial\mathcal{B}_{\bar{u}_w}$	Boundary on which water pressure is imposed
$\partial\mathcal{B}_{\bar{\boldsymbol{x}}}$	Boundary on which displacements are imposed
c	Cohesion
c_v	Coefficient of consolidation
C_{ads}	Parameter of the microstructural water retention model
CEC	Cation exchange capacity
$\boldsymbol{d}$	Rate of deformation tensor

$\boldsymbol{D}^e$	Global elastic tensor
D_g^w	Diffusion coefficient of water vapour in air
D_g^{w*}	Effective diffusion coefficient of water vapour in the porous medium
D_{g0}^w	Diffusion coefficient of water vapour in air at reference conditions
D_l^a	Diffusion coefficient of dissolved air
D_l^{a*}	Effective diffusion coefficient of dissolved air in the porous medium
$\boldsymbol{D}$	Elastoplastic constitutive tensor
$\boldsymbol{D}^e$	Elastic constitutive tensor
$\boldsymbol{D}^{e*}$	Generalized elastic constitutive tensor
$\boldsymbol{D_c^e}$	Elastic constitutive matrix for the contact problem
$\boldsymbol{D_c^{ep}}$	Elastoplastic constitutive matrix for the contact problem
e	Void ratio
e_{Hg}	Intruded mercury void ratio
e_i	Initial void ratio
e_m	Microstructural void ratio
e_m^*	Water ratio corresponding to fully saturated micropores
e_{m0}	Microstructural void ratio of dry material
e_M	Macrostructural void ratio
e_w	Water ratio
e_{wm}	Microstructural water ratio
e_{wM}	Macrostructural water ratio
$\bar{\boldsymbol{e}}_1$	Normal vector at point $\bar{\boldsymbol{x}}^1$
e	Electric elementary charge ($= 1.602 \times 10^{-19}$ C)
E	Characteristic energy of adsorption
E_0	Characteristic energy of adsorption for a reference vapour
E_{oed}	Oedometric modulus
$\boldsymbol{E}$	Fourth-order elastic stiffness tensor
f	Yield surface
$f\,(x)$	Pore size density function
f_b	Mass fraction of bentonite
f_L^a	Longitudinal total mass flux of air in the interface
f_L^w	Longitudinal total mass flux of water in the interface
f_T^a	Transversal total mass flux of air in the interface

f_T^w	Transversal total mass flux of water in the interface
$\boldsymbol{f^a}$	Total mass flux of air
$\boldsymbol{f^w}$	Total mass flux of water
$\boldsymbol{f_g^a}$	Mass flux of dry air
$\boldsymbol{f_g^w}$	Mass flux of water vapour
$\boldsymbol{f_l^a}$	Mass flux of dissolved air
$\boldsymbol{f_l^w}$	Mass flux of liquid water
$\boldsymbol{f_{OB}}$	Vector of elementary out-of-balance forces
$\boldsymbol{F}$	Deformation gradient of the mapping $\mathcal{B} = \varphi(\mathcal{B}_0)$
$\boldsymbol{F}^\tau$	Deformation gradient between the two configuration $\tau 1$ and $\tau 2$
$\boldsymbol{F_{OB}}$	Vector of global out-of-balance forces
g	Gravity acceleration
g	Flow surface
g_N	Gap function
g_{Ni}	Initial gap aperture
g_T	Tangential displacement
g_T^{sl}	Non-recoverable displacement in the tangential direction
$\boldsymbol{g}$	Vector of gravity acceleration
G	Shear modulus
$G^{\tau 1}$	Air flow residual
H	Sample height
H_a	Henry's constant
H_i	Initial sample height
i_{gL}^a	Longitudinal diffusive flux of dry air in the interface
i_{gL}^w	Longitudinal diffusive flux of water vapour in the interface
i_{lL}^a	Longitudinal diffusive flux of dissolved air in the interface
$\boldsymbol{i_g^a}$	Diffusive flux of dry air
$\boldsymbol{i_g^w}$	Diffusive flux of water vapour
$\boldsymbol{i_l^a}$	Diffusive flux of dissolved air
$\boldsymbol{I}$	Identity matrix or tensor
J	Jacobian of the deformation gradient
$\boldsymbol{J}^e$	Jacobian matrix of the mapping from (ξ, η) to (x_1, x_2)
J_2	Second invariant of the deviatoric stress tensor

J_3	Third invariant of the deviatoric stress tensor
k	Boltzmann constant ($= 1.38 \times 10^{-23}$ J/K)
k	Parameter describing the increase in cohesion with suction
k_g	Gas permeability
k_{gL}	Longitudinal gas permeability of the interface
k_{rg}	Gas relative permeability
k_{rw}	Water relative permeability
k_w	Water permeability
k_{wL}	Longitudinal water permeability of the interface
$\boldsymbol{k}$	Local element stiffness matrix
K	Elastic bulk modulus
K_g	Gas permeability for totally dry conditions
K_l^a	Constant of the Henry's law (3.56)
K_N	Penalty coefficient for normal contact
K_s	Bulk modulus for changes in suction
K_T	Penalty coefficient for shear contact behaviour
K_w	Water permeability for fully saturated conditions
K_{w0}	Reference water permeability measured at the reference porosity ϕ_0
$\boldsymbol{K}$	Global stiffness matrix
$\boldsymbol{L}$	Velocity gradient tensor
m	Parameter of van Genuchten water retention model
m^a	Total air storage
m^w	Total water storage
m_{dry}	Mass of the dried sample
m_g^a	Dry air storage
m_g^w	Water vapour storage
m_l^a	Dissolved air storage
m_l^w	Liquid water storage
m_s	Mass of the solids
m_{sample}	Mass of the sample
m_{sb}	Mass of the bentonite solid particles
m_w	Mass of water
m_π	Mass of the π phase

M_a	Molecular mass of dry air (= 0.029 kg/mol)
M_w	Molecular mass of water (= 0.018 kg/mol)
M_θ	Slope of the critical state line
n	Parameter of van Genuchten water retention model
n	Parameter of Van Eekelen model
n_0	Ion concentration in the electrolyte
n_{ads}	Parameter of the microstructural water retention model
n_k	Parameter of the relative permeability law
$\boldsymbol{n}$	Unit normal vector
$\boldsymbol{n}_{\mathrm{d}\boldsymbol{\varepsilon}^p}$	direction of plastic strain rates in the stress space
$\boldsymbol{N}_{(\xi,\eta)}$	Vector of the shape functions
p	Mean net stress
p_0	Preconsolidation pressure at current suction
p_0^*	Preconsolidation pressure for saturated conditions
p_c	Reference stress in Alonso *et al.* (1990) model
p_{min}	Minimum mean net stress
p_N	Total normal contact pressure
p_s	Left intercept of the LC yield surface
P_e^*	External virtual power
$\bar{q}_a$	Total air flux imposed on the boundary $\partial\mathcal{B}_{q^a}$
q_{gL}	Longitudinal volumetric flux of the gas phase in the interface
q_{lL}	Longitudinal volumetric flux of the liquid phase in the interface
$\bar{q}_w$	Total water flux imposed on the boundary $\partial\mathcal{B}_{q^w}$
$\boldsymbol{q}_g$	Volumetric flux of the gas phase
$\boldsymbol{q}_l$	Volumetric flux of the liquid phase
q	Deviatoric stress
Q^a	Air sink/source term
Q^w	Water sink/source term
r	Parameter defining the minimum soil compressibility (at infinite suction)
r_C	Reduced radius for axisymmetric triaxial stress path of compression
r_E	Reduced radius for axisymmetric triaxial stress path of extension
R	Universal gas constant (= 8.3143 J/mol·K)

$R^{\tau 1}$	Mechanical residual
RH	Relative humidity
$\boldsymbol{R}$	Rigid body rotation tensor
$\boldsymbol{R}$	Rotation matrix
s	(Matric) suction
$\boldsymbol{s}$	Deviatoric stress tensor
s_{AE}	Air-entry value
s_t	Total suction
S_P	Swelling pressure
S_r	Degree of saturation
S_r^*	Threshold degree of saturation in the mechanical model
S_{rHg}	Degree of saturation of mercury
S_{rm}	Degree of saturation of the microstructure
S_{rM}	Degree of saturation of the macrostructure
$S_{r,res}$	Residual degree of saturation
s_0	Hardening parameter of the Suction Increase yield surface
S_S	Specific surface area
t	Time
t_{gT}	Transversal gas transmissivity of the interface
t_i	Initial time
t_{wT}	Transversal water transmissivity of the interface
$\bar{\boldsymbol{t}}$	Imposed Cauchy traction vector
T	Temperature
T_0	Reference temperature
$\boldsymbol{T}$	Transformation matrix in Equation (3.99)
u	Non-dimensional potential at the mid-plane between two clay layers
u_a	Air pressure
u_{atm}	Atmospheric pressure
u_g	Gas pressure
$\bar{u}_g$	Imposed gas pressure
u_{g0}	Reference gas pressure
u_{gi}	Initial gas pressure
u_{Hg}	Mercury pressure

u_l	Liquid pressure
u_v	Vapour pressure
u_v^0	Saturated vapour pressure
u_w	Water pressure
$\bar{u}_w$	Imposed water pressure
u_{w0}	Reference water pressure
u_{wi}	Initial water pressure
$\boldsymbol{u}$	Displacement (field)
$\bar{\boldsymbol{u}}$	Imposed displacement (field)
$\boldsymbol{u}_i$	Initial displacement (field)
$\boldsymbol{U}$	Stretching tensor
$\boldsymbol{U}_{(\xi,\eta)}$	Vector of interpolated unknowns
$\boldsymbol{U_N}$	Vector of nodal unknowns
$\boldsymbol{U_{Nc}}$	Vector of nodal unknowns of the interface element
$\boldsymbol{v}$	Velocity tensor
w	Gravimetric water content
w_B^e	Effective bentonite water content
w_L	Liquid limit
w_P	Plastic limit
$W^{\tau 1}$	Water flow residual
δW_E	External virtual power
δW_I	Internal virtual power
x	Entrance pore size (diameter)
x_c	Distance from the clay layer surface
x_l^a	Dissolved air mass fraction
$\boldsymbol{x}$	Coordinates in the current configuration
$\bar{\boldsymbol{x}}^1$	Closest point projection of a point of $\boldsymbol{x}^2$ of the boundary $\partial\mathcal{B}_c^2$ onto $\partial\mathcal{B}_c^1$
X_{min}	Size of the smallest pores
$\boldsymbol{X}$	Coordinates in the reference configuration
z	Valency of electrolyte ion

Greek symbols

α	Parameter of van Genuchten water retention model
$\boldsymbol{\alpha}_s$	Elastic tensor for suction changes
β	Parameter controlling the swelling tendency of aggregates in Equation (2.9)
β_0	Parameter of the microstructure evolution law (2.10)
β_1	Parameter of the microstructure evolution law (2.10)
β_D	Similarity constant in Dubinin's theory
ε^{σ}	Component of the strain tensor due to stress changes at fixed suction
ε_0	Dielectric permittivity of the vacuum ($= 8.8542 \times 10^{-12}$ C^2/J·m)
ε_d	Deviatoric strain
ε_N	Strain norm
ε_r	Dielectric constant of the electrolyte
ε_v	Volumetric strain
ε_v^e	Elastic volumetric strain
ε_v^p	Plastic volumetric strain
ε_v^{pp}	Plastic volumetric strain associated to stress changes
ε_v^s	Volumetric strain associated to suction changes
ε_v^{sp}	Plastic volumetric strain associated to suction changes
$\varepsilon_{v,FS}$	Swelling potential
ε_{vp}	Volumetric strain associated with changes in net stress
ε_{vs}	Volumetric strain associated with changes in suction
$\boldsymbol{\varepsilon}$	(True) strain tensor
$\boldsymbol{\varepsilon}^*$	Vector of generalized strain variables
η_g	Volume fraction of the gas phase
η_l	Volume fraction of the liquid phase
η_s	Volume fraction of the solid phase
η_π	Volume fraction of the π phase
θ	Lode's angle
θ_{Hg}	Contact angle between mercury and the pore wall
θ_{ws}	Contact angle between water and a soil particle
κ	Slope of the unloading–reloading line for changes in mean net stress

κ'	Apparent swelling index
κ^{-1}	Debye-Hückel length
κ_s	Slope of the reversible wetting–drying line for changes in suction
$\boldsymbol{\kappa}$	Vector of plastic internal variables
λ'	Apparent compression index
$\lambda(0)$	Slope of saturated virgin consolidation line
λ	Slope of virgin consolidation line at current suction
λ^p	Plastic multiplier
λ_s	Slope of the virgin drying line
μ	Friction coefficient
μ_g	Dynamic viscosity of the gas phase
μ_w	Dynamic viscosity of water
π_{osm}	Osmotic suction
ρ	Density of mixture
ρ^π	Reduced density of the homogenised continuous π phase
ρ_a	Dry air density
ρ_d	Dry density
ρ^e_{db}	Effective bentonite dry density
ρ_{di}	Initial dry density
ρ_g	Density of the gas phase
ρ^a_l	Dissolved air density
ρ_s	Density of solid particles
ρ_{sb}	Density of bentonite solid particles
ρ_{sm}	Equivalent solid density of a mixture
ρ_{ss}	Density of sand solid particles
ρ_v	Density of water vapour
ρ_w	Density of liquid water
ρ_{w0}	Reference water density at water pressure $u_w = u_{w0}$
ρ_π	Real density of the π phase
σ_1	Axial net stress in triaxial conditions
σ_3	Lateral net stress in triaxial conditions
σ_{Hg}	Surface tension of mercury
σ_R	Repulsive swelling pressure

σ_v	Total vertical stress
σ_w	Surface tension of water
$\boldsymbol{\sigma}$	Tensor of net stress
$\boldsymbol{\sigma'}$	Tensor of effective stress
$\boldsymbol{\sigma}^*$	Vector of generalized stress variables
$\boldsymbol{\sigma_c}$	Contact stress vector
$\boldsymbol{\sigma_t}$	Tensor of total (Cauchy) stress
$\tilde{\boldsymbol{\sigma}}_{\boldsymbol{t}}$	Jaumann objective total stress rate
$\boldsymbol{\Sigma_c}$	Projection of the local stress vector $\boldsymbol{\sigma}_{\boldsymbol{c}}^i$ in the global coordinates
τ	Tortuosity
τ	Contact shear stress
φ	Friction angle
φ_C	Triaxial compression friction angle
φ_E	Triaxial extension friction angle
ϕ	Porosity
ϕ_0	Reference porosity
ϕ_m	Microporosity
ϕ_M	Macroporosity
χ	Bishop's parameter
χ_w	Water compressibility
ψ	Total water potential
ψ_g	Gravitational potential
ψ_m	Matric potential
ψ_o	Osmotic potential
ψ_p	External pressure potential
Ψ	Electrical potential
Ψ_0	Electrical potential at the clay layer surface
ω	Parameter controlling the rate of increase of soil stiffness with suction
$\boldsymbol{\omega}$	Spin tensor
Ω	Volume of the control space
Ω_g	Volume of the gas phase
Ω_l	Volume of the liquid phase
Ω_m	Volume of micropores

Ω_M	Volume of macropores
Ω_s	Volume of solids
Ω_{sb}	Volume of bentonite solid particles
Ω_v	Volume of voids
Ω_{vM}	Volume of macrovoids
Ω_{wm}	Volume of water in the micropores
Ω_π	Volume of the π phase

Notations and operators

$\cdot$	Inner product of two vectors ($\boldsymbol{a} \cdot \boldsymbol{b} = a_i b_i$) or inner product with single contraction of two tensors ($\boldsymbol{a} \cdot \boldsymbol{b} = a_{ij} b_{jk}$)
$:$	Inner product of two second-order tensors ($\boldsymbol{a} : \boldsymbol{b} = a_{ij} b_{ij}$) or inner product with double contraction of tensors of rank two or higher ($\boldsymbol{a} : \boldsymbol{b} = a_{ijkl} b_{kl}$)
$(\cdot)^T$	Transpose
$\mathrm{d}(\cdot)$	Increment
$\delta(\cdot)$	Kinematically admissible virtual field
$\Delta(\cdot)$	Variation
$\partial(\cdot)/\partial x$	Partial derivative with respect to a variable x
$\mathrm{d}(\cdot)/\mathrm{d}x$	Total derivative with respect to a variable x
$\dot{(\cdot)} = \mathrm{d}(\cdot)/\mathrm{d}t$	Time derivative
$\nabla(\cdot)$	Gradient
$\nabla \cdot (\cdot)$	Divergence
δ_{ij}	Kronecker delta ($\delta_{ij} = 1$ if $i = j$, $\delta_{ij} = 0$ otherwise)
ϵ_{ijk}	Levi-Civita symbol
$\langle \cdot \rangle$	Macaulay bracket
$\sum(\cdot)$	Summation

Chapter 1

Introduction

1 Motivations and general context

Electricity production in nuclear power plants, but also nuclear medicine, agriculture, scientific research and many types of industries, use radioactivity. These activities inevitably generate radioactive wastes that are classified into different categories depending on their activity and the half-life period of their radioactive isotopes (IAEA, 2009). Among these wastes, the high-level and intermediate-level radioactive wastes are the most harmful to the human health and the environment. They both contain long-lived radionuclides whose decay is extremely slow, and they remain therefore toxic over long time periods. As a consequence, the long-term management of these wastes has become of great concern to the nuclear industry, including nuclear power plant operators and government agencies responsible for safety.

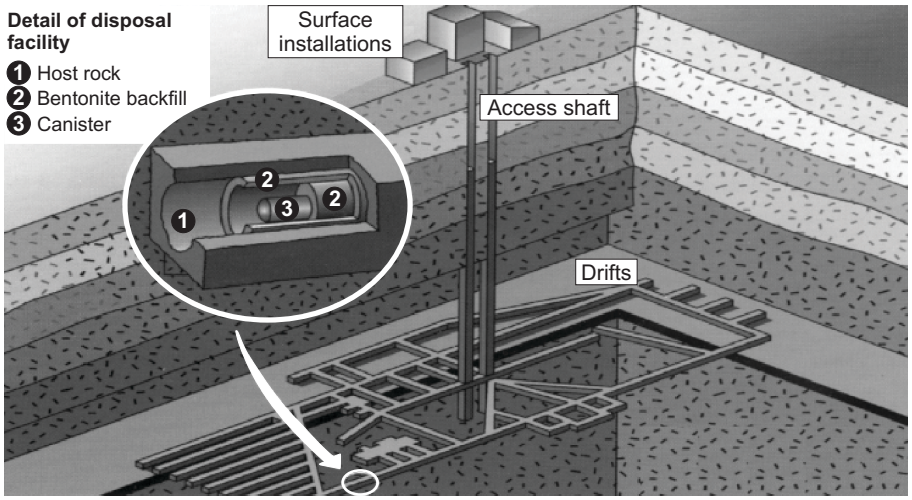

Figure 1.1: Conceptual scheme of deep geological repository for radioactive waste (Gens *et al.*, 2009).

In this context, deep geological disposal constitutes one of the most promising solutions for the safe isolation of high-level and intermediate-level radioactive wastes (OECD/NEA, 1995; NEA, 2008). It consists in disposing the wastes in deep and stable geological forma-

tions with good confining conditions, in order to ensure that the rate of any radionuclide release remains below some prescribed limits (Chapman & McKinley, 1987). Depending on the country, different concepts of disposal are considered (see Sellin & Leupin, 2013, for a review). Yet, in all cases, the safe isolation of the radioactive waste relies on a multi-barrier concept, according which isolation is provided by a combination of natural and engineered barriers. Figure 1.1 presents a conceptual scheme of deep geological repository for radioactive waste. While the surrounding geological formation (typically clay, claystone or granite) constitutes a natural barrier, the engineered barriers, sometimes termed engineered barrier system or EBS, include different manufactured components, such as the canisters, buffers and backfilling materials.

The first engineered barrier is the canister. It is generally made of steel or copper and contains the radioactive waste. The canister is designed to retain the radionuclides for thousands of years (Sellin & Leupin, 2013). Canisters are emplaced in horizontal drifts or in vertical boreholes. In the French CIGEO concept (Labalette *et al.*, 2009), the space between the canisters and the geological formation is filled by concrete and bentonite-based materials are used as backfill materials in access galleries and shafts of the deep geological repository, as well as at the disposal cells dedicated to intermediate level waste[1] (Figure 1.2). On the other hand, in the Spanish, Swedish and Swiss concepts, among others, the space between the canisters and the geological formation is filled using compacted or granular bentonite, or a combination of both.

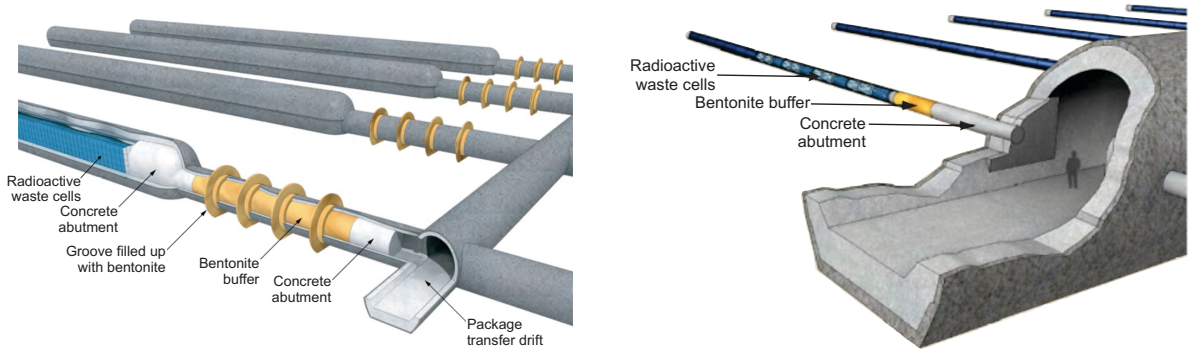

(a) Concept for the intermediate-level long-lived waste.

(b) Concept for the high-level waste.

Figure 1.2: CIGEO concept for the deep geological repository of intermediate-level long-lived and high level radioactive waste (Andra, 2005).

In all concept designs, bentonite-based materials have indeed been selected for their

- **High swelling capacity**: the installation of the bentonite buffer within a gallery involves unavoidable technological gaps between the engineered barrier and the host rock. Initially unsaturated, the bentonite barrier will be subjected to hydration from the surrounding saturated host rock. During this process, it will expand and fill the technological gaps. Once in contact with the host rock, the bentonite buffer will

[1]This choice of not using bentonite as a buffer between the canister and the host rock has been motivated by retrievability concerns.

develop swelling stresses, close fractures of the excavation damaged zone, and form a tight contact with the surrounding geological formation in order to limit preferential pathways.

- **Low permeability**: compacted bentonite has a very low permeability which will significantly delay the radionuclides migration. Placed between the canister and the geological formation, the bentonite barrier also aims at limiting water flow from the host rock to the canister in order to retard corrosion of the canister and release of radionuclides.

- **Important retention capacities**: bentonite has good retention capacities that should, together with the low permeability, limit the release of radionuclides to the environment.

The hydromechanical behaviour of bentonite-based materials under repository conditions is complex, owing for the strongly coupled multi-physical and multi-scale processes taking place. Because of the central role of bentonite in the repository safety, an excellent understanding and efficient prediction capability of the material behaviour are of paramount importance.

2 Objectives

During the life of the repository, different strongly coupled hydromechanical processes will affect the bentonite barrier. This thesis was motivated by the challenging task of better understanding and modelling the hydromechanical behaviour of compacted bentonite-based materials under *in situ* conditions. More specifically, the objectives of the PhD research included:

- the identification of the conditions, mains features and significant aspects to be considered in constitutive and numerical models. This work is essentially based on both an extensive literature review and on the experience gained by the geomechanics research group of the University of Liege on modelling the multi-physical behaviour of geomaterials (see the PhD thesis of Li, 1999; Collin, 2003; Gerard, 2011, among others).

- the development of a hydromechanical model able to better reproduce the behaviour of compacted bentonite under repository conditions. Classic hydromechanical models for clays show indeed some limitations in reproducing the strongly coupled behaviour of expansive materials.

- the implementation of the developed model in the finite element code `LAGAMINE`, its verification and its validation against experimental data from laboratory tests.

- the application of the developed model to reproduce the behaviour of a bentonite plug under repository conditions. More particularly, the PGZ2 *in situ* test, carried out by the Andra in its Meuse/Haute-Marne underground research laboratory, will be modelled.

3 Outline of the thesis

The manuscript consists of 8 chapters covering the literature review and developments achieved during the PhD research. The chapters are organised in a logical sequence, starting with the description of the material at a microscopic scale and progressively addressing the problem at larger scales.

In **Chapter 2**, the hydromechanical processes taking place in bentonites are described from a microscopic point of view. The mineralogical composition, structure and physicochemical properties of bentonites are presented and used to explain the hydration and swelling mechanisms. The influence of hydraulic and mechanical loading on the structure of the materials is then described and analysed. Constitutive models for the evolution of the microstructure are presented.

Chapter 3 presents the general framework adopted in this research work to model the hydromechanical behaviour of bentonite-based materials. The equations governing the problem, including balance equations, constitutive models and equilibrium restrictions, are developed and the finite element formulation for porous media is presented. Rather than presenting any original contribution, this chapter set the basis for the developments presented in the next chapters.

Chapter 4 is devoted to the water retention properties of compacted bentonites. These properties are strongly influenced by the dry density of the material and the confining conditions. Accordingly, classic water retention models are not able to reproduce the water retention behaviour of bentonite-based materials under repository conditions where significant dry density changes are observed. Based on an in-depth understanding of the material microstructure and water retention mechanisms, a new model for the water retention behaviour of compacted bentonites is developed and validated.

Chapter 4 is dedicated to the development of a mechanical model for saturated and partially saturated bentonite. The Barcelona Basic Model developed by Alonso *et al.* (1990) is selected as a starting model and is implemented in the finite element code `LAGAMINE`. The model is used to reproduce the behaviour of different bentonite-based materials along various stress paths. Owing for important limitations in reproducing the swelling pressure developed under confined conditions, the Barcelona Basic Model is enhanced to account for the important air-entry value of bentonites.

Chapter 6 extends the multiphase flow model presented in Chapter 3 to account for the evolution of material microstructure along hydromechanical stress paths. In particular, a dependency of the permeability on the macrostructural void ratio is introduced. The influence of the newly introduced hydromechanical coupling on the hydration kinetics of bentonite is highlighted.

Chapter 7 develops the problem at one step larger scale and is devoted to the hydromechanical behaviour of interfaces. Interfaces and technological gaps are unavoidable features in underground disposals that have long been disregarded from both experimental

and numerical point of views. The existing data are presented and the lacks are highlighted. An experimental study is carried out in order to better characterize the normal hydromechanical behaviour of interfaces. Then, a zero-thickness interface element is presented and used to model interfaces and technological gaps.

Chapter 8 aims at validating the developed models by modelling two laboratory and *in situ* experiments carried out on the same material, namely the Bentogaz 2 and PGZ2 tests. The Bentogaz 2 test was performed by the French Atomic Energy Commission (CEA) in order to study the water saturation and gas migration processes in compacted bentonite (Gatabin & Guillot, 2008; Gatabin *et al.*, 2011). Its extensive instrumentation provide valuable information to validate our model. The PGZ2 experiment is then modelled and the complex behaviour of the buffer is explained in the light of the new model.

Finally, **Chapter 9** concludes with a summary and outlooks for future works.

Chapter 2

Microscopic approach to coupled processes

1 Introduction

The role of engineered barriers in geological disposal of radioactive waste is to form a tight contact with the host rock, and thereby limit the release of radionuclides to the biosphere. The low permeability and important swelling capacity of bentonites are therefore essential properties. In order to characterize the swelling capacity of compacted bentonites, two macroscopic physical quantities can be measured: the swelling potential and the swelling pressure. These quantities are determined after saturation of a bentonite sample under different confining conditions. The swelling potential $\Delta H/H_i$ corresponds to the ratio between the change in sample height ΔH upon saturation under oedometer conditions, and its initial height H_i. On the contrary, the swelling pressure S_P is defined as the pressure required to prevent volume changes upon wetting. Figure 2.1 presents the evolution of the swelling pressure of five reference bentonites with dry density. While important differences are observed between the different bentonites, they all show an increase of their swelling pressure with dry density. Furthermore, the swelling pressures reached upon saturation

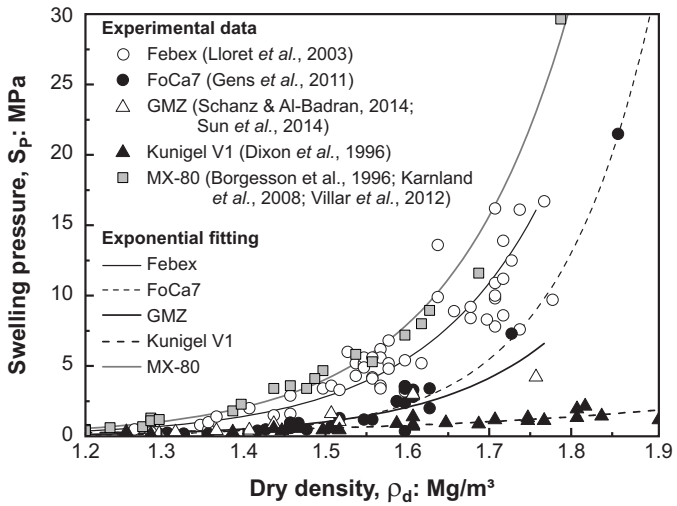

Figure 2.1: Evolution of the swelling pressure of five reference bentonites with dry density.

(typically of the order of few MPa to around 15 MPa for dry densities ranging between 1.5 and 1.7 Mg/m^3) are significantly higher than for non-swelling clays (few hundreds kPa).

While the swelling capacity of compacted bentonite is firstly observed at the macroscopic scale, this property essentially results from physicochemical phenomena taking place at a microscopic scale. Therefore, a good comprehension of the material microstructure is of paramount importance for a better understanding of the hydromechanical behaviour of compacted bentonites and for the development of physically-based constitutive models.

In this chapter, the mineralogical composition of bentonites is first presented. Then, the structure and coupled processes taking place in compacted bentonites are described starting from the smallest scale of interest, namely the scale of the clay minerals. Accordingly, the structure and physicochemical properties of clay minerals are presented. Attention is then focused on the hydration and swelling mechanisms in smectites, the main constituents of bentonites. Increasing the scale of observation, the structure of compacted bentonites is then addressed. The water storage and hydration mechanisms are analysed. Finally, the different factors affecting the material structure are presented and a new model for the microstructure evolution is proposed. All along this chapter, the idea is to provide keys for a better understanding of the macroscopic behaviour and coupled processes in compacted bentonite-based materials.

2 Definition and mineralogical composition of bentonites

The name bentonite dates back to the late 19^{th} century when Knight (1898) used the term to describe highly plastic and swelling clays from the Cretaceous Fort Benton group in Wyoming, USA. The first definitions of bentonite (Hewitt, 1917; Wherry, 1917; Ross & Shannon, 1926) suggested a genetic origin of the material, generally from the alteration of tuff or volcanic ash. Nowadays, the term bentonite has lost its mineralogical definition and refers to any smectite-rich material regardless of its geological origin (Grim, 1968). More specifically, in the context of nuclear waste disposal, bentonite primarily consists of montmorillonite, a clay mineral of the smectite group which exhibits significant swelling upon hydration (Apted, 1995).

Table 2.1 presents the mineralogical composition of five reference bentonites which are studied as potential barriers for the isolation of high-level and intermediate-level radioactive waste. Besides montmorillonite, these bentonites contain variable quantities of other clay minerals (generally kaolinite and illite, which are non-swelling clay minerals), quartz[1], feldspars, plagioclase, gypsum, pyrite and calcite. They can also hold small amounts of organic matter (usually less than 0.5%). Although present in limited quantities, some of these accessory minerals may influence the properties of bentonites, especially their chemical reactivity (Sellin & Leupin, 2013).

[1] In Table 2.1, the content in SiO_2 corresponds to the total content in quartz, cristobalite and tridymite.

Bentonite	**Origin**	**Phyllosicilicate**	**SiO_2**	**K-feldspar**	**Plagioclase**
Febex[a]	Spain	92% interstratified montmorillonite–illite (10–15% illite)	2%	traces	2%
FoCa7[b]	France	80–85% interstratified smectite–kaolinite (50% Ca-beidellite, 50% kaolinite) 4–6% kaolinite	1.4–6%		
GMZ[c]	China	75.4% montmorillonite 0.8% kaolinite	20%	4.3%	
Kunigel V1[d]	Japan	46–49% montmorillonite	29–38%	2.7–5.5%	4%
MX-80[e]	USA	75–90% montmorillonite	2.8–15.2%	2–8%	9.2%

[a]Fernandez (2004), Lloret & Villar (2007)
[b]Proust *et al.* (1990), Bruno (1993), Lajudie *et al.* (1994)
[c]Wen (2006)
[d]JNC (2000), Nakashima (2004)
[e]Lajudie *et al.* (1994), Madsen (1998), Montes-H (2002)

Table 2.1: Mineralogical composition (main minerals) of five reference bentonites.

3 Structure of clay minerals

3.1 Structure and mineralogy

Clay minerals belong to the phyllosilicate group. The term phyllosilicate derives from the Greek *phyllon*, leaf, emphasizing the layered structure of clay minerals. This structure is based on the combination of two basic crystal structural units, namely the tetrahedral sheet and the octahedral sheet.

The tetrahedral sheet is also called silica sheet. As shown in Figure 2.2(a), it is made up of silica tetrahedra $(SiO_4)^{4-}$, which are linked together by sharing three of their four oxygen ions. All tetrahedra of the silica sheet are oriented in the same direction and define hexagonal cavities. Similarly, Figure 2.2(b) shows the structure of the octahedral sheet, also termed alumina sheet. The octahedral sheet is composed of aluminium or magnesium octahedra in which the cation bonds with six oxygen atoms or hydroxyl groups. Octahedra are all laid on a triangular face and linked together by sharing their six oxygens or hydroxyls.

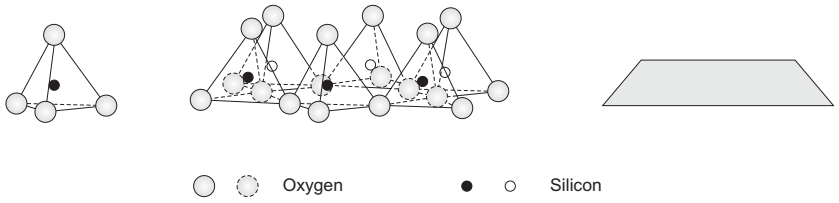

(a) Silica tetrahedron, tetrahedral sheet and schematic representation of the tetrahedral sheet.

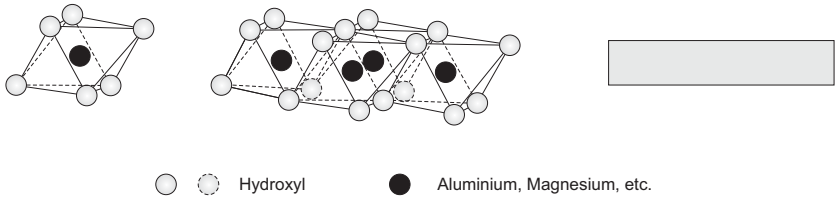

(b) Aluminium or magnesium octahedron, octahedral sheet and schematic representation of the octahedral sheet.

Figure 2.2: Basic crystal structural units of phyllosilicates (Mitchell & Soga, 2005).

Tetrahedral and octahedral sheets bond together to form layers. Two types of layers are defined, namely the TO layer and the TOT layer. The TO layer, also called 1:1 layer, is made up of one tetrahedral sheet and one octahedral sheet, and has a thickness of 7.2 Å. On the other hand, the TOT layer, or 2:1 layer, consists of an octahedral sheet sandwiched between two tetrahedral sheets. Its thickness in the absence of any polar molecule is 9.6 Å. In both cases, strong primary bonds exist between the sheets of a same layer (Stçepkowska, 1990).

Conversely, the bonds between two successive layers are generally weaker. The type of layers and the nature of the interlayer determine the properties of the different clay minerals and, in particular, their behaviour in presence of water. On this basis, clay

minerals are classified into different groups, as depicted in Figure 2.3. The main clay minerals composing bentonites, namely smectite, kaolinite and illite, are to be found in this classification.

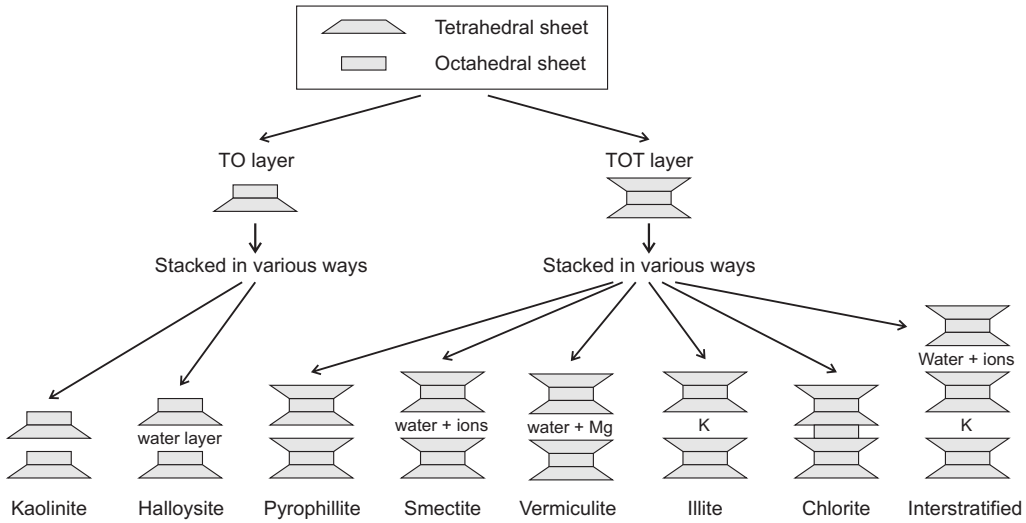

Figure 2.3: Classification of clay minerals (Mitchell & Soga, 2005).

The structure of kaolinite is based on the TO layer, whereas the structures of smectite and illite are built on the TOT layer. In kaolinite, hydroxyl groups and oxygen ions of two consecutive layers are bonded through hydrogen bonds which maintain the interlayer closed and prevent swelling. Only the external surfaces can adsorb water, allowing a weak swelling. In smectites, water molecules and ions are able to penetrate the interlayer space, causing the expansion of the mineral upon wetting. Conversely, the interlayer space of illite is occupied by potassium ions whose molecular size is close to the one of the hexagonal cavities of the tetrahedral sheet, and which therefore strongly lock the layers together through ionic bonds, hence preventing swelling. When layers of different types are stacked together, the mineral is referred to as a mixed-layer or interstratified mineral, and its behaviour depends on the nature of the different layers and interlayers.

Finally, clay layers stack together to form particles. Depending on the nature of the interlayer and the water content, the number of layers in a particle may vary from a few to several hundreds (Saiyouri *et al.*, 2004). The behaviour of the different clay minerals in presence of water is further discussed in the next two sections, with a special attention given to smectites.

3.2 Physicochemical properties

A fundamental characteristic of clay minerals is their electronegativity. The surface of phyllosilicates is indeed not electrically neutral and surface charges exist (Table 2.2). These charges have two different origins:

- **Isomorphous substitutions**, which refer the replacements of ions in the tetrahedral or octahedral sheets for other ions, without significant change in the layer structure. When a cation in a tetrahedral or octahedral sheet is replaced by a lower

valency ion, the substitution leads to an excess of negative charge at the surface of the layer. The most common isomorphous substitutions in clay minerals are Al^{3+} for Si^{4+} in the tetrahedral sheet and Mg^{2+}, Fe^{2+} and Mn^{2+} for Al^{3+} in the octahedral sheet.

Isomorphous substitutions are common in smectites which explains their important surface charges compared to other phyllosilicates (Table 2.2). Depending on the position of the charges, smectites are classified into montmorillonites, whose charges are predominantly in octahedral position, and beidellite, whose charges are predominantly located in tetrahedral position. Bentonites are mainly composed of montmorillonite.

- **Local charges**, which are due to broken bonds and an incomplete neutralization of charges on the edges of the layers. The value of these local charges depends on the pH of the solution (Grunberger, 1995). In acid environments, charges are positive due to the fixation of H^+ protons on the O^{2-} anions; they are negative if the solution is basic.

  According to Mitchell & Soga (2005), local charges are thought to contribute up to 20% towards the total charge deficit.

		Kaolinite	**Illite**	**Montmorillonite**
Surface charges	(meq/100 g)	5–15	20–40	80–100

Table 2.2: Range of surface charges in kaolinite, illite and montmorillonite (Yong *et al.*, 2009).

The natural tendency is to ensure electroneutrality of the clay particle and therefore, the layer will tend to adsorb cations present in the environment. These cations that form the interlayer are called exchangeable cations as they can be exchanged with other cations of the solution (Van Olphen, 1963). According to Sposito *et al.* (1984), exchangeable cations are adsorbed at the surface of the layer by at least three different mechanisms:

- **Inner-sphere complexation**, by which cations bind to the clay surface (through primary bonds) without any interposed water molecule.
- **Outer-sphere complexation**, by which solvated cations are attracted and bonded to the clay surface through hydrogen bonds and electrostatic forces.

  Inner-sphere and outer-sphere complexes form the Stern layer (Stern, 1924) (Figure 2.4). These complexes may be insufficient to balance the negative charges at the clay surface, so that a third mechanism allows to neutralize the residual charges.
- **Electrostatic attraction** of solution cations, resulting from the presence of unbalanced charges at the surface of the clay layer. The attracted cations from the solution form the diffuse double layer (Figure 2.4).

As mentioned by Sposito *et al.* (1984), outer-sphere complexes differ from cations adsorbed in the diffuse layer in their residence time, i.e. the amount of time that a cation remains

adsorbed at a given position. The residence time of cations from the diffuse layer is of the order of 10 ps, which is significantly shorter than the 100 ps residence time of outer-sphere complexes and over 10 ns of inner-sphere complexes (the strongest the bonding, the longest the residence time).

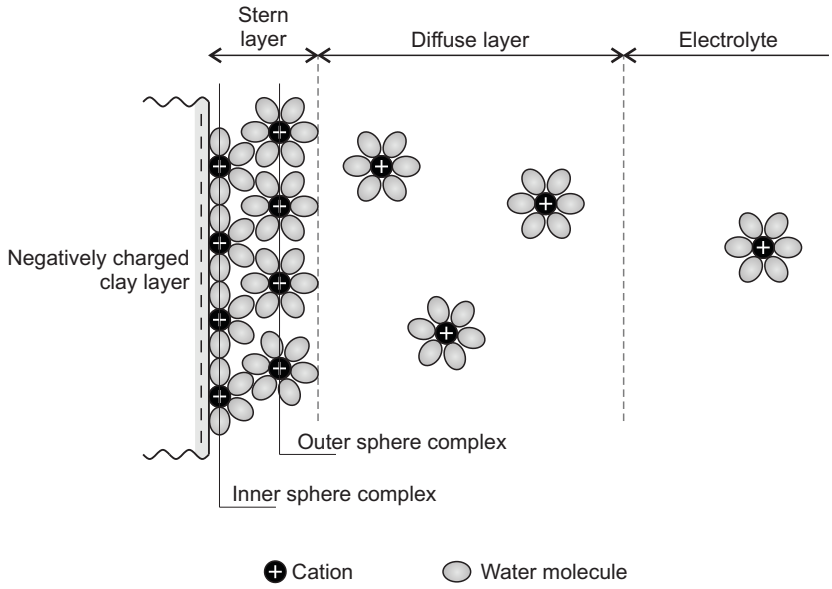

Figure 2.4: Mechanisms of cation adsorption at the surface of a clay layer (after Meunier, 2005; Yong *et al.*, 2009).

The cation exchange capacity (CEC) measures the ability of smectites to adsorb cations from the solution. The CEC is defined as the number of exchangeable positive charges per 100 g of dry clay mineral. It is expressed in milliequivalents per 100 g of dry clay (meq/100 g). In general, the interlayer comprises a mixture of different cation species, essentially Na^{+}, Ca^{2+} and Mg^{2+} in bentonites. Table 2.3 presents the CEC and main exchangeable cations of five reference bentonites. Based on the nature of the dominating exchangeable cations, bentonites are referred to as sodium bentonite or calcium bentonite: Febex and Foca7 are calcium bentonites, GMZ and Kunigel V1 are sodium-calcium bentonites, while MX-80 is a sodium bentonite. As explained in the next section, the nature of the exchangeable cation influences the swelling capacity of the bentonite, with a higher capacity in sodium bentonites.

Finally, another important physicochemical parameter of clay minerals is their specific surface area S_S, expressed in m^2/g. The total specific surface area comprises both the interlayer surface area and the clay particle external surface area. Table 2.3 presents the values of specific surface area for five reference bentonites. Obviously, a strong correlation of the CEC with the specific surface is observed, the CEC being all the more important that the specific surface is large.

Bentonite	**CEC**	**Exchangeable cations**			**Specific**
		Na^+	**Ca^{2+}**	**Mg^{2+}**	**surface**
	(meq/100 g)	(meq/100 g)	(meq/100 g)	(meq/100 g)	(m^2/g)
Febex[a]	111	25	47	36	725
FoCa7[b]	69	3	63		454
GMZ[c]	77.3	43	29	12	570–597
Kunigel V1[d]	73	41	29	3	389–687
MX-80[e]	76–88	61–67	8–10	3–5	512–800

[a]Lloret & Villar (2007)
[b]Saiyouri *et al.* (2004)
[c]Wen (2006), Ye *et al.* (2009)
[d]Komine & Ogata (1996), JNC (2000), Marcial *et al.* (2002), Komine (2004)
[e]Pusch (1982), Madsen (1998), Bradbury & Baeyens (2003), Villar (2007)

Table 2.3: Cation exchange capacity and specific surface of five reference bentonites.

3.3 Hydration and swelling mechanisms in smectites

The swelling capacity of clay minerals refers to their ability to expand upon hydration and shrink upon drying. Accordingly, a good understanding of the hydration mechanisms is required to puzzle out the swelling mechanisms. Starting from dry conditions, two regimes of swelling are generally identified (Norrish, 1954):

- **Crystalline swelling**, which is predominant at low water contents and corresponds to the progressive intercalation of discrete layers of water in the interlayer space (development of the Stern layer). In the case of smectites, one, two, three or four layers of water molecules are sequentially intercalated, leading the interlayer to increase sequentially from 9.6 Å with no water to 12.6 Å, 15.6 Å, 18.6 Å and 21.6 Å respectively. Figure 2.5(a) presents the evolution of the interlayer thickness during hydration of compacted MX-80 bentonite.

  As shown in Figure 2.5(b), the insertion of layers of water molecules in the interlayer space leads to a reorganisation of the solid matrix (Tessier, 1978). During hydration, clay particles initially made of 350 layers divide into smaller structures of around 10 layers. These smaller particles are able to fix high amount of water and form water layers up to 100 Å thick (Saiyouri *et al.*, 2000).

- **Osmotic swelling**, which is associated with interactions of the diffuse double layer. Under high water content, the interlayer is a highly concentrated medium as compared with the bulk solution. As a consequence of the difference in cation concentrations, the cations near the clay surface tend to diffuse away. However, the negative electric field at the clay surface prevents the cation to freely diffuse. Contrary to crystalline swelling, swelling is a continuous phenomenon in the osmotic domain. Furthermore, it occurs both between clay layers and between clay particles (Cases *et al.*, 1990; Mitchell & Soga, 2005).

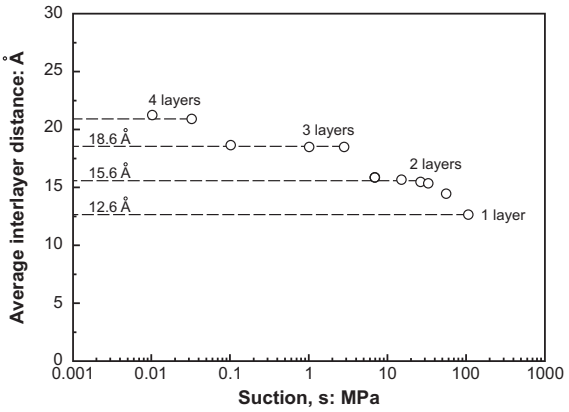

(a) Increase in the number of adsorbed water layers.

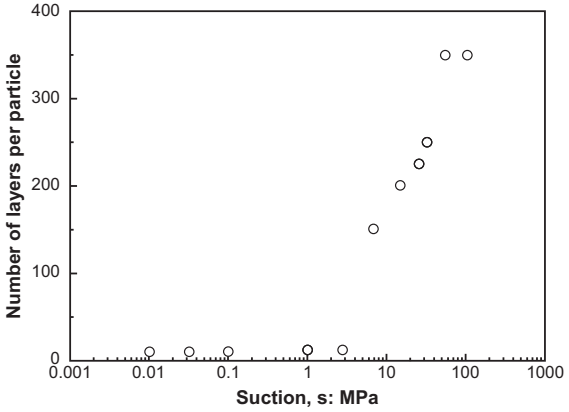

(b) Decrease in the number of stacked layers per particle.

Figure 2.5: Effect of hydration (suction decrease) on particles of MX-80 bentonite (Saiyouri *et al.*, 2004).

Neglecting the existence of the Stern layer, the clay – water system has traditionally been described using the diffuse double layer (DDL) theory early developed by Gouy (1910) and Chapman (1913). In the DDL theory, a unique particle surrounded by an ionic solution is considered. The clay layer is supposed uniformly charged over its surface and ions are considered as point charges without interaction. The electrical potential Ψ around the clay layer (Figure 2.6(a)) is then given by

$$\Psi = \Psi_0 \exp\left(-\kappa x_c\right) \tag{2.1}$$

where Ψ_0 is the electrical potential at the clay layer surface and x_c is the distance from the clay layer surface. κ^{-1} is the Debye-Hückel length given by

$$\kappa^{-1} = \left(\frac{\varepsilon_r \varepsilon_0 kT}{2n_0 \mathrm{e}^2 z^2}\right)^{1/2} \tag{2.2}$$

where ε_r is the dielectric constant of the electrolyte, ε_0 is the dielectric permittivity of the vacuum ($= 8.8542 \times 10^{-12}$ C^2/J·m), k is the Boltzmann constant ($= 1.38 \times 10^{-23}$ J/K), T is the absolute temperature, n_0 is the ion concentration in the electrolyte, e is the electric elementary charge ($= 1.602 \times 10^{-19}$ C) and z the valency of the ion in the electrolyte.

The diffuse double layer theory can be used to describe the behaviour of colloidal solutions in which clay minerals are dispersed in a continuous liquid phase (Van Olphen, 1963). However, in compacted bentonites, the density is such that clay minerals interact through their diffuse double layer and a repulsion force takes place, similarly to two magnets that are brought close to each other. This repulsion force may be assimilated to a swelling pressure (Figure 2.6(b)). Bolt (1956) used the diffuse double layer theory to predict the swelling pressure developed between two parallel clay layers. Although one can show that this hypothesis is not satisfied in compacted bentonites (see Segad *et al.*, 2010, for a discussion), the theory provides interesting qualitative results. In particular, the repulsive swelling pressure σ_R is expressed as

$$\sigma_R = 2n_0 kT\left(\cosh u - 1\right) \tag{2.3}$$

where u is a non-dimensional potential at the mid-plane between the two clay layers[2]. This non-dimensional potential u will be all the more important given that the electrical potential Ψ around a single clay layer is large.

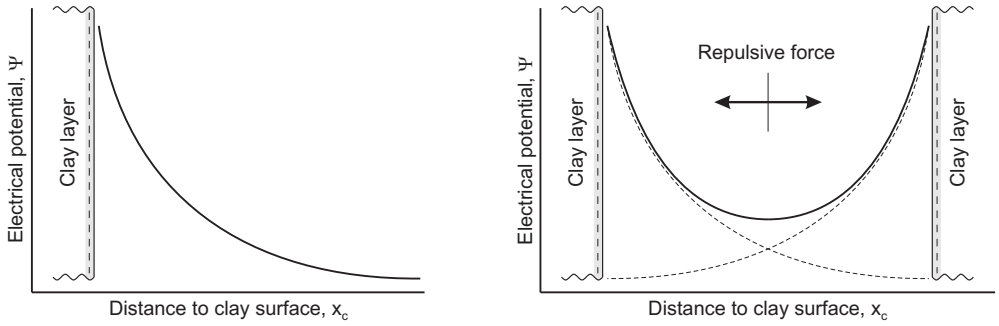

(a) Single clay layer. (b) Two parallel clay layers.

Figure 2.6: Representation of the double diffuse layer, according to Gouy-Chapman theory. Evolution of the electrical potential as a function of the distance from the clay layer surface.

Despite the restrictive assumptions behind the double diffuse layer theory, some interesting and qualitative conclusions may be drawn concerning the factors affecting the swelling pressure of bentonite-based materials:

- the higher the dry density, the higher the swelling pressure (Figure 2.1). Under the assumption of homogeneous and parallel particle distribution, an increase in the dry density yields a decrease in the distance between clay minerals, hence an increase in the mid-plane potential u (Figure 2.6(b)).

- the higher the CEC, the higher the swelling pressure. A high CEC corresponds to an important surface charge density, hence an important electric potential Ψ_0 and an important mid-plane potential u.

- the lower the valency z of the exchangeable cation, the higher the mid-plane potential u and the higher the swelling pressure. Accordingly, the swelling properties are enhanced for sodium bentonites compared to calcium bentonites.

Analysing in details the mineralogical composition (Table 2.1), cation exchange capacity and specific surface (Table 2.3) of the five reference bentonites, the obvious difference in swelling pressure developed by the different materials may be partly explained by the diffuse double layer theory. For instance, one can observe that the low montmorillonite content of Kunigel V1 bentonite is associated with low swelling pressures. Conversely, the important montmorillonite content and Na^+ dominant exchangeable cation of MX-80 bentonite lead to the development of very high swelling pressures upon hydration under constant volume conditions.

[2]Details concerning the precise determination of u can be found in Van Olphen (1977) and Tripathy *et al.* (2004).

4 Structure of compacted bentonites

4.1 Experimental techniques

The microstructure of compacted bentonites[3] can be investigated by using different experimental techniques depending on the type of information required and the scale under consideration. The information that may be obtained from microstructural experimental study includes the pore types, distribution and connectivity, the arrangement and distribution of clay particles and aggregates, the aggregate size and morphology, and the inter-particle contact orientations and contact force directions (Romero & Simms, 2008). The scale that can be investigated ranges from the nm to the mm. Figure 2.7 presents the range of applications of five experimental techniques that are commonly used to study the structure of compacted bentonites:

- **Adsorption techniques** are used to determine the specific surface area of clay minerals. Different gases, including nitrogen and carbon dioxide, as well as methylene blue, can be used as sorbates. A description of the different adsorption techniques can be found in Adamson (1990) and Santamarina *et al.* (2002).

- **X-ray diffraction (XRD)** allows the characterization of the mineral phases present in samples. Qualitative and semi-quantitative descriptions of the nature of the clay minerals are possible. The technique may also be used to investigate the effects of the hydration process at the scale of the clay layers (see Cases *et al.*, 1997; Devineau *et al.*, 2006; Likos & Lu, 2006; Villar *et al.*, 2012, among others). A complete presentation and guide for the interpretation of XRD results are found in Moore & Reynolds (1997).

- **Mercury intrusion porosimetry (MIP)** is a qualitative and quantitative technique used to investigate the pore size distribution (PSD) of a porous sample. The principle is based on the injection of mercury into a sample previously dried. Appendix A presents the methodology for the interpretation of mercury intrusion porosimetry results. A review of the applications of MIP for the investigation of unsaturated soils microstructure is presented by Romero & Simms (2008).

- **Electron microscopy** provides essentially qualitative information on the pore structure via micrographs of the material, although some quantitative information may be obtained by using digital image analysis. Different techniques exist, such as Scanning Electron Microscopy (SEM), Environmental Scanning Electron Microscopy (ESEM), Transmission Electron Microscopy (TEM). A review of the applications of ESEM for the investigation of unsaturated soils microstructure is presented by Romero & Simms (2008).

- **Computed tomography (CT)**, including microfocus tomography (μCT), is a high-resolution non-destructive 3D observation technique based on the combination of a high number of X-ray images. This class of experimental techniques provides similar information to electron microscopy but in three dimensions.

[3]In this work, the term microstructure is used to refer to the structure of materials as observed at a small scale, called microscopic scale, typically ranging from 1 nm to 1 mm.

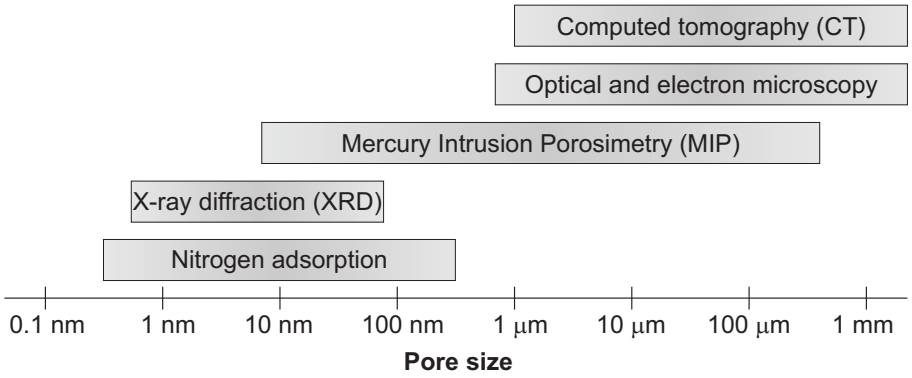

Figure 2.7: Range of applications of various experimental techniques used to investigate the microstructure of porous materials.

4.2 Experimental observations and representation

Figures 2.8(a) and 2.8(b) present ESEM micrographs of compacted Febex and GMZ bentonites respectively. In these micrographs, aggregates with sizes of the order of 20 μm are clearly observed. These aggregates are clusters of clay particles and are formed upon compaction of bentonite dry of optimum. Besides the clay layer and the clay particle, the aggregate represents a third level of organisation in compacted bentonites. Accordingly, the space between aggregates defines a new pore family, called inter-aggregate porosity, or macroporosity.

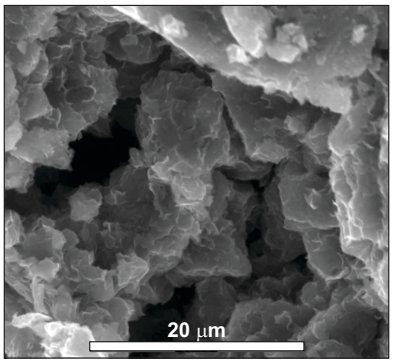

(a) Compacted Febex bentonite with dry density $\rho_d = 1.72$ Mg/m^3 and water content $w = 13.7\%$ (Lloret *et al.*, 2003).

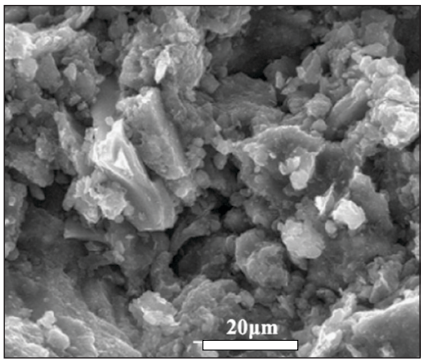

(b) Compacted GMZ bentonite with dry density $\rho_d = 1.75$ Mg/m^3 and water content $w = 11.1\%$ (Ye *et al.*, 2009).

Figure 2.8: Micrographs of two compacted bentonites obtained using an environmental scanning electron microscope.

Mercury intrusion porosimetry provides further insight into the structure of the compacted bentonites and the pore size distribution. Figure 2.9 presents the pore size distributions obtained by Lloret *et al.* (2003) on Febex bentonite compacted to dry densities of 1.5 Mg/m^3 and 1.8 Mg/m^3. In this figure, a bimodal distribution is clearly observed, the two peaks being in the range of pore sizes of 10 nm and 10 μm for the highest dry density, and 10 nm and 40 μm for the lowest dry density. The size of the larger pores is consistent with the inter-aggregate pores observed in Figure 2.8(a).

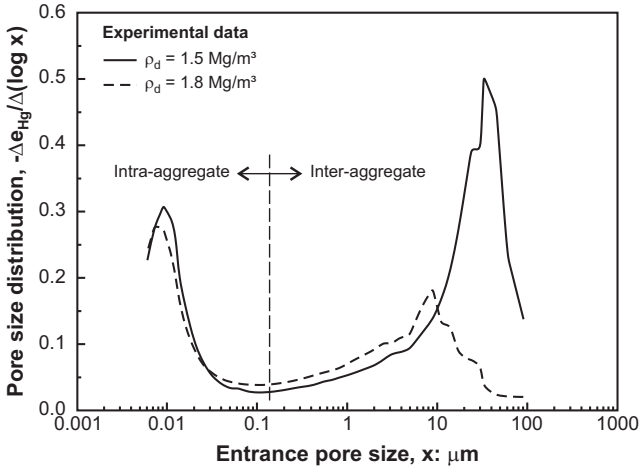

Figure 2.9: Pore size distribution of Febex bentonite compacted at different dry densities, $\rho_d = 1.5$ Mg/m^3 and $\rho_d = 1.8$ Mg/m^3 (Lloret *et al.*, 2003).

In Figure 2.9, the pore family with the peak around 10 nm corresponds to the intra-aggregate porosity, and more specifically the inter-particle porosity. Note that pores smaller than around 6 nm (corresponding essentially to intra-particle pores) cannot be investigated by using mercury intrusion porosimetry. The intra-aggregate porosity is therefore not homogeneous and includes pores between particles (inter-particle porosity) and inside a particle (inter-layer porosity). In the following, the term microporosity is used to refer to the total intra-aggregate porosity.

4.3 Water storage and hydration mechanisms

Water in compacted bentonite is present under different forms: structural water, adsorbed water and capillary or free water (Kezdi, 1974; Stçepkowska, 1990). Structural water or hydroxyl is part of the minerals structure and does not leave the solid phase below 350°C. It is therefore excluded from water content measurements which are obtained after drying the sample at a temperature slightly over 100°C. Adsorbed water corresponds to the water which is adsorbed on both internal and external surfaces of the clay minerals, i.e. which is stored in the intra-aggregate pores (micropores). Finally, capillary or free water is stored in the macropores. Figure 2.10 presents a conceptual representation of the structure of compacted bentonites and the different types of water.

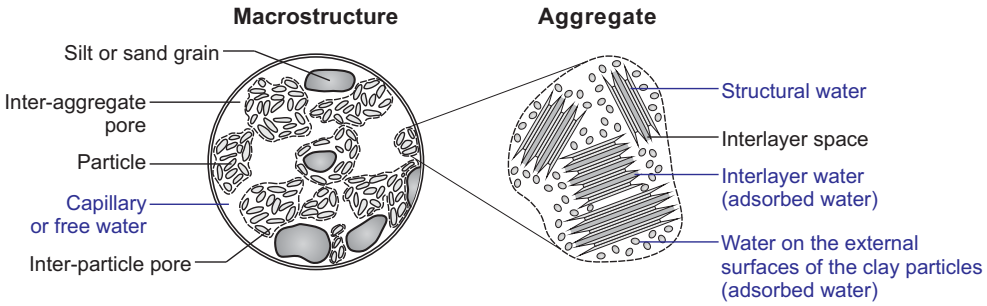

Figure 2.10: Conceptual representation of the structure of compacted bentonite (in black) and the different water storage mechanisms (in blue) (modified after Gens & Alonso, 1992; Jacinto *et al.*, 2012).

The physical state of water in the vicinity of the charged clay layers differs from the one of bulk water, and both values of viscosity and density are affected (Langmuir, 1917; Baver & Winterkorn, 1935; Winterkorn, 1943). Low (1979) and Bourg *et al.* (2003) showed that the viscosity of the adsorbed water is higher than the one of bulk water. Moreover, due to the strong physicochemical interactions between water and the clay particles, the density of adsorbed water is significantly higher than that of bulk water (Hawkins & Egelstaff, 1980; Derjaguin *et al.*, 1986; Swenson *et al.*, 2000; Jacinto *et al.*, 2012), and may reach values higher than 1.4 Mg/m^3 (Figure 2.11(a)).

From a practical point of view, the water density has a strong influence on the computed degree of saturation. The degree of saturation S_r is indeed obtained from the gravimetric water content w according to

$$S_r = \frac{\rho_s}{\rho_w}\frac{w}{e} \tag{2.4}$$

where ρ_s is the density of the solids, ρ_w is the water density and e is the void ratio (defined as the ratio between the volume of voids and the volume of solids). When the degree of saturation is calculated with the density of bulk water ($\rho_w = 1$ Mg/m^3), values higher than 1 are systematically obtained close to saturation (Villar, 2002; Marcial, 2003; Jacinto *et al.*, 2012). Knowing the water content and void ratio of presumably saturated samples, Villar (2000) computed the equivalent water density in compacted Febex bentonite. Figure 2.11(b) shows that the mean water density is higher for denser samples, although water densities higher than 1 are found for looser samples.

In practice, the different types of water cannot be easily separated. Thermogravimetric analysis is generally used to this end, although the interpretation of the results is not straightforward (Cases *et al.*, 1997, 1995; Salles *et al.*, 2009). At relative humidities lower than 90%, water is mainly found in the interlayer and adsorbed on the external surface of the particles. When the relative humidity increases, some capillary condensation is believed to take place in the macropores. However, as discussed in the next section, important porosity redistribution occurs upon wetting and leads a reduction of the macroporosity under confined conditions, hence limiting the amount of free water. The amount of free water in compacted bentonites is therefore usually estimated to be only a few percent of the total water, under saturated conditions (Pusch *et al.*, 1990; Bradbury & Baeyens, 2003; Fernandez *et al.*, 2004).

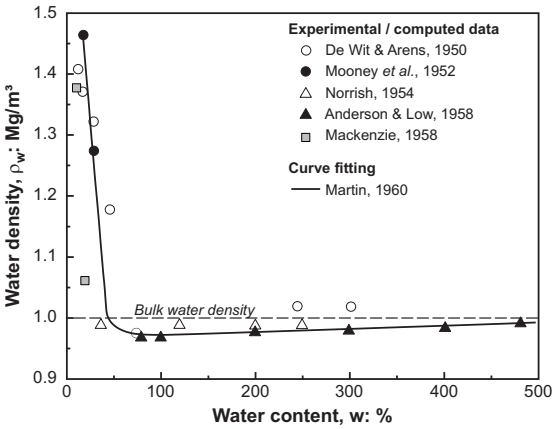

(a) Water density in sodium montmorillonite as a function of water content (Martin, 1960).

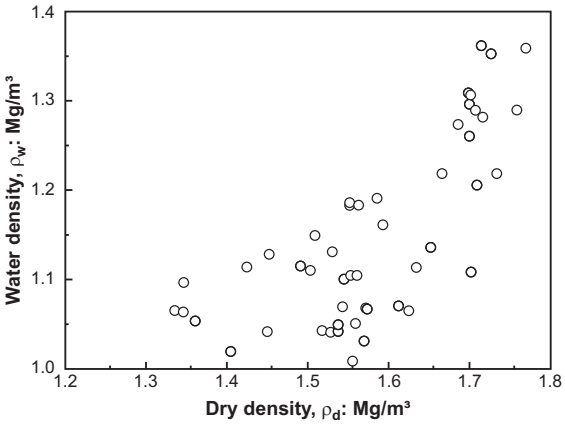

(b) Water density in Febex bentonite as a function of dry density (Villar, 2000).

Figure 2.11: Water density in compacted bentonites.

4.4 Factors affecting the structure

The mechanisms affecting the structure of soils may be classified into internal and external factors. Internal factors (also called intrinsic) include the mineralogy, clay particles size and morphology, and water chemistry. External factors are the compaction method and its energy, and the water content. In this section, the structure evolution is only considered from the point of view of the pore size distribution, as little information is available about the morphology of the pores and aggregates structure.

4.4.1 Mechanical loading

Figure 2.9 presents the pore size distributions of Febex bentonite compacted at two different dry densities, namely 1.5 Mg/m^3 and 1.8 Mg/m^3, but the same water content. In both cases, a bimodal pore size distribution is observed, even at high dry density. The compaction process has two main effects. Firstly, regarding the porous volume, increasing the compaction effort at constant water content decreases the volume of macropores, while the volume of micropores is hardly affected. Secondly, compaction shifts the size of dominant macropores towards smaller pore radii.

4.4.2 Water content changes

As a result of the sensitivity of clay minerals to water, the structure of compacted bentonites is significantly affected by changes in water content. An increase in the water content leads indeed to the swelling of clay layers and particles, hence aggregates. Figure 2.12 shows the evolution of the pore size distribution of MX-80 bentonite compacted to a dry density of 1.79 Mg/m^3 and hydrated under constant volume conditions. The experimental data show an increase of volume of the smaller pores and a progressive decrease of the inter-aggregate pore volume. Consequently, the structure of the material evolves from a bimodal pore size distribution (as-compacted material) towards a mono-modal distribution under fully saturated conditions. According to Romero (2013), the evolu-

tion of the macropores volume upon changes in water content is the consequence of both multi-scale and multi-physical processes. During wetting, the expanding clay particles invade indeed the macropores, hence decreasing the macropores volumes. On the other hand, wetting is likely to lead to collapse of the macrostructure. At the macroscopic scale, collapse is indeed often detected during saturation of compacted bentonites and is generally interpreted as an instability of the material structure.

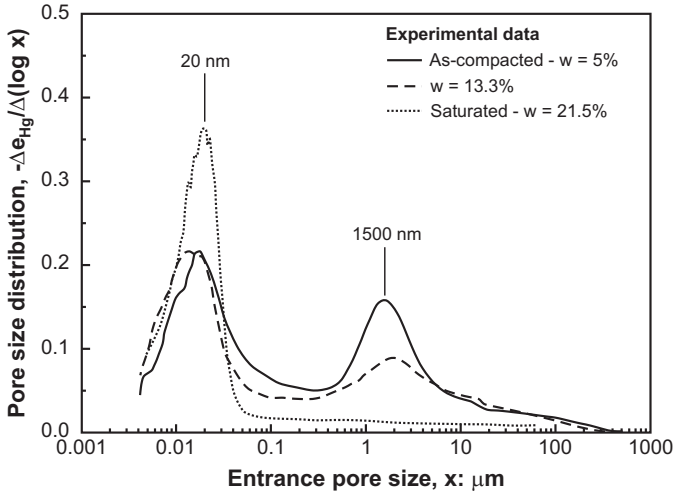

Figure 2.12: Influence of the water content on the pore size distribution of MX-80 bentonite compacted to a dry density $\rho_d = 1.79$ Mg/m^3 and hydrated under constant volume conditions (Seiphoori *et al.*, 2014)

Figure 2.13 presents an interesting picture, obtained by cryo-Focused Ion Beam nanotomography (see Keller *et al.*, 2014, for details on this technique), of partially saturated MX-80 bentonite compacted to a dry density of 1.46 Mg/m^3 with a water content of 22.6%. The picture shows that the inter-aggregate pores are filled with a loose material comparable to a gel or colloidal solution. This material is characterized by a special structures referred to as honeycomb (Keller *et al.*, 2014). For higher dry densities (1.67 Mg/m^3), Keller *et al.* (2014) did not observe such a structure, presumably because of the lack of large inter-aggregate pores (Figure 2.12).

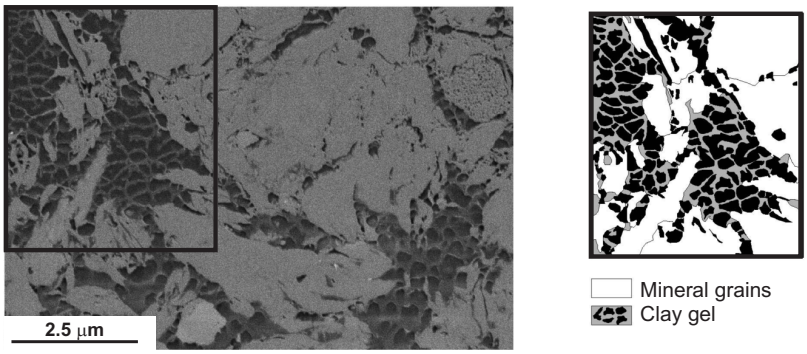

Figure 2.13: Microstructure of compacted MX-80 bentonite with dry density $\rho_d = 1.46$ Mg/m^3 and water content $w = 22.6\%$ obtained by cryo-Focused Ion Beam nanotomography (Keller *et al.*, 2014).

Wang *et al.* (2013a) observed a different behaviour of the microstructure of a MX-80 bentonite/sand mixture hydrated under confined conditions, and noticed the development of two-dimensional fissure-like pores. These pores were detected with both mercury intrusion porosimetry (pore group with a mean diameter of 50 μm and 1 μm in Figure 2.14(a)) and scanning environmental microscope (Figure 2.14(b)). Wang *et al.* (2013a) suggested that these pores may result from the division of clay particles within the aggregates due to swelling. However, further investigations are required since the release of the swelling pressure before freeze-drying of the sample could also influence the observations.

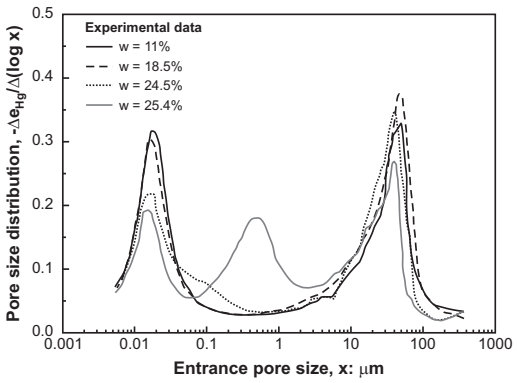

(a) Evolution of the pore size distribution.

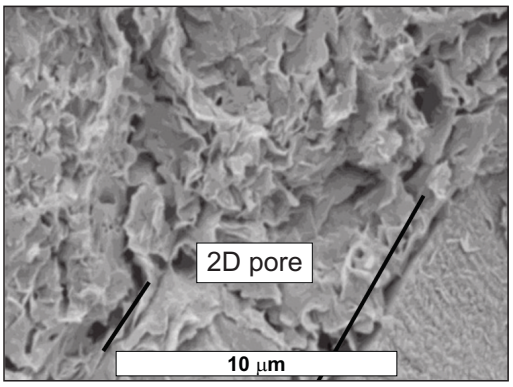

(b) Micrograph for saturated conditions ($w = 25.5\%$).

Figure 2.14: Development of two-dimensional fissure like pores during hydration of a MX-80 bentonite/sand mixture under constant volume conditions (Wang *et al.*, 2013a)

Finally, few experimental data are available concerning the reversibility of the microstructure behaviour upon wetting and drying cycles. According to Romero (2013), the aggregates of as-compacted bentonites swell and shrink almost reversibly upon wetting and drying. Therefore Romero (2013) qualifies the aggregates of compacted clayey soils as a permanent feature of the microstructure. However, Seiphoori *et al.* (2014) observed significant and permanent modifications of the structure of granular MX-80 bentonite saturated under constant volume conditions. Indeed, no significant structural changes were observed upon drying. Seiphoori *et al.* (2014) interpreted this irreversibility of the structure behaviour as a consequence of the irreversible subdivision of smectite particles (see Section 3.3).

4.4.3 Ageing

Ageing effects refer to time-dependent phenomena. These effects were studied by Delage *et al.* (2006) on MX-80 bentonite (Figure 2.15). The study showed that significant changes in the material structure were observed when bentonite samples were maintained under constant volume and constant water content for different periods of time ranging from 1 day to 90 days. In particular, a decrease in the inter-aggregate porosity and an increase in the non-intruded porosity (interpreted as inter-layer porosity) were observed. These observations were interpreted in terms of progressive placement of interlayer water molecules within the particles and subdivision of clay particles.

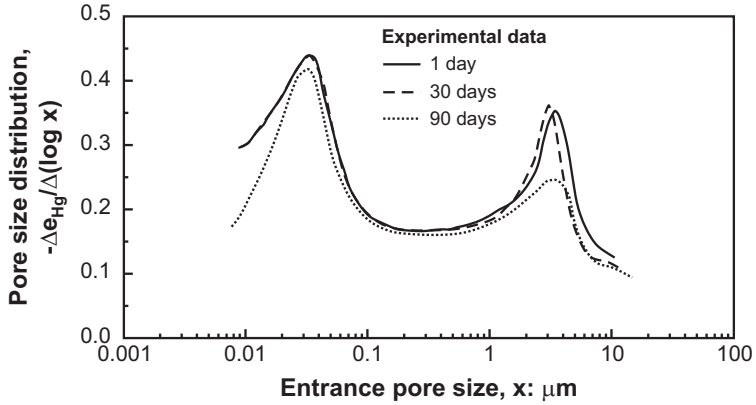

Figure 2.15: Changes in pore size distribution with time of compacted MX-80 bentonite with dry density $\rho_d = 1.61$ Mg/m^3 and water content $w = 8.2\%$ (Delage *et al.*, 2006).

4.5 Model for the microstructure evolution

In the previous section, the effects of hydraulic and mechanical loading on the microstructure of compacted bentonites were underlined. In particular, the experimental observations showed that the microstructure of compacted bentonites created upon compaction was not fixed, but evolving along hydromechanical stress paths. In this section, attention is focused on quantifying the evolution of the microstructure.

The experimental technique the most often used to gather quantitative information on the structure of porous media is mercury intrusion porosimetry. While the technique provides only partial information on the material microstructure, the results can be used to obtain a scalar measure of the interconnected pore sizes and volumes. Accounting for this limitation, mercury intrusion porosimetry data are used and analysed in this work in order to highlight tendencies in the evolution of the pore size distribution of compacted bentonites along hydromechanical stress paths. In particular, the following quantities are defined:

- the **microporosity** ϕ_m is the ratio between the micropores volume Ω_m and the total volume Ω

$$\phi_m = \frac{\Omega_m}{\Omega}. \tag{2.5}$$

  The microporosity coincides with the total intra-aggregate porosity and includes both inter- and intra-particles pores.

- the **microstructural void ratio** e_m is the ratio between the micropores volume Ω_m and the solid volume Ω_s

$$e_m = \frac{\Omega_m}{\Omega_s} = \frac{\phi_m}{\phi} e \tag{2.6}$$

  where ϕ and e are respectively the (total) porosity and void ratio.

- the **macroporosity** ϕ_M is the ratio between the macropores volume Ω_M and the total volume Ω

$$\phi_M = \frac{\Omega_M}{\Omega}. \tag{2.7}$$

The macroporosity coincides with the inter-aggregate porosity.

- the **macrostructural void ratio** e_M is the ratio between the macropores volume Ω_M and the solid volume Ω_s

$$e_M = \frac{\Omega_M}{\Omega_s} = \frac{\phi_M}{\phi} e \tag{2.8}$$

with the total porosity $\phi = \phi_m + \phi_M$ and total void ratio $e = e_m + e_M$.

From a practical point of view, these quantities can be estimated based on experimental pore size distributions. Therefore a criterion should be defined to distinguish micropores from macropores. Three main approaches are identified and briefly summarized:

- **Approach 1**: an entrance pore size is selected based on the pore size distribution of the as-compacted material and is used to separate intra-aggregate and inter-aggregate pores.

- **Approach 2**: data from a mercury intrusion and extrusion cycles are used. The difference between the intruded and extruded mercury volume is assumed to correspond to the inter-aggregate porosity (Delage & Lefebvre, 1984; Delage *et al.*, 1996).

- **Approach 3**: the entrance pore size coinciding with the dominant peak of the pore size distribution of the material saturated under constant volume conditions is detected. It is used to separate intra-aggregate and inter-aggregate pores (Della Vecchia, 2009; Romero *et al.*, 2011).

The different criteria are further described and discussed in Romero *et al.* (2011). In addition, a fourth approach, based on the discrimination of water retention domains, was proposed by Romero *et al.* (1999). Yet, if the approaches are conceptually different, they basically provide similar quantitative results in terms of porosities evolution.

Based on the experimental observations presented in the previous section, two main conclusions can be drawn. Firstly, mechanical loading does not affect the volume of micropores. This is at least true for the range of loads and dry densities commonly investigated. Secondly, hydraulic loading strongly affects the micropores volume. In particular, wetting yields an increase of the micropores volume. Accordingly, Romero *et al.* (2011) suggested to plot the microstructural void ratio e_m obtained from the analysis of pore size distributions as a function of the water ratio e_w (defined as the ratio between the volume of water and the volume of solids). By doing so, Romero *et al.* (2011) and Della Vecchia *et al.* (2013) observed that, below a given water ratio $e_w = e_m^*$, the microstructural void ratio of moderately active clays was almost constant and not affected by the water ratio. On the contrary, for higher water ratios, the microstructural void ratio increases almost linearly with the water ratio. Therefore, Romero *et al.* (2011) and Della Vecchia *et al.* (2013) proposed the following law for the evolution of the microstructural void ratio with the water ratio

$$e_m = e_m^* + \beta \langle e_w - e_m^* \rangle \tag{2.9}$$

where $\langle\rangle$ designates the Macaulay brackets (ramp function), e_m^* is the water ratio corresponding to fully saturated micropores and β quantifies the swelling tendency of the aggregates.

In this work, a large number of mercury intrusion porosimetry results on different bentonites were analysed. The materials include Febex bentonite (Lloret *et al.*, 2003; Lloret & Villar, 2007; Romero *et al.*, 2011), Kunigel V1 bentonite (Romero, 2012, and present work), MX-80 bentonite (Delage *et al.*, 2006; Wang, 2012; Seiphoori *et al.*, 2014) and a mixture of MX-80 bentonite and sand (Wang *et al.*, 2013c; Saba *et al.*, 2014). The analysis of the experimental results and their representation in the $(e_w - e_m)$ plane does not allow identifying any threshold water content below which the microstructural water ratio remains constant. On the contrary, the micropores volume appears to be continuously evolving with the water ratio (Figure 2.16). This observation is in accordance with results presented by Romero *et al.* (2011) on Febex and MX-80 bentonites.

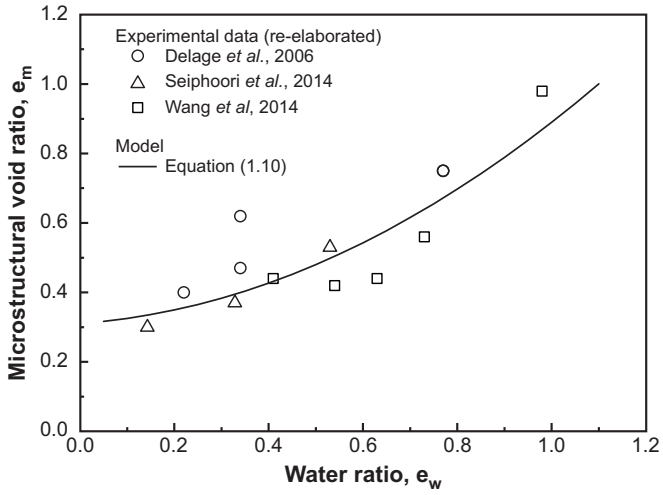

Figure 2.16: Evolution of the microstructural void ratio e_m with the water ratio e_w from MIP results on compacted MX-80 bentonite.

Accordingly, the following relation is adopted to describe the evolution of microstructural void ratio with the water ratio

$$e_m = e_{m0} + \beta_0 e_w + \beta_1 e_w^2 \tag{2.10}$$

where e_{m0} is the microstructural void ratio for the dry material ($e_w = 0$) and β_0 and β_1 are parameters that quantify the swelling potential of the aggregates. Table 2.4 presents the model parameters calibrated for four bentonite-based materials, namely Febex, Kunigel V1 and MX-80 bentonites, and a mixture of MX-80 bentonite and sand. In particular, Figure 2.16 provides an example of the calibration for MX-80 bentonite, using experimental data from Delage *et al.* (2006), Seiphoori *et al.* (2014) and Wang *et al.* (2014).

Three remarks are formulated concerning the proposed model. First of all, it should be noted that for high values of dry density and water content, Equation (2.10) may lead to values of e_m higher than the total void ratio e. In this case, it is assumed that the

Material	e_{m0}	β_0	β_1
Febex	0.35	0.25	0.15
Kunigel V1	0.4	0.03	0.21
MX-80	0.31	0.1	0.48
MX-80/sand mixture (70/30)	0.29	0.1	0.18

Table 2.4: Parameters of the microstructure evolution law for four bentonite-based materials.

microstructure is completely developed and $e_m = e$. This remark is directly related to the fact that Equation (2.10) does not provide any limiting value of e_m with e_w, although such a limit probably exists. However, the proposed relation is meant to describe the microstructure of compacted bentonites for which the range of water ratios is limited to $0.15 \preceq e_w \preceq 0.95$. Finally, in a reasonable range of water ratios, Equation (2.10) provides predictions similar to those of the bilinear expression proposed by Romero *et al.* (2011), whilst providing a continuous evolution of e_m with the water ratio.

5 Conclusions and anticipated contributions

Bentonite-based materials are characterized by important hydromechanical coupling, making its constitutive and numerical modelling difficult. The roots of these coupled processes lie at a very small scale which can be investigated by using modern experimental techniques. In this chapter, effort was devoted to the description of coupled processes at the scales of the clay particles and material microstructure. Under repository conditions, the main load acting on the engineered barrier is the hydration from the surrounding geological formation (thermal effects are not considered in this work). Accordingly, attention was first focused on the physicochemical properties of smectites and the hydration and swelling mechanisms of these minerals. At the scale of the clay particle, hydration leads to an increase of the average interlayer distance and a division of the clay particles into smaller structures, both contributing to the particle swelling. A precise description of the processes is complex. Yet, the diffuse double layer theory provides interesting qualitative results on the factors affecting swelling. In particular, the theory allows a first explanation of the considerably different swelling pressures reached by different bentonites upon saturation.

The hydration and swelling mechanisms were then addressed at the scale of the compacted material microstructure. The experimental data show that hydration of compacted bentonite under confined conditions is associated with a progressive increase of the micropores volume and a decrease of the inter-aggregate porosity. On the contrary, under unconfined conditions, swelling taking place at the clay layer yields important swelling strains observed at the macroscopic scale. Based on the interpretation of a large number of pore size distributions on compacted bentonites, a model for the microstructure evolution is proposed in this chapter. The modelling of the macroscopic swelling, among other features of

the mechanical behaviour, will be treated in Chapter 5. In both confined and unconfined conditions, important modifications of the water retention and transfer properties are expected during hydration and swelling of compacted bentonite-based materials. These issues will be addressed in Chapter 4 and Chapter 6 respectively.

Chapter 3

Macroscopic approach to coupled processes

1 Introduction

Under repository conditions, engineered barriers experience complex and strongly coupled hydromechanical processes. On one hand, hydration from the surrounding geological formation leads to swelling of the bentonite buffer, progressive filling of the technological gaps and development of swelling pressure against the gallery wall. On the other hand, swelling of the bentonite yields important structural changes which significantly affect the hydraulic properties of the material. In Chapter 2, swelling of bentonite-based materials was studied from a microscale point of view. Its influence on the material structure and, conversely, the influence of the material composition and structure on the swelling behaviour, were analysed in detail. Yet, in order to predict the behaviour of the engineered barrier under repository conditions, numerical modelling at a large scale (typically the scale of geo-structures) and over long time periods should be performed.

The aim of this chapter is to present the general framework adopted in this research work to model the hydromechanical behaviour of bentonite-based materials. The framework is based on the theory of partially saturated porous media. Accordingly, bentonite is considered as a multiphase porous medium composed of solid, liquid and gas phases. In order to encompass the different hydromechanical processes involved under *in situ* conditions, the proposed formulation includes a description of the mechanical behaviour, water flow and air flow.

The chapter is organised as follows. First, the equations governing the hydromechanical problem are presented. The different theories of porous media are summarized and the balance equations of the porous medium are developed. In order to link the dependent variables to the main unknowns, a number of constitutive laws are required. In particular, attention is focused on the water retention model, the mechanical model and the multiphase flow law. In this work, the different phases of the porous medium are assumed to be in thermodynamic equilibrium and the equilibrium restrictions are expressed. Finally, the finite element formulation for porous media, including the linearization of the field equations and the finite element discretization, is presented. Emphasis is placed on

the hydromechanical coupling terms classically considered in porous media and on their numerical treatment. Rather than presenting any original contribution, this chapter set the basis for the developments presented in the next chapters.

2 Theories of porous media

The complex structure of compacted bentonites makes its full description, including the description of the different phases[1] and their interactions, almost impossible. Therefore, modelling approaches generally substitute the real discontinuous porous medium by idealized homogeneous continua.

The formulation of the model starts with the physical description of the system, i.e. the real porous material. The concept of volume fractions is used to describe multiphase porous media. The volume fraction η_π of the phase π is defined as

$$\eta_\pi = \frac{\Omega_\pi}{\Omega} \tag{3.1}$$

where Ω_π is the volume of the phase π and Ω is the total volume of the control space, with

$$\sum_{\pi=1}^{N} \eta_\pi = 1 \tag{3.2}$$

and N the number of phases. In this work, bentonite-based materials are considered as three-phase porous media consisting of solid, liquid and gas phases. Accordingly, the following volume fractions are defined

$$\eta_s = 1 - \phi \tag{3.3}$$

$$\eta_l = S_r \phi \tag{3.4}$$

$$\eta_g = (1 - S_r)\, \phi \tag{3.5}$$

where the subscripts s, l and g identify the solid, liquid and gas phases respectively, ϕ is the total porosity defined as the ratio between the total porous volume Ω_v and the volume of the control space Ω

$$\phi = \frac{\Omega_v}{\Omega} = \frac{\Omega_l + \Omega_g}{\Omega} \tag{3.6}$$

and S_r is the degree of saturation, defined as the ratio between the volume of the liquid phase Ω_l and the porous volume Ω_v

$$S_r = \frac{\Omega_l}{\Omega_v}. \tag{3.7}$$

An important issue directly associated with the concept of volume fractions is the experimental determination of the different fractions. While the notion of solid grain is clearly defined in granular materials, the strong physicochemical interactions between water and

[1] Phases are defined as portions of matter with smoothly changing physical properties and mineralogical composition which are separated from one another by well-defined boundaries (Koliji, 2008).

clay minerals make the discrimination of these two phases less evident in bentonites. Conventionally, the volume fractions are determined experimentally on the basis of material weighting and measuring. It yields that the considered solid phase contains strongly bounded water. Yet, as this water has a very limited mobility, it is considered as a part of the solid phase (Hueckel & Pellegrini, 1989; Hueckel, 1992a).

Three main approaches exist to describe porous media and build the idealized homogeneous continua:

- **Macroscopic theories**
  Macroscopic theories are based on the consolidation theory proposed by Terzaghi (1943), and later extended by Biot (1941, 1956, 1962, 1972). In these theories, the porous medium is studied at the macroscopic scale. Accordingly, stresses and other related concepts are macroscopic concepts. In addition, the different phases are not treated separately, and the balance equations are written for the whole porous medium, without any distinction between the different phases and species (or constituents). Further extensions of Biot's work include the contributions of Coussy (1995) and Dormieux *et al.* (1995).

- **Theories of mixtures**
  In the theories of mixtures, the porous medium is also studied at the macroscopic scale but the different phases are treated separately. All phases are assumed to occupy the same region of space simultaneously, and consequently, every point of the idealized system consists of a mixture of phases (Figure 3.1). The theory of mixtures was initially developed to solve multi-components gas mixtures. Bowen (1980, 1982) used the concept of volume fractions to extend the theory to multiphase porous media. The concept of volume fractions is used to create homogenised continua of reduced densities, so that the methods of continuum mechanics can be applied. Let us consider the real density of the phase π, ρ_π

$$\rho_\pi = \frac{m_\pi}{\Omega_\pi}, \tag{3.8}$$

  with m_π the mass of the π phase, the reduced density of the homogenised continuum corresponding to the phase π is then given by

$$\rho^\pi = \eta_\pi \rho_\pi. \tag{3.9}$$

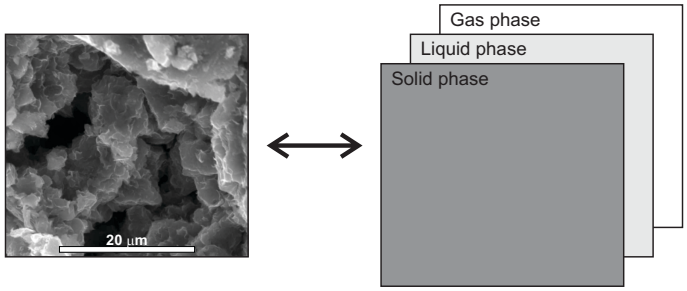

Figure 3.1: Definition of equivalent continua. Example for theories of mixtures.

In mixture theories, balance equations are expressed at the macroscopic scale (for each phase or species), and constitutive models are also introduced at this scale.

- **Averaging theories (or hybrid mixture theories)**
  In averaging theories (Hassanizadeh & Gray, 1979a,b, 1980), two structural levels are defined, namely a microscopic scale, corresponding to the pore level, and a macroscopic scale, which corresponds to the representative elementary volume (REV). At the microscopic level, the system is viewed as the superposition of interpenetrating continua. In opposition to the mixture theory, each continuum occupies only a part of the space. The different continua are separated by interfaces which have their own thermodynamic properties. Balance equations (and sometimes constitutive laws) are introduced at this scale.

  Averaging techniques are then used to obtain averaged (over the REV) macroscopic field equations. Different averaging methods may be used, ranging from analytical to numerical (e.g. Finite Element Square method). Special care should be taken to select the size of the REV (see Bear, 1972; Hassanizadeh & Gray, 1979a; Bachmat & Bear, 1986; De Marsily, 1986, for a discussion).

Although attractive, averaging theories require the description of phenomena at a microscopic scale, typically the size of few aggregates. However, in practice, this scale is difficult to investigate in bentonites and very few experimental data are available. Therefore, the approach of mixture theories is adopted in this work. It enables indeed the description of fluid flow and deformation of the porous medium, and coupled phenomena may be easily tackled. In this framework, experimental data only at a macroscopic scale are needed. This scale corresponds typically to the one investigated at the laboratory of geomechanics when performing fluid transfer and mechanical tests. Although no information concerning the microstructure is directly provided in theories of mixtures, they may be introduced to better describe the coupled behaviour of porous materials at the macroscopic scale.

3 Balance equations

The balance equations are obtained for a mixture composed of three species, namely mineral, water and air, distributed in three phases, namely solid, liquid and gas (Figure 3.2). Accordingly, the kinematics of the porous medium is described by its displacement field $\boldsymbol{u}$, liquid pressure field u_l and gas pressure field u_g (one field for each homogenised continuum). Unless otherwise specified, the subscripts s, l and g refer to the solid, liquid and gas phase properties, while the superscripts w and a refer to the properties of water and air[2]. In the present formulation, it is assumed that the mineral species and the solid phase coincide. The liquid phase contains both water and dissolved air in concentration x_l^a. However, it is assumed that the liquid phase properties are not affected by the amount of dissolved air and they therefore correspond to the ones of liquid water. Consequently, the liquid pressure u_l is equal the water pressure u_w, whose symbol is preferred in the following. Finally, the gas phase is a perfect mixture of dry air and water vapour. The

[2]The hydromechanical formulation presented in this chapter may be extended to gas species different than air (considered here as a single species). However, for the sake of clarity, the letter a is used to denote the gas species, while g denotes the gas phase.

partial pressure of dry air is denoted as u_a and the partial pressure of water vapour, u_v. According to Dalton's law, the total pressure of the gas phase u_g is equal to the sum of the partial pressures.

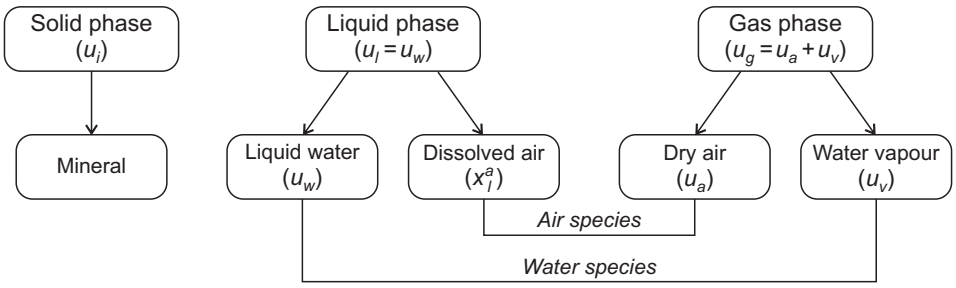

Figure 3.2: Definition of phases (solid, liquid and gas) and species (mineral, water and air). The mineral species and the solid phase are assumed to coincide.

In the following, the different balance equations, namely the mass balance equations and the momentum balance equation, are expressed in local form. In the case of thermo-hydro-mechanical analysis, an additional energy balance equation should be expressed.

3.1 Mass balance equations

The compositional approach (Panday & Corapcioglu, 1989; Olivella *et al.*, 1994; Collin, 2003) is adopted to establish the mass balance equations. It consists of balancing species rather than phases. This approach has the advantage that phase exchange terms cancel out, which is particularly useful when equilibrium is assumed.

3.1.1 Solid mass balance equation

For a given volume of mixture Ω, the mass balance of the solid phase reads

$$\frac{\partial}{\partial t}\Big[\rho_s\,(1-\phi)\,\Omega\Big] = 0 \tag{3.10}$$

where ρ_s is the density of the solids. If the solid particles are assumed incompressible (i.e. ρ_s is a constant), then Equation (3.10) reduces to

$$\frac{\dot{\Omega}}{\Omega} = \frac{\dot{\phi}}{1-\phi} \tag{3.11}$$

where the superior dot denotes a time derivative.

3.1.2 Fluid mass balance equations

The water mass and air mass balance equations are expressed as

$$\underbrace{\dot{m}_l^w + \nabla\cdot\boldsymbol{f_l^w}}_{\text{Liquid water}} + \underbrace{\dot{m}_g^w + \nabla\cdot\boldsymbol{f_g^w}}_{\text{Water vapour}} = Q^w \tag{3.12}$$

$$\underbrace{\dot{m}_g^a + \nabla\cdot\boldsymbol{f_g^a}}_{\text{Dry air}} + \underbrace{\dot{m}_l^a + \nabla\cdot\boldsymbol{f_l^a}}_{\text{Dissolved air}} = Q^a \tag{3.13}$$

where m_l^w, m_g^w, m_g^a and m_l^a are respectively the masses of liquid water, water vapour, dry air and dissolved air inside the porous volume Ω, $\boldsymbol{f_l^w}$, $\boldsymbol{f_g^w}$, $\boldsymbol{f_g^a}$ and $\boldsymbol{f_l^a}$ are the mass fluxes of liquid water, water vapour, dry air and dissolved air, and Q^w and Q^a are water and air source terms. In these equations, the terms of time partial derivatives correspond to the change in fluid storage in the porous medium, while the divergence of fluxes express the difference between the input and output fluxes of a given volume of mixture Ω. These terms express that porous media, unlike classic continua, are thermodynamically open (Coussy, 1995).

The different terms of Equations (3.12) and (3.13) corresponding to the change in fluid storage are expressed as

$$\dot{m}_l^w = \frac{\partial}{\partial t}\left(\rho_w S_r \phi\ \Omega\right) \tag{3.14}$$

$$\dot{m}_g^w = \frac{\partial}{\partial t}\Big[\rho_v\left(1-S_r\right)\phi\ \Omega\Big] \tag{3.15}$$

$$\dot{m}_g^a = \frac{\partial}{\partial t}\Big[\rho_a\left(1-S_r\right)\phi\ \Omega\Big] \tag{3.16}$$

$$\dot{m}_l^a = \frac{\partial}{\partial t}\left(\rho_l^a S_r \phi\ \Omega\right) \tag{3.17}$$

where ρ_w, ρ_v, ρ_a and ρ_l^a are respectively the densities of liquid water, water vapour, dry air and dissolved air. These relationships introduce coupling between the mechanical and hydraulic problems. Indeed, changes in porosity directly affect the fluids storage capacity.

For a unit porous volume ($\Omega = 1$), Equations (3.12) and (3.13) become

$$\underbrace{\frac{\partial}{\partial t}\left(\rho_w S_r \phi\right) + \nabla \cdot \boldsymbol{f_l^w}}_{\text{Liquid water}} + \underbrace{\frac{\partial}{\partial t}\Big[\rho_v\left(1-S_r\right)\phi\Big] + \nabla \cdot \boldsymbol{f_g^w}}_{\text{Water vapour}} = Q^w \tag{3.18}$$

$$\underbrace{\frac{\partial}{\partial t}\left[\rho_a\left(1-S_r\right)\phi\right] + \nabla \cdot \boldsymbol{f_g^a}}_{\text{Dry air}} + \underbrace{\frac{\partial}{\partial t}\left(\rho_l^a S_r \phi\right) + \nabla \cdot \boldsymbol{f_l^a}}_{\text{Dissolved air}} = Q^a. \tag{3.19}$$

3.2 Momentum balance equation

The balance of momentum is expressed for the entire mixture. For quasi-static loading, the equation reduces to the equilibrium of stresses

$$\nabla \cdot \boldsymbol{\sigma_t} + \boldsymbol{b} = \boldsymbol{0} \tag{3.20}$$

where $\boldsymbol{\sigma_t}$ is the total Cauchy stress tensor (with compressive stress taken as positive), and $\boldsymbol{b}$ is the body force vector. If the only body force is gravity, $\boldsymbol{b}$ is equal to $\rho \boldsymbol{g}$, where ρ is the density of the mixture

$$\rho = \rho_s\left(1-\phi\right) + \rho_w S_r \phi + \rho_g\left(1-S_r\right)\phi \tag{3.21}$$

with ρ_g the density of the gas phase (defined later by Equation (3.52)), and $\boldsymbol{g}$ is the gravity acceleration vector.

4 Constitutive equations

The balance equations presented in the previous section involve a number of dependent variables, such as the degree of saturation, fluid fluxes and the stress tensor. These dependent variables should be related to the main unknowns of the problem, namely the displacements, water pressure and gas pressure, in order to fully describe the behaviour of the porous medium. The relationships that link the dependent variables to the unknowns are called constitutive equations. Three main constitutive equations are involved in the hydromechanical description of partially saturated porous media: the water retention model, the mechanical model and the multiphase flow model.

4.1 Water retention model

4.1.1 Water potential and concept of suction

The total potential of water ψ is defined as the amount of work per unit mass of pure water required to transport reversibly and isothermally an infinitesimal quantity of water from a reservoir of pure water at a specified elevation and atmospheric pressure to the point under consideration (Aitchison, 1965). The total potential is often expressed as the sum of four contributions, such that

$$\psi = \psi_g + \psi_p + \psi_m + \psi_o \tag{3.22}$$

where ψ_g is the gravitational potential, ψ_p the external pressure potential, ψ_m the matric potential and ψ_o the osmotic potential. The sum of the matric and osmotic potentials is referred to as the internal potential.

In soil mechanics, the concept of suction is often used as an alternative to the internal potential. The gravitational and external pressure potentials are indeed not relevant for constitutive modelling of the soil (Gens, 2010). The suction is an energy per unit volume (instead of per unit mass) and is expressed in terms of pressure. The total suction s_t is defined as

$$s_t = s + \pi_{osm} \tag{3.23}$$

where s is the matric suction and π_{osm} is the osmotic suction. The matric suction is associated to the interactions between liquid and solid, while the osmotic suction is related to differences in water chemistry. In this work, the effects of the osmotic suction on the hydromechanical behaviour of compacted bentonites are not considered, so that the matric suction is the only contribution to the total suction.

The matric suction contains two distinct contributions, namely the capillary suction and the adsorption suction (Baker & Frydman, 2009; Frydman, 2012; Blatz *et al.*, 2009; Lu & Likos, 2004). The capillary suction is associated to capillary phenomena, while the adsorption suction results from electrochemical interactions between the water and the clay minerals. In this work, the (matric) suction is defined as the gas pressure in excess of the water pressure

$$s = u_g - u_w. \tag{3.24}$$

In fact, this definition corresponds to the capillary suction, and not to the matric suction (see Baker & Frydman, 2009, for a discussion). However, essentially for historical reasons, it is used to express quantitatively the degree of attachment of the liquid phase onto the solid phase, regardless the attraction mechanism. Therefore, the suction as defined by Equation (3.24) reflects interactions between water and solid and should be differentiated from capillary phenomena (Gens, 2010).

4.1.2 Constitutive models

The water retention curve is defined as the relationship between the amount of water stored in a porous medium and suction. The amount of water stored may be expressed in terms of water content, water ratio or degree of saturation. Yet, the degree of saturation, which provides normalisation of the volume fractions of the liquid and gas phases, is directly involved in the mass balance equations. Figure 3.3 presents the typical shape of a water retention curve for granular materials. Starting from *dry* conditions, four main water retention domains may be identified. The first domain is referred to as the residual state. The degree of saturation S_r takes a residual value of $S_{r,res}$ which is the lowest degree of saturation that can be reached upon drying. In this domain, water is adsorbed around the surface of the grains. The liquid phase is discontinuous while the gas phase is continuous. The second domain is referred to as the pendular state. Water is present under the form of bonds between grains, so that continuity of the liquid and gas phases is not ensured. If hydration is further continued, the third domain, called funicular state, is reached. The liquid phase is continuous while gas forms bubbles. Finally, full saturation of the material is achieved for a suction s_{AE} termed air-entry pressure. This air-entry pressure is the suction below which the pores are filled with water ($S_r = 1$) and above which the pores are drained ($S_r < 1$).

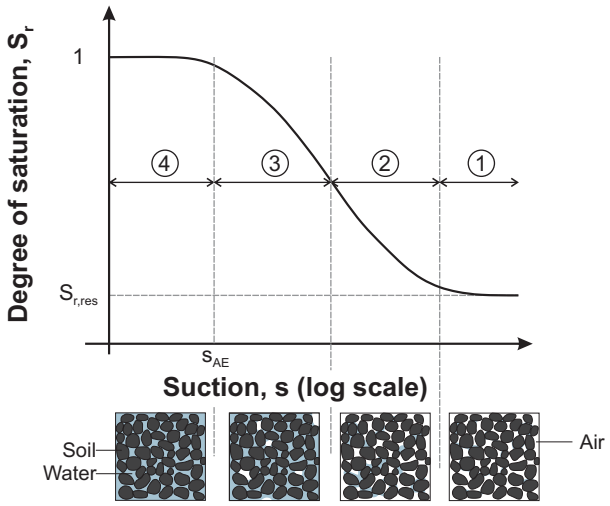

Figure 3.3: Water retention curve and schematic stages of saturation in porous media (modified after Nuth & Laloui, 2008a).

A large number of constitutive models have been developed to represent the water retention behaviour of porous media. One of the most famous is the one proposed by van

Genuchten (1980). It is expressed as

$$S_r = S_{r,res} + (1 - S_{r,res}) \left[1 + \left(\frac{s}{\alpha}\right)^n\right]^{-m} \tag{3.25}$$

where $S_{r,res}$ is the residual degree of saturation, α is a parameter associated with the air-entry value and m and n are model parameters. Note that α does not correspond to the definition of the air-entry value *stricto sensu* as for $s = \alpha$, the degree of saturation is equal to $S_r = 2^{-m}$, which is different from unity for $m \neq 0$. Finally, n is associated to the rate of desaturation of the soil, while m is linked to the curvature of the water retention curve in the high suction range.

In granular materials, the water retention behaviour is directly controlled by the pore size distribution of the material. Indeed, according to the framework introduced by Millington & Quirk (1961) and Mualem (1976), the pores in a porous medium can be represented, as a first approximation, as a bundle of different sized cylindrical tubes. Under this assumption, which disregards the connectivity between the pores, during a wetting process, the different classes of pores are sequentially filled starting from the smallest ones. In particular, if all pores smaller than X are saturated, the degree of saturation is defined as

$$S_r(X) = \int_{X_{min}}^{X} f(x)\,\mathrm{d}x \tag{3.26}$$

where X_{min} is the size of the smallest pores and $f(x)$ indicates the generic pore size distribution of a porous medium. The Laplace equation allows to associate a value of suction s to each pore size x. It is expressed as

$$s(x) = \frac{4\sigma_w \cos\theta_{ws}}{x} \tag{3.27}$$

where σ_w is the surface tension of water (the pore fluid), and θ_{ws} is the contact angle between water and the soil particles. The quantity $(4\sigma_w \cos\theta_{ws})$ is constant for a given soil mineralogy and chemical composition of the pore fluid. Therefore it yields

$$S_r(X) = \int_{X_{min}}^{X} f\left(\frac{4\sigma_w \cos\theta_{ws}}{s}\right)\mathrm{d}x = S_r(s) \tag{3.28}$$

where the relationship $S_r(s)$ is the water retention model.

4.2 Mechanical constitutive model

The momentum balance equation (3.20) introduces the total Cauchy stress tensor which should be related to the main unknowns of the problem. Yet, contrary to classic continuous media, the mechanical behaviour of porous media is not only controlled by the total stress, but it is also influenced by the fluids occupying the porous space. Therefore, alternative stress variable(s) should be defined. In the case of saturated porous media, the concept of effective stress was early introduced by Terzaghi (1936). In this section, the concept of effective stress in saturated soils is first presented. Then, the definition of adequate stress variables in unsaturated porous media is considered. Finally, important aspects of constitutive models for unsaturated soils are discussed. Further reviews of constitutive modelling of unsaturated soils can be found in Gens (1996); Wheeler & Karube (1995); Gens *et al.* (2006); Sheng *et al.* (2008b) and Sheng (2011).

4.2.1 Effective stress in saturated porous media

Terzaghi (1936) introduced the concept of effective stress to describe the mechanical behaviour of fully saturated porous media. The effective stress transforms a real multiphase porous medium into a mechanically equivalent single-phase continuum. It is defined as

$$\boldsymbol{\sigma}' = \boldsymbol{\sigma_t} - u_w \boldsymbol{I} \tag{3.29}$$

where $\boldsymbol{\sigma}'$ is the effective stress tensor (defined positive in compression) and $\boldsymbol{I}$ is the identity tensor. Note that this definition assumes that the solid minerals and water are incompressible and that the contact between minerals is punctual.

The validity of Terzaghi's effective stress to describe the behaviour of expansive clays has been subject of debate for several years (Graham *et al.*, 1992; Hueckel, 1992a; Masin & Khalili, 2016). According to Terzaghi, the load is indeed supported by the effective stress and the fluid pore pressure only, so that physicochemical interactions between clay particles are not considered. However, these are likely to contribute to load support. Attempts to incorporate physicochemical effects in the definition of effective stress include the works of Sridharan & Venkatappa (1973); Hueckel (1992b,a); Schreyer Bennethum *et al.* (1997); Mainka *et al.* (2014), among others.

A constitutive model for saturated geomaterials relates the effective stress (whatever its definition) increments to the strain increments. It reads

$$\mathrm{d}\boldsymbol{\sigma}' = \boldsymbol{D} : \mathrm{d}\boldsymbol{\varepsilon} \tag{3.30}$$

where $\boldsymbol{D}$ is a constitutive tensor and $\boldsymbol{\varepsilon}$ is the strain tensor. Alternatively, the previous relationship can be expressed in terms of effective stress and strain rates

$$\dot{\boldsymbol{\sigma}}' = \boldsymbol{D} : \dot{\boldsymbol{\varepsilon}}. \tag{3.31}$$

The definition of the effective stress yields a first important hydromechanical coupling. Indeed, changes in water pressure u_w directly affects the mechanical behaviour of the porous medium.

4.2.2 Stress variables in unsaturated porous media

The choice of constitutive variables is an inevitable issue in modelling unsaturated soils. Over the years, the choice of appropriate stress variables to model the behaviour of unsaturated soils has indeed been an intensively debated issue. Two main approaches are generally distinguished:

- The extension of the effective stress definition for saturated porous media towards unsaturated states;
- The definition of two independent stress variables (while only one, the effective stress, is used for saturated media).

Each of these two approaches has advantages and drawbacks. They are briefly described in the newt two sections. Further discussion and historical review can be found in Khalili *et al.* (2004) and Nuth & Laloui (2008b).

4.2.2.1 Effective stress approach

In the effective stress approach, Terzaghi's definition of the effective stress (Equation (3.29)) is extended to the partial saturation domain. One of the most famous definition was proposed by Bishop (1959). It is given by

$$\boldsymbol{\sigma'} = (\boldsymbol{\sigma_t} - u_g \boldsymbol{I}) + \chi \left(u_g - u_w\right) \boldsymbol{I} \tag{3.32}$$

where χ is a material parameter, called Bishop's parameter, which depends on the degree of saturation. It takes the value of 1 for fully saturated states and 0 for totally dry states. Experimental results on unsaturated soils evidence the relation between χ and the degree of saturation (Jennings & Burland, 1962; Fredlund & Rahardjo, 1993). Note that, since Bishop's stress depends on the material properties, it is not strictly speaking an effective stress (Sheng *et al.*, 2008b). Indeed, in this case, the effective stress space depends on the material behaviour and changes with its state. Accordingly, the constitutive behaviour of the material results from both constitutive relations and the stress space in which the constitutive model is defined.

When working with constitutive models for unsaturated soils, the main advantage of the effective stress approach is that the models previously developed for saturated soils are straightforwardly extended to the unsaturated domain. In addition, there is a continuous and smooth transition from saturated to unsaturated states. However, the determination of the different model parameters from laboratory tests is often complex. In addition, the effective stress approach has shown limitations in representing the important swelling of compacted clays and bentonites. The approach is also incapable of reproducing the collapse phenomenon upon wetting paths under high stress levels. Indeed, upon hydration, the fluid pressure increases, producing a decrease in the effective stress. Accordingly, the material swells, while compaction is observed experimentally.

In order to overcome this issue, constitutive models written in terms of a generalized effective stress generally introduce suction as a variable and define a Loading-Collapse curve, similarly to the Barcelona Basic Model (introduced in Section 4.2.2.2 and further described in Chapter 5), (see for instance Jommi & di Prisco, 1994; Bolzon *et al.*, 1996; Loret & Khalili, 2000; Wheeler *et al.*, 2003; Sheng *et al.*, 2004; Laloui & Nuth, 2005; Della Vecchia *et al.*, 2013, among many others).

4.2.2.2 Independent variables approach

According to Fredlund & Rahardjo (1993), the number of independent variables is directly linked to the number of phases. For a saturated porous material, only one variable is required: the effective stress. For partially saturated soils, Coleman (1962), Bishop & Blight (1963), Fredlund & Morgenstern (1977) and Alonso *et al.* (1990), among others, showed that two independent variables enable to overcome the limitations of the single effective stress. In particular, Fredlund & Morgenstern (1977) demonstrated that any pair of $\boldsymbol{\sigma} = \boldsymbol{\sigma_t} - u_g$, $\boldsymbol{\sigma'} = \boldsymbol{\sigma_t} - u_w$ and suction $s = u_g - u_w$, where

$$\boldsymbol{\sigma} = \boldsymbol{\sigma_t} - u_g \boldsymbol{I} \tag{3.33}$$

is the net stress tensor, could be used to describe the behaviour of unsaturated soils. In most cases, the net stress and suction are selected to work in the unsaturated domain. This couple of variables is primarily justified by the fact that the variables are directly accessible during experimental tests. Once that the material is saturated, the effective stress $\boldsymbol{\sigma_t} - u_w$ is often used instead of the net stress.

Null tests can be performed to verify the applicability of the coupled of variables. Indeed, if the components of the variables are changed identically so that the variables do not change ($\Delta\sigma_{t,ij} = \Delta u_g = \Delta u_w$), no volume change nor distortion should be observed.

Finally, the main drawback of the independent variables approach is that the extension of constitutive models for saturated materials is not straightforward. Specific constitutive models, accounting for the different independent variables, should be developed. In addition, there might be lack of continuity in the transition between saturated and unsaturated states.

The first and most famous complete constitutive model for unsaturated soils is the Barcelona Basic Model (BBM) developed by Alonso *et al.* (1990). The model uses suction and net stress as independent variables. As an extension of the Modified Cam-Clay model (Roscoe & Burland, 1968), the Barcelona Basic Model is formulated in the framework of elastoplasticity theory and critical state models. An important contribution of the BBM is the definition of the Loading-Collapse (LC) curve. This yield surface represents the evolution of the preconsolidation pressure with suction, and allows reproducing easily the collapse phenomenon upon wetting under high stress level. The three dimensional yield surface of the model is presented in Figure 3.4.

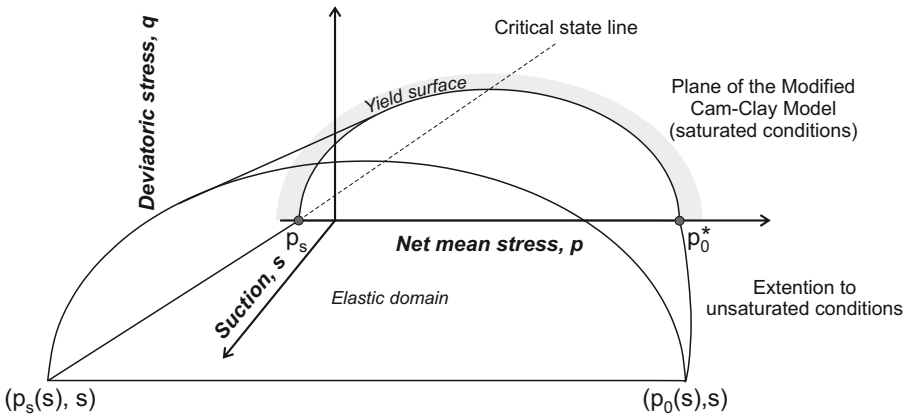

Figure 3.4: Three dimensional yield surface of Barcelona Basic Model (Alonso *et al.*, 1990).

The Barcelona Basic Model pioneered the development of almost all advanced constitutive models for unsaturated soils, being formulated with independent stress variables or an effective stress. Examples of models written in terms of independent variables include the ones of Cui *et al.* (1995); Wheeler & Sivakumar (1995); Cui & Delage (1996); Alonso *et al.* (1999); Collin *et al.* (2002); Sánchez *et al.* (2005); Sheng *et al.* (2008a).

4.3 Multiphase flow model

The fluid mass balance equations (3.18) and (3.19) involve mass fluxes of water and air which should be related to the displacement, water pressure and gas pressure fields. In this section, the equations for multiphase flow in porous media are developed with particular emphasis placed on the hydromechanical coupling relationships.

4.3.1 Fluid transfer equations

In both liquid and gas phases, water and air fluxes are a combination of advective and non-advective fluxes. Advective fluxes are associated to the phase movements, while non-advective fluxes are associated to the motion of species within phases. The mass fluxes of liquid water, water vapour, dry gas and dissolved gas are given respectively by

$$\boldsymbol{f}_{\boldsymbol{l}}^{\boldsymbol{w}} = \rho_w \boldsymbol{q}_{\boldsymbol{l}} \tag{3.34}$$

$$\boldsymbol{f}_{\boldsymbol{g}}^{\boldsymbol{w}} = \rho_v \boldsymbol{q}_{\boldsymbol{g}} + \boldsymbol{i}_{\boldsymbol{g}}^{\boldsymbol{w}} \tag{3.35}$$

$$\boldsymbol{f}_{\boldsymbol{g}}^{\boldsymbol{a}} = \rho_a \boldsymbol{q}_{\boldsymbol{g}} + \boldsymbol{i}_{\boldsymbol{g}}^{\boldsymbol{a}} \tag{3.36}$$

$$\boldsymbol{f}_{\boldsymbol{l}}^{\boldsymbol{a}} = \rho_l^a \boldsymbol{q}_{\boldsymbol{l}} + \boldsymbol{i}_{\boldsymbol{l}}^{\boldsymbol{a}} \tag{3.37}$$

where $\boldsymbol{q}_{\boldsymbol{l}}$ and $\boldsymbol{q}_{\boldsymbol{g}}$ are the advective fluxes of the liquid and gas phases respectively, and $\boldsymbol{i}_{\boldsymbol{g}}^{\boldsymbol{w}}$, $\boldsymbol{i}_{\boldsymbol{g}}^{\boldsymbol{a}}$ and $\boldsymbol{i}_{\boldsymbol{l}}^{\boldsymbol{a}}$ are the diffusive fluxes of water vapour, dry air and dissolved air. Note that, in Equation (3.34), water diffusion in the liquid phase is neglected due to the small amount of dissolved air.

4.3.1.1 Advective fluxes

Advective fluxes of both liquid and gas phases are described by the generalized Darcy's law for partially saturated porous media. The mass fluxes of the liquid and gas phases are given by

$$\boldsymbol{q}_{\boldsymbol{l}} = -\frac{k_w}{\mu_w} \left(\nabla u_w + \rho_w \boldsymbol{g} \right) \tag{3.38}$$

$$\boldsymbol{q}_{\boldsymbol{g}} = -\frac{k_g}{\mu_g} \left(\nabla u_g + \rho_g \boldsymbol{g} \right) \tag{3.39}$$

where k_w and k_g are the water and gas permeabilities of the partially saturated medium, and μ_w and μ_g are the dynamic viscosities of liquid water[3] and the gas phase respectively.

In non-reactive porous media[4], the water and gas permeabilities strongly depend on the degree of saturation. Accordingly, the water and gas permeabilities are generally expressed as

$$k_w = K_w k_{rw} \left(S_r \right) \tag{3.40}$$

[3]Rigorously, the permeability, dynamic viscosity and density of the liquid phase, not liquid water, should be considered in Equation (3.38). However, as mentioned above, the effects of dissolved air on the properties of the liquid phase are neglected in this work.

[4]Non-reactive porous media here refer to porous media with *fixed* structure.

$$k_g = K_g k_{rg}\left(S_r\right) \tag{3.41}$$

where K_w and K_g are respectively the water permeability in fully saturated conditions and gas permeability in totally dry conditions, and k_{rw} and k_{rg} are the water and gas relative permeabilities which are functions of the degree of saturation. For a given degree of saturation, the water relative permeability is defined as the ratio between the unsaturated water permeability and the saturated water permeability. It takes a value of 0 for theoretically completely dry conditions and 1 for saturated conditions. Accordingly, the gas relative permeability is the ratio between the unsaturated gas permeability and the gas permeability for totally dry conditions. In non-reactive porous materials, the relative permeability takes into account the change in cross section responsible for water flow with the amount of water in the porous material.

While the generalized Darcy's law is treated here as a constitutive law, it has been obtained from balance equations and thermodynamic principles in averaging theories (see Hassanizadeh & Gray, 1980; Lewis & Schrefler, 1998, for instance). The generalized Darcy's law may indeed be derived from the equation of the linear momentum balance for the liquid phase, assuming that inertial, viscous and phase changes effects are negligible. One can show that these assumptions are valid if water flow is sufficiently slow (Lewis & Schrefler, 1998), as this is the case in compacted bentonite-based materials, hence providing a theoretical background for the use of Darcy's law in low permeability porous media.

4.3.1.2 Diffusive fluxes

The diffusive fluxes are governed by Fick's law. According to Fick's law, the diffusive flux is proportional to the gradient of mass fraction of species, the proportionality coefficient being the hydrodynamic dispersion coefficient. The diffusive fluxes of water vapour and dissolved air read

$$\boldsymbol{i_g^w} = -D_g^{w*}\rho_g \nabla\left(\frac{\rho_v}{\rho_g}\right) = -\boldsymbol{i_g^a} \tag{3.42}$$

$$\boldsymbol{i_l^a} = -D_l^{a*}\rho_w \nabla\left(\frac{\rho_l^a}{\rho_w}\right) \tag{3.43}$$

where D_g^{w*} and D_l^{a*} are the effective diffusion coefficients of water vapour and dissolved air in the porous medium. These coefficients depend on the porous volume of the material, its structure and its water content. Philip & de Vries (1957) suggested to express the diffusion coefficients as

$$D_g^{w*} = \phi\left(1 - S_r\right)\tau D_g^w \tag{3.44}$$

and

$$D_l^{a*} = \phi S_r \tau D_l^a \tag{3.45}$$

where S_r and $(1 - S_r)$ are the liquid and gas degrees of saturation respectively, τ is the tortuosity, and D_g^w and D_l^a are the diffusion coefficients of water vapour in air and dissolved air in water, which are independent of the porous medium. In Equation (3.44), the product $\phi\left(1 - S_r\right)$ expresses the fact that vapour diffusion occurs through the gas phase

of a porous medium, assuming that the total porosity contributes to vapour diffusion. On the other hand, the tortuosity takes into account the fact that the path of a water molecule is not rectilinear but that vapour flow occurs in a tortuous porous medium (Figure 3.5). Accordingly, the effective length covered by a water molecule (L_e) is larger than the straight line distance (L).

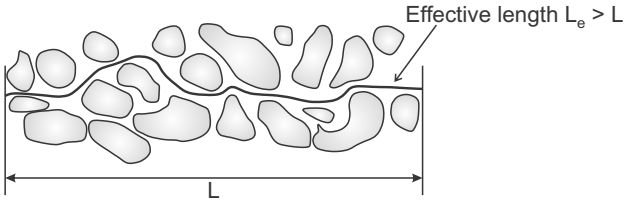

Figure 3.5: Concept of tortuosity in granular porous media (Shackelford *et al.*, 1989).

Equations (3.42) and (3.43) then become

$$\boldsymbol{i_g^w} = -\phi\,(1 - S_r)\,\tau D_g^w \rho_g \nabla\left(\frac{\rho_v}{\rho_g}\right) = -\boldsymbol{i_g^a} \tag{3.46}$$

$$\boldsymbol{i_l^a} = -\phi S_r \tau D_l^a \rho_w \nabla\left(\frac{\rho_l^a}{\rho_w}\right). \tag{3.47}$$

The diffusion coefficient D_g^w depends on the gas pressure and temperature, but is independent of the porous medium. For a gas mixture of water vapour and dry air, the law proposed by Philip & de Vries (1957) is used

$$D_g^w = 5.893 \times 10^{-6}\left(\frac{T^{2.3}}{u_g}\right) \tag{3.48}$$

where T is the temperature (T and u_g should be expressed in K and Pa respectively). For a mixture of water vapour with any other gas species than air, the diffusion coefficient can be expressed as

$$D_g^w = D_{g0}^w\left(\frac{u_{g0}}{u_g}\right)\left(\frac{T}{T_0}\right)^{1.75} \tag{3.49}$$

where D_{g0}^w is the diffusion coefficient of the gas mixture at $T_0 = 273.15$ K and $u_{g0} = 0.1$ MPa. The diffusion coefficient of water vapour in air D_l^a is equal to $5.03{\times}10^{-9}$ m^2/s.

4.3.2 Liquid density variation

The liquid water bulk density ρ_w is a function of the water pressure u_w according to

$$\rho_w = \rho_{w0}\left(1 + \frac{u_w - u_{w0}}{\chi_w}\right) \tag{3.50}$$

where ρ_{w0} is the liquid water density at the reference water pressure u_{w0}, and χ_w is the water compressibility, equal to 2×10^9 Pa at 20°C. As discussed in Chapter 2, the strong physicochemical interactions between water and clay minerals in compacted bentonites are likely to lead to values of water density higher than 1 Mg/m^3 for saturated conditions. Accordingly, values of ρ_{w0} higher than 1 Mg/m^3 will be assumed for $u_w = 0.1$ MPa. Still, the evolution of the water density in the unsaturated domain remains unclear and should be further investigated.

4.3.3 Gas density variation

The gas phase is considered as a ideal mixture of ideal gases, namely dry air (or any other gas species) and water vapour, that is

$$u_g = u_a + u_v. \tag{3.51}$$

The density of the gas phase is obtained using Dalton's law. It yields

$$\rho_g = \rho_a + \rho_v \tag{3.52}$$

with ρ_a and ρ_v the densities of dry air and water vapour, respectively

$$\rho_a = \frac{M_a}{RT} u_a \tag{3.53}$$

$$\rho_v = \frac{M_w}{RT} u_v \tag{3.54}$$

where R is the universal gas constant (= 8.3143 J/mol·K), T is the absolute temperature in Kelvin, and M_a and M_w are the molecular mass of dry air (= 0.029 kg/mol) and water (= 0.018 kg/mol) respectively.

4.3.4 Fluid properties

The fluid flow equations presented in this chapter require parameters for water and air. The dynamic viscosities and densities of liquid water, water vapour and dry air are presented in Table 3.1. Unless otherwise specified, these values are used throughout the present work.

	Dynamic viscosity μ (Pa·s)	**Density ρ** (kg/m^3)
Liquid water	10^{-3}	1000
Water vapour	10^{-5}	Kelvin's law
Dry air	18.6×10^{-6}	1.205

Table 3.1: Dynamic viscosity and density of liquid water, water vapour and dry air (defined at $T_0 = 20$°C and $u_{w0} = u_{g0} = 0.1$ MPa).

5 Equilibrium restrictions

Equilibrium restrictions relate dependent variables with the kinematics variables. They are obtained assuming thermodynamic equilibrium between the different phases of the species. This hypothesis is justified by the fast kinetics of the dissolution processes compared to the transport phenomena in compacted bentonite-based materials.

5.1 Kelvin's law

In this work, we assume that water vapour is always in thermodynamic equilibrium with liquid water. Kelvin's law expresses the pressure of water vapour u_v as a function of suction according to

$$u_v = u_v^0 \exp\left(\frac{-sM_w}{RT\rho_w}\right) \tag{3.55}$$

where u_v^0 is the saturated pressure of water vapour. For a given temperature, the saturated pressure of water vapour is a constant. It may be calculated from the Clausius-Clapeyron equation or obtained from empirical relationships (see Garrels & Christ, 1965; Ewen & Thomas, 1989).

5.2 Henry's law

Henry's law expresses the equilibrium between dissolved air in the liquid phase and dry air in the gas phase. Under constant temperature, the amount of dissolved air is proportional to the air partial pressure

$$u_a = K_l^a x_l^a \tag{3.56}$$

where K_l^a is a constant. This law may be written in terms of densities, so that

$$\rho_l^a = H_a \rho_a \tag{3.57}$$

where H_a is called the Henry's constant and is equal to 0.0234 for air.

6 Finite element formulation

The hydromechanical formulation presented in the previous sections is expressed as a series of local equations expressed in a differential form. However, in order to be used in finite element analysis, the balance equations need to be expressed in a weak form and the constitutive equations should be discretized. The theoretical developments leading to the formulation of a coupled finite element are presented in this section.

6.1 Kinematics

Let us consider a deformable porous body $\mathcal{B}$. At time $t = t_0$, the material point X has the coordinates $\boldsymbol{X}$ in the reference configuration $\mathcal{B}_0$ (Figure 3.6). In this work, the finite element code `LAGAMINE` (Charlier, 1987) is used and the updated Lagrangian formulation is adopted to describe the kinematics of $\mathcal{B}$. Accordingly, all quantities are measured with respect to the current configuration $\mathcal{B} = \varphi(\mathcal{B}_0)$, where φ is the mapping that associates a material point X of the reference configuration $\mathcal{B}_0$ with its current position $\boldsymbol{x} = \varphi(\boldsymbol{X})$. This deformation is characterized by a deformation gradient $\boldsymbol{F}$ such that

$$F_{ij} = \frac{\partial x_i}{\partial X_j} \tag{3.58}$$

with $i, j = 1, 2$ for two-dimensional analysis and $i, j = 1, 3$ for three-dimensional analysis. Note that the Jacobian $J = \det \boldsymbol{F}$ of this transformation must be strictly positive to keep the mapping continuous and bijective, hence preventing self-penetration of the body.

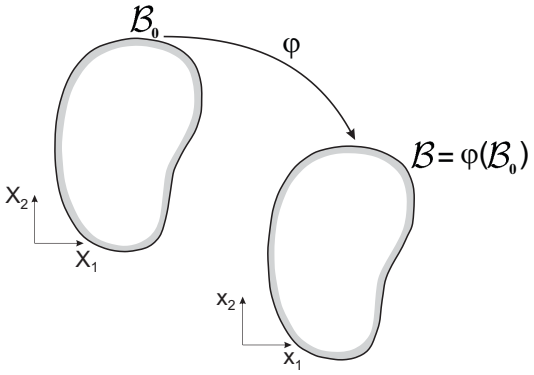

Figure 3.6: Definition of the different configurations of a deformable body $\mathcal{B}$: $\mathcal{B}_0$ and (X_1, X_2) are the reference configuration and basis respectively, and $\mathcal{B}$ and (x_1, x_2) are the current configuration and basis.

The polar decomposition of the deformation gradient $\boldsymbol{F}$ leads to

$$\boldsymbol{F} = \boldsymbol{R} \cdot \boldsymbol{U} \tag{3.59}$$

where $\boldsymbol{R}$ is the rigid body rotation tensor which does not generate any strain, and $\boldsymbol{U}$ is the stretching tensor. The true strain tensor $\boldsymbol{\varepsilon}$, defined as

$$\boldsymbol{\varepsilon} = \ln \boldsymbol{U} \tag{3.60}$$

is used in `LAGAMINE` (Charlier, 1987).

The velocity $\boldsymbol{v}$ of a material point in the current configuration $\mathcal{B}$ is given by

$$\boldsymbol{v} = \frac{\mathrm{d}\boldsymbol{x}}{\mathrm{d}t} = \dot{\boldsymbol{x}} \tag{3.61}$$

where t denotes time and the superior dot denotes a derivative with respect to time. Accordingly, the velocity gradient $\boldsymbol{L}$ is defined as

$$\boldsymbol{L} = \frac{\partial \boldsymbol{v}}{\partial \boldsymbol{x}} = \frac{\partial \boldsymbol{v}}{\partial \boldsymbol{X}} \frac{\partial \boldsymbol{X}}{\partial \boldsymbol{x}} = \dot{\boldsymbol{F}} \cdot \boldsymbol{F}^{-1} \tag{3.62}$$

and can be split into symmetrical and anti-symmetrical parts

$$\boldsymbol{L} = \frac{1}{2}\left(\boldsymbol{L} + \boldsymbol{L}^T\right) + \frac{1}{2}\left(\boldsymbol{L} - \boldsymbol{L}^T\right) = \boldsymbol{d} + \boldsymbol{\omega} = \dot{\boldsymbol{\varepsilon}} + \boldsymbol{\omega} \tag{3.63}$$

where the superscript T stands for the transpose operator. The symmetrical part of $\boldsymbol{L}$ defines the rate of deformation (or stretching) tensor $\boldsymbol{d}$, and the anti-symmetrical part of $\boldsymbol{\omega}$ is called the spin tensor. In this work, the notation $\dot{\boldsymbol{\varepsilon}}$ is preferred to $\boldsymbol{d}$, as it is more commonly used in geomechanics. However, it should be clear that $\dot{\boldsymbol{\varepsilon}}$ is not a time derivative of the strain tensor $\boldsymbol{\varepsilon}$.

The total Cauchy stress tensor $\boldsymbol{\sigma_t}$ is associated with the Cauchy strain rate. However, in large deformation analysis, the incremental formulation requires to define an objective stress rate. Indeed the stress rate should be frame independent, so that any rigid-body motion does not induce stress within the material. Here, the objectivity of the stress tensor is satisfied by adopting the Jaumann objective stress rate $\tilde{\boldsymbol{\sigma}}_{\boldsymbol{t}}$

$$\tilde{\boldsymbol{\sigma}}_{\boldsymbol{t}} = \dot{\boldsymbol{\sigma}}_{\boldsymbol{t}} - \boldsymbol{\omega} \cdot \boldsymbol{\sigma_t} - \boldsymbol{\sigma_t} \cdot \boldsymbol{\omega}^T. \tag{3.64}$$

6.2 Initial and boundary conditions

For model closure, initial and boundary conditions should be defined. The initial conditions describe the entire fields of displacements $\boldsymbol{u}$, water pressures u_w and gas pressures u_g on $\mathcal{B}_i$ at time $t = t_i$

$$\boldsymbol{u} = \Delta\boldsymbol{x} = \boldsymbol{u}_i, \qquad u_w = u_{wi}, \qquad u_g = u_{gi}. \tag{3.65}$$

At all time $t > t_i$, boundary conditions should be defined on the boundary $\partial\mathcal{B}$ of the body $\mathcal{B}$. Classic boundary conditions are classified as either Dirichlet or Neumann type. Dirichlet boundary conditions correspond to imposed displacements or fluid pressures. They may be expressed as

$$\boldsymbol{u} = \bar{\boldsymbol{u}}, \quad \text{on } \partial\mathcal{B}_{\bar{\boldsymbol{x}}} \qquad u_w = \bar{u}_w, \quad \text{on } \partial\mathcal{B}_{\bar{u}_w} \quad u_g = \bar{u}_g, \qquad \text{on } \partial\mathcal{B}_{\bar{u}_g}. \tag{3.66}$$

On the other hand, Neumann boundary conditions correspond to imposed force or fluid flux. For the displacement field, the traction boundary condition reads

$$\bar{\boldsymbol{t}} = \boldsymbol{n} \cdot \boldsymbol{\sigma_t}, \quad \text{on } \partial\mathcal{B}_t \tag{3.67}$$

where $\bar{\boldsymbol{t}}$ is the imposed Cauchy traction vector and $\boldsymbol{n}$ is the unit normal vector to $\partial\mathcal{B}$. Similarly, the Neumann boundary conditions for water pressure and gas pressure fields read

$$\boldsymbol{n} \cdot \boldsymbol{f^w} + \bar{q}^w = 0, \quad \text{on } \partial\mathcal{B}_{q^w} \qquad \boldsymbol{n} \cdot \boldsymbol{f^a} + \bar{q}^a = 0, \quad \text{on } \partial\mathcal{B}_{q^a} \tag{3.68}$$

where $\bar{q}^w$ and $\bar{q}^a$ are water and air total fluxes imposed at the surface (positive if incoming), and $\boldsymbol{f^w}$ and $\boldsymbol{f^a}$ are inside total fluxes of water and air species in both liquid and gas phases such that

$$\boldsymbol{f^w} = \boldsymbol{f_l^w} + \boldsymbol{f_g^w} \tag{3.69}$$

$$\boldsymbol{f^a} = \boldsymbol{f_l^a} + \boldsymbol{f_g^a} \tag{3.70}$$

with the mass fluxes $\boldsymbol{f_l^w}$, $\boldsymbol{f_g^w}$, $\boldsymbol{f_l^a}$ and $\boldsymbol{f_g^a}$ defined in Equations (3.34) to (3.37).

6.3 Weak form of the balance equations

The balance equations (3.10), (3.18) and (3.19) are local balance equations. However, in order to address boundary-value problems over large domains, weak forms of the equations are required. The weak form of the balance of momentum (3.20) is obtained by using the rate form of the principle of virtual work. For any kinematically admissible[5] virtual velocity field $\delta\dot{\boldsymbol{u}}$, equilibrium is satisfied if the internal virtual power δW_I is equal to the external one δW_E

$$\underbrace{\int_{\mathcal{B}} \boldsymbol{\sigma_t} \cdot \nabla\left(\delta\dot{\boldsymbol{u}}\right) \mathrm{d}\Omega}_{\delta W_I} = \underbrace{\int_{\mathcal{B}} \boldsymbol{b} \cdot \delta\dot{\boldsymbol{u}} \mathrm{d}\Omega + \int_{\partial\mathcal{B}_t} \bar{\boldsymbol{t}} \cdot \delta\dot{\boldsymbol{u}} \mathrm{d}\Gamma}_{\delta W_E}. \tag{3.71}$$

[5] A kinematically admissible field respects the solid continuity and boundary conditions.

Note that in an updated Lagrangian formulation, the integrals are evaluated in the current configuration.

By analogy between mechanical and hydraulic problems, the virtual work theorem is used to derive the weak form of the fluid mass balance equations (3.18) and (3.19). The water and air mass balance equations read respectively in a weak form

$$\underbrace{\int_{\mathcal{B}} \left[\dot{m}^w \delta u_w - \boldsymbol{f^w} \cdot \nabla\left(\delta u_w\right)\right] \mathrm{d}\Omega}_{\delta W_I} = \underbrace{\int_{\mathcal{B}} Q^w \delta u_w \mathrm{d}\Omega - \int_{\partial \mathcal{B}_{q^w}} \bar{q}^w \delta u_w \mathrm{d}\Gamma}_{\delta W_E} \tag{3.72}$$

and

$$\underbrace{\int_{\mathcal{B}} \left[\dot{m}^a \delta u_g - \boldsymbol{f^a} \cdot \nabla\left(\delta u_g\right)\right] \mathrm{d}\Omega}_{\delta W_I} = \underbrace{\int_{\mathcal{B}} Q^a \delta u_g \mathrm{d}\Omega - \int_{\mathcal{B}_{q^a}} \bar{q}^a \delta u_g \mathrm{d}\Gamma}_{\delta W_E} \tag{3.73}$$

where δu_w and δu_g are the virtual water and gas pressure fields, m^w and m^a are total mass of water and air inside the current configuration $\mathcal{B}$ given by

$$m^w = m_l^w + m_g^l = \rho_w S_r \phi + \rho_v \left(1 - S_r\right) \phi \tag{3.74}$$

$$m^a = m_g^a + m_l^a = \rho_a \left(1 - S_r\right) \phi + \rho_l^a S_r \phi \tag{3.75}$$

and Q^w and Q^a are respectively water and air source terms.

6.4 Time discretization

The balance equations (3.71) to (3.73) should be verified at any time t. In order to solve numerically this non-linear problem, the loading process is discretized into finite time steps Δt, which may be of different sizes. The system of equations is then solved for any time $t = \sum_{k=1}^{\alpha} \Delta t_k$ with $\alpha \in \mathbb{N}$, using for every time step a full Newton-Raphson procedure.

A fully implicit finite difference scheme is used to define the time derivatives of the displacement, water pressure and gas pressure fields

$$\dot{u}_i^{t+\Delta t} = \frac{u_i^{t+\Delta t} - u_i^t}{\Delta t} = \frac{\Delta u_i}{\Delta t} \tag{3.76}$$

$$\dot{u}_w^{t+\Delta t} = \frac{u_w^{t+\Delta t} - u_w^t}{\Delta t} = \frac{\Delta u_w}{\Delta t} \tag{3.77}$$

$$\dot{u}_g^{t+\Delta t} = \frac{u_g^{t+\Delta t} - u_g^t}{\Delta t} = \frac{\Delta u_g}{\Delta t}. \tag{3.78}$$

6.5 Linearization of the field equations

Because of the important hydromechanical coupling and the complex constitutive models adopted in geomechanics, Equations (3.71) to (3.73) are highly non-linear relations and their analytical solution is almost impossible. In order to solve numerically the system of field equations, a Newton-Raphson scheme is used to find a solution of the displacement and pressure fields, for which equilibrium is achieved. The aim of this section is to transform the system of non-linear equations into an auxiliary linear problem, similarly to the approaches of Borja & Alarcón (1995), Chambon *et al.* (2001), Collin *et al.* (2006) and Gerard *et al.* (2008).

Let us consider a known configuration $\mathcal{B}^t$ at time t in equilibrium with the boundary conditions. The objective is to find the configuration in equilibrium at the end of the time step ($\tau = t + \Delta t$). A first guess of the new configuration $\mathcal{B}^{\tau 1}$ is realized, for which the equilibrium is not met. Mechanical, water flow and air flow residuals, respectively $R^{\tau 1}$, $W^{\tau 1}$ and $G^{\tau 1}$ appear in the balance equations

$$\int_{\mathcal{B}^{\tau 1}} \sigma^{\tau 1}_{t,ij} \frac{\partial\left(\delta u_i\right)}{\partial x^{\tau 1}_j} \mathrm{d}\Omega^{\tau 1} - \int_{\mathcal{B}^{\tau 1}} b_i \delta u_i \mathrm{d}\Omega^{\tau 1} - \int_{\partial\mathcal{B}^{\tau 1}_t} \bar{t}^{\tau 1}_i \delta u_i \mathrm{d}\Gamma^{\tau 1} = R^{\tau 1} \tag{3.79}$$

$$\int_{\mathcal{B}^{\tau 1}} \left[\left(\dot{m}^w\right)^{\tau 1} \delta u_w - \left(f^w\right)^{\tau 1}_i \frac{\partial\left(\delta u_w\right)}{\partial x^{\tau 1}_i} \right] \mathrm{d}\Omega^{\tau 1} - \int_{\mathcal{B}^{\tau 1}} \left(Q^w\right)^{\tau 1} \delta u_w \mathrm{d}\Omega^{\tau 1} + \int_{\partial\mathcal{B}^{\tau 1}_{q^w}} \left(\bar{q}^w\right)^{\tau 1} \delta u_w \mathrm{d}\Gamma^{\tau 1} = W^{\tau 1} \tag{3.80}$$

$$\int_{\mathcal{B}^{\tau 1}} \left[\left(\dot{m}^a\right)^{\tau 1} \delta u_g - \left(f^a\right)^{\tau 1}_i \frac{\partial\left(\delta u_g\right)}{\partial x^{\tau 1}_i} \right] \mathrm{d}\Omega^{\tau 1} - \int_{\mathcal{B}^{\tau 1}} \left(Q^a\right)^{\tau 1} \delta u_g \mathrm{d}\Omega^{\tau 1} + \int_{\partial\mathcal{B}^{\tau 1}_{q^a}} \left(\bar{q}^a\right)^{\tau 1} \delta u_g \mathrm{d}\Gamma^{\tau 1} = G^{\tau 1}. \tag{3.81}$$

The aim is to find a new configuration $\mathcal{B}^{\tau 2}$, close to $\mathcal{B}^{\tau 1}$, for which the residuals $R^{\tau 2}$, $W^{\tau 2}$ and $G^{\tau 2}$ vanish. In order to get the auxiliary linear problem, the system of field equations corresponding to $\mathcal{B}^{\tau 2}$ are written in configuration $\mathcal{B}^{\tau 1}$ and the resulting equations are subtracted from the corresponding initial equations written in configuration $\mathcal{B}^{\tau 1}$. This yields the following equations

$$\int_{\mathcal{B}^{\tau 1}} \frac{\partial\left(\delta u_i\right)}{\partial x^{\tau 1}_k} \left(\sigma^{\tau 2}_{t,ij} \frac{\partial x^{\tau 1}_k}{\partial x^{\tau 2}_j} \det \boldsymbol{F}^{\tau} - \sigma^{\tau 1}_{t,ik} \right) \mathrm{d}\Omega^{\tau 1} - \int_{\mathcal{B}^{\tau 1}} \delta u_i \left(\rho^{\tau 2} \det \boldsymbol{F}^{\tau} - \rho^{\tau 1} \right) g_i \mathrm{d}\Omega^{\tau 1} = -R^{\tau 1} \tag{3.82}$$

$$\int_{\mathcal{B}^{\tau 1}} \left\{ \left[\left(\dot{m}^w\right)^{\tau 2} \det \boldsymbol{F}^{\tau} - \left(\dot{m}^w\right)^{\tau 1} \right] \delta u_w - \frac{\partial\left(\delta u_w\right)}{\partial x^{\tau 1}_k} \left[\left(f^w\right)^{\tau 2}_i \frac{\partial x^{\tau 1}_k}{\partial x^{\tau 2}_i} \det \boldsymbol{F}^{\tau} - \left(f^w\right)^{\tau 1}_k \right] \right\} \mathrm{d}\Omega^{\tau 1} = \int_{\partial\mathcal{B}^{\tau 1}_{q^w}} \left[\left(\bar{q}^w\right)^{\tau 2} \det \boldsymbol{F}^{\tau} - \left(\bar{q}^w\right)^{\tau 1} \right] \delta u_w \mathrm{d}\Gamma^{\tau 1} - W^{\tau 1} \tag{3.83}$$

$$\int_{\mathcal{B}^{\tau 1}} \left\{ \left[(\dot{m}^a)^{\tau 2} \det \boldsymbol{F}^\tau - (\dot{m}^a)^{\tau 1} \right] \delta u_g - \frac{\partial (\delta u_g)}{\partial x_k^{\tau 1}} \left[(f^a)_i^{\tau 2} \frac{\partial x_k^{\tau 1}}{\partial x_i^{\tau 2}} \det \boldsymbol{F}^\tau - (f^a)_k^{\tau 1} \right] \right\} \mathrm{d}\Omega^{\tau 1}$$
$$= \int_{\partial \mathcal{B}_{q^a}^{\tau 1}} \left[(\bar{q}^a)^{\tau 2} \det \boldsymbol{F}^\tau - (\bar{q}^a)^{\tau 1} \right] \delta u_g \mathrm{d}\Gamma^{\tau 1} - G^{\tau 1} \quad (3.84)$$

where $b_i = \rho g_i$, with ρ the density of the mixture defined in equation (3.21) and $\det \boldsymbol{F}^\tau$ is the Jacobian of

$$F_{ij}^\tau = \frac{\partial x_i^{\tau 2}}{\partial x_j^{\tau 1}} \quad (3.85)$$

describing the transformation in large deformations of coordinates in configuration $\mathcal{B}^{\tau 2}$ to the ones in configuration $\mathcal{B}^{\tau 1}$, and, following Einstein's notation, repeated indices i, j and k mean summation.

Let us define

$$\mathrm{d}\gamma^{\tau 1} = \gamma^{\tau 2} - \gamma^{\tau 1} \quad (3.86)$$

where γ denotes any variable or quantity. Using Taylor expansion and discarding terms in degrees greater than one yields

$$\frac{\partial x_k^{\tau 1}}{\partial x_j^{\tau 2}} = \frac{\partial x_k^{\tau 2} - \partial \mathrm{d}x_k^{\tau 1}}{\partial x_j^{\tau 2}} = \frac{\partial x_k^{\tau 2} - \partial \mathrm{d}u_k^{\tau 1}}{\partial x_j^{\tau 2}} \simeq \delta_{jk} - \frac{\partial \mathrm{d}u_k^{\tau 1}}{\partial x_j^{\tau 1}} \quad (3.87)$$

and

$$\det \boldsymbol{F}^\tau = \epsilon_{ijk} \left(\delta_{1i} + \frac{\partial u_1^{\tau 1}}{\partial x_i^{\tau 1}} \right) \left(\delta_{2j} + \frac{\partial u_2^{\tau 1}}{\partial x_j^{\tau 1}} \right) \left(\delta_{3k} + \frac{\partial u_3^{\tau 1}}{\partial x_k^{\tau 1}} \right) \simeq 1 + \frac{\partial \mathrm{d}u_i^{\tau 1}}{\partial x_i^{\tau 1}} \quad (3.88)$$

where δ_{jk} is the Kronecker symbol and ϵ_{ijk} is the Levi-Civita symbol.

Using these relations, and assuming $\bar{t}_i$, Q^w and Q^a, and $\bar{q}^w$ and $\bar{q}^a$ position and fluid pressures independent, equations (3.82) to (3.84) may be expressed as functions of the only unknowns u_i, u_w and u_g.

For any kinematically admissible displacement field δu_i, the linearization of the momentum balance equation leads to

$$\int_{\mathcal{B}^{\tau 1}} \frac{\partial (\delta u_i)}{\partial x_k^{\tau 1}} \left(\mathrm{d}\sigma_{t,ik}^{\tau 1} - \sigma_{t,ij}^{\tau 1} \frac{\partial \mathrm{d}u_k^{\tau 1}}{\partial x_j^{\tau 1}} + \sigma_{t,ik}^{\tau 1} \frac{\partial \mathrm{d}u_m^{\tau 1}}{\partial x_m^{\tau 1}} \right) \mathrm{d}\Omega^{\tau 1}$$
$$- \int_{\mathcal{B}^{\tau 1}} \delta u_i \left[\rho^{\tau 1} \frac{\partial \mathrm{d}u_m^{\tau 1}}{\partial x_m^{\tau 1}} + \mathrm{d}\rho^{\tau 1} \right] g_i \mathrm{d}\Omega^{\tau 1} = -R^{\tau 1} \quad (3.89)$$

where $\mathrm{d}\sigma_{t,ik}^{\tau 1}$ is related to the displacement field through the mechanical constitutive model and, ρ being defined by Equation (3.21),

$$\mathrm{d}\rho^{\tau 1} = \mathrm{d}\rho_w^{\tau 1} (S_r)^{\tau 1} \phi^{\tau 1} + \mathrm{d}\rho_g^{\tau 1} \left[1 - (S_r)^{\tau 1} \right] \phi^{\tau 1}$$
$$+ \left(\rho_w^{\tau 1} - \rho_g^{\tau 1} \right) (\mathrm{d}S_r)^{\tau 1} \phi^{\tau 1}$$
$$+ \left\{ -\rho_s + \rho_w^{\tau 1} (S_r)^{\tau 1} + \rho_g^{\tau 1} \left[1 - (S_r)^{\tau 1} \right] \right\} \mathrm{d}\phi^{\tau 1} \quad (3.90)$$

with

$$\mathrm{d}\phi^{\tau 1} = \left(1 - \phi^{\tau 1}\right) \frac{\mathrm{d}\Omega^{\tau 1}}{\Omega} = \left(1 - \phi^{\tau 1}\right) \frac{\partial \mathrm{d}u_m^{\tau 1}}{\partial x_m^{\tau 1}}. \tag{3.91}$$

Equation (3.91) is derived from the solid mass balance equation assuming the solid phase incompressible and is equivalent to Equation (3.11).

For any kinematically admissible water pressure field δu_w, the linearization of the water mass balance equation leads to

$$\begin{aligned}\int_{\mathcal{B}^{\tau 1}} \left[(\mathrm{d}\dot{m}^w)^{\tau 1} + (\dot{m}^w)^{\tau 1} \frac{\partial \mathrm{d}u_m^{\tau 1}}{\partial x_m^{\tau 1}} \right] \delta u_w \mathrm{d}\Omega^{\tau 1} \\ - \int_{\mathcal{B}^{\tau 1}} \frac{\partial \left(\delta u_w\right)}{\partial x_k^{\tau 1}} \left[(\mathrm{d}f^w)_k^{\tau 1} - (f^w)_i^{\tau 1} \frac{\partial \mathrm{d}u_k^{\tau 1}}{\partial x_i^{\tau 1}} + (f^w)_k^{\tau 1} \frac{\partial \mathrm{d}u_m^{\tau 1}}{\partial x_m^{\tau 1}} \right] \mathrm{d}\Omega^{\tau 1} = -W^{\tau 1}\end{aligned} \tag{3.92}$$

where $(f^w)_i^{\tau 1}$ is related to the water and gas pressure field through the multiphase flow model.

Accordingly, the linearization of the air mass balance equation is obtained for any kinematically admissible gas pressure field δu_g

$$\begin{aligned}\int_{\mathcal{B}^{\tau 1}} \left[(\mathrm{d}\dot{m}^a)^{\tau 1} + (\dot{m}^a)^{\tau 1} \frac{\partial \mathrm{d}u_m^{\tau 1}}{\partial x_m^{\tau 1}} \right] \delta u_g \mathrm{d}\Omega^{\tau 1} \\ - \int_{\mathcal{B}^{\tau 1}} \frac{\partial \left(\delta u_g\right)}{\partial x_k^{\tau 1}} \left[(\mathrm{d}f^a)_k^{\tau 1} - (f^a)_i^{\tau 1} \frac{\partial \mathrm{d}u_k^{\tau 1}}{\partial x_i^{\tau 1}} + (f^a)_k^{\tau 1} \frac{\partial \mathrm{d}u_m^{\tau 1}}{\partial x_m^{\tau 1}} \right] \mathrm{d}\Omega^{\tau 1} = -G^{\tau 1}\end{aligned} \tag{3.93}$$

where $(f^a)_i^{\tau 1}$ is related to the water and gas pressure field through the multiphase flow model.

Equations (3.89), (3.92) and (3.93) highlight the different contributions coming from geometrical non-linear effects (since the configurations $\mathcal{B}^{\tau 1}$ and $\mathcal{B}^{\tau 2}$ are distinguished) and from the multi-physical coupling.

6.6 Finite element discretization and formulation

The finite element method lies on the spatial discretization of each continuum body into finite elements. In this work, the coupled finite element `MWAT 2D` is used to model solid bodies (Collin, 2003). This element is an isoparameteric element with eight nodes and four integration points (Figure 3.7). Each node has five degrees of freedom, namely the spatial coordinates, water pressure, gas pressure and temperature[6].

[6]The developments presented in this Chapter are restricted to isothermal conditions, i.e. as if there were only four degrees of freedom. An energy balance equation is required to solve non-isothermal problems. Interested reader may refer to Collin (2003) for additional information on this issue.

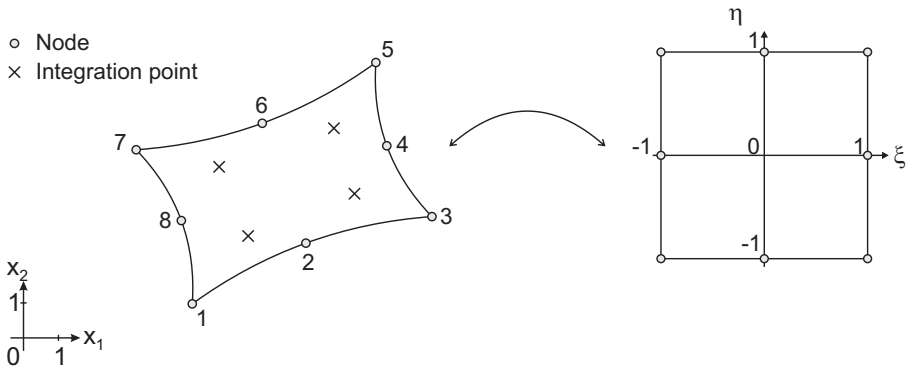

Figure 3.7: Two-dimensional finite element `MWAT 2D` with eight nodes and four integration points (left) and its corresponding parent element (right).

Let us define the vector of nodal unknowns $\boldsymbol{U_N}$

$$\boldsymbol{U_N}^{T\,(1\times 32)} = [\boldsymbol{U_N}_1\ \boldsymbol{U_N}_2\ \boldsymbol{U_N}_3\ \boldsymbol{U_N}_4\ \boldsymbol{U_N}_5\ \boldsymbol{U_N}_6\ \boldsymbol{U_N}_7\ \boldsymbol{U_N}_8] \tag{3.94}$$

with

$$\boldsymbol{U}_{\boldsymbol{N}i}^{T} = [u_{1i}\ u_{2i}\ u_{wi}\ u_{gi}] \qquad \text{for } i = 1, 8 \tag{3.95}$$

8 being the number of nodes.

Nodal unknowns are interpolated over the element using quadratic serendipity shape functions $\boldsymbol{N}_{(\xi,\eta)}$ (Zienkiewicz & Taylor, 2000), so that

$$\boldsymbol{U}_{(\xi,\eta)} = \boldsymbol{N}_{(\xi,\eta)} \cdot \boldsymbol{U_N} \tag{3.96}$$

where $\boldsymbol{U}_{(\xi,\eta)}$ is the vector of interpolated displacement, water pressure and gas pressure fields expressed in terms of natural coordinates associated to the parent element ($-1 \leq \xi \leq 1$ and $-1 \leq \eta \leq 1$).

In order to define the local element stiffness matrix, Equations (3.89), (3.92) and (3.93) are written in matrix form

$$\int_{\Omega} \boldsymbol{\delta U}_{(x_1,x_2)}{}^{T} \cdot \boldsymbol{E} \cdot \mathbf{d}\boldsymbol{U}_{(x_1,x_2)} \mathrm{d}\Omega = -R - W - G \tag{3.97}$$

where the superscript $\tau 1$ is omitted for the sake of readability. In this equation, $\mathbf{d}\boldsymbol{U}_{(x_1,x_2)}$ is defined as

$$\mathbf{d}\boldsymbol{U}_{(x_1,x_2)}^{(1\times 12)} \equiv \left[\frac{\partial \mathrm{d}u_1}{\partial x_1}\ \frac{\partial \mathrm{d}u_1}{\partial x_2}\ \frac{\partial \mathrm{d}u_2}{\partial x_1}\ \frac{\partial \mathrm{d}u_2}{\partial x_2}\ \mathrm{d}u_1\ \mathrm{d}u_2\ \frac{\partial \mathrm{d}u_w}{\partial x_1}\ \frac{\partial \mathrm{d}u_w}{\partial x_2}\ \mathrm{d}u_w\ \frac{\partial \mathrm{d}u_g}{\partial x_1}\ \frac{\partial \mathrm{d}u_g}{\partial x_2}\ \mathrm{d}u_g\right] \tag{3.98}$$

and $\boldsymbol{\delta U}_{(x_1,x_2)}^{\boldsymbol{T}}$ has the same structure as $\mathbf{d}\boldsymbol{U}_{(x_1,x_2)}$ with corresponding virtual quantities.

The finite element spatial discretization is introduced in equation (3.97) using the transformation matrices $\boldsymbol{T}$ and $\boldsymbol{B}$, which connect $\mathbf{d}\boldsymbol{U}_{(x_1,x_2)}$ to the nodal variables $\mathbf{d}\boldsymbol{U}_N$

$$\mathbf{d}\boldsymbol{U}_{(x_1,x_2)} = \boldsymbol{T} \cdot \mathbf{d}\boldsymbol{U}_{(\xi,\eta)} \tag{3.99}$$

$$\mathbf{d}\boldsymbol{U}_{(\xi,\eta)} = \boldsymbol{B} \cdot \mathbf{d}\boldsymbol{U}_N. \tag{3.100}$$

Integration of equation (3.97) on one finite element yields

$$\boldsymbol{\delta U}_N{}^T \cdot \left(\int_{-1}^{1} \int_{-1}^{1} \boldsymbol{B}^T \cdot \boldsymbol{T}^T \cdot \boldsymbol{E} \cdot \boldsymbol{T} \cdot \boldsymbol{B} \ \det \boldsymbol{J}^e \ \mathrm{d}\xi \mathrm{d}\eta \right) \cdot \mathbf{d}\boldsymbol{U}_N = \boldsymbol{\delta U}_N{}^T \cdot \boldsymbol{k} \cdot \mathbf{d}\boldsymbol{U}_N \tag{3.101}$$

where $\boldsymbol{k}$ is the local element stiffness matrix, $\boldsymbol{J}^e$ is the Jacobian matrix of the mapping from (ξ, η) to (x_1, x_2) and $\boldsymbol{E}$ contains all the terms of linearized balance equations (3.89), (3.92) and (3.93). It may be expressed in the form

$$\boldsymbol{E}^{(12\times12)} = \begin{bmatrix} \boldsymbol{E}_{\boldsymbol{MM}}^{(6\times6)} & \boldsymbol{E}_{\boldsymbol{WM}}^{(6\times3)} & \boldsymbol{E}_{\boldsymbol{GM}}^{(6\times3)} \\ \boldsymbol{E}_{\boldsymbol{MW}}^{(3\times6)} & \boldsymbol{E}_{\boldsymbol{WW}}^{(3\times3)} & \boldsymbol{E}_{\boldsymbol{GW}}^{(6\times3)} \\ \boldsymbol{E}_{\boldsymbol{MG}}^{(3\times6)} & \boldsymbol{E}_{\boldsymbol{WG}}^{(3\times3)} & \boldsymbol{E}_{\boldsymbol{GG}}^{(3\times3)} \end{bmatrix} \tag{3.102}$$

where the matrices $\boldsymbol{E}_{\boldsymbol{MM}}$, $\boldsymbol{E}_{\boldsymbol{WW}}$ and $\boldsymbol{E}_{\boldsymbol{GG}}$ are the classic stiffness matrices for mechanical, water flow and gas flow problems, and the off-diagonal matrices contain multi-physical coupling terms. For example, the matrix $\boldsymbol{E}_{\boldsymbol{MW}}$ expresses the influence of mechanics (M) on water flow (W).

When the presence of water vapour is taken into account, the exact analytical computation of these matrices becomes a difficult task. In this case, the terms of the different matrices are computed numerically using a perturbation technique. An additional loop is then required at the level of the multiphase flow law. Each term of the stiffness matrices is computed by finite differences between a perturbed and an unperturbed states, using the velocity at the integration point (Collin, 2003). The choice of adequate perturbation amplitude is an important issue. In particular, the order of magnitude of the perturbation should be consistent with the order of magnitude of the perturbed quantity. Therefore, to increase robustness, mechanical and hydraulic perturbations are distinguished in the multiphase flow law routine.

The residual terms $\boldsymbol{R}$, $\boldsymbol{W}$ and $\boldsymbol{G}$ in equation (3.97) are computed for each element thanks to the following relationship

$$-R - W - G = P_e^* - \boldsymbol{\delta U}_N^T \int_{-1}^{1} \int_{-1}^{1} \boldsymbol{B}^T \cdot \boldsymbol{T}^T \cdot \boldsymbol{\sigma}_{\boldsymbol{G}} \det \boldsymbol{J}^e \mathrm{d}\xi \mathrm{d}\eta \equiv \boldsymbol{\delta U}_N^T \cdot \boldsymbol{f}_{\boldsymbol{OB}} \tag{3.103}$$

with

$$\boldsymbol{\sigma}_{\boldsymbol{G}}^T = [\sigma_{t,11} \ \ldots \ \sigma_{t,22} \ f_1^w \ f_2^w \ \dot{m}^w \ f_1^a \ f_2^a \ \dot{m}^a] \tag{3.104}$$

where $\boldsymbol{f}_{\boldsymbol{OB}}$ is the vector of elementary out-of-balance forces. The external virtual power P_e^* contains the contributions of the body forces for the mechanical and fluid problems, except the term related to gravity volume force, which is introduced in the $\boldsymbol{\sigma}_{\boldsymbol{G}}$ vector.

6.7 Global solution

The global stiffness matrix $\boldsymbol{K}$ and out-of-balance force vector $\delta\boldsymbol{U}$ are obtained by assembling the elementary matrices given equations (3.101) and (3.103). The resulting auxiliary system writes

$$\boldsymbol{K} \cdot \delta\boldsymbol{U} = -\boldsymbol{F_{OB}} \tag{3.105}$$

where $\boldsymbol{F_{OB}}$ is the global out-of-balance vector. After solving the resulting auxiliary linear system, a new configuration is found and the equilibrium is verified. A monolithic (fully coupled) procedure is adopted where the entire stiffness matrix is computed at each iteration of the Newton-Raphson procedure.

7 Conclusions and anticipated contributions

While Chapter 2 was dedicated to the microstructural description of coupled processes in bentonites, this chapter was focused on the conceptual modelling of the hydromechanical processes at the macroscopic scale. The approach adopted in this work consists in representing compacted bentonite-based materials as multiphase porous media composed of solid, liquid and gas phases which are assumed to be in thermodynamic equilibrium. The balance equations are expressed using the compositional approach, while the balance of momentum is expressed for the entire mixture. This framework involves a number of constitutive relations, namely a water retention model, a mechanical model and a multiphase flow law which should be defined. Finally, in order to be able to model boundary-value problems, the formulation of a coupled finite element, implemented in the finite element code `LAGAMINE`, is developed.

As stated before, this chapter does not aim at presenting any new contribution. The objective is rather to introduce the existing framework, highlight which coupled processes are classically considered and which are not, and point out the limitations of the model to represent the hydromechanical behaviour of buffer materials. In particular, in the presented formulation, hydromechanical couplings are introduced essentially through two terms. First of all, changes in porosity will affect the storage capacity of the porous medium, hence the flow of fluids. On the other hand, changes in pore pressures, suction and degree of saturation will yield modifications in the mechanical state of the porous volume. However, the importance of volume changes directly depends on the constitutive mechanical model that is adopted. In addition, while the microstructure of bentonites is observed to change significantly along hydromechanical stress paths, its effects on the hydromechanical properties of bentonite are not considered in the formulation presented in this chapter.

Therefore, it will be necessary to further develop the presented framework in order to reproduce the hydromechanical behaviour of bentonite under repository conditions. In particular, the development presented in this PhD work will focus on the constitutive models that are adopted and the consideration of microstructural changes of the material during hydromechanical loading. The development of the different constitutive models follows the structure of this chapter and the different models are presented in the three following chapters. In Chapter 4, a water retention model, accounting for structural and

volume changes of bentonites, will be developed. This model will be able to reproduce the evolution of the water retention properties of bentonites under various confining conditions. The issue related to the mechanical behaviour of saturated and partially saturated bentonites is treated in Chapter 5. Finally, the evolution of the transfer properties with volume and structural changes are considered in Chapter 6.

Chapter 4

Development of a water retention model

1 Introduction

The water retention capacity of compacted bentonites is one of the fundamental properties required for predicting the behaviour of unsaturated engineered barriers. In the context of deep geological repositories for nuclear waste, bentonite-based materials are generally manufactured and emplaced at their hygroscopic water content. Suction in these partially saturated materials reaches several tens, even hundreds of MPa. Under repository conditions, the engineered barrier experiences hydration from the saturated host rock. Because of the existence of technological gaps, the periphery of the engineered barrier swells under free conditions first. During this stage, technological gaps are progressively filled by bentonite and the effective density of the buffer decreases. When contact between the geological formation and the engineered barrier is reached, the global volume constraints imposed to the bentonite buffer are close to constant volume conditions and a swelling pressure develops on the gallery wall. The objective of the engineered barrier is to form a tight contact with the surrounding formation and to create a zone of low permeability that is able to limit water flow around the excavated galleries, thereby delaying the release of radionuclides to the biosphere.

Experimental observations from large-scale *in situ* tests have shown that this transient stage of hydration may lead to a non-homogeneous distribution of dry density within the bentonite buffer. The Full-scale High Level Waste Engineered Barriers (FEBEX) experiment conducted in the Grimsel Test Site (GTS), Switzerland, aimed at studying the behaviour of an engineered barrier made up of compacted blocks of bentonite. While the initial dry density of the blocks was 1.60 Mg/m^3, Villar *et al.* (2005) measured dry densities ranging from 1.45 to 1.70 Mg/m^3 upon dismantling. The Engineered Barrier (EB) experiment, performed at the Mont Terri Underground Research Laboratory, Switzerland, provides another interesting picture of how complex the density reorganization could be (Figure 4.1). The EB experiment aimed at demonstrating the feasibility of granular bentonite barriers. In this test, a dummy canister is emplaced on a bed of compacted bentonite blocks, while granular bentonite is used to fill the remaining space. The initial dry density of the blocks was 1.69 Mg/m^3 and the initial average dry density of the granu-

lar mixture was estimated between 1.30 and 1.36 Mg/m^3, the dry density of the bentonite grains being higher than 2.10 Mg/m^3 (Garcia-Siñeriz *et al.*, 2015). After dismantling the experiment, Mayor & Velasco (2014) and Garcia-Siñeriz *et al.* (2015) showed that density gradients had developed from the floor towards the top of the gallery, where the dry density was initially the lowest. The density redistribution has been explained by the higher swelling potential of compacted blocks which compressed the upper part of the gallery, and by water accumulation in the lower part of the buffer (as a consequence of gravity) which promoted swelling of the bentonite blocks.

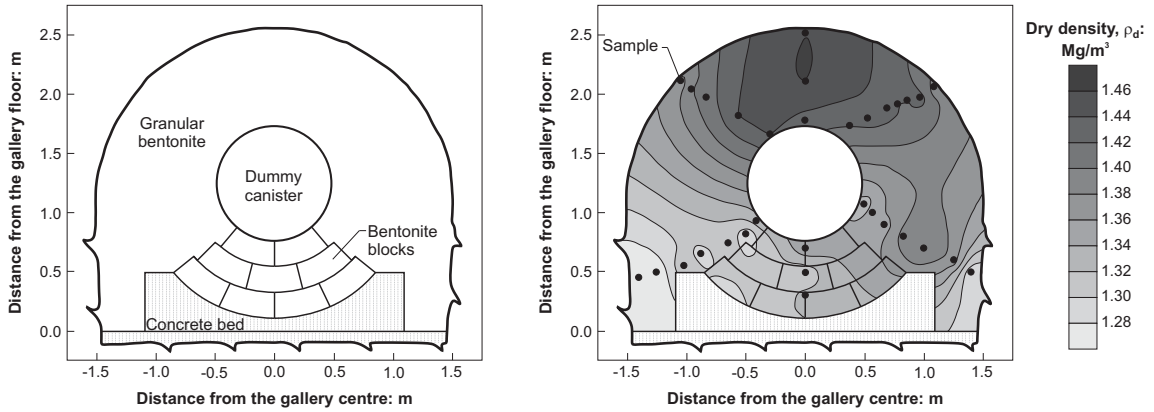

(a) Experimental set-up.

(b) Dry density profile after dismantling.

Figure 4.1: Engineered Barrier (EB) *in situ* experiment (Mayor & Velasco, 2014).

In order to better understand the water retention behaviour of bentonite-based materials under *in situ* conditions, laboratory tests have been performed at various dry densities and under different volume constraints (see Loiseau *et al.*, 2002; Lloret *et al.*, 2003; Villar, 2007; Ye *et al.*, 2009; Wang *et al.*, 2013c; Seiphoori *et al.*, 2014; Gatabin *et al.*, 2016, among others). They have shown that the retention capacity of compacted bentonites was significantly affected by the dry density of the material and the volume constraints imposed upon wetting.

Despite the experimental evidences, numerical analyses have generally considered a unique relationship between suction and the degree of saturation, hence disregarding the evolution of the water retention properties with the hydromechanical state of the barrier (see Dupray *et al.*, 2011; Sánchez *et al.*, 2012b; Thomas *et al.*, 2013, among others). Indeed classical approaches for modelling the water retention behaviour are based on parameters to be fitted using experimental data. If this approach gives reasonable results for granular soils or low-activity clay materials, considerable errors may be made in the case of expansive materials which undergo strongly coupled hydromechanical processes.

In this chapter, the experimental techniques used for the determination of the water retentions properties of porous media, and especially expansive materials, are reviewed first. Experimental observations on the water retention behaviour of compacted bentonites are then presented and interpreted in the light of the material microstructure evolution. The essential features are highlighted and used for the development of a new water retention

model dedicated to compacted bentonite-based materials. The model aims at interpreting all experimental data within a unified framework, and predicting the water retention behaviour of the buffer under repository conditions. It is presented and validated against experimental data on different compacted bentonite-based materials. Finally, its numerical implementation in the finite element code `LAGAMINE` is discussed.

2 Experimental techniques

The water retention curve summarises the dependence on suction of the amount of water stored in a soil. It is built point by point by progressively wetting or drying a soil sample. More specifically, the experimental characterization consists in determining the water content of a sample brought to a known suction, or conversely, measuring the suction of a sample of known water content.

The experimental techniques used for the determination of the water retention properties are divided into two categories depending if suction is controlled or measured. In the case of expansive materials such as compacted bentonites, these techniques have to take into account two aspects (Villar, 2007): bentonite-based materials involve high suctions and they experience important swelling upon hydration under free volume conditions, or conversely high swelling stresses under restrained swelling.

Three main techniques have been developed to control suction within a soil sample:

- **Axis translation (or overpressure) technique**
  The principle of the axis translation technique is based on the definition of the matric suction $s = u_g - u_w$, where u_g and u_w are respectively the air and water pore pressures. The method involves the translation of the reference pore gas pressure u_g through an artificial increase of the air pressure inside the sample. The water pressure u_w within the sample is controlled, so that a matric suction is imposed to the sample. In order to maintain this suction, a high air-entry value ceramic disc is used at the interface between the unsaturated sample and the water in the measuring system (Figure 4.2). The air-entry value of the ceramic disc limits the application of the axis translation technique to suctions up to 1.5 MPa[1].

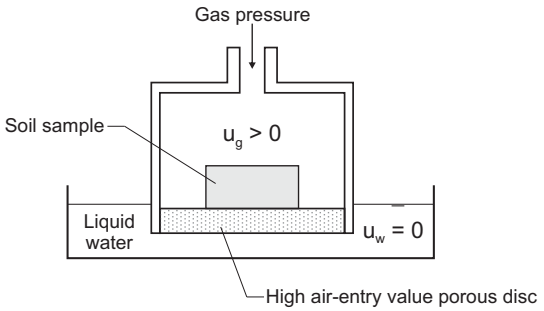

Figure 4.2: Principle of the axis translation technique (Richards, 1941).

[1]This technique may be implemented in laboratory mechanical cells. In this case, cellulose acetate membranes can be used instead of ceramic discs, so that matric suctions up to 7 MPa can be reached.

- **Osmotic technique**
  The osmotic technique is based on the principle of osmosis. It consists in placing in contact, through a semi-permeable membrane, a soil specimen and an aqueous solution of large sized polyethylene glycol (PEG) molecules (Figure 4.3). Since PEG molecules cannot cross the membrane, a difference of chemical concentration, hence osmotic suction, is maintained between the sample and the PEG solution. In order to balance the water potentials, water transfer occurs between the soil and the PEG solution until reaching a given matric suction. Depending on the PEG concentration, suctions ranging between 0.1 and 10 MPa may be imposed.

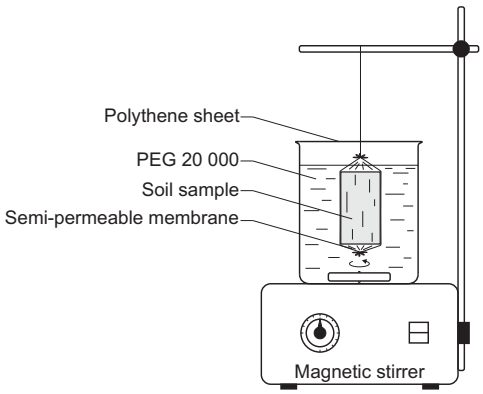

Figure 4.3: Suction control using the osmotic technique (Delage & Cui, 2001).

- **Vapour control technique**
  This technique consists in imposing a constant relative humidity to a soil sample, thanks to (generally) saturated saline solutions with known concentrations. Water transfer occurs in the vapour phase and the total suction is therefore controlled. This technique can impose total suctions up to several hundreds of MPa. Its main drawback is the very long time required to reach equilibrium.

The principles of these three experimental techniques are presented for unstressed samples. However, they may be used in conjunction with mechanical laboratory cells to study the hydromechanical behaviour of partially saturated porous media under controlled stress or controlled volume conditions. A detailed description of each of these techniques, as well as their main advantages and drawbacks, can be found in Delage *et al.* (2008).

Besides these three techniques, two additional methods can be used to measure suctions:

- **High capacity tensiometers**
  The principle of tensiometers consists in measuring negative water pressures in analogous way to positive pressures. Pressures within a water reservoir and in the soil pores are allowed to attain equilibrium through a high air-entry value porous disc which must remain saturated to ensure continuity between the soil liquid phase and the reservoir (Figure 4.4). When equilibrium is achieved, the negative pressure is measured using a gauge. High capacity tensiometers can measure matric suctions up to 1.8 MPa.

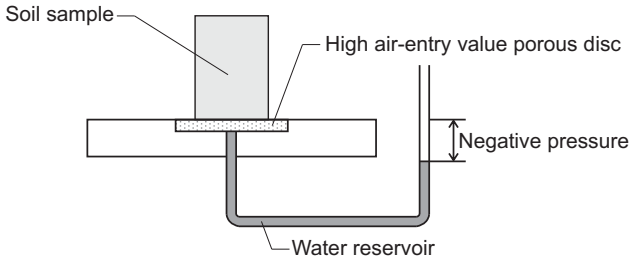

Figure 4.4: Principle of tensiometers (Delage & Cui, 2001).

- **High range psychrometers**
  This technique is based on the measurement of the relative humidity in the vicinity of the soil pore water. Using Kelvin's law (Equation (3.55)), the corresponding total suction is obtained. The relative humidity is determined through the measurement of the dew point temperature of the considered atmosphere. The lowest the dew point temperature, the highest the suction. High range psychrometers are able to investigate a wide range of total suctions (between 1 and 70 MPa).

For each imposed or measured suction value, the determination of the water retention curve implies the measurement of the water content. The water content is determined after oven drying the sample (generally at 110°C during 24 to 48 hours[2]). It is defined as

$$w = \frac{m_w}{m_s} = \frac{m_{sample} - m_{dry}}{m_{dry}} \tag{4.1}$$

where m_w is the mass of water in the sample, obtained as the difference between the mass of the sample m_{sample} and the mass of the dried sample m_{dry}, and m_s is the mass of the solid particles, which is equal to m_{dry}.

In order to express water retention curves in terms of degrees of saturation, measurements of the sample volume are needed for each point of the curve. When the sample is wetted under confined or controlled volume conditions, the volume is accurately known. In the case of free swelling or drying paths, the sample volume is generally determined by measuring the dimensions of the sample (Delage *et al.*, 1998; Olchitzky, 2002; Villar, 2002; Gatabin *et al.*, 2016). The degree of saturation is defined as

$$S_r = \frac{\Omega_l}{\Omega_v} = \frac{\rho_s}{\rho_w}\left(\frac{m_{sample} - m_{dry}}{\rho_s \Omega - m_{dry}}\right) = \frac{\rho_s}{\rho_w}\frac{w}{e} \tag{4.2}$$

where Ω_l and Ω_v are respectively the volumes of liquid water and voids in the sample, Ω is the sample volume, ρ_s and ρ_w are respectively the density of solid particles and liquid water, and e is the void ratio.

Finally, the water ratio e_w is defined as the ratio of the liquid water volume Ω_l to the solid volume Ω_s

$$e_w = \frac{\Omega_l}{\Omega_s} = eS_r = \frac{\rho_s}{\rho_w} w. \tag{4.3}$$

[2]Although this temperature is not sufficient to eliminate all interlayer water of smectites, it is often used as a reference value.

The amount of water stored in a porous medium may be thus expressed in various ways (water content, degree of saturation, water ratio). Very often, experimentalists prefer the water content which is the raw data directly obtained from laboratory tests. In addition, no information on the porous volume is needed and no assumption is required concerning the water density. On the other hand, people dealing with numerical models prefer the degree of saturation as balance equations are based on this variable (see Section 3.1 of Chapter 3). However, as discussed by Romero *et al.* (2011), none of these variables has definite advantages over the others. Therefore, in this chapter, the water retention curve will be sometimes represented in terms of water content or water ratio, sometimes in terms of degree of saturation depending on what emphasis is placed.

3 Experimental observations

In this section, experimental data are exploited to highlight the main features of the water retention behaviour of compacted bentonites. For the sake of comparison, experimental data from a same study are used to underscore a given feature. Experimental data on compacted materials generally exhibit good repeatability, so that data scattering is not directly considered.

3.1 Water retention domains

The existence of two water retention domains has been highlighted by presenting experimental data in terms of water content versus suction. Romero *et al.* (1999) published pioneering results of water retention curves of Boom clay compacted at different dry densities. Upon compaction, samples of Boom clay displayed bimodal pore size distributions. Compacted samples were then hydrated under free swelling conditions using the vapour equilibrium technique. The following observations can be made from Figure 4.5:

- **For high suction values** (above around 2 MPa), the amount of water stored in the soil is not affected by the dry density. In this domain, water is mainly adsorbed at the surface of the clay particles and water retention is mainly controlled by the physicochemical properties of the clay minerals, in particular the specific surface (Tuller & Or, 2005). For this reason, this retention domain of intra-aggregate governing suction is often called microstructural water retention domain.
- **For lower suction values**, the water content is sensitive to variations of the dry density. Water is believed to be stored by capillarity in the macropores, which are affected by changes in dry density (see Chapter 2). The suction range in which the water content is affected by the dry density is called the macrostructural water retention domain.

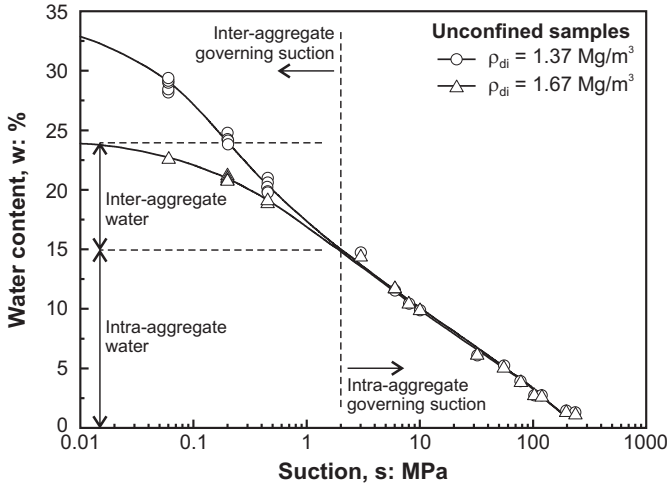

Figure 4.5: Water retention curves of Boom clay compacted at two dry densities, obtained under unconfined conditions (Romero *et al.*, 1999). ρ_{di} denotes the initial dry density.

The independence of the water retention properties at high suction values may also be observed in the compaction plane in which the contours of equal suction are represented. Figure 4.6 shows such a representation for compacted Boom clay. It is observed that, for high suction values, the lines of equal suction are vertical, which expresses the independence of the water content on dry density. On the other hand, for water contents higher than 15%, the compaction process modifies the suction of the specimen, especially as the water content is high.

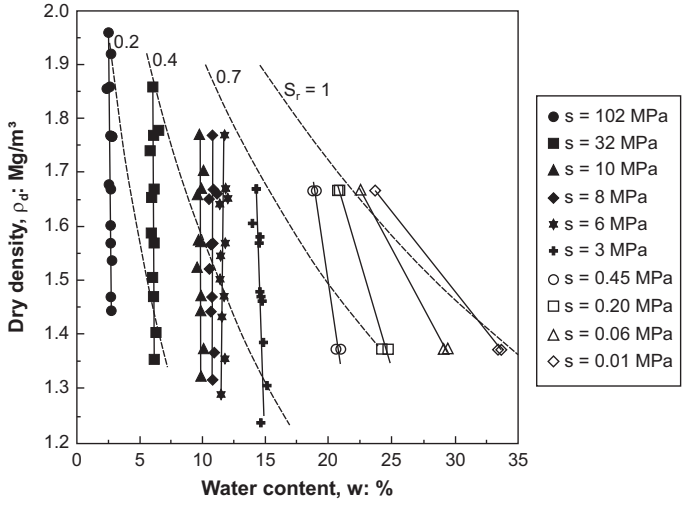

Figure 4.6: Static compaction curves of Boom clay with contours of equal suction (Romero *et al.*, 1999).

While these observations were made for a compacted clay with low activity, similar observations have been reported by Lloret *et al.* (2003) and Villar (2007) on Febex bentonite, by Loiseau *et al.* (2002) on a Kunigel V1 bentonite/sand mixture, Agus *et al.* (2013) on various Calcigel bentonite/sand mixtures, Seiphoori *et al.* (2014) on granular MX-80 bentonite, among others.

Figure 4.7 presents the water retention curves of compacted Febex bentonite under both confined and unconfined conditions, obtained by Lloret *et al.* (2003). Samples of Febex bentonite were compacted to different dry densities and then wetted by controlling the surrounding relative humidity. Up to a suction of about 15 MPa, the water retention curve is independent from the dry density, while for lower values of suction, it becomes dry density dependent. Compared with Figure 4.5, we observe that the amount of water stored by adsorption is significantly higher for Febex bentonite than it is for compacted Boom clay. This may be explained by the higher specific surface of Febex bentonite (725 m^2/g, compared to 53 m^2/g for Boom clay) and the higher montmorillonite content in bentonites (Boom clay contains between 10 and 20% of smectite).

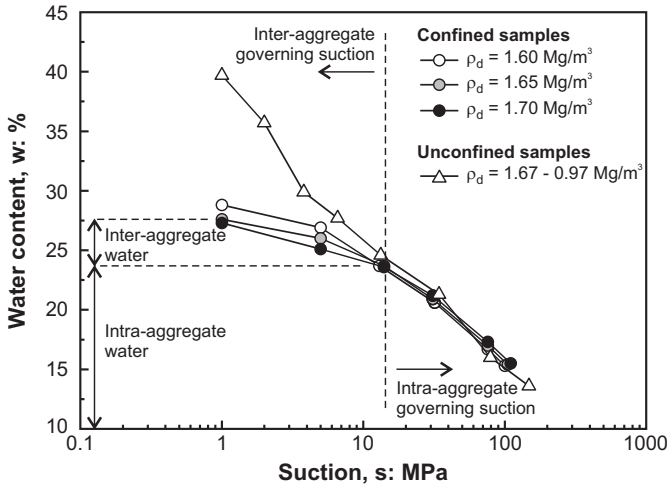

Figure 4.7: Water retention curves of compacted Febex bentonite obtained under confined and unconfined conditions (Lloret *et al.*, 2003).

3.2 Effect of the initial dry density

The effect of the dry density on the bentonite structure is essentially related to changes in the inter-aggregate pore volume and dimensions, as discussed in Chapter 2. Within a relatively large range of dry densities and water contents, it has been observed that the compaction process mainly affects the macrostructural pore volume. Therefore, changes in dry density primarily influences the inter-aggregate water retention domain where water is stored by capillarity. When the density increases, the pore size decreases, so that the pores can sustain a higher suction before emptying.

The air-entry value is defined as the suction beyond which air breaks into the saturated porous space. It is often used to quantify the effect of the dry density on the water retention curve. Seiphoori *et al.* (2014) studied the influence of dry density on the water retention curve of compacted MX-80 bentonite. Samples of granular MX-80 bentonite were compacted to three different dry densities, namely 1.50, 1.65 and 1.79 Mg/m^3, and subjected to a wetting path under constant volume conditions. The corresponding suction was measured using a dew-point chilled mirror psychrometer. Figure 4.8(a) presents the three water retention curves in terms of degree of saturation versus suction. In this plane,

the water retention curves of samples compacted at different dry densities are normalized and the effect of the dry density on the air-entry value is easier to observe. In order to further highlight this influence, Figure 4.8(b) presents the evolution of the air-entry value s_{AE} as a function of the void ratio e. The data are modelled using a power law of the form

$$s_{AE} = \left(\frac{A}{e}\right)^{B} \tag{4.4}$$

where A and B are material parameters. Such a law has been adopted by Gallipoli *et al.* (2003), Tarantino & De Col (2008) and Gallipoli (2012) in water retention models. Its nature is basically phenomenological and related to the hydraulic response of the porous medium. However, it implicitly describes the role of macrostructure on the hydraulic properties.

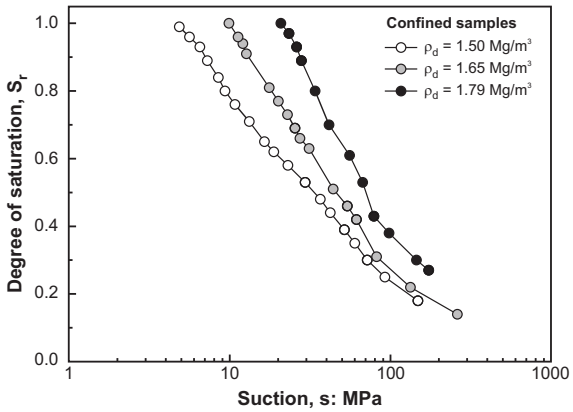

(a) Water retention curves of MX-80 bentonite compacted at three different dry densities.

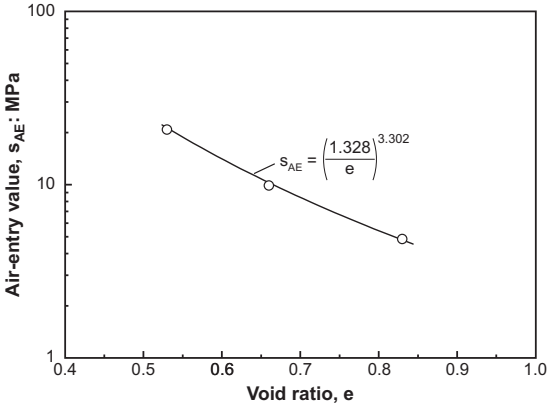

(b) Evolution of the air-entry value as a function of the void ratio.

Figure 4.8: Effect of the dry density on the water retention curve of compacted MX-80 bentonite obtained under confined conditions (Seiphoori *et al.*, 2014).

3.3 Effect of the volume constraints

A specificity of expansive materials is the sensitivity of their water retention properties to the volume constraints. This is a consequence of the sensitivity of the material to suction changes (swelling or shrinking behaviour) which directly affects the dry density of the material. In particular, experimental data on compacted bentonites show that, for a given suction, the quantity of water stored is greater under free swelling conditions than it is under prevented swelling. This can be observed in Figure 4.7 for compacted Febex bentonite.

The presentation of experimental data in the $(s - S_r)$ plane provides further insight into the effects of volume constraints on the water retention behaviour of compacted bentonites. Wang *et al.* (2013c) and Gatabin *et al.* (2016) used the vapour equilibrium technique to investigate the water retention properties of a compacted MX-80 bentonite/sand mixture under both free swelling and constant volume conditions. As can be observed in Figure 4.9(a), the volume constraint significantly impacts the water retention behaviour

of the mixture compacted at a dry density of 2.03 Mg/m^3. For the samples wetted under confined conditions, hydration led to an increase of the degree of saturation. On the contrary, the decrease of suction did not significantly impact the degree of saturation of the samples wetted under free conditions, in the investigated range of suctions at least[3].

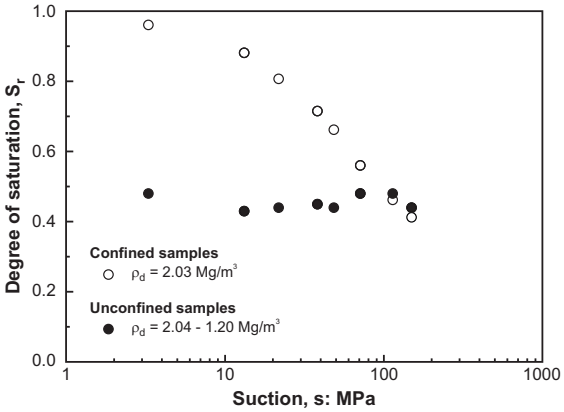

(a) Water retention curves obtained under confined and unconfined conditions.

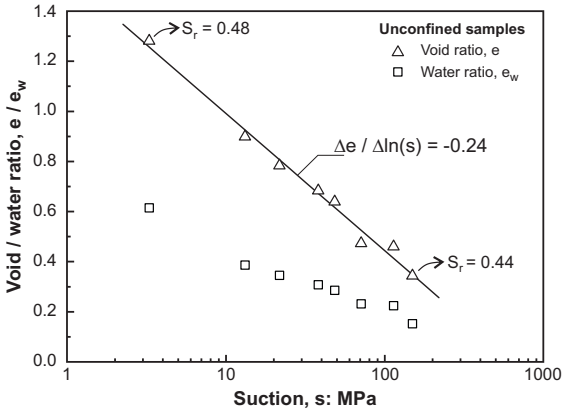

(b) Evolution of the water and void ratios upon wetting under unconfined conditions.

Figure 4.9: Water retention behaviour of a MX-80 bentonite/sand mixture compacted at a dry density $\rho_d = 2.03$ Mg/m^3 (Gatabin *et al.*, 2016).

This observation is a direct consequence of the strong hydromechanical coupling in compacted bentonites. Let us write the degree of saturation as the ratio between the water ratio e_w, and the void ratio e

$$S_r = \frac{e_w}{e}. \tag{4.5}$$

This expression evidences the dependence of the degree of saturation on both water ratio and void ratio. Tarantino (2009) introduced the concept of *hydraulic wetting* to describe an increase of the degree of saturation due to an increase of the water ratio. Accordingly, the term *mechanical wetting* was used for an increase of the degree of saturation resulting from a decrease of the void ratio. When bentonite samples are hydrated under constant volume conditions, only the water ratio is modified and the degree of saturation univocally increases. On the contrary, during hydration under free swelling conditions, swelling strains develop as the material takes water, and both water ratio and void ratio are affected. In this case, hydraulic wetting occurs simultaneously as mechanical drying.

In order to quantify both processes, Figure 4.9(b) presents the evolution of the water ratio along the wetting path, together with the evolution of the void ratio, for the free swelling samples. As can be observed, swelling strains developed upon wetting are particularly important (around 66% when the sample is hydrated to a suction of 3 MPa). In addition, the increase in void ratio upon wetting is more important than the water uptake, i.e. the samples swell more than they take water, hence a relatively constant degree of saturation.

[3]For lower values of suction, the determination of the water retention properties under unconfined conditions becomes difficult as the sample loses its integrity.

The same figure can be plotted using the data from Wang *et al.* (2013c). Wang *et al.* (2013c) determined the water retention curve of the same mixture but compacted to a lower dry density of 1.67 Mg/m^3 (Figure 4.10(b)). In the high suction range, the water ratio follows the same branch as for the investigated mixture, both under constant volume and free swelling conditions. However, as a direct consequence of the lower density of clay particles in the mixture, the material exhibits smaller swelling strains upon wetting. For the sake of comparison, the swelling modulus for changes in suction, $\kappa_s \simeq -\Delta e/\Delta \ln(s)$ is around 0.24 for the initial dry density of 2.03 Mg/m^3 but reduces to 0.039 when the initial dry density decreases to 1.67 Mg/m^3. As a consequence, the degree of saturation of the mixture studied by Wang *et al.* (2013c) increases upon wetting (Figure 4.10(a)).

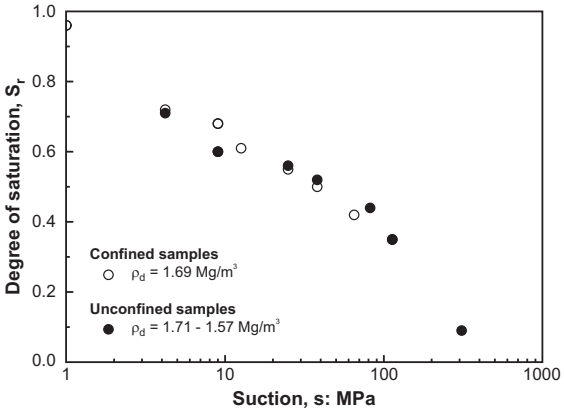

(a) Water retention curves obtained under confined and unconfined conditions.

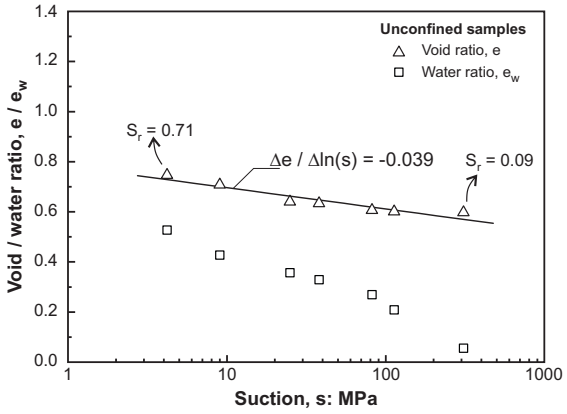

(b) Evolution of the water and void ratios upon wetting under unconfined conditions.

Figure 4.10: Water retention behaviour of a compacted mixture of MX-80 bentonite and sand compacted at a dry density $\rho_d = 1.67$ Mg/m^3 (Wang *et al.*, 2013c).

3.4 Other features

In the previous sections, attention was paid to the influence of hydromechanical coupling on the water retention behaviour. However, other factors may affect the water retention properties of compacted bentonites, such as temperature, hysteresis and the water composition. They are briefly presented in this section.

High-level radioactive waste contains radionuclides which are strongly heat emitting. In some concepts of geological disposal, the heating arising from the canisters may induce significant temperature changes in the bentonite barrier. In this case, the thermo-hydro-mechanical behaviour of bentonite should be considered. The effect of temperature on the water retention properties of compacted bentonites has been investigated by Imbert *et al.* (2005) on FoCa7 clay, Tang & Cui (2005) on MX-80 bentonite and Lloret & Villar (2007) on Febex bentonite, among others. These studies have shown that an increase in temperature decreases the water retention capacity of bentonites (Figure 4.11). Yet, the influence of temperature on the water retention properties seems to be less important than the effect of dry density, for instance.

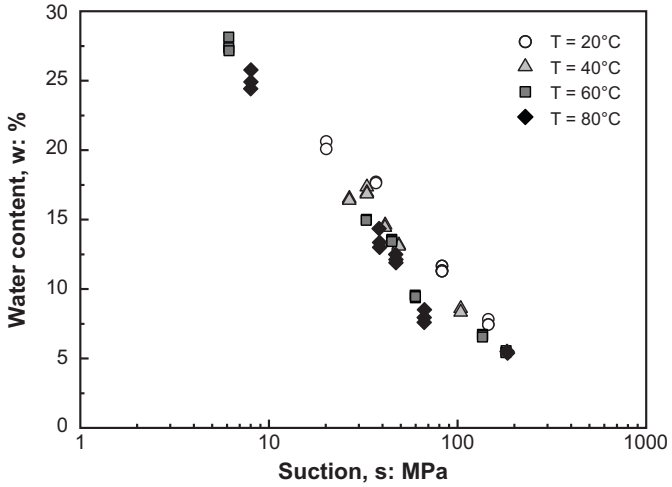

Figure 4.11: Effect of temperature of the water retention curve of compacted MX-80 bentonite obtained under unconfined conditions (Tang & Cui, 2005).

The experimental data presented in the previous sections were obtained along wetting paths. These paths correspond to the stress imposed to the bentonite buffer subjected to hydration from the host rock. However, if temperature increases significantly, or in the case of gas migration, a drying path may be followed. In this case, the study of the hysteresis behaviour of the water retention curve is of particular interest. However, from an experimental point of view, the existence of hysteresis is not clear yet. Delage *et al.* (1998) did not observe any significant hysteresis in the retention curves of FoCa7 clay (Figure 4.12(a)), which can be explained in terms of the very dense state of the samples in which quasi-reversible intra-aggregate effects are predominant compared to inter-aggregate capillary phenomena. Villar (2004a) also observed very little hysteresis on compacted MX-80 bentonite. However, Lloret & Villar (2007) observed hysteresis on Febex bentonite. For a given suction, the water content reached upon drying was higher than on wetting. More recently, Seiphoori *et al.* (2014) observed significant differences between wetting and drying paths (Figure 4.12(b)), which was explained by irreversible microstructural changes upon the first wetting, unlike Delage *et al.* (1998).

Finally, the influence of water salinity has been studied by Mata *et al.* (2002) on various mixtures of MX-80 bentonite and sand, and Villar (2004a) on MX-80 bentonite. Changes in water composition, and salinity in particular, could indeed occur over the life of repositories. While Villar (2004a) could not highlight any significant effect of water salinity, Mata *et al.* (2002) showed that salinity decreased the water capacity of bentonites.

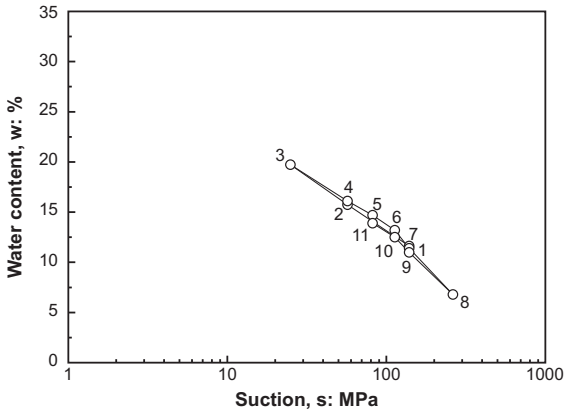

(a) Wetting/drying cycles on unconfined FoCa7 clay. The numbers in correspond to the different stages of imposed suction.

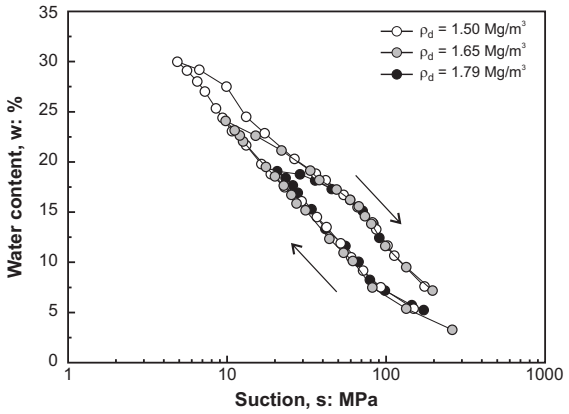

(b) Wetting/drying cycle on confined MX-80 bentonite compacted to different dry densities.

Figure 4.12: Hysteresis of the water retention curve. Experimental data on (a) FoCa7 clay (Delage *et al.*, 1998) and (b) MX-80 bentonite (Seiphoori *et al.*, 2014).

4 Mathematical formulation

Water retention models have traditionally been formulated as a unique relationship between suction and the degree of saturation or water content (Brooks & Corey, 1964; van Genuchten, 1980). Accordingly, materials compacted to different dry densities and which exhibit different water retention properties have been described using different sets of model parameters. If this approach has been successfully applied for granular soils and low activity clay materials, it cannot describe accurately the water retention behaviour of highly expansive materials such as bentonites. Indeed, in the case of compacted bentonites, the material swells significantly upon wetting, resulting in important changes in dry density. Consequently, the dependency of the water retention curve on the dry density of the material is a major issue and explains why classical water retention models have failed in describing the water retention properties of expansive materials. For instance, the behaviour observed in Figure 4.9(a) cannot be reproduced using classical water retention models.

Based on the experimental observations presented in Section 3 and the water retention mechanisms thoroughly described in Chapter 2, a new water retention model is developed. The proposed water retention model is formulated in terms of water ratio e_w in order to evidence the role of the different water retention mechanisms, namely adsorption in the microstructure (inter-layer porosity and inter-particle porosity) and capillary storage in the inter-aggregate porosity. Accordingly, the water ratio e_w is expressed as the superposition of a contribution from the water stored in the micropores e_{wm} and a second contribution from the water contained in the macropores e_{wM} (Figure 4.13)

$$e_w = e_{wm} + e_{wM}. \tag{4.6}$$

It should be mentioned that, in reality, the volume of adsorbed water content is greater than the intra-aggregate pore volume as measured in mercury intrusion porosimetry tests.

Indeed some water is adsorbed at the surface of the aggregates (Lloret *et al.*, 2003). Yet this phenomenon is not explicitly taken into account in the present model.

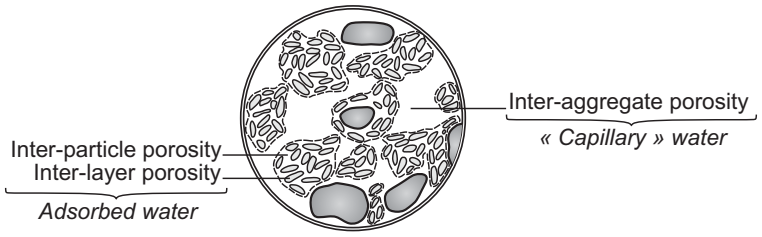

Figure 4.13: Conceptual representation of the water retention mechanisms in compacted bentonites.

The degree of saturation S_r is then expressed as

$$S_r = \frac{e_w}{e} = \frac{e_m}{e} S_{rm} + \frac{e_M}{e} S_{rM} \tag{4.7}$$

where e_m and $e_M = e - e_m$ are respectively the microstructural and macrostructural void rations, and S_{rm} and S_{rM} the microstructural and macrostructural degrees of saturation. The degrees of saturation are therefore not additive, as the global degree of saturation is obtained by the sum of the microstructural and macrostructural degrees of saturation, weighted by the corresponding volumetric fractions.

In the following, thermodynamic equilibrium between the microstructure and macrostructure is assumed. Accordingly, the current value of suction applies to both structural levels. The formulation of the proposed water retention model includes three parts, namely the descriptions of the microstructural water retention domain, the macrostructural domain and the microstructure evolution.

4.1 Microstructural water retention domain

Water in the microstructure is mainly stored by adsorption. Several adsorption isotherms[4] have been proposed in the literature by the community of physicists. While the first basis of these isotherms are generally phenomenological, several models have later been justified physically. In particular, Dubinin's theory (Dubinin & Radushkevich, 1947) was developed for activated carbon and zeolites, which contain cavities of molecular dimensions. The micropores of these materials control their adsorptive nature. Later, Kraehenbuehl *et al.* (1987) used Dubinin's theory to describe the bentonite – water system and Fernández & Rivas (2005) to model the water retention behaviour of Febex bentonite.

In this thesis, Dubinin's isotherm is adopted to describe the water retention behaviour of the microstructure. Its equation takes the form

$$\Omega_{wm} = \Omega_m \exp\left\{ - \left[\frac{RT}{\beta_D E_0} \ln\left(\frac{u_v^0}{u_v} \right) \right]^{n_{ads}} \right\} \tag{4.8}$$

[4] An isotherm is a relationship between the amounts of adsorbate adsorbed on the surface of a material and pressure, at constant temperature.

where Ω_{wm} is the volume of water adsorbed in the micropores at temperature T and relative pressure u_v/u_v^0, R is the universal gas constant (= 8.314 J/mol·K), and Ω_m is the total volume of the micropores, n_{ads} is a specific parameter of the system, called heterogeneity factor. β_D is termed similarity constant and $E = \beta_D E_0$ is the characteristic adsorption energy for the given system. E_0 is the characteristic energy of adsorption for a reference vapour for which $\beta_D = 1$.

Equation (4.8) may be expressed in terms of water ratio by dividing both sides of the equation by the the volume of solid particles Ω_s. It yields

$$e_{wm} = e_m \exp\left\{-\left[\frac{RT}{\beta_D E_0}\ln\left(\frac{u_v^0}{u_v}\right)\right]^{n_{ads}}\right\}. \tag{4.9}$$

Furthermore, Kelvin's law may be used to express the relative pressure u_v/u_v^0 in terms of suction s

$$RH = \frac{u_v}{u_v^0} = \exp\left(\frac{-sM_w}{RT\rho_w}\right) \tag{4.10}$$

where RH is the relative humidity, M_w is the molecular mass of water (= 0.018 kg/mol) and ρ_w its density. Gathering the constant parameters, the following expression is finally adopted for the microstructural water retention domain

$$e_{wm}(s, e_m) = e_m \exp\left[-(C_{ads}s)^{n_{ads}}\right] \tag{4.11}$$

where n_{ads} and C_{ads} are material parameters. The parameter n_{ads} controls the curvature of the water retention curve in the high suction range, while C_{ads} is associated to the rate of desaturation of the soil (Figure 4.14). It is related to the original Dubinin equation through

$$C_{ads} = \frac{M_w}{\rho_w \beta_D E_0}. \tag{4.12}$$

For typical values of $E = \beta_D E_0$ ranging between 1 and 10 kJ/mol, C_{ads} varies between 0.018 and 0.0018 MPa^{-1}.

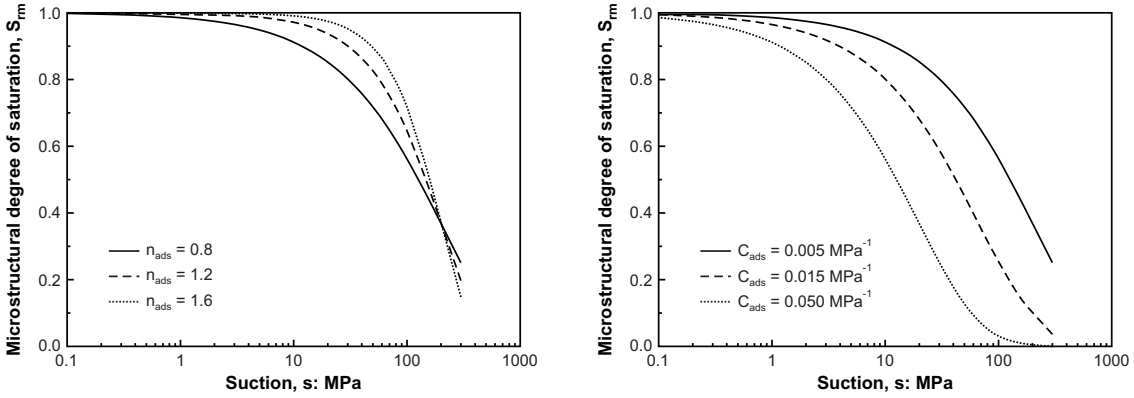

(a) Influence of n_{ads} ($C_{ads} = 0.005$ MPa^{-1}). (b) Influence of C_{ads} ($n_{ads} = 0.8$).

Figure 4.14: Influence of the microstructural parameters on the shape of the microstructural water retention curve ($e_m = 0.3$ is constant).

4.2 Macrostructural water retention domain

The van Genuchten (1980) water retention model has been successfully used to model the water retention behaviour of a wide variety of soils. It is generally expressed as

$$S_r(s) = \left[1 + \left(\frac{s}{\alpha}\right)^n\right]^{-m} \tag{4.13}$$

where m and n are material parameters, and α is related to the air-entry value s_{AE}. Alternatively, the van Genuchten equation may expressed in terms of water ratio e_w

$$e_w(s, e) = e\left[1 + \left(\frac{s}{\alpha}\right)^n\right]^{-m}. \tag{4.14}$$

In this thesis, the van Genuchten equation is selected to model the macrostructural water retention domain. Accordingly, the void ratio e is replaced by the macrostructural void ratio $e_M = e - e_m$, and the macrostructural water retention model reads

$$e_{wM}(s, e, e_m) = (e - e_m)\left[1 + \left(\frac{s}{\alpha}\right)^n\right]^{-m}. \tag{4.15}$$

In order to represent the influence of the bentonite structure on the air-entry value, the parameter α is assumed to depend on the macrostructural void ratio. The following law is adopted

$$\alpha = \frac{A}{e - e_m} \tag{4.16}$$

where A controls the dependence of the air-entry pressure on the macrostructural void ratio. If the total void ratio is replaced by the macrostructural void ratio, this law is similar to Equation (4.4) for $B = 1$. The influence of the void ratio on the macrostructural water retention curve is highlighted in Figure 4.15.

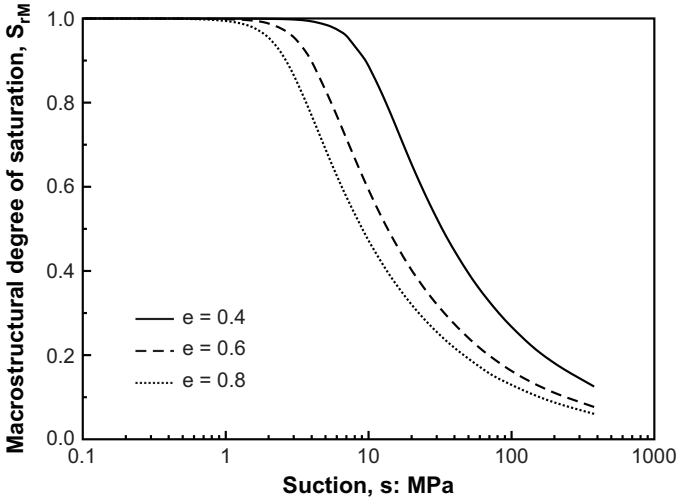

Figure 4.15: Influence of void ratio on the shape of the macrostructural water retention curve. The parameters of the model are $A = 0.3$ MPa, $n = 3$, $m = 0.15$ and $e_m = 0.3$.

4.3 Microstructure evolution

As discussed in Chapter 2, the microstructure of bentonite is significantly affected by changes of its water content. In particular, the evolution of the microstructure during wetting or drying paths may be characterized by the evolution of the microstructural void ratio e_m. In order to account for structural changes of the material along the water retention curve, the microstructural model (2.10) proposed in Chapter 2 is introduced in the water retention model. It reads

$$e_m = e_{m0} + \beta_0 e_w + \beta_1 e_w^2 \tag{4.17}$$

where e_{m0} is the microstructural void ratio for the dry material ($e_w = 0$) and β_0 and β_1 are parameters that quantify the swelling potential of the aggregates. The model is calibrated for Febex, Kunigel V1 and MX-80 bentonites, as well as for a mixture of 70% MX-80 and 30% dry sand, in Chapter 2 (Table 2.4).

The influence of the microstructure evolution on the water retention curve is highlighted in Figure 4.16. In this figure, the water retention curves for two values of e_m constant are represented, together with the water retention curve considering microstructure evolution. As observed, the increase of microstructural void ratio upon wetting under constant void ratio e yields an increase of the apparent air-entry value as a consequence of the decrease of the macrostructural void ratio.

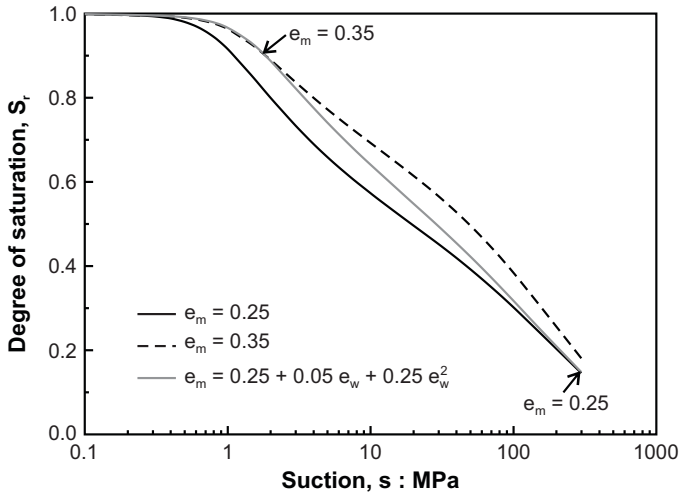

Figure 4.16: Influence of microstructure evolution on the shape of the (global) water retention curve. The parameters of the model are $C_{ads} = 0.005$ MPa^{-1}, $n_{ads} = 0.8$, $e = 0.6$, $A = 0.3$ MPa, $n = 3$ and $m = 0.15$.

5 Calibration procedure

The proposed water retention model requires eight parameters, including three characterizing the evolution of the microstructural void ratio with the water ratio. When experimental pore size distributions (PSD) are available, they should be used first to calibrate

the microstructure evolution law (4.17). The interpretation of the PSD curves is based on the distinction between micropores and macropores (see Chapter 2 for the criteria). For each experimental pore size distribution, it provides one couple $(e_w - e_m)$ corresponding to one point in the $(e_w - e_m)$ plane. The parameters of the evolution law can then be determined by best fitting.

The microstructural parameter C_{ads} controls the water retention behaviour at high values of suction. The calibration of the parameter is made easier by presenting experimental data in the $(s - e_w)$ plane, since the independence on dry density is highlighted. However, it should be noted that a measure of the samples volume is still required to compute the microstructural water content. More specifically, the parameter C_{ads} controls the slope of the water retention curve. As shown in Figure 4.17, the higher C_{ads}, the steeper the slope of the water retention curve in the $(s - S_r)$ plane.

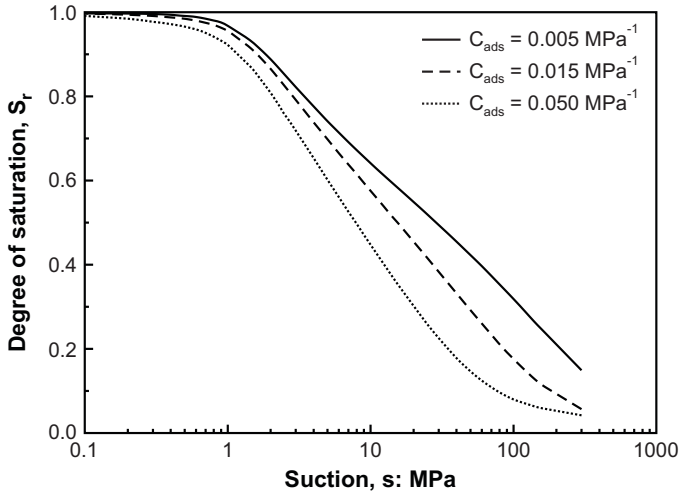

Figure 4.17: Influence of C_{ads} on the shape of the (global) water retention curve. The parameters of the model are $n_{ads} = 0.8$, $e = 0.6$, $A = 0.3$ MPa, $n = 3$, $m = 0.15$, $e_{m0} = 0.25$, $\beta_0 = 0.05$ and $\beta_1 = 0.25$.

In order to calibrate the macrostructural water retention model, experimental data for different dry densities are required. The macroscopic parameter a allows for tracking the dependency of the water retention on void ratio. The parameters n and m have shown to hardly vary from one material to another (see Section 6of this chapter). The following values can be used in a first approximation: $n = 3$ and $m = 0.15$.

6 Experimental validation

The proposed water retention model is validated against experimental data from the literature. Attention is focused on bentonite-based materials in which coupled hydromechanical phenomena are extremely strong. Yet the model can be used for compacted clays with lower activity and which display an aggregated structure upon compaction.

6.1 Febex bentonite

Villar (2000) and Lloret *et al.* (2005) determined the water retention curves of Febex bentonite compacted to different dry densities, namely 1.60, 1.65 and 1.70 Mg/m^3. Compacted samples were hydrated under both confined and unconfined conditions using the vapour equilibrium technique. Under unconfined conditions, the dimensions of the samples were measured in order to determine their density, hence their degree of saturation.

The water retention curves under confined condition are used to calibrate the water retention model. The calibrated parameters are: $C_{ads} = 0.0028$ MPa^{-1}, $n_{ads} = 0.78$, $A = 0.24$ MPa, $n = 3$ and $m = 0.15$. As shown in Figure 4.18, the model succeeds in capturing the increase of air entry pressure with increasing dry density.

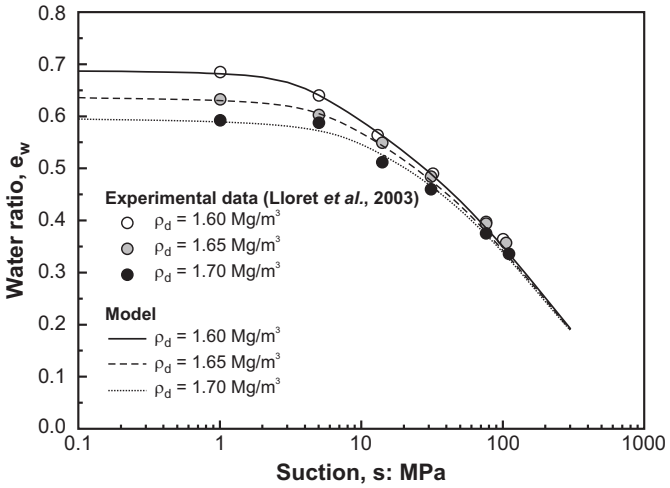

Figure 4.18: Calibration of the water retention model against experimental data (Lloret *et al.*, 2003) on Febex bentonite compacted at three different dry densities. Wetting path under confined conditions.

The model is then validated against data under unconfined conditions (Figure 4.19(a)). In this case, the values of void ratio determined experimentally were used to compute the degree of saturation. A fairly good agreement is obtained for samples wetted under free volume conditions, although overestimation of the degree of retention becomes significant for suctions below 2 MPa. Yet, this suction domain is the one where the volume changes are the most important and where the uncertainties on the measurements are the largest. Figure 4.19(b) presents the evolution of the void ratio upon wetting. As can be observed in the figure, hydration yields important volume changes, with the void ratio reaching a value of 1.6. This very large increase of the porous volume significantly affects the water retention behaviour of Febex bentonite. For the sake of illustration, the water retention curves predicted by the initial and final dry densities are represented in Figure 4.19(a). Comparison between both curves shows that an increase in the void ratio decreases the air-entry value and modifies the slope of the curve in the $(s - S_r)$ plane.

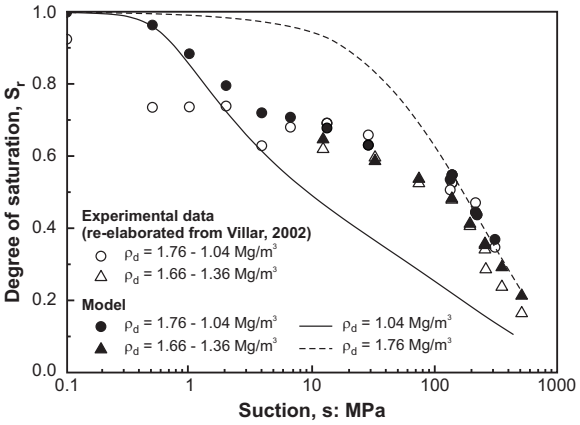

(a) Degree of saturation.

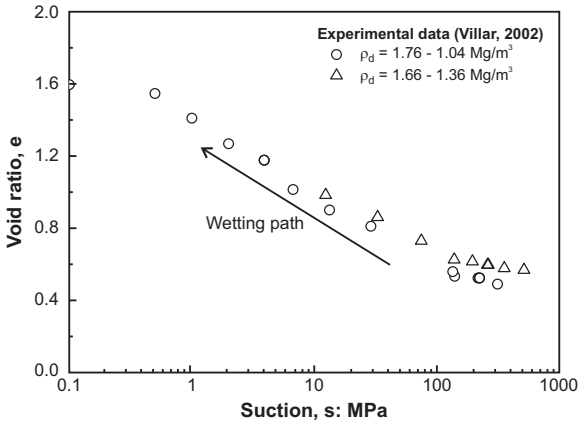

(b) Void ratio (experimental).

Figure 4.19: Comparison between experimental data (Villar, 2002) and model predictions on compacted Febex bentonite. Wetting path under unconfined conditions.

Finally, the model is used to reproduce the water retention behaviour of granular Febex bentonite (Figure 4.20(a). This material, investigated by Alonso *et al.* (2011), consists in a mixture of bentonite pellets of very high dry densities (up to 1.95 Mg/m^3). Accordingly, three pore families may be distinguished, namely micropores and macropores in the bentonite pellets, and large pores between the pellets.

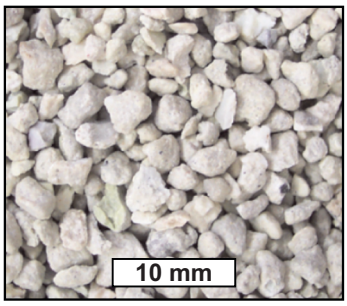

(a) Photograph of the granular mixture.

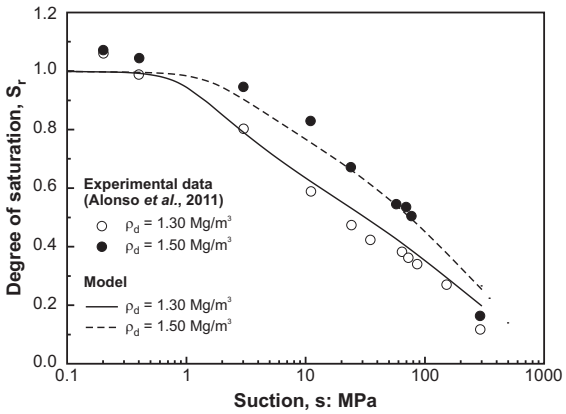

(b) Comparison between experimental data and model predictions.

Figure 4.20: Water retention properties of granular Febex bentonite (Alonso *et al.*, 2011). The maximum pellet size is 4 mm.

The water retention curves for two dry densities of the mixture were determined under constant volume conditions using the vapour transfer technique. Figure 4.20(b) compares the experimental data with the model predictions. Although developed within a double-porosity framework, the model succeeds in tracking the evolution of the degree of saturation upon wetting under constant volume conditions. In the high suction range, the water retention behaviour of the mixture is mainly controlled by the bentonite pellets. On

the other hand, the large inter-pellet pores do not significantly affects the water retention behaviour of the material as they tend to disappear upon isochoric wetting.

6.2 MX-80 bentonite

Villar (2004a) investigated the water retention properties of MX-80 bentonite under confined conditions. Samples of MX-80 bentonite were uniaxially compacted to different dry densities and water contents. After equalization, a hole was drilled in the samples and a relative humidity sensor was installed in order to measure the sample relative humidity. The corresponding suction was obtained using Kelvin's law.

Figure 4.21 represents the experimental data in the $(s - S_r)$ plane together with the model predictions. The calibrated parameters are: $C_{ads} = 0.0075$ MPa^{-1}, $n_{ads} = 1.5$, $A = 0.2$ MPa, $n = 3$ and $m = 0.15$. As observed in Figure 4.21, the degrees of saturation estimated by the water retention model compare favourably with the measured degrees of saturation. In addition, the evolution of the air entry value is consistent with the data obtained by Seiphoori *et al.* (2014).

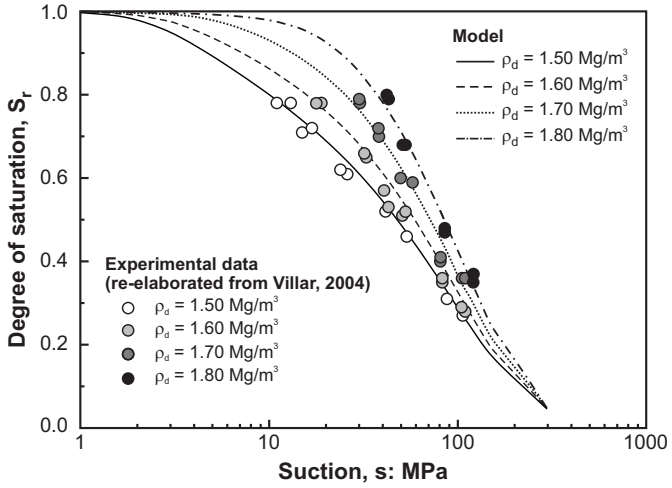

Figure 4.21: Comparison between experimental data (re-elaborated from Villar (2004a)) and model predictions on MX-80 bentonite compacted at four different dry densities.

6.3 MX-80 bentonite/sand mixture

The water retention properties of a mixture of 70% MX-80 bentonite and 30% sand mixture were studied by Wang *et al.* (2013c) and Gatabin *et al.* (2016) under both confined and unconfined conditions. Figure 4.22 presents the experimental water retention curves obtained under confined conditions, together with the model calibration. The calibrated parameters are: $C_{ads} = 0.0053$ MPa^{-1}, $n_{ads} = 0.79$, $A = 0.2$ MPa, $n = 3$ and $m = 0.15$. The model provides excellent fitting of the experimental data.

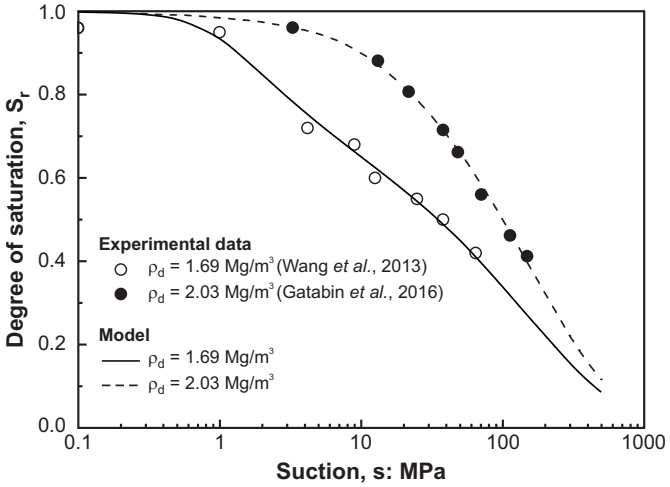

Figure 4.22: Calibration of the water retention model against experimental data (Wang *et al.*, 2013c; Gatabin *et al.*, 2016) on a MX-80 bentonite/sand mixture compacted at two different dry densities. Wetting path under confined conditions.

The model is validated against experimental data on wetting paths under unconfined conditions. Figures 4.23(a) and 4.23(b) present the evolution of the degree of saturation of the compacted mixtures upon wetting. In both cases, the model remarkably succeeds in tracking the evolution of the degree of saturation over the whole range of investigated suctions. Note that, in Figure 4.23(b), experimental data and model predictions are superposed at suctions of 150 MPa, 71 MPa, 48 MPa, 38 MPa and 13 MPa. For the sake of completeness, the water retention curves predicted for the initial and final dry densities are also represented in Figure 4.23(a), and for the different current void ratios in Figure 4.23(b). As observed in Figure 4.23(b), an important decrease in the air entry pressure is associated with the important swelling of the dense material.

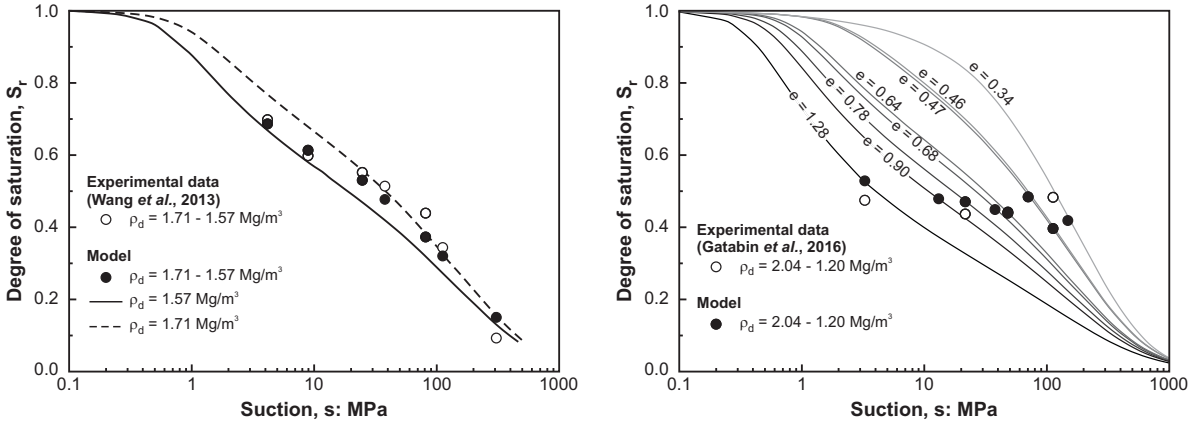

(a) Initial dry density $\rho_d = 1.71$ Mg/m^3.

(b) Initial dry density $\rho_d = 2.04$ Mg/m^3.

Figure 4.23: Comparison between experimental data (Wang *et al.*, 2013c; Gatabin *et al.*, 2016) and model predictions on a MX-80 bentonite/sand mixture compacted at two different dry densities. Wetting path under unconfined conditions.

In order to better understand the mechanisms behind the competing effects, the evolution of the total, microstructural and macrostructural void ratios upon wetting is analysed. Under confined conditions, wetting leads to an increase of the microstructural void ratio (following the evolution predicted by Equation (4.17)), hence a decrease of the macroporous volume (Figure 4.24(a)). On the other hand, when the sample is wetted under free swelling conditions, the overall swelling of the sample is more important than the development of the microstructure (Figure 4.24(b)). An increase in the inter-aggregate volume is predicted. Unfortunately, no experimental information on the evolution of pore size distributions upon wetting under unconfined conditions is available in the literature.

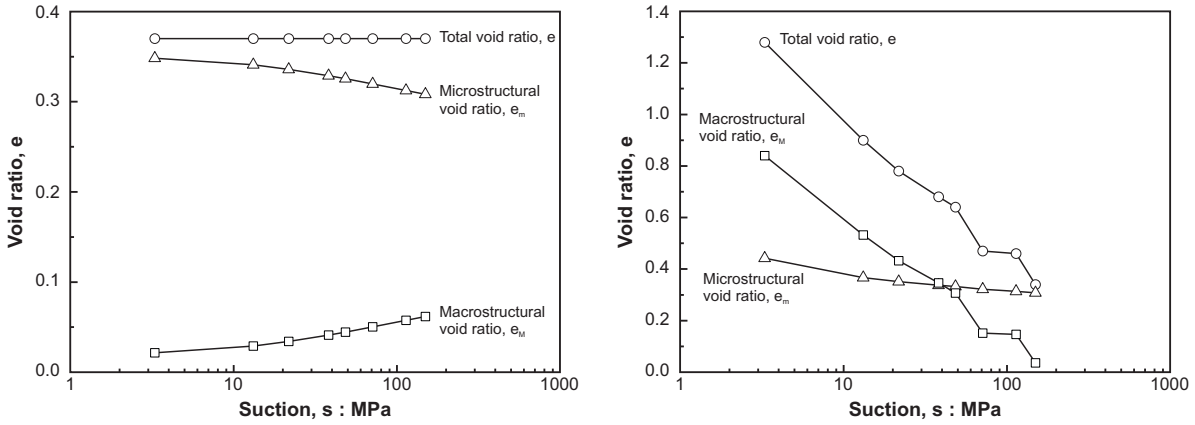

(a) Wetting under confined conditions.

(b) Wetting under unconfined conditions.

Figure 4.24: Model predictions for the evolution upon wetting of the total, microstructural and macrostructural void ratios of a compacted MX-80 bentonite/sand mixture.

6.4 Summary

Table 4.1 presents the values of the model parameters calibrated for three bentonite-based materials, namely Febex and MX-80 bentonites, and a mixture of MX-80 bentonite and sand. As can be observed, the macrostructural parameters hardly depend on the considered material and the values of $A = 0.2$ MPa, $n = 3$ and $m = 0.15$ may be assumed as a first approximation. A possible explanation for this observation is that the macrostructural parameters are rather affected by the compaction process than the physicochemical properties of the material. On the other hand, the microstructural parameters vary for the different materials. It is likely that they depend on physicochemical properties of the materials, such as the specific surface area and the cation exchange capacity.

Material	Microstructure		Macrostructure		
	C_{ads}	n_{ads}	A	n	m
	(MPa^{-1})		(MPa)		
Febex	0.0028	0.78	0.24	3	0.15
MX-80	0.0075	1.5	0.2	3	0.15
MX-80/sand mixture	0.0053	0.79	0.2	3	0.15

Table 4.1: Parameters of the water retention model for three bentonite-based materials.

7 Implementation in LAGAMINE

The water retention model developed in this chapter is defined in the form of an implicit function relating the water ratio e_w to the suction s, void ratio e and microstructural void ratio e_m. Combining Equations (4.6), (4.11), (4.15) and (4.16), the water ratio e_w is given by

$$e_w = e_m \exp\left[-\left(C_{ads}s\right)^{n_{ads}}\right] + (e - e_m)\left\{1 + \left[(e - e_m)\frac{s}{A}\right]^n\right\}^{-m} = e_w\left(s, e, e_m\right) \tag{4.18}$$

where the microstructural void ratio e_m is itself a function of the water ratio

$$e_m = e_{m0} + \beta_0 e_w + \beta_1 e_w^2 = e_m\left(e_w\right). \tag{4.19}$$

Therefore, in order to compute the degree of saturation $S_r = e_w/e$, it is necessary to solve the system of non-linear equations (4.18) and (4.19). The water ratio being bounded by $e_w = 0$ and $e_w = e$, the simple and robust bisection technique is adapted to solve the non-linear system of equations. Therefore, the zero of the following function should be determined

$$R_w^{(k)} = e_w^{(k-1)} - e_w\left(s, e, e_m^{(k)}\right) \tag{4.20}$$

with

$$e_m^{(k)} = e_m\left(e_w^{(k-1)}\right) \tag{4.21}$$

at iteration k. The iterative procedure is stopped when the inequality $|R_w^{(k)}| < TOL$ is verified. A value of TOL equal to 10^{-14} is adopted. The microstructural model (4.19) is implemented in the routine `POROM2` of the code `LAGAMINE`, while the implementation of the water retention model (4.18), including the numerical solving using the modified bisection technique, is realised in the routine `FKRSAT`.

The local convergence of the iterative procedure is verified in representing the evolution of the residuals with the number of iterations. A linear convergence rate is expected from the bisection technique. It implies that the residual $R_w^{(k)}$ reduces between iterations $k-1$ and k such that

$$|R_w^{(k)}| \approx L^{(k)}|R_w^{(0)}| \tag{4.22}$$

where L is a constant. The previous inequality becomes in a logarithmic scale

$$\log\left(|R_w^{(k)}|\right) \approx k\log\left(L\right) + \log\left(R_w^{(0)}\right) \tag{4.23}$$

which describes a straight line with a slope equal to 1 in the $\left(|R_w^{k-1}| - |R_w^k|\right)$ plane. An example of such a rate of convergence is provided in Figure 4.25 for two steps of saturation tests under confined and unconfined conditions.

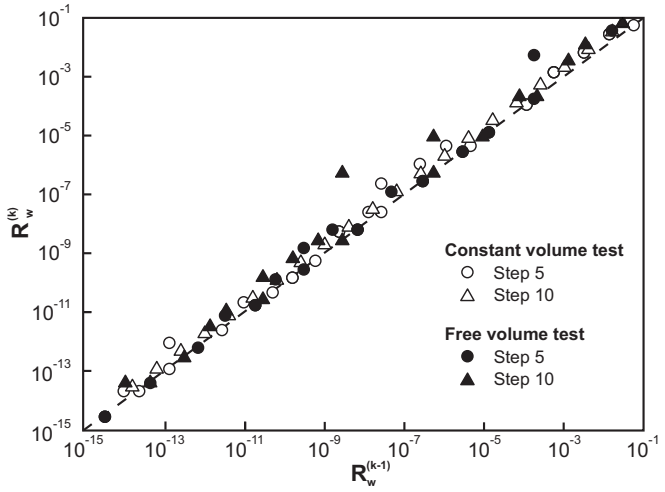

Figure 4.25: Local convergence of the iterative procedure to solve the water retention model.

Finally, the developed water retention model introduces additional coupling between both hydraulic and mechanical aspects. Indeed, both microstructural and total void ratios affect the water retention curve which is not any more a function of only suction. Accordingly, the stiffness matrices $\boldsymbol{E_{WW}}$, $\boldsymbol{E_{WM}}$, $\boldsymbol{E_{WG}}$, $\boldsymbol{E_{GG}}$, $\boldsymbol{E_{GM}}$ and $\boldsymbol{E_{GW}}$ should be updated. In particular, the introduction of microstructural features into the water retention model affects the purely hydraulic matrices (since the microstructural void ratio is a function only of the water ratio). On the other hand, the introduction of the total void ratio modifies the matrices $\boldsymbol{E_{WM}}$ and $\boldsymbol{E_{GM}}$.

8 Conclusions

The water retention properties of compacted bentonite-based materials are of main importance for the geological disposal of radioactive waste. While Chapter 2 provided a detailed description and insight of the hydromechanical processes occurring at the microscale, this chapter deals with the water retention properties at the macro scale. The main features of the water retention properties of compacted bentonites are first reviewed and explained at the light of the bentonite structure. A particularity of bentonites is that the density of the material is evolving not only along mechanical paths, but foremost upon wetting and drying.

Based on experimental observations at both micro- and macroscales, a phenomenological water retention model is developed. The model accounts for the double structure of compacted bentonite-based materials, and its evolution along hydromechanical stress paths. The water retention mechanism in the microstructure is supposed to be adsorption, while

water is retained by capillarity in the macrostructure.

The model succeeds in representing the water retention behaviour of bentonite-based materials compacted to different dry densities and wetted under both confined and unconfined conditions. The model provides a better understanding of the influence of the complex hydromechanical processes on the water retention curve, interpreting all experimental data within a unified framework. In addition, its simplicity, together with the limited number of parameters, make the model suitable for its implementation in numerical codes aimed at performing real scale simulations. Remarkably, some of the model parameters introduced have indeed been shown to take approximately the same value for several bentonites, providing a significant basis for preliminary design when dedicated experiments are missing.

Chapter 5

Mechanical constitutive behaviour

1 Introduction

In the context of radioactive waste disposal, one of the major functions of engineered barriers is to form a tight contact with the surrounding geological formation. Two aspects of the mechanical behaviour of bentonites are therefore fundamental: their swelling potential and their swelling pressure. The swelling potential refers to the ability of a soil to expand during wetting under unconfined conditions. This property is essential as technological gaps between materials of the disposal cannot be avoided during installation. As a matter of fact, technological gaps reached 6.6% of the total volume in the FEBEX mock-up test (Martin *et al.*, 2006), 14% in the SEALEX *in situ* test carried out in the Tournemire Underground Research Laboratory (Barnichon & Deleruyelle, 2009), and a minimum of 14% in the PGZ2 experiment realized in the Meuse/Haute-Marne Underground Research Laboratory (de La Vaissière, 2013). Under repository conditions, the first role of bentonite is thus to seal the existing technological gaps which could act as preferential pathways for the radionuclides migration. Therefore, the swelling potential of bentonites is generally associated to their self-sealing capacity.

The second key aspect is the swelling pressure developed upon wetting under confined conditions. When volume changes are prevented, the swelling capacity of clay particles, which occurs at the microscopic scale, is expressed at the macroscopic scale by an increase of the confining pressure. Accordingly, once that contact between the bentonite barrier and the host rock is reached, a swelling pressure develops against the gallery wall. This swelling pressure should be sufficiently high to create a good seal and close fractures of the excavation-damaged zone, but it should not exceed the effective stress of the geological formation. In this case, it could indeed damage the host rock and create preferential pathways for radionuclides migration (Sellin & Leupin, 2013).

For safety assessment, the sealing of technological gaps and the development of swelling pressure are two fundamental aspects that need to be accurately evaluated, represented and modelled. From an experimental point of view, different laboratory tests are classically performed to characterize the macroscopic swelling behaviour of bentonites (Figure 5.1). First of all, the swelling potential $\varepsilon_{v,FS}$ is obtained by wetting a bentonite sample under unconfined conditions (path 1 in Figure 5.1). Suction is generally decreased step-

wise (by using different saturated saline solutions) and the volume changes are measured for each suction step[1]. On the other hand, the swelling pressure S_P is defined as the pressure required to prevent volume changes of a sample upon wetting. Based on this definition, three methods can be used to evaluate the swelling pressure:

- **Swelling pressure tests**, which consist in the hydration of samples under confined conditions (path 2 in Figure 5.1). The swelling pressure that is measured is termed S_{P1} in Figure 5.1.
- **Swell-consolidation tests**, which consist in first, saturating a sample in an oedometer cell with a constant vertical load and then, once that full saturation of the sample is achieved, progressively loading the sample in order to reach the initial void ratio (path 3 in Figure 5.1). The stress for which the initial void ratio is recovered is denoted S_{P2} in Figure 5.1 and is a second estimation of the swelling pressure.
- **Swell-under-load tests**, which consist in saturating different samples under different constant loads (path 6 in Figure 5.1). The swelling pressure S_{P3} is then defined as the vertical pressure under which no strain is recorded upon wetting.

These three experimental techniques provide three estimations of the swelling pressure. In particular, the difference between S_{P1}, S_{P2} and S_{P3} evidences stress path dependency of the mechanical behaviour of bentonite. Further comparison can be found in Agus (2005) and Wang *et al.* (2012).

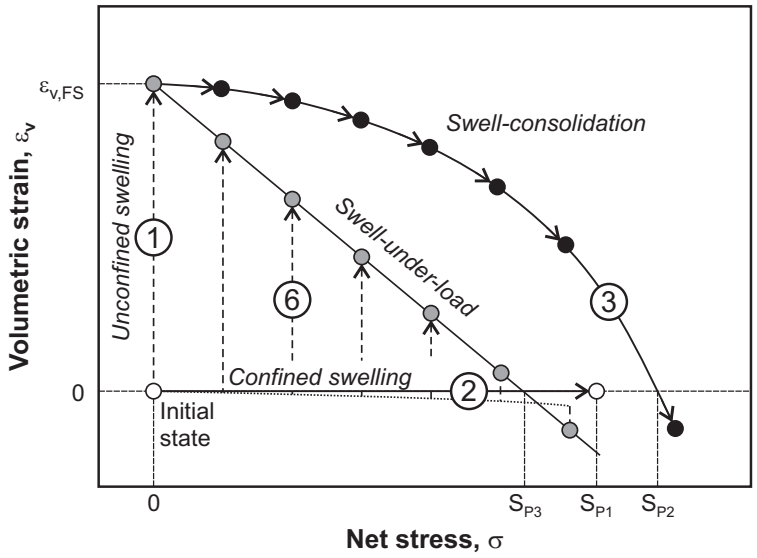

Figure 5.1: Experimental techniques for the characterization of the swelling capacity of soils (after Sridharan *et al.*, 1986). The numbers 1, 2, 3 and 6 refer to the stress paths represented in Figure 5.2.

In order to relate the void ratio with the mean net stress and suction, the concept of state surface was early introduced by Matyas & Radhakrishna (1968). The state surface

[1]For totally unconfined samples, the swelling potential is difficult to determine because bentonite samples lose their integrity when suction approaches zero (due to very high swelling strain). Therefore, the swelling potential is often evaluated by soaking bentonite samples under oedometer conditions with a very low applied load. It is then expressed as $\varepsilon_{v,FS} = \Delta H/H_i$.

is the locus of points representing all possible states of the material in the $(\sigma - s - e)$ space[2]. In particular, the stress paths followed by the experimental techniques described above can be represented in this space, as shown in Figure 5.2. Furthermore, the figure highlights the ability of the state surface concept to tackle some features of the mechanical behaviour of unsaturated soils, namely the increase of the material stiffness with suction (as evidenced by the stress paths 3 and 4) and the development of swelling or collapse strain along a wetting path depending on the stress state of the material (as evidenced by the stress paths 1 and 6).

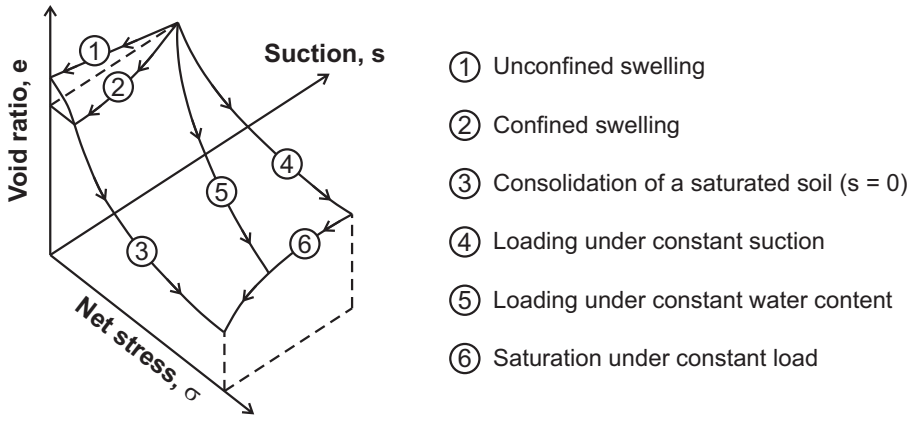

Figure 5.2: State surface approach for unsaturated soils (Matyas & Radhakrishna, 1968).

Examples of state surfaces include the models developed by Aitchison & Martin (1973), Fredlund & Morgenstern (1976), Lloret & Alonso (1985) and Gatmiri & Delage (1995). Although attractive by its simplicity, the state surface approach suffers from important shortcomings. In particular, state surfaces are defined only along monotonous stress paths, and the result is stress path independent. Each model of this type is developed for a given problem or given experimental conditions. Therefore, it addresses partial aspects of behaviour but does not establish consistent links between different features of behaviour (Gens, 2010). The approach is therefore not suitable to be implemented in a finite element code and solve boundary value problems. To overcome these shortcomings, constitutive models for unsaturated soils, pioneered by the work of Alonso *et al.* (1990), were developed in the framework of elastoplasticity theory. This approach is used in this work to study the mechanical behaviour of compacted bentonite-based materials.

In this chapter, the main and relevant experimental observations on the mechanical behaviour of saturated and partially saturated bentonites are first reviewed. The criteria for the selection and the development of a constitutive model are then listed and the Barcelona Basic Model (Alonso *et al.*, 1990) is selected as starting model. The model is thoroughly described, from isotropic conditions to three-dimensional conditions. Its implementation in the finite element code `LAGAMINE`, using a return-mapping algorithm, is then detailed. The Barcelona Basic Model is then validated against experimental data on several bentonite-based materials. While the model succeeds in tackling important features of bentonites behaviour, it exhibits some limitations in reproducing the swelling

[2]Here, σ is a scalar which represents either the vertical net stress or the mean net stress.

behaviour under confined conditions. The limitations are highlighted and the model is extended to better represent this important feature. Finally, the new model is validated and its parameters are summarized.

2 Experimental observations

In order to gain a comprehensive understanding of the mechanical behaviour of saturated and partially saturated bentonites, laboratory tests should be performed along simple stress paths. These stress paths are generally represented in the space of net stress (mean stress p or vertical stress σ_v), deviatoric stress (q) and suction (s), which are the quantities that can be directly controlled, measured or determined by laboratory equipment. The laboratory equipment used to carry out tests on unsaturated soils consists indeed in adapting classical techniques for saturated soils in order to control or measure suction. The techniques of suction control and measurement were presented in Chapter 4. Further information and detailed description of the techniques for mechanical investigation of partially saturated soils can be found in Fredlund & Rahardjo (1993), Delage (2002) and Tarantino *et al.* (2008), among others. The classically investigated stress paths include mechanical loading under constant suction, hydraulic loading under constant stress and shearing path under constant suction. They are represented in Figure 5.3.

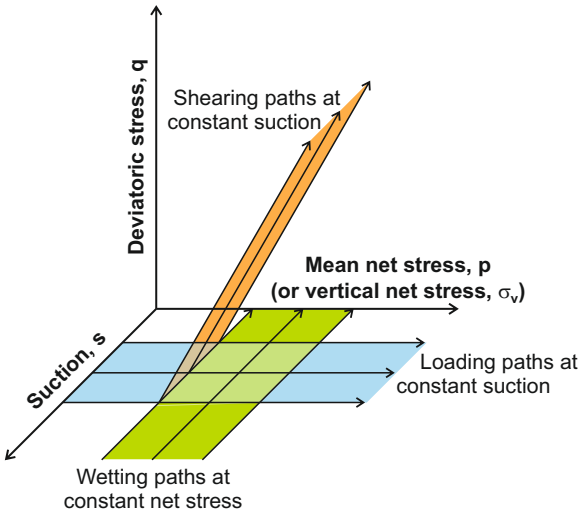

Figure 5.3: Classically investigated stress paths in the $(p - q - s)$ space.

In this section, the main and relevant experimental observations on the mechanical behaviour of saturated and unsaturated bentonites are reviewed. Note that, while there is an extensive literature concerning the behaviour of unsaturated soils, the experimental data on compacted bentonites are limited. One of the reasons for this scarcity of data is probably associated with the difficulty and important time required to perform laboratory tests.

2.1 Mechanical loading under constant suction

The compressibility behaviour of soils is traditionally studied through oedometer tests which are one-dimensional loading tests. These tests provide the evolution of void ratio (or volumetric strain) with the applied vertical stress. Because the horizontal confining stress is generally not measured, oedometer tests do not provide complete information on the stress state of the material (Gens & Alonso, 1992). Yet, oedometer tests are far less complex to carry out than triaxial tests and are therefore often preferred.

Figure 5.4 presents the results of an oedometer test performed on a mixture of MX-80 bentonite and sand with respective proportions of 80/20 in dry mass, compacted at a dry density of 1.5 Mg/m^3, and loaded at a constant suction of 80 MPa (Alonso *et al.*, 2005b). Upon loading, the material shows a gradual decrease in volume, with a quasi-bilinear response in the $(\ln \sigma_v - e)$ plane. The change of slope around a vertical stress of 5 MPa corresponds to the development of irreversible plastic strains, i.e. yielding. The corresponding net stress is called the apparent preconsolidation stress and is denoted p_0. Beyond the apparent preconsolidation stress, the evolution of the void ratio upon loading follows a virgin (or normal) compression line whose slope in the $(\ln p - e)$ plane is denoted λ. Upon unloading, the material experiences swelling. The response of the material is linear in the $(\ln \sigma_v - e)$ plane and the slope of the curve is generally close to the one of the elastic loading path. The slope of the unloading–reloading line for changes in mean net stress, expressed in the $(\ln p - e)$ plane, is denoted κ. The irreversible strain created during the plastic loading path is clearly evidenced in Figure 5.4.

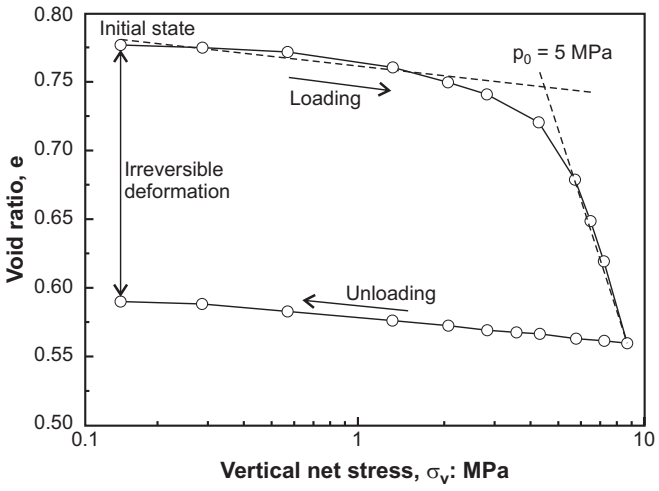

Figure 5.4: Controlled-suction oedometer test (s = 80 MPa) on a mixture of MX-80 bentonite and sand compacted at a dry density $\rho_d = 1.5$ Mg/m^3 (Alonso *et al.*, 2005b).

Oedometer tests performed at different suction values show that the preconsolidation stress is suction dependent and that the yield stress increases with increasing suction. This feature of unsaturated soils mechanical behaviour is highlighted in Figure 5.5. Figure 5.5 shows results of loading tests carried out by Lloret *et al.* (2003) at different constant suction values on compacted Febex bentonite. The apparent preconsolidation pressures for the different suction values are marked by arrows in Figure 5.5(a) and their evolution

with suction is summarized in Figure 5.5(b). Note that this increase of the preconsolidation pressure with suction is not typical of compacted bentonites only, but is observed in all unsaturated soils. In the case of granular material, Wheeler & Karube (1995) demonstrated that the increase of the apparent preconsolidation pressure with suction could be explained by an increase of normal forces created by meniscus water bridges, suction providing additional stabilisation against inter-particle slippage. Similarly, suction also provides stabilising forces in clays which allows the material to sustain higher stresses before yield.

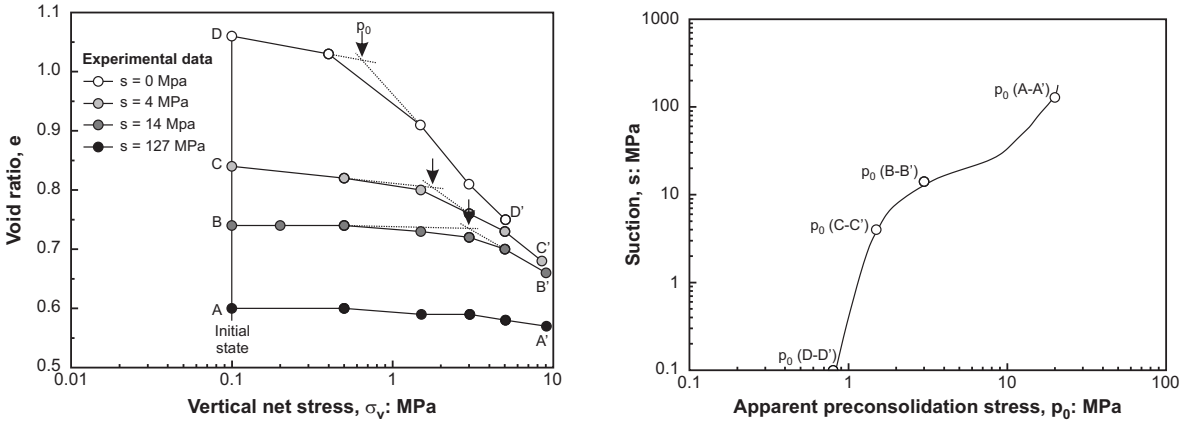

(a) Change in void ratio during loading at constant suction.

(b) Relationship between the apparent preconsolidation stress and suction.

Figure 5.5: Controlled-suction oedometer tests on Febex bentonite compacted at an initial dry density $\rho_d = 1.70$ Mg/m^3 (Lloret *et al.*, 2003).

In addition to the preconsolidation pressure, the slope of the normal compression line also exhibits suction dependency. For compacted Febex bentonite, Figure 5.5(a) shows an increasing slope λ with decreasing suction. Such behaviour was also observed by Cui & Delage (1996) on a compacted silt, Charlier *et al.* (1997) on a sandy silt and Ye *et al.* (2012) on GMZ bentonite, among others. However, Wheeler & Sivakumar (1995) and Geiser *et al.* (2006) observed different behaviours on a compacted speswhite kaolin and on different fine-grained soils respectively. In particular, Geiser *et al.* (2006) showed a non-monotonic evolution of the compression index with suction, with an increase of the slope of the normal compression line with decreasing suction, except for very low suctions for which a decrease of λ is observed. Geiser *et al.* (2006) suggested that the first increase could be associated with the increase of suction in the saturated domain, while an increase in suction in the unsaturated domain tends to reduce the compressibility. The opposite tendency is observed by Marcial (2003) and Wang *et al.* (2013c) on MX-80 bentonite and a compacted mixture of MX-80 bentonite and sand, respectively.

2.2 Hydraulic loading under constant stress

The swelling behaviour is one of the most fundamental properties of compacted bentonites. Figure 5.6(a) presents the evolution of void ratio with suction for unconfined samples of FoCa7 clay subjected to different wetting and drying cycles (Delage *et al.*, 1998). On

the other hand, Figure 5.6(b) shows the evolution of void ratio for a mixture of MX-80 bentonite and sand compacted to two different dry densities and wetted under free swelling conditions (Wang *et al.*, 2013c; Gatabin *et al.*, 2016). Upon wetting under unconfined conditions, both materials show a gradual increase in volume, with a quasi-linear response in the $(\ln s - e)$ plane. In addition, no hysteresis effect is observed in Figure 5.6(a) upon drying. The slope of the reversible wetting–drying line is conventionally denoted κ_s. As evidenced in Figure 5.6(b), the slope κ_s is a function of the initial dry density ρ_{di} of the material. In particular, an increase of the slope is observed for increasing dry density ($\kappa_s = 0.24$ for $\rho_{di} = 2.04$ Mg/m^3 against $\kappa_s = 0.039$ for $\rho_{di} = 1.67$ Mg/m^3). This behaviour can be explained by the larger amount of clay particles (the scale at which the swelling processes take place) in the denser material.

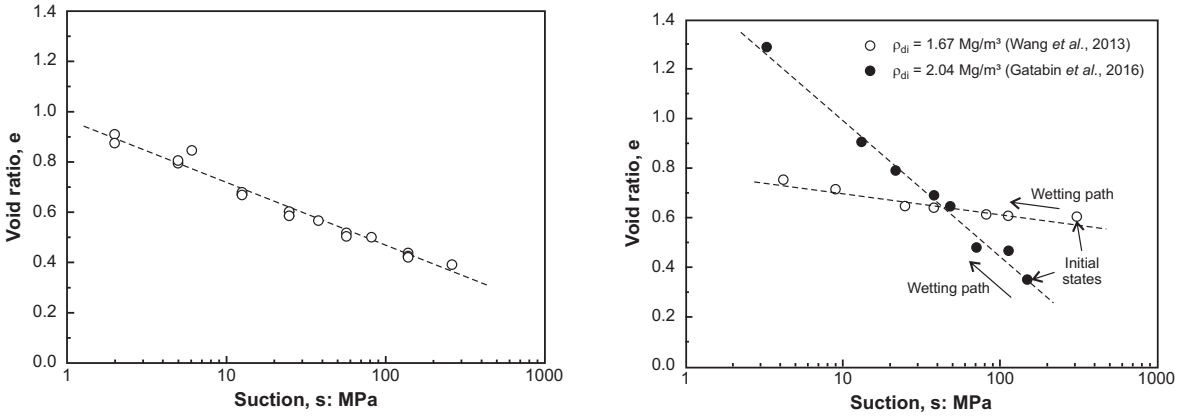

(a) FoCa7 clay (Delage *et al.*, 1998).

(b) Mixture of MX-80 bentonite and sand (Wang *et al.*, 2013c; Gatabin *et al.*, 2016).

Figure 5.6: Influence of suction changes on the volumetric behaviour of compacted bentonite-based materials, under unconfined conditions.

Let us now consider the case of wetting under stress (Figure 5.7). Dang & Robinet (2005) presented controlled-suction oedometer tests on compacted MX-80 bentonite. The tests were carried out for different values of over-consolidation ratios (OCR), defined as the ratio between the maximum stress state experienced by the material (i.e. the compaction pressure) and the current stress state, ranging between 1 and 356. The data show that all normally consolidated samples (for which OCR = 1) experienced positive strains, known as collapse strains, upon wetting. On the other hand, for the highly over-consolidated samples, negative strains, known as swelling strains, are observed. These swelling strains are all the more important that the OCR is high. For intermediate over-consolidation ratios (OCR = 1.8), swelling strains are observed first, but the material experiences collapse when the suction is further decreased. Depending of the confining stress, the material exhibits thus different features. During wetting under low stresses, swelling is produced, while under high stresses, the soil undergoes volumetric compression, i.e. collapse.

At the microscale, the collapse phenomenon may be explained by structural changes of the material upon wetting. Della Vecchia (2009) carried out saturation tests on Boom clay under different confining conditions and analysed the pore size distribution of the material at the end of each test. Figure 5.8 shows that the sample saturated under a

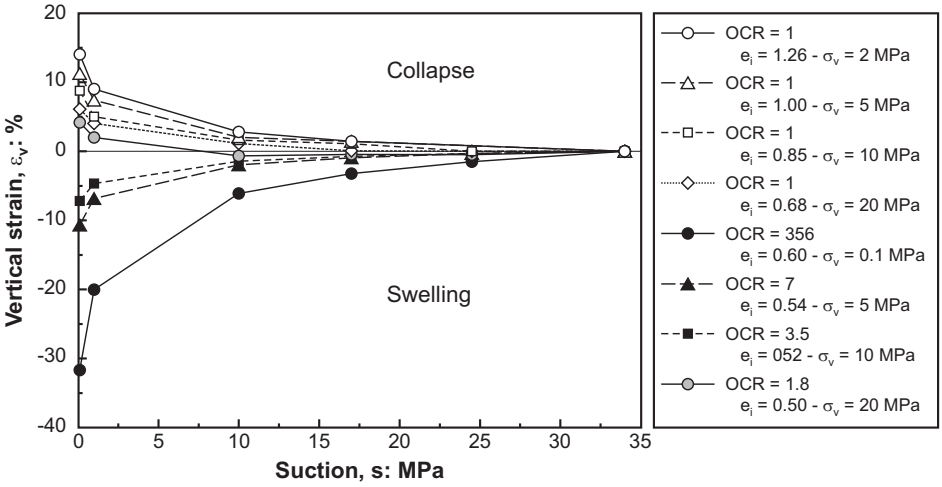

Figure 5.7: Wetting path on MX-80 bentonite under oedometer conditions and different over-consolidation ratios (Dang & Robinet, 2005).

constant vertical stress of 600 kPa experienced important collapse, as highlighted by the important decrease in the macroporous volume. On the other hand, the sample wetted under a lower vertical stress experienced swelling. Marcial (2003) provided a detailed explanation of the phenomenon. Starting from (dry) as-compacted conditions, water enters the micropores, separates the clay layers and particles and aggregates swell. As soon as the particles are separated by water, the attractive forces between these particles decrease. Consequently, the particles *leave* the aggregates and fill the macropores. The aggregate swelling tends to decrease the shear resistance between aggregates. Under confined conditions, when the swelling pressure reaches a given value, the shear stress at the contact between aggregates exceeds this resistance, aggregates slip on each other, and the structure is reorganized. At the macroscopic scale, this reorganization leads to a smaller swelling pressure. For the lowest density, the swelling potential is not sufficient to provoke the structure reorganization.

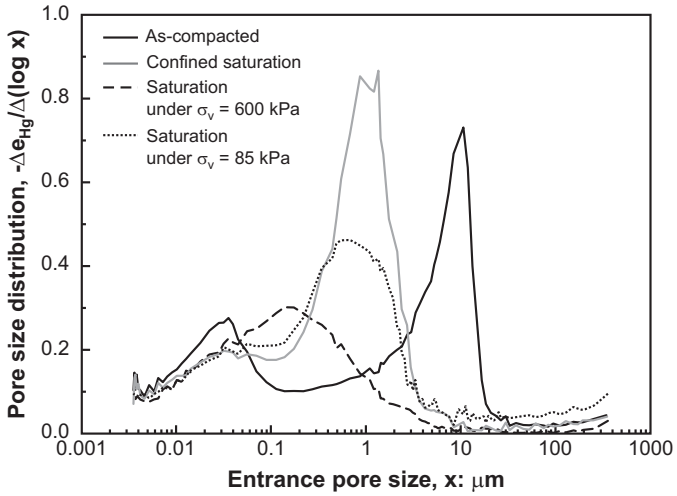

Figure 5.8: Pore size distributions of compacted Boom clay saturated with different mechanical constraints (Della Vecchia, 2009).

2.3 Shear strength behaviour

The shear behaviour of soils is investigated in triaxial apparatus or direct shear box. In both cases, several shear tests should be performed under different confining pressures, each test providing one point of the failure surface.

The shear strength behaviour of unsaturated soils, *a fortiori* of compacted bentonites, has been poorly characterized. Very few data are available, most of the information on bentonite mechanical behaviour being obtained from oedometer tests. Yet, experimental data on various unsaturated soils have generally highlighted an increase of the apparent shear strength with suction (Blight, 1966; Escario & Saez, 1986; Cui, 1993), and no change in the slope of the critical state line with suction (Escario & Saez, 1986). Accordingly, cohesion increases with suction, while the friction angle is not affected.

Recently, Romero (2012) provided interesting data on the shear strength behaviour of Kunigel V1 bentonite compacted to a dry density of 1.36 Mg/m^3. Triaxial tests were carried out under different confining stresses and constant suction values (from 0 to 140 kPa). The experimental data confirm the increase in cohesion with suction and the constant friction angle. In addition, Romero (2012) showed that, in the investigated range of suctions, a linear evolution of cohesion $c(s)$ is observed with suction s, such that

$$c(s) = c(0) + ks \tag{5.1}$$

where $c(0)$ is the suction under saturated conditions and k is a constant controlling the increase of cohesion. For higher suction values, a non-linear behaviour (defining a maximum shear strength) is expected (Escario & Saez, 1987; Fredlund *et al.*, 1987).

2.4 Remark on anisotropy

Anisotropy of soils refers to the directional dependency of material behaviour. Depending on the compaction procedure, the fabric of soils may exhibit anisotropy (Denis, 1991; Hicher *et al.*, 2000). Hattab & Fleureau (2011) analysed the changes in particle orientation during one-dimensional consolidation. They showed that loading resulted in a preferential orientation of the particles, perpendicular to the loading direction. The directions of micropores were also affected. In addition, they showed that loading an initially anisotropic structure erased the anisotropy if the loading stress is sufficiently high. At the macroscopic scale, anisotropy of swelling strains was detected by Gatabin *et al.* (2016). Gatabin *et al.* (2016) compacted uniaxially samples made of a mixture of MX-80 bentonite and sand. The samples were then wetted under unconfined conditions to different values of suctions. For each equilibrated suctions, the dimensions of the samples were measured in order to determine the axial, radial and total strain. These strains developed upon suction imposition are presented in Figure 5.9. An important anisotropy is observed, the axial strain being twice the radial one.

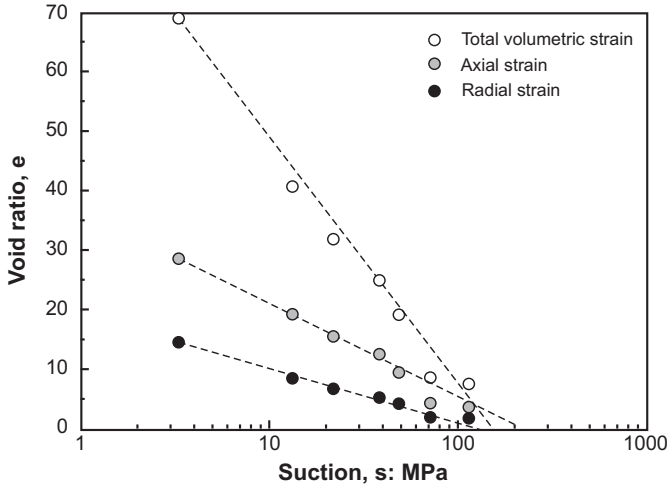

Figure 5.9: Relationship between the total, axial and radial strains and suction during wetting under unconfined conditions of a mixture of MX-80 bentonite and sand (Gatabin *et al.*, 2016).

3 Criteria for the development of a constitutive model

In order to model the coupled hydromechanical behaviour of compacted bentonite-based materials, a mechanical model should be selected and implemented in the finite element code `LAGAMINE`. Three main criteria should be considered for selecting a constitutive model (Wheeler & Karube, 1995):

- The ability of the model to adequately represent the **significant aspects** of behaviour for a **given application**.
  This PhD work focuses on the behaviour of compacted bentonite-based materials used as engineered barriers for the geological disposal of nuclear waste. In our case, the significant mechanical aspect to be considered is the non-linear swelling behaviour under restricted swelling conditions. The hydraulic and mechanical stresses acting of the bentonite buffer are reasonably monotonous and the stakes concerning the cyclic behaviour are not considered as high.

- The number of **parameters** and the possibility of measuring them in the laboratory.
  Laboratory tests on compacted bentonites are long and complex, and available experimental data are limited. The model parameters should thus be obtained from a limited number of (relatively) simple laboratory tests.

- The **ease of implementing** the model within a finite element code.
  The final goal is to model boundary-value problems, including large-scale experiments.

Based on these considerations, the Barcelona Basic Model (Alonso *et al.*, 1990) is selected as a starting point. The robustness and capacities of the model are indeed proven, as certified by the important number of publications on large-scale problems using this model

(see Rothfuchs *et al.*, 2007; Sánchez *et al.*, 2010; Rutqvist *et al.*, 2011; Zandarin *et al.*, 2011; Jaime *et al.*, 2015, among many others). Its formulation in terms of net stress and suction allows an easier calibration than other models formulated using an effective stress.

4 Barcelona Basic Model

The Barcelona Basic Model (BBM) was proposed by Alonso *et al.* (1990) and pioneered the development of mechanical constitutive models for partially saturated soils. Most of the existing models for unsaturated soils rely indeed on the concepts that were introduced by Alonso *et al.* (1990). The idea behind the model is the extension of an existing model for saturated soils to unsaturated conditions. As stated by Gens *et al.* (2006),

> *there is nothing special in an unsaturated soil apart from the simple fact that some part of the pore space is occupied by air.*

Accordingly, the behaviour of unsaturated soils should be modelled consistently and full saturation considered as a limiting case. Therefore, the Barcelona Basic Model consists in the extension of the Modified Cam-Clay Model (Roscoe & Burland, 1968) to unsaturated conditions, by using suction as an additional stress variable. It is formulated adopting net stress[3] $\boldsymbol{\sigma}$ and suction s as stress variables.

The complete formulation of the Barcelona Basic Model is presented in this section. For the sake of clarity, the model is first formulated for isotropic stress states which corresponds the simplest stress state of a body. The formulation is then progressively extended to triaxial and three-dimensional stress states.

4.1 Formulation for isotropic stress states

Under isotropic stress conditions ($\sigma_1 = \sigma_2 = \sigma_3$), the mechanical stress state is described using the mean net stress $p = \sigma_i$ and suction s. Both changes in the mean net stress and in suction are assumed to produced only volumetric strains $\varepsilon_v = \varepsilon_i$. Accordingly, the space $(p - s - \varepsilon_v)$ is relevant for the description of the model and yield limits should be defined in the plane $(p - s)$.

4.1.1 Modified Cam-Clay Model for saturated conditions

For saturated conditions, the Barcelona Basic Model coincides with the Modified Cam-Clay Model (Roscoe & Burland, 1968). The Modified Cam-Clay model belongs to the family of elastoplastic strain-hardening models[4]. Accordingly, the total strain increment can be decomposed into an elastic part and a plastic part. For isotropic stress states, the increment of total volumetric strain $\mathrm{d}\varepsilon_v$ is equal to

$$\mathrm{d}\varepsilon_v = \mathrm{d}\varepsilon_v^e + \mathrm{d}\varepsilon_v^p \tag{5.2}$$

[3]It is worth reminding that the net stress $\boldsymbol{\sigma}$ is defined as $\boldsymbol{\sigma} = \boldsymbol{\sigma_t} - u_a \boldsymbol{I}$ for $s < 0$ and $\boldsymbol{\sigma} = \boldsymbol{\sigma'} = \boldsymbol{\sigma_t} - u_w \boldsymbol{I}$ for saturated states, where $\boldsymbol{I}$ is the identity tensor.

[4]The main concepts of the elastoplasticity framework are reminded in Appendix B

where $d\varepsilon_v^e$ and $d\varepsilon_v^p$ are respectively the elastic and plastic components of the incremental volumetric strain.

In the elastic domain, the increment of volumetric strain associated to changes in mean net stress is given by

$$d\varepsilon_v^e = \frac{\kappa}{1+e}\frac{dp}{p} = \frac{dp}{K} \tag{5.3}$$

where κ is the slope of the unloading-reloading line and e is the void ratio (Figure 5.10). Elasticity in the Modified Cam-Clay Model is non-linear as the bulk modulus K is a function of both the void ratio and the mean net stress according to

$$K = \frac{(1+e)\,p}{\kappa}. \tag{5.4}$$

Once that the mean net stress reaches the preconsolidation stress (yield limit) p_0^*, plastic strain is generated (Figure 5.10). The evolution of the plastic strain is then governed by the hardening law

$$d\varepsilon_v^p = \frac{\lambda(0)-\kappa}{1+e}\frac{dp_0^*}{p_0^*} \tag{5.5}$$

where $\lambda(0)$ is the slope of saturated virgin consolidation line.

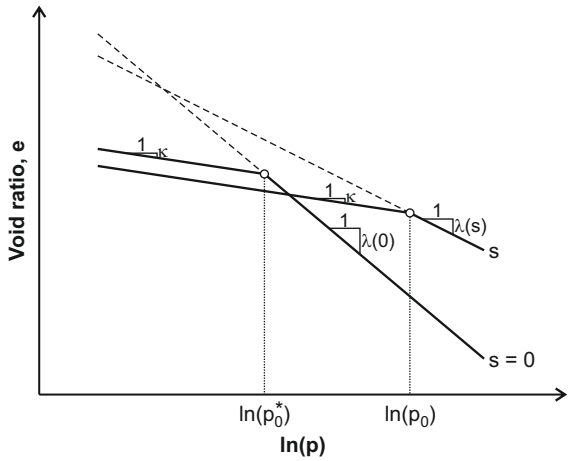

Figure 5.10: Compression curves for saturated and unsaturated states (Alonso *et al.*, 1990).

4.1.2 Extension to unsaturated conditions

The extension of the Modified Cam-Clay Model to unsaturated conditions involves considering both the influence of suction on the loading and unloading behaviour under constant suction, and the influence of suction changes.

4.1.2.1 Influence of suction on the loading and unloading behaviour

In the Barcelona Basic Model, the slope κ of the unloading-reloading line for changes in mean net stress is assumed constant. On the other hand, the slope λ of the virgin

compression line and the yield stress p_0 are functions of suction. More specifically, the slope of the virgin compression line is supposed to decrease with increasing suction (Figure 5.10). The following law is adopted

$$\lambda(s) = \lambda(0)\big[\,(1-r)\exp\left(-\omega s\right) + r\big] \tag{5.6}$$

where r and ω are material parameters. r is related to the maximum stiffness of the soil (for an infinite suction) and ω controls the rate of increase of the soil stiffness with suction.

In addition, the elastic domain increases with increasing suction, so that the higher the suction, the higher is the stress that the soil can sustain before yielding. In particular, the evolution of the preconsolidation pressure $p_0(s)$ with suction follows

$$p_0(s) = p_c \left(\frac{p_0^*}{p_c}\right)^{\frac{\lambda(0)-\kappa}{\lambda(s)-\kappa}} \tag{5.7}$$

where p_c is a reference net pressure. Equation (5.7) defines a yield curve in the $(p-s)$ plane called the Loading-Collapse (LC) curve (Figure 5.11). This curve is a fundamental aspect of the Barcelona Basic Model. One will get later back on this yield curve in Section 4.1.2.3.

Owing for the dependence of the virgin compression line and the yield stress on suction, the hardening law (5.5) of the LC curve becomes

$$\mathrm{d}\varepsilon_v^p = \frac{\lambda(s)-\kappa}{1+e}\frac{\mathrm{d}p_0}{p_0}. \tag{5.8}$$

Using Equations (5.6) and (5.7), Equation (5.8) reduces to

$$\mathrm{d}\varepsilon_v^p = \frac{\lambda(0)-\kappa}{1+e}\frac{\mathrm{d}p_0^*}{p_0^*} \tag{5.9}$$

which corresponds to the former hardening law (5.5).

4.1.2.2 Influence of suction changes

Under partially saturated conditions, suction changes bring an additional contribution to the increment of total strain. In particular, suction changes are assumed to yield only volumetric strain. Accordingly, in the elastic domain, the total strain increment is given by

$$\mathrm{d}\varepsilon_v^e = \mathrm{d}\varepsilon_{vp}^e + \mathrm{d}\varepsilon_{vs}^e = \frac{\kappa}{1+e}\frac{\mathrm{d}p}{p} + \frac{\kappa_s}{1+e}\frac{\mathrm{d}s}{s+u_{atm}} = \frac{\mathrm{d}p}{K} + \frac{\mathrm{d}s}{K_s} \tag{5.10}$$

where $\mathrm{d}\varepsilon_{vp}^e$ and $\mathrm{d}\varepsilon_{vs}^e$ are the elastic increments of volumetric strain associated to changes in net stress and changes in suction, respectively, κ_s is the slope of the reversible wetting-drying line, u_{atm} is the atmospheric pressure and K_s is the bulk modulus for changes in suction, expressed as

$$K_s = \frac{(1+e)\,(s+u_{atm})}{\kappa_s}. \tag{5.11}$$

Along a drying path, there is a threshold suction s_0 beyond which irreversible plastic strain are created. The threshold suction $s = s_0$ defines a second yield curve in the $(p-s)$

plane called the suction Increase (SI) curve[5]. The SI surface is represented in Figure 5.11. Its expression is given by

$$f_{SI} \equiv s = s_0. \tag{5.12}$$

Once this suction s_0 is reached, the increment of plastic volumetric strain produced by further increase of in suction is given by

$$\mathrm{d}\varepsilon_v^p = \frac{\lambda_s - \kappa_s}{1+e} \frac{\mathrm{d}s_0}{s_0 + u_{atm}} \tag{5.13}$$

where λ_s is the slope of the virgin drying line.

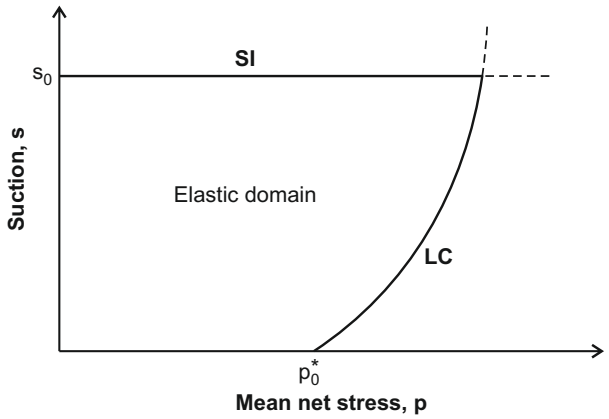

Figure 5.11: Yield curves of the Barcelona Basic Model for isotropic stress states: Loading-Collapse (LC) and Suction Increase (SI) curves.

It is important to note that the total increment of plastic volumetric strain $\mathrm{d}\varepsilon_v^p$ appears in both Equation (5.9) and Equation (5.13). Accordingly, irreversible strains control the position of the LC and SI yield surfaces and the hardening of both yield surfaces is coupled. Depending on the sign of the volumetric plastic strain, hardening or softening of the yield surface will take place.

4.1.2.3 Remark on the Loading-Collapse curve

Let us consider a sample whose stress state is initially located on the yield curve $(\mathrm{LC})_1$ (Figure 5.12). Its suction is denoted s_1 and its mean net stress p_1. This sample is now loaded at constant suction to a mean net stress p_2. As a consequence, the stress state of the sample evolves following the stress path L and the yield curve moves from $(\mathrm{LC})_1$ to $(\mathrm{LC})_2$. The movement of the yield curve comes along with irreversible plastic volumetric strains. According to the hardening law (5.9), these plastic strains are equal to the strains that would be obtained from a consolidation test under saturated conditions, going from $(p_0^*)_1$ to $(p_0^*)_2$.

[5]In the context of the present work, in which thermal effects are not considered, the most relevant stress path is the wetting path. Consequently, the SI yield surface has a limited relevance. Yet, for the sake of completeness, the complete formulation of the Barcelona Basic Model is presented and implemented in `LAGAMINE`.

Let us now consider a second sample with the same initial state. This sample is wetted under constant mean net stress. As a consequence, the stress state evolves following a stress path denoted C, and the LC curve moves similarly to the previous case, and irreversible plastic volumetric strains are created. These strains correspond to the collapse of the soil structure. Consequently, the concept of Loading-Collapse curve allows a consistent modelling of compressive strains due to loading and collapse strains due to wetting.

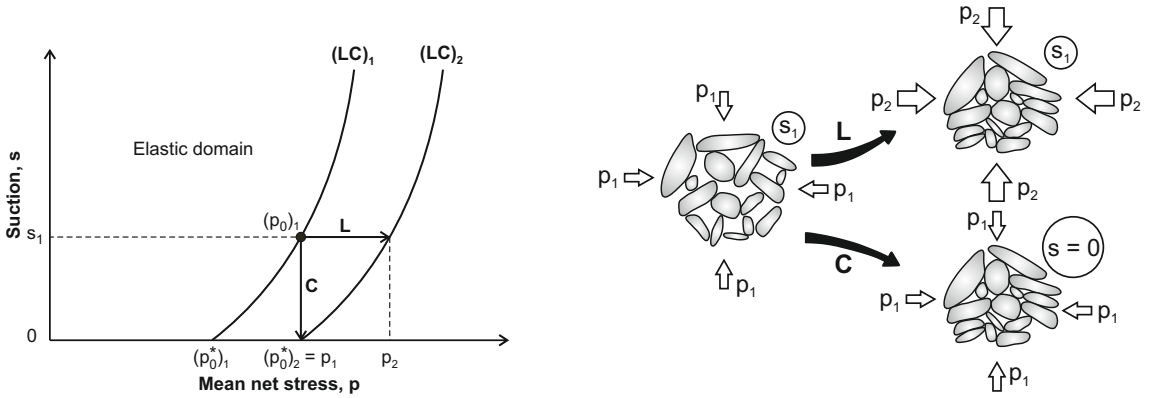

(a) Displacement of the LC yield curve.

(b) Structure evolution.

Figure 5.12: Effects of loading at constant suction (L) and wetting at constant mean net stress (C) on the LC curve and soil structure (Gens, 2010).

4.2 Formulation for triaxial stress states

Under triaxial conditions ($\sigma_1 \neq \sigma_2 = \sigma_3$), the mechanical stress state can be described by the mean net stress p, suction s and the deviatoric stress $q = (\sigma_1 - \sigma_3)$.

4.2.1 Elastic domain

In the elastic domain, changes in the deviatoric stress yield deviatoric deformation according to

$$\mathrm{d}\varepsilon_d^e = \frac{1}{3} G \mathrm{d}q \tag{5.14}$$

where $\mathrm{d}\varepsilon_d^e$ is the elastic increment of deviatoric strain and G is the shear modulus. This modulus may be chosen as a constant or as a function of the bulk modulus K following

$$G = \frac{3\,(1-2\nu)\,K}{2\,(1+\nu)} \tag{5.15}$$

where ν is Poisson's ratio. In both cases, the shear modulus is assumed to be independent of suction.

4.2.2 Yield surfaces

In the $(p-q)$ plane, the Barcelona Basic Model considers the Modified Cam-Clay yield surface (Figure 5.13(a))

$$f_{LC} \equiv q^2 - M_\theta^2\,(p + p_s)\,(p_0 - p) = 0 \tag{5.16}$$

where M_θ is the slope of the critical state line, p_s is the left intercept of yield surface and p_0 is the apparent preconsolidation pressure at a suction s. The increase of the apparent cohesion with increase suction is included by considering p_s as an evolving function of suction according to

$$p_s(s) = \frac{c(s)}{\tan\varphi} = \frac{c(0) + ks}{\tan\varphi} \tag{5.17}$$

where $c(0)$ is the cohesion under saturated conditions and k is a parameter controlling the increase of cohesion.

The slope of the critical state line is linked to the friction angle φ through

$$M_\theta = \frac{6\sin\varphi}{3 - \sin\varphi} \qquad \text{or} \qquad \varphi = \arcsin\left(\frac{3M_\theta}{6 + M_\theta}\right). \tag{5.18}$$

Finally, the SI surface is assumed to be independent of the stress level. The three-dimensional representation of the Barcelona Basic Model is presented in Figure 5.13(b).

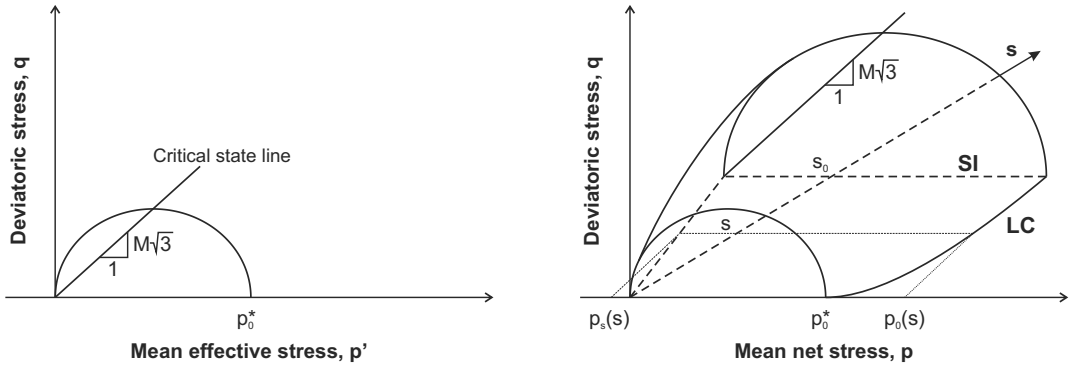

(a) Modified Cam-Clay Model.

(b) Barcelona Basic Model.

Figure 5.13: Representation of the Modified Cam-Clay model and the Barcelona Basic Model in the $(p - q)$ plane.

4.2.3 Flow rule

The triaxial formulation of the Barcelona Basic Model is completed with a non-associated flow rule. In particular, the following non-associated flow rule is defined

$$\frac{\mathrm{d}\varepsilon_d^p}{\mathrm{d}\varepsilon_v^p} = \frac{2q\alpha}{M_\theta^2\,(2p + p_s - p_0)} \tag{5.19}$$

where α is chosen in such a way that Equation (5.19) predicts zero lateral strain for stress states corresponding to Jacky's K_0 values, that is

$$\alpha = \frac{M_\theta\,(M_\theta - 9)\,(M_\theta - 3)}{9\,(6 - M_\theta)}\,\frac{1}{1 - \frac{\kappa}{\lambda(0)}}. \tag{5.20}$$

Accordingly, the flow surface is given by

$$g_{LC} \equiv \alpha q^2 - M_\theta^2\,(p + p_s)\,(p_0 - p) = 0. \tag{5.21}$$

4.3 Formulation for three-dimensional stress states

Finally, under three-dimensional conditions, the mechanical stress state is described by the mean net stress p, suction s, the second invariant of the deviatoric stress tensor J_2 and the Lode's angle θ. The second invariant of the deviatoric stress tensor is defined as

$$J_2 = \sqrt{\frac{1}{2}\boldsymbol{s} : \boldsymbol{s}} \tag{5.22}$$

where $\boldsymbol{s}$ is the deviatoric stress tensor given by $\boldsymbol{s} = \boldsymbol{\sigma} - p\boldsymbol{I}$. The Lode's angle θ gives the direction of the stress path in the deviatoric plane. It is given by

$$\theta = -\frac{1}{3}\sin^{-1}\left(\frac{3\sqrt{3}}{2}\frac{J_3}{J_2^2}\right) \tag{5.23}$$

with J_3 the third invariant of the deviatoric stress tensor, such that

$$J_3 = \frac{1}{3}s_{ij}s_{jk}s_{ki}. \tag{5.24}$$

4.3.1 Elastic domain

In the elastic domain, the stress increment is related to the increments of strains and suction through

$$\mathrm{d}\boldsymbol{\sigma} = \boldsymbol{D}^e : \mathrm{d}\boldsymbol{\varepsilon}^e + \boldsymbol{\alpha}_s \mathrm{d}s \tag{5.25}$$

where $\boldsymbol{D}^e$ is the global elastic tensor and $\boldsymbol{\alpha}_s$ is the elastic tensor for suction changes, given respectively by

$$D^e_{ijkl} = 2G\delta_{ik}\delta_{jl} + \left(K - \frac{2}{3}G\right)\delta_{ij}\delta_{kl} \tag{5.26}$$

and

$$\boldsymbol{\alpha}_s = \frac{1}{K_s}\boldsymbol{D}^e : \boldsymbol{I} \tag{5.27}$$

where K and G are the bulk and shear moduli given by Equations (5.4) and (5.15) respectively, and K_s is obtained from Equation (5.11).

4.3.2 Yield surfaces

The elastic domain is bounded by the following yield surface

$$f_{LC} \equiv 3J_2^2 + M_\theta^2 (p + p_s)(p - p_0) = 0 \tag{5.28}$$

where M_θ is the slope of the critical state line, p_s considers the dependence of shear strength on suction through Equation (5.17) and p_0 is the apparent preconsolidation pressure at a suction s according to Equation (5.7).

For three-dimensional stress states, the slope of the critical state line M_θ is a function of the Lode angle θ and determines the shape of the failure surface in the deviatoric plane. Different formulations have been proposed for M_θ (see Drucker & Prager, 1952;

Matsuoka & Nakai, 1974; Lade & Duncan, 1977; van Eekelen, 1980; Sheng *et al.*, 2000, among others). In Figure 5.14, two of them, namely Drucker & Prager (1952) and van Eekelen (1980) criteria, are compared to the Mohr-Coulomb criterion in the deviatoric plane of the principal stress space.

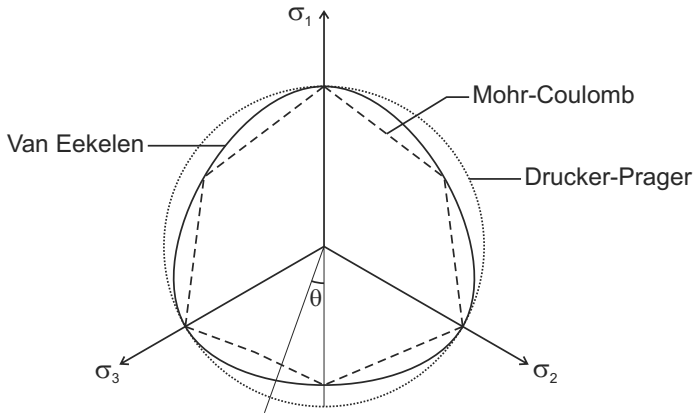

Figure 5.14: Limit surfaces for Mohr-Coulomb, Drucker-Prager and Van Eekelen criteria in the deviatoric plane ($\varphi = 20°$).

In order to approximate the Mohr-Coulomb failure criterion, van Eekelen (1980) model is adopted. Accordingly, the slope of the critical state line M_θ is defined as

$$M_\theta = a\,(1 + b\sin 3\theta)^n \tag{5.29}$$

where a, b and n are parameters. The parameter n is a constant defining the convexity of the failure surface in the deviatoric plane. It is taken equal to -0.229 to ensure convexity of the surface (van Eekelen, 1980; Barnichon, 1998). a and b depend on the triaxial compression and extension friction angles, φ_C and φ_E respectively and are given by

$$a = \frac{r_C}{(1+b)^n} \qquad \text{and} \qquad b = \frac{\left(\frac{r_C}{r_E}\right)^{1/n} - 1}{\left(\frac{r_C}{r_E}\right)^{1/n} + 1} \tag{5.30}$$

where r_C and r_E are the reduced radii for axisymmetric triaxial stress paths of compression and extension defined as

$$r_C = \frac{2\sin\phi_C}{\sqrt{3}\,(3 - \sin\phi_C)} \qquad \text{and} \qquad r_E = \frac{2\sin\phi_E}{\sqrt{3}\,(3 + \sin\phi_E)}. \tag{5.31}$$

Note that even for $\varphi_C = \varphi_E = \varphi$, the reduced radii are different for compression and extension stress paths.

Finally, the expression of the SI yield surface (5.12) remains unchanged.

4.3.3 Flow rule

Under three-dimensional stress state, the flow surface corresponding to the LC surface becomes

$$g_{LC} \equiv \alpha 3J_2^2 - M_\theta^2\,(p + p_s)\,(p_0 - p) = 0. \tag{5.32}$$

5 Implementation in LAGAMINE

The Barcelona Basic Model (BBM) is defined in the form of incremental relationships

$$\tilde{\boldsymbol{\sigma}} = \tilde{\boldsymbol{\sigma}}\left(\dot{\boldsymbol{\varepsilon}}, \boldsymbol{\sigma}, s, \boldsymbol{\kappa}\right) \tag{5.33}$$

where $\tilde{\boldsymbol{\sigma}}$ is the objective Jaumann net stress rate, $\dot{\boldsymbol{\varepsilon}}$ is the rate of deformation, $\boldsymbol{\sigma}$ is the current net stress state, s is suction, and $\boldsymbol{\kappa}$ is a vector of internal plastic variables.

However, the finite element formulation does not require the stress rate, but the stress state at the end of each time step. The relations (5.33) should thus be integrated over each time step. Let us define $\boldsymbol{\sigma}_A$, the stress state at time t. Given known incremental strains $\Delta\boldsymbol{\varepsilon}$ and suction changes Δs over the time step Δt[6], the integration routine aims at integrating the constitutive relationships in order to update the stress state and determine $\boldsymbol{\sigma}_B$ at time $t + \Delta t$. Because the Barcelona Basic Model is highly non-linear, the constitutive model cannot be integrated analytically and numerical integration is necessary.

Different schemes have been used for the integration of constitutive models for unsaturated soils (see Vaunat *et al.*, 2000; Collin *et al.*, 2002; Sheng *et al.*, 2003; Sánchez *et al.*, 2008; Solowski & Gallipoli, 2010; Solowski *et al.*, 2012; Cattaneo *et al.*, 2014, among others). In this thesis, the cutting plane algorithm, proposed by Ortiz & Simo (1986), is extended for the implementation of the Barcelona Basic Model. The algorithm falls within the category of return-mapping algorithms (Simo & Taylor, 1985) and accordingly involves two consecutive steps (Figure 5.15)

1. The stress path is assumed to be elastic and an elastic predictor (or trial stress) $\boldsymbol{\sigma}_E$ is computed. The yield criteria $\boldsymbol{f} = [f_{LC}\ f_{SI}]$ are evaluated at this state. If the stress is located inside the elastic domain, the final state is elastic and equal to the trial stress[7].

2. If the elastic trial stress is violating one or both yield criteria, a plastic return-mapping, called plastic corrector is computed to return the stress state onto the yield surface. In the cutting plane algorithm, an iterative procedure is used to restore the consistency of the mechanical state. At each iteration, the incremental constitutive equations are integrated using an explicit forward Euler scheme.

In this section, the cutting plane algorithm is extended to tackle the following specific features of the Barcelona Basic Model

- The strain rate is a function of both the stress rate and suction rate. A mixed stress-strain control is required. This aspect is discussed in Section 5.1.

[6] The Barcelona Basic Model is rate independent. Consequently, in a purely mechanical analysis, time is a fictitious variable.

[7] As noted by Vaunat *et al.* (2000), the condition $\boldsymbol{f}(\boldsymbol{\sigma}, \boldsymbol{\kappa}) \leq 0$ is not necessarily true on the softening side of the critical state line. In this case, the issue is not only numerical, but is also linked to the non-uniqueness of the problem. Depending on the amount of softening, the evolution problem may indeed become ill-posed and local instabilities (strain localization, critical softening) may take place (Conti *et al.*, 2013). This problem is out of the scope of this thesis. Interested readers may refer to the works of Sulem & Vardoulakis (1995), Chambon *et al.* (1997) and Conti *et al.* (2013).

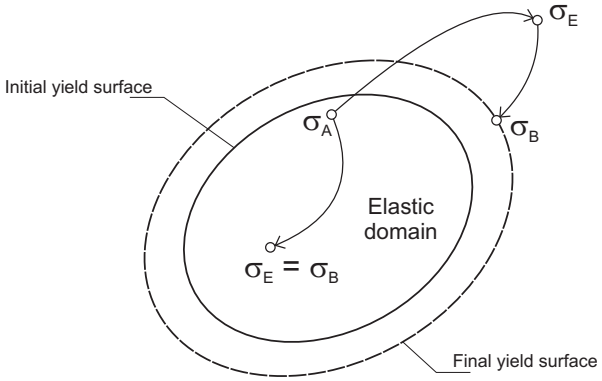

Figure 5.15: Geometric interpretation of return-mapping algorithms: $\boldsymbol{\sigma}_A$ is the initial stress, $\boldsymbol{\sigma}_E$ the elastic predictor and $\boldsymbol{\sigma}_B$ the final (updated) stress.

- The elastic behaviour is non-linear and stress dependent. Using the initial elastic moduli may lead to wrong estimation of the elastic predictor, so that a special consideration is required. This aspect is discussed in Section 5.2.
- The Barcelona Basic Model is characterized by two yield surfaces, namely the Loading-Collapse (LC) curve and the Suction Increase (SI) curve, whose intersection produces a corner. The algorithm has to cope with the activation of one or both plastic mechanisms. This aspect is discussed in Section 5.3.

5.1 Generalized variables and mixed control

In the formulation of the Barcelona Basic Model, stress and suction play a similar role. For algorithmic convenience, Vaunat *et al.* (2000) introduced the following generalized variables

$$\boldsymbol{\sigma}^{*T} = [\sigma_{11}\ \sigma_{22}\ \sigma_{33}\ \sigma_{12}\ \sigma_{13}\ \sigma_{23}\ s] \tag{5.34}$$

and

$$\boldsymbol{\varepsilon}^{*T} = [\varepsilon^{\sigma}_{11}\ \varepsilon^{\sigma}_{22}\ \varepsilon^{\sigma}_{33}\ \varepsilon^{\sigma}_{12}\ \varepsilon^{\sigma}_{13}\ \varepsilon^{\sigma}_{23}\ \varepsilon^{s}_{v}] \tag{5.35}$$

where $\varepsilon^{\sigma}_{ij}$ are the components of strains due to stress changes at fixed suction, and ε^{s}_{v} is the volumetric strain associated to suction changes at fixed stresses, so that

$$\varepsilon_{ij} = \varepsilon^{\sigma}_{ij} + \delta_{ij}\frac{\varepsilon^{s}_{v}}{3} \tag{5.36}$$

and ε_{ij} are the components of total strains.

In `LAGAMINE`, as in most finite element codes, the total strain field and the increment of suction are given as input of the stress integration routine. Based on these inputs, the stress field should be updated while respecting equilibrium equations and the yield criteria. The problem is said to be *strain controlled*.

In our case, integration is not controlled only by the strain field, but also by one stress variable, namely suction. With the generalized variables defined in (5.34) and (5.35),

suction is indeed considered as a stress and the ε_v^s as a strain. However, this suction-dependent strain depends on the value of suction, which is an input of the integration routine. In this case, the problem is said to be *mixed stress-strain controlled* and classical stress integration algorithms should be adapted.

In order to integrate the Barcelona Basic Model, the mixed control procedure proposed by Vaunat *et al.* (2000) is employed. This procedure is based on the partial inversion of the stiffness matrix $\boldsymbol{D}^e$ in order to compute the elastic predictor. The elastic strain increment $\Delta\varepsilon_v^{se}$ is then computed analytically from the imposed suction increment Δs. During elastoplastic corrections, the plastic increment of deformation $\Delta\varepsilon_v^{sp}$ is computed according to the hardening laws of the yield surfaces.

5.2 Elastic predictor

Starting from the stress state $\boldsymbol{\sigma}_A^*$ at the beginning of the step, the stress increment $\Delta\boldsymbol{\sigma}^{*e}$ corresponding to a purely elastic response is computed according to

$$\Delta\boldsymbol{\sigma}_E^{*e} = \boldsymbol{D}^{*e}\big(\boldsymbol{\sigma}_E\big)\Delta\boldsymbol{\varepsilon}^* \tag{5.37}$$

where $\boldsymbol{D}^{*e}$ is the generalized elastic stiffness matrix given by

$$\boldsymbol{D}^{*e} = \begin{bmatrix} K+\frac{4}{3}G & K-\frac{2}{3}G & K-\frac{2}{3}G & 0 & 0 & 0 & -K \\ K-\frac{2}{3}G & K+\frac{4}{3}G & K-\frac{2}{3}G & 0 & 0 & 0 & -K \\ K-\frac{2}{3}G & K-\frac{2}{3}G & K+\frac{4}{3}G & 0 & 0 & 0 & -K \\ 0 & 0 & 0 & 2G & 0 & 0 & 0 \\ 0 & 0 & 0 & 0 & 2G & 0 & 0 \\ 0 & 0 & 0 & 0 & 0 & 2G & 0 \\ 0 & 0 & 0 & 0 & 0 & 0 & K_s \end{bmatrix} \tag{5.38}$$

with K the bulk modulus, K_s an elastic modulus associated to suction changes and G the shear modulus given by

$$K = \frac{(1+e)\,p}{\kappa} \qquad K_s = \frac{(1+e)\,(s+p_{atm})}{\kappa_s} \qquad G = \frac{3\,(1-2\nu)}{2\,(1+\nu)}K. \tag{5.39}$$

Note that, according to these equations, the bulk and shear moduli become zero at zero mean net stress, which can lead to numerical problems. Therefore, as suggested by Sheng *et al.* (2000), a minimum mean net stress p_{min}, below which the bulk and shear moduli are kept constant, is introduced. In this work, a value of $p_{min} = 10$ kPa is used.

In the framework of non-linear elasticity, the stiffness matrix depends on the stress state. Therefore, the integration process, even in the elastic domain, requires iterating. Based on the elastic increment $\Delta\tilde{\boldsymbol{\sigma}}^{*e}$, the elastic predictor $\boldsymbol{\sigma}_E^*$ is obtained

$$\boldsymbol{\sigma}_E^{*(k+1)} = \boldsymbol{\sigma}_A^{*(k)} + \Delta\tilde{\boldsymbol{\sigma}}^{*e(k)} \tag{5.40}$$

where k and $k+1$ are iteration numbers. The convergence criterion verifies that the stress state does not evolve any more. It is described in Section 5.3.3.

5.3 Plastic corrector

As soon as the elastic predictor violates a yield criterion, plastic strains are generated. These plastic strains are characterized by their direction and size. The plastic flow surface enables to compute the direction according to

$$\boldsymbol{n}_{\mathrm{d}\varepsilon^p} = \frac{\partial \boldsymbol{g}}{\partial \boldsymbol{\sigma}^*} \tag{5.41}$$

and the consistency condition enables to determine their amplitude

$$\Delta\varepsilon^{*p} = \Delta\lambda^p \frac{\partial \boldsymbol{g}}{\partial \boldsymbol{\sigma}^*} \tag{5.42}$$

The Barcelona Basic Model is characterized by two yield surfaces, the Loading Collapse (LC) curve and the Suction Increase (SI) curve. Accordingly, the stress integration algorithm has to cope with the activation of one or both plastic mechanisms. The two cases are studied in the next two sections.

5.3.1 Activation of one single plastic mechanism

Let us assume that the yield surface f is activated. In this section, the cutting plane algorithm (Figure 5.16), proposed by Ortiz & Simo (1986), is extended to cope with the stress integration of the Barcelona Basic Model and restore the consistency of the mechanical state. Accordingly, the up-dated stress state $\boldsymbol{\sigma}_B^*$ is determined iteratively by successive applications of Euler forward steps

$$\boldsymbol{\sigma}_B^{*(k+1)} = \boldsymbol{\sigma}_B^{*(k)} + \Delta\boldsymbol{\sigma}^{*p(k+1)} \tag{5.43}$$

where $\Delta\boldsymbol{\sigma}^{*(k+1)}$ is the plastic strain increment. The first elastic predictor is used as starting point of the iterative process.

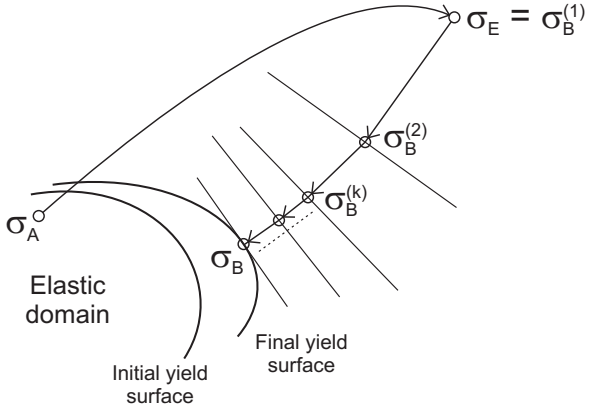

Figure 5.16: Geometric interpretation of the cutting plane algorithm for the case of associative hardening plasticity (modified after Ortiz & Simo, 1986).

The plastic strain increment is computed according to

$$\Delta\boldsymbol{\sigma}^{*p(k+1)} = -\boldsymbol{D}^{*e}\left(\boldsymbol{\sigma}_B^{*(k)}\right) \cdot \Delta\boldsymbol{\varepsilon}^{*p(k+1)} \tag{5.44}$$

where $\Delta\boldsymbol{\varepsilon}^{*p(k+1)}$ is the plastic strain increment at iteration $k+1$, whose value is given by the hardening rule

$$\Delta\boldsymbol{\varepsilon}^{*p(k+1)} = \Delta\lambda^p \frac{\partial g}{\partial \boldsymbol{\sigma}_E^{*(k+1)}} \tag{5.45}$$

with $\Delta\lambda^p$, the plastic multiplier increment and g the flow surface related to the yield surface f.

At every iteration, the yield criterion f is linearised around the current values of trial stresses and state variables, in order to compute the plastic multiplier increment

$$\begin{aligned} f_B^{(k+1)} &= f\left(\boldsymbol{\sigma}_E^{*(k+1)} + \Delta\boldsymbol{\sigma}^{*p(k+1)}, \boldsymbol{\kappa}_E^{(k+1)} + \Delta\boldsymbol{\kappa}^{(k+1)}\right) \\ &= f\left(\boldsymbol{\sigma}_E^{*(k+1)}, \boldsymbol{\kappa}_E^{(k+1)}\right) + \frac{\partial f}{\partial \boldsymbol{\sigma}_E^{*(k+1)}}\Delta\boldsymbol{\sigma}^{*p(k+1)} + \frac{\partial f}{\partial \boldsymbol{\kappa}_E^{(k+1)}}\Delta\boldsymbol{\kappa}^{(k+1)} \end{aligned} \tag{5.46}$$

with

$$\Delta\boldsymbol{\kappa}^{(k+1)} = \frac{\mathrm{d}\boldsymbol{\kappa}}{\mathrm{d}\boldsymbol{\varepsilon}^{p(k+1)}}\Delta\boldsymbol{\varepsilon}^{p(k+1)} = \Delta\lambda^p \frac{\mathrm{d}\boldsymbol{\kappa}}{\mathrm{d}\boldsymbol{\varepsilon}^{p(k+1)}}\frac{\partial g}{\partial \boldsymbol{\sigma}_E^{*(k+1)}} \tag{5.47}$$

using the expression (5.45) of the hardening rule.

By enforcing the consistency condition $f_B^{(k+1)} = 0$, the increment of the plastic multiplier is obtained

$$\Delta\lambda^p = \frac{f\left(\boldsymbol{\sigma}_E^{*(k+1)}, \boldsymbol{\kappa}_E^{(k+1)}\right)}{\dfrac{\partial f}{\partial \boldsymbol{\sigma}_E^{*(k+1)}} \cdot \boldsymbol{D}^{*e} \cdot \dfrac{\partial g}{\partial \boldsymbol{\sigma}_E^{*(k)}} - \dfrac{\partial f}{\partial \boldsymbol{\kappa}_E^{(k+1)}}\dfrac{\mathrm{d}\boldsymbol{\kappa}}{\mathrm{d}\boldsymbol{\varepsilon}^{p(k+1)}}\dfrac{\partial g}{\partial \boldsymbol{\sigma}_E^{*(k+1)}}} \tag{5.48}$$

so that the stress state can be updated using equation (5.43). The different derivatives are presented in Appendix D.

5.3.2 Activation of both LC and SI mechanisms

When both Loading Collapse and Suction Increase surfaces are activated, the consistency conditions should be verified for each mechanism. In our case, the two mechanisms are not independent and

$$\Delta\boldsymbol{\kappa} = \frac{\mathrm{d}\boldsymbol{\kappa}}{\mathrm{d}\varepsilon_v^p}\Delta\varepsilon_v^p = \frac{\mathrm{d}\boldsymbol{\kappa}}{\mathrm{d}\varepsilon_v^p}\left(\Delta\varepsilon_v^{pp} + \Delta\varepsilon_v^{sp}\right) \tag{5.49}$$

where $\Delta\varepsilon_v^{pp}$ is the change in plastic volumetric strain associated to stress changes, and $\Delta\varepsilon_v^{sp}$ is the change in plastic volumetric strain associated to suction changes.

In this case, the system of equations to be solved consist in the consistency condition of the LC mechanism and the hardening law of the SI curve, namely

$$\begin{aligned} &f_{LC}\left(\boldsymbol{\sigma}_E^{*(k+1)}, \boldsymbol{\kappa}_E^{(k+1)}\right) \\ &\quad - \frac{\partial f_{LC}}{\partial \boldsymbol{\sigma}_E^{*(k+1)}} \cdot \boldsymbol{D}^{*e} \cdot \left(\Delta\lambda_{LC}^p \frac{\partial g_{LC}}{\partial \boldsymbol{\sigma}_E^{*(k+1)}} + \Delta\boldsymbol{\varepsilon}_v^{sp}\right) + \frac{\partial f_{LC}}{\partial \boldsymbol{\kappa}_E^{(k+1)}}\frac{\mathrm{d}\boldsymbol{\kappa}}{\mathrm{d}\varepsilon_v^{p(k+1)}}\frac{\partial g_{LC}}{\partial \boldsymbol{\sigma}_E^{*(k+1)}} = 0 \end{aligned} \tag{5.50}$$

$$\Delta s^p = K_s^p \left(\Delta \varepsilon_v^{sp} + \frac{\partial g_{LC}}{\partial \boldsymbol{\sigma}_E^{*(k+1)}} \Delta \lambda_{LC}^p \right). \tag{5.51}$$

The solution to this system of equations is given by

$$\Delta \lambda_{LC}^p = \frac{f_{LC}\left(\boldsymbol{\sigma}_E^{*(k+1)}, \boldsymbol{\kappa}_E^{(k+1)}\right) - \dfrac{\partial f_{LC}}{\partial \boldsymbol{\sigma}_E^{*(k+1)}} \cdot \boldsymbol{D}^{*e} \cdot \Delta \lambda_{LC}^p \dfrac{\partial g_{LC}}{\partial \boldsymbol{\sigma}_E^{*(k+1)}} + \dfrac{\partial f_{LC}}{\partial \boldsymbol{\kappa}_E^{(k+1)}} \dfrac{\mathrm{d}\boldsymbol{\kappa}}{\mathrm{d}\varepsilon_v^{p(k+1)}} \Delta \varepsilon_v^{sp}}{\dfrac{\partial f_{LC}}{\partial \boldsymbol{\sigma}_E^{*(k+1)}} \cdot \boldsymbol{D}^{*e} \dfrac{\partial g_{LC}}{\partial \boldsymbol{\sigma}_E^{*(k+1)}} + \dfrac{\partial f_{LC}}{\partial \boldsymbol{\sigma}_E^{*(k+1)}} \cdot \boldsymbol{D}^{*e} \dfrac{\partial g_{LC}}{\partial \boldsymbol{\sigma}_E^{*(k+1)}}} \tag{5.52}$$

and

$$\Delta \varepsilon_v^p = \Delta \varepsilon_v^{sp} - \frac{\partial g_{LC}}{\partial \boldsymbol{\sigma}_E^{*(k+1)}} \Delta \lambda_{LC}^p. \tag{5.53}$$

5.3.3 Convergence condition

Convergence is reached once that the consistency conditions

$$\boldsymbol{f}\left(\boldsymbol{\sigma}_B^{*(k+1)}, \boldsymbol{\kappa}_B^{(k+1)}\right) \simeq 0 \tag{5.54}$$

are verified. In this work, the convergence condition is written in terms of stress increment between iterations k and $k+1$ such that

$$1 - \mathrm{TOL} \leq \max \left| \frac{\sigma_{ij,B}^{(k+1)}}{\sigma_{ij,B}^{(k)}} \right| \leq 1 + \mathrm{TOL}. \tag{5.55}$$

A value of $\mathrm{TOL} = 10^{-4}$ is chosen. Accordingly, convergence is reached when the maximum relative change in stress between two successive iterations is less than 0.01%. This criterion is independent from the problem and system of unit.

5.4 Substepping procedure

The cutting plane algorithm is known to be first-order accurate. During large loading steps where yielding occurs, difficulties may appear in returning back to the yield surface. In such situations, a possible strategy is to use smaller time steps in the global resolution algorithm. However, this solution is not reasonable since the most restrictive integration point will control the global problem. An alternative approach consists in subdividing locally the current time step into several sub-steps (which can be different for each integration point).

A sub-stepping procedure is used in the integration of the Barcelona Basic Model within `LAGAMINE`. A time step Δt is divided into NINTV sub-steps δt

$$\delta t = \frac{\Delta t}{\mathrm{NINTV}} \tag{5.56}$$

and strain and suction are assumed to vary linearly on the time step, so that

$$\delta\varepsilon_{ij} = \frac{\Delta\varepsilon_{ij}}{\text{NINTV}} \qquad \delta s = \frac{\Delta s}{\text{NINTV}} \tag{5.57}$$

where Δ denotes changes on the global time step, and δ changes on the local sub-step.

The value of NINTV may either be constant, or computed according to the current normal strain rate.

$$\text{NINTV} = \min\left\{1 + \frac{\dot{\varepsilon}_N \Delta t}{\text{DIV}}, 1500\right\} \tag{5.58}$$

where DIV is a parameter of the law (a value of 5.10^{-3} generally provides good results) and $\dot{\varepsilon}_N$ is the norm of the strain rate defined as

$$\dot{\varepsilon}_N = \sqrt{\dot{\varepsilon}_{ij}\dot{\varepsilon}_{ij}}. \tag{5.59}$$

Accordingly, for each integration point, the number of sub-steps is computed according to the strain rate: the number of sub-steps is higher where the strains are important, which allows a more accurate integration of the model.

5.5 Verification

The verification process consists in controlling that a computational model accurately represents the underlying mathematical model. In order to verify the stress integration of the Barcelona Basic Model, the response of the model along various stress paths were compared to the corresponding analytical solutions within the elastic domain. Additionally, the numerical responses over the whole stress range were compared to the ones provided by Alonso *et al.* (1990). The complete verification is provided in Appendix **??**.

6 Experimental validation

The Barcelona Basic Model is validated against experimental data on bentonite-based materials from the literature. Three materials are considered, namely Febex bentonite, Kunigel V1 bentonite and a mixture of MX-80 bentonite and sand. The model parameters are presented in Table 5.1.

Material	ρ_{di} (Mg/m^3)	κ	κ_s	$\lambda(0)$	p_0^* (MPa)	p_c (MPa)	r	ω (MPa^{-1})
Febex	1.70	0.008	0.075	0.12	0.4	0.02	0.55	0.25
Kunigel V1	1.36	0.014	0.046	0.051	0.232			
MX-80/sand mixture	1.67	0.025	0.073	0.12	1.40	0.01	0.8	0.09

Table 5.1: Parameters of the Barcelona Basic Model for Febex bentonite, Kunigel V1 bentonite and a mixture of MX-80 bentonite and sand.

6.1 Febex bentonite

Four controlled-suction oedometer tests on Febex bentonite were performed by Lloret *et al.* (2003). The samples of Febex bentonite were compacted at a dry density of 1.70 ± 0.02 Mg/m^3 and a water content varying between 12.9 and 14.2%. For each sample, the test consisted in

- reaching a given suction under a vertical stress of 0.1 MPa;
- loading the material under constant suction;
- wetting the material up to a suction of 0.1 MPa.

The different stress paths followed in the oedometer tests are represented in Figure 5.17 in the suction versus vertical net stress plane. The suction values reached during the first wetting path are 127 MPa (A), 14 MPa (B), 4.1 MPa (C) and 0 corresponding to full saturation (D). The loading path was then performed up to a vertical stress of 9 MPa, except for the fully saturated sample (A–D–D' path in Figure 5.17) which was loaded up to 5 MPa. These four tests were used to calibrate the Barcelona Basic Model whose parameters are given in Table 5.1. Note that as triaxial tests and shear tests were not available, the parameters for the deviatoric behaviour were assumed: $\nu = 0.35$, $c(0) = 0.1$ MPa, $k = 0.046$ and $\varphi = 15°$.

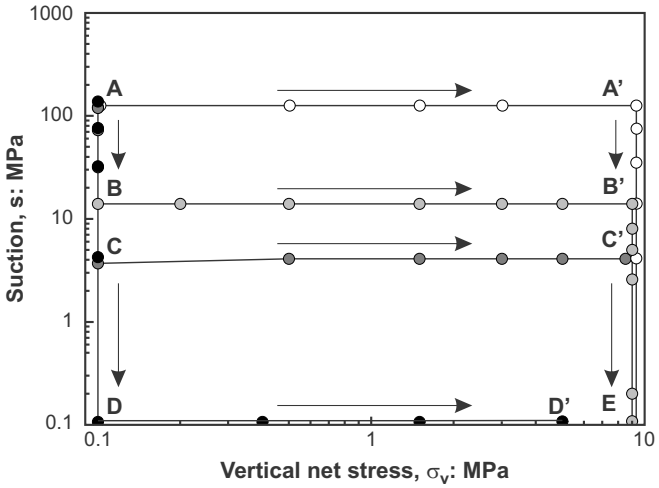

Figure 5.17: Generalized stress paths followed in four controlled-suction oedometer tests performed by Lloret *et al.* (2003) on Febex bentonite.

Figure 5.18 compares the numerical predictions with the experimental results for the first wetting path and the loading path under constant suction. Upon wetting under a vertical stress of 0.1 MPa, the samples experience swelling. The lower the suction value reached upon wetting, the higher the welling strain. As highlighted in Figure 5.18, a good agreement is obtained between the modelled swelling strain and the experimental data. Once that the target suction value is reached, the different samples are loaded under constant suction. Figure 5.18 shows that the decrease in the apparent preconsolidation pressure with decreasing suction is well captured by the model. In addition, both experimental and numerical results show an increase in the plastic slope with decreasing suction.

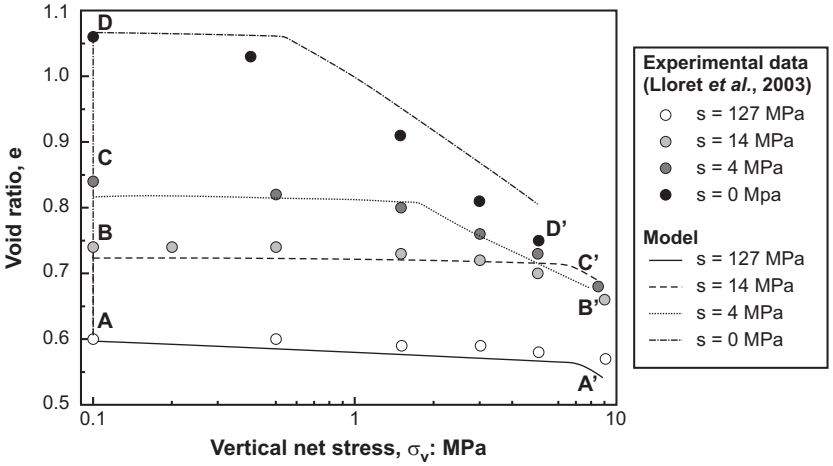

Figure 5.18: Controlled-suction oedometer tests on Febex bentonite. Comparison between experimental data (Lloret *et al.*, 2003) and model responses on loading paths.

Figure 5.19 presents the stress paths followed by the different samples in the $(\ln s - e)$ plane. Important changes in void ratio are observed upon wetting under vertical stress (paths A–B, A–C and A–D). On the other hand, changes in void ratio are significantly smaller when the vertical stress is higher (paths A'–A" and B'–B") due to important collapse strain. As shown in Figure 5.19, numerical results are in good agreement with the experimental data, except for the stress path A'–A" corresponding to a wetting path starting from a suction of 127 MPa and under a constant vertical stress of 9.1 MPa. Indeed, for this path, the model predicts swelling strains that are not observed experimentally, contrary to the path A–B (wetting path to a suction of 14 MPa at a vertical stress of 0.1 MPa). Yet, this sample is characterized by the lowest initial dry density (1.68 Mg/m^3) which is likely to result in a lower swelling capacity. As a matter of fact, if the slope of the reversible wetting–drying line for changes in suction, κ_s, is decreased from 0.075 to 0.065, the void ratio of the saturated sample changes from 0.70 to 0.64 for an observed value of 0.59.

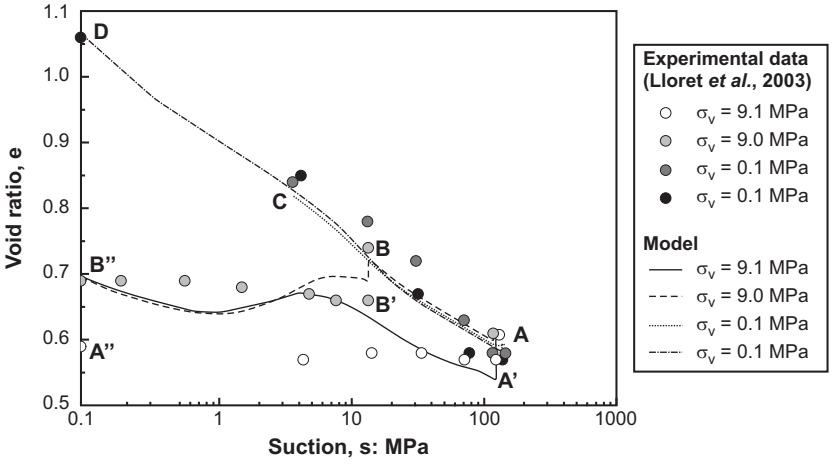

Figure 5.19: Controlled-suction oedometer tests on Febex bentonite. Comparison between experimental data (Lloret *et al.*, 2003) and model responses on wetting paths.

6.2 Kunigel V1 bentonite

Romero (2011) investigated the mechanical behaviour of Kunigel V1 bentonite. Samples of Kunigel V1 bentonite were compacted at a dry density of 1.36 Mg/m^3 and a water content of 35%. The parameters of the Barcelona Basic Model for the saturated material (Table 5.1) are determined along a saturation path at a vertical stress of 10 kPa, followed by a loading path up to 1 MPa and finally an unloading path. Then, Romero (2011) investigated the effects of mean net stress and suction on the shear behaviour of compacted Kunigel V1 bentonite. Triaxial tests were carried out at two different suction values (0.3 and 0.5 MPa) and three different confining stresses (0.3, 0.4 and 0.5 MPa).

Figures 5.20(a) and 5.20(b) presents the experimental data together with the model response. A clear increase in shear strength is observed for increasing confining pressures and increasing suctions. This feature is well captured by the Barcelona Basic Model if the shear strength parameters of the Barcelona Basic Model are calibrated using the experimental data. In particular, the friction angle φ is found to be equal to 13.9° and the coefficient k ruling the increase of cohesion with suction is taken equal to 0.046, considering a null cohesion under saturated conditions.

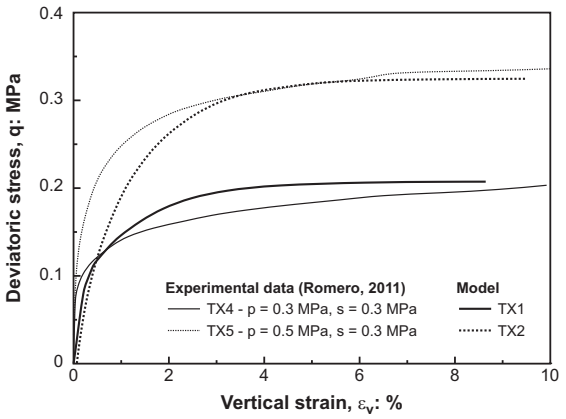

(a) Shearing at $s = 0.3$ MPa.

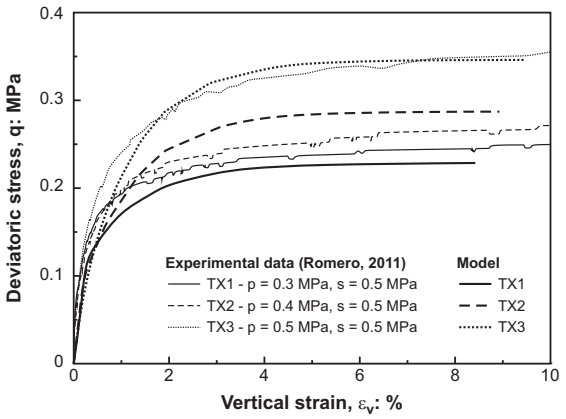

(b) Shearing at $s = 0.5$ MPa.

Figure 5.20: Controlled-suction triaxial shear tests on Kunigel V1 bentonite. Comparison between experimental data (Romero, 2011) and model responses.

6.3 MX-80 bentonite/sand mixture

Wang *et al.* (2013c) investigated the mechanical behaviour of a compacted mixture of MX-80 bentonite and sand, with respective proportions of 70/30 in dry mass. The samples were compacted at a dry density of 1.67 Mg/m^3 and a water content of 11%. Controlled suction oedometer tests were then performed at three different suction values, namely 4.2, 12.6 and 38 MPa. For each sample, the test consisted in

- reaching a given suction under a vertical stress of 0.1 MPa;
- loading the material under constant suction up to a vertical stress of 50 MPa;

- unloading the material under constant suction.

Figures 5.21 present the experimental data together with the model response for the three controlled-suction oedometer tests. The model succeeds in reproducing the swelling strain developed upon wetting, as well as the compressive strain developed upon loading. Moreover, the increase in preconsolidation pressure with increasing suction is well captured by the model.

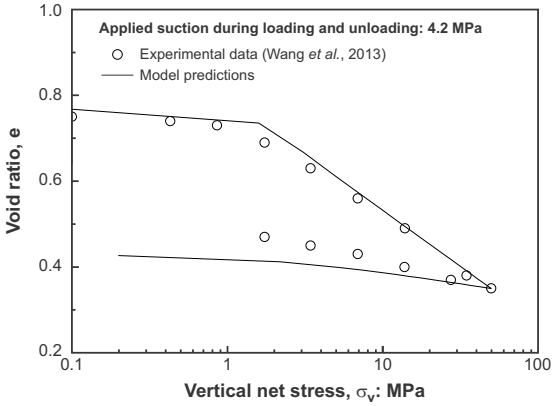

(a) Loading and unloading at a suction $s = 4.2$ MPa.

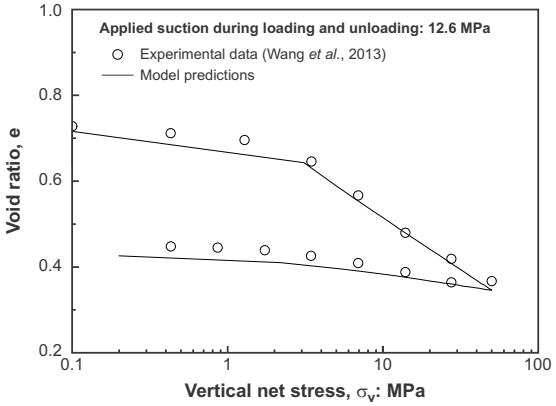

(b) Loading and unloading at a suction $s = 12.6$ MPa.

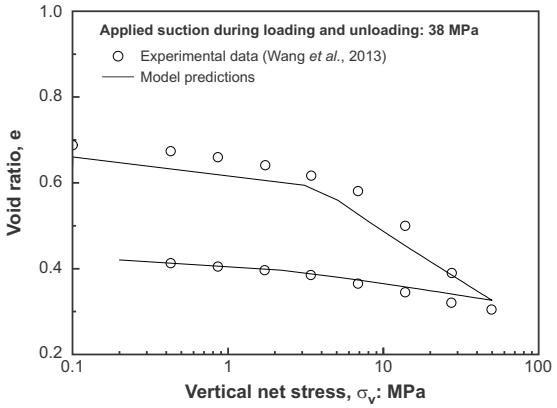

(c) Loading and unloading at a suction $s = 38$ MPa.

Figure 5.21: Controlled-suction oedometer tests on a MX-80 bentonite/sand mixture compacted at a dry density $\rho_d = 1.67$ Mg/m^3. Comparison between experimental data (Wang *et al.*, 2013c) and model responses.

7 Limitations of the Barcelona Basic Model and new formulation

In the previous section, the capacity of the Barcelona Basic Model to reproduce the behaviour of bentonite-based materials along simple stress paths was highlighted. However, an important limitation of the original Barcelona Basic Model is the difficulty to satisfactorily reproduce swelling pressure tests (Gens & Sánchez, 2014). Indeed, the use of the BBM with the previously calibrated parameters results in a significant overestimation of the swelling pressure of the materials.

In order to overcome this shortcoming, the approach adopted by the Barcelona research group consists in introducing suction and/or stress dependent elastic parameters κ and κ_s (see for instance Delahaye & Alonso, 2002; Vaunat & Gens, 2005; Zandarin *et al.*, 2011; Sánchez *et al.*, 2012b). Accordingly, the slope of the unloading–reloading line for changes in mean net stress is supposed to vary according to

$$\kappa(s) = \kappa_0 \left[1 - \alpha_1 s - \alpha_2 \ln\left(\frac{s + u_{atm}}{u_{atm}}\right)\right] \tag{5.60}$$

with κ_0 the elastic stiffness in saturated conditions, α_1 and α_2 model parameters and u_{atm} the atmospheric pressure. On the other hand, the following law is used to describe the dependency of the slope of the reversible wetting–drying line on the mean net stress

$$\kappa_s(p) = \kappa_{s,0} \left[1 + \alpha_p \ln\left(\frac{p}{p_{ref}}\right)\right] \exp\left(\alpha_s s\right) \tag{5.61}$$

with $\kappa_{s,0}$, α_p and α_s model parameters and p_{ref} the reference pressure.

In order to evidence the limitations of the BBM in reproducing the development of swelling pressure upon wetting, swelling pressure tests performed on Febex bentonite are modelled using the parameters determined by Sánchez *et al.* (2012b). Sánchez *et al.* (2012b) used the laws defined in Equations (5.60) and (5.61). Figures 5.22 present the evolution through time of the swelling pressure developed upon hydration. In addition, the evolution of the injected volume of water is also represented. As highlighted by Figures 5.22, Equations (5.60) and (5.61) are essential to predict reasonable (and physical) swelling pressure values. However, the introduced relationships are generally calibrated by back-analysis of swelling pressure tests without any experimental evidence nor clear physical meaning of the parameters. The reasons for the limitations of the BBM in reproducing the swelling pressure are investigated in this section.

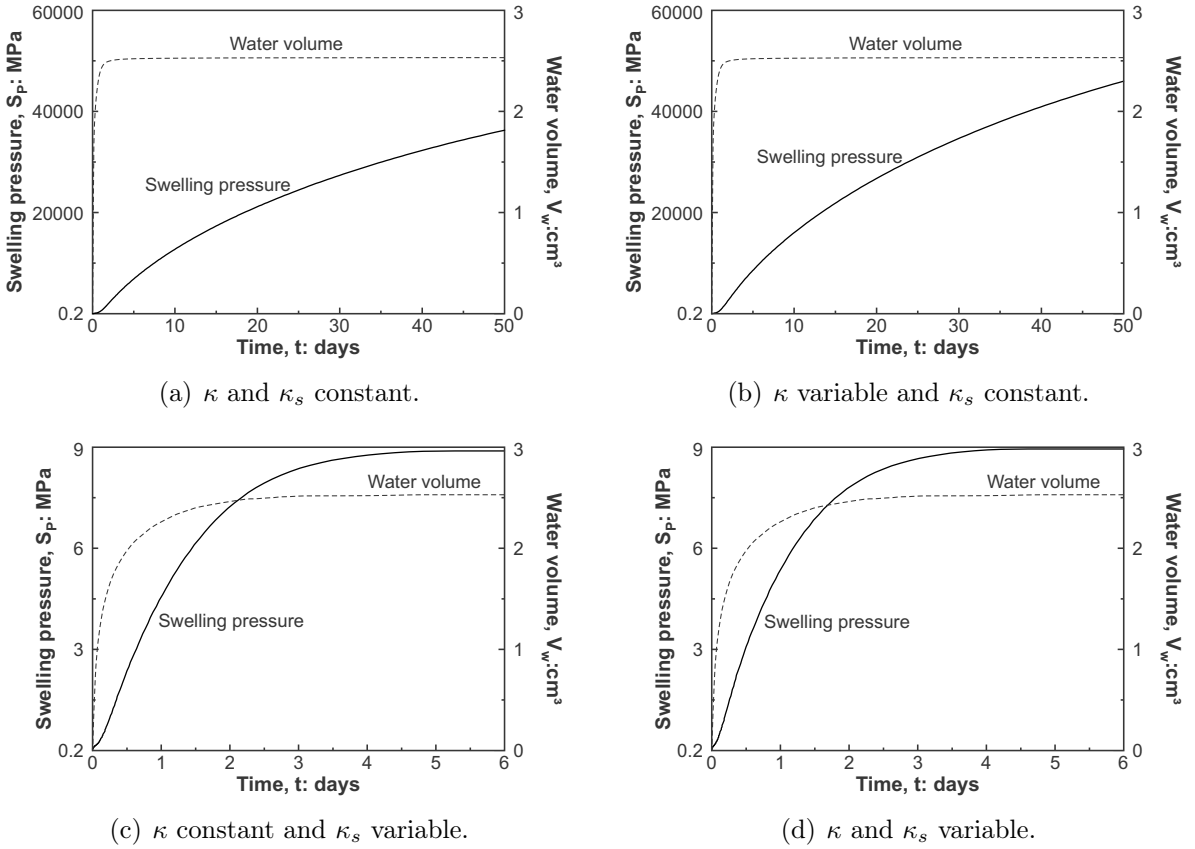

(a) κ and κ_s constant.

(b) κ variable and κ_s constant.

(c) κ constant and κ_s variable.

(d) κ and κ_s variable.

Figure 5.22: Influence of Equations (5.60) and (5.61) on the development of swelling pressure.

The Barcelona Basic Model is formulated in terms of net stress and suction and for a null suction, the model coincides with the Modified Cam-Clay Model. Accordingly, the BBM implicitly assumes that saturation is achieved when suction comes to zero and predicts swelling strains as far as the suction is positive, regardless the saturation state of the material. However, bentonite-based materials are characterized by an important air-entry value and the material is able to sustain important suction values without desaturating. Consequently, along a saturation path, the material is saturated before reaching zero suction.

As explained in Chapter 2, swelling of compacted bentonites is associated with the intrusion of water within the interlayer space. Consequently, along a wetting path, no further increase of the swelling pressure with decreasing suction is to be expected once that the material is saturated. Unfortunately, very few experimental data are available concerning the mechanical behaviour of clays at low suction values and it is worth mentioning the work of Agus *et al.* (2013). Agus *et al.* (2013) investigated the swelling pressure development of Calcigel bentonite and a mixture of Caligel and sand upon suction decrease. Figure 5.23 shows that below around 1 MPa of suction, the swelling pressure is almost constant.

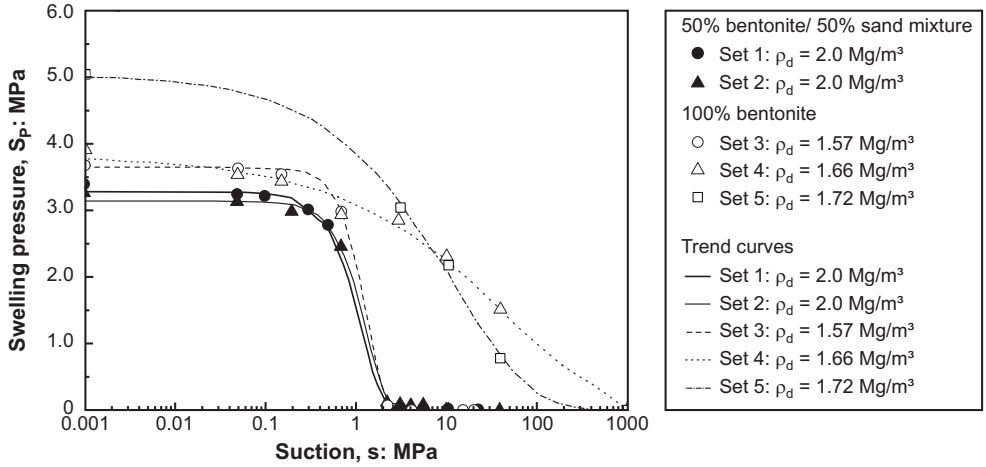

Figure 5.23: Swelling pressure development upon suction decrease. Experimental data on a mixture of Calcigel bentonite and quartz sand with a respective proportion of 50/50 in dry mass, and on pure Calcigel bentonite (Agus *et al.*, 2013).

Figure 5.24 presents the water retention curve obtained along a wetting path and under constant volume conditions by Agus *et al.* (2013). The air-entry value of the different materials is of the order of 0.5 to 1 MPa and corresponds approximately to the threshold suction beyond which the swelling pressure does not evolve anymore.

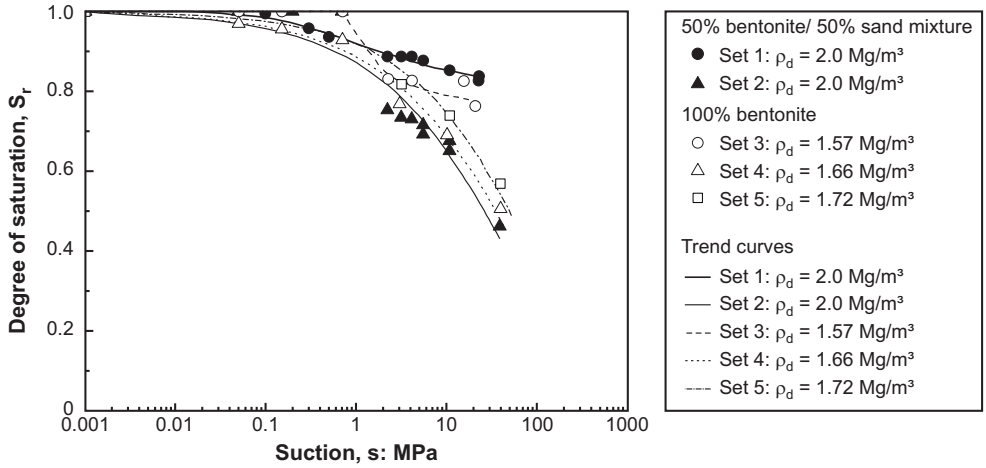

Figure 5.24: Water retention curves of a mixture of Calcigel bentonite and quartz sand with a respective proportion of 50/50 in dry mass, and on pure Calcigel bentonite compacted to different dry densities (Agus *et al.*, 2013). Wetting path under constant volume conditions.

Based on these experimental observations and our comprehension of the swelling mechanisms, a threshold suction, below which the sample does not experience swelling strains, is introduced in the Barcelona Basic Model (Figure 5.25). It yields

$$\kappa_s = 0, \qquad \text{if } s < s^* \tag{5.62}$$

where s^* is a threshold suction which may be assimilated to the air-entry suction s_{AE}.

However, the water retention curve developed in Chapter 4 does not have a clear definition of the air-entry value. The criteria $s < s^*$ in Equation (5.62) is therefore not adequate. A definition in terms of the degree of saturation is therefore adopted

$$\kappa_s = 0, \qquad \text{if } S_r > S_r^* \tag{5.63}$$

where S_r^* is a threshold degree of saturation. For $S_r^* = 1$, the original Barcelona Basic Model is recovered.

As discussed in Chapter 2, the physical state of water in the vicinity of the charged clay layers differs from the one of bulk water. Due to the strong physicochemical interactions between water and the clay particles, the density of adsorbed water is significantly higher than that of bulk water and may reach values higher than 1.4 Mg/m^3. Accordingly, when the degree of saturation is calculated with the density of bulk water ($\rho_w = 1$ Mg/m^3), values higher than 1 are systematically obtained close to saturation. The exact suction below which a material is saturated is therefore uncertain. Therefore threshold degrees of saturation around 0.95–0.98 are realistic values to be used in numerical models[8].

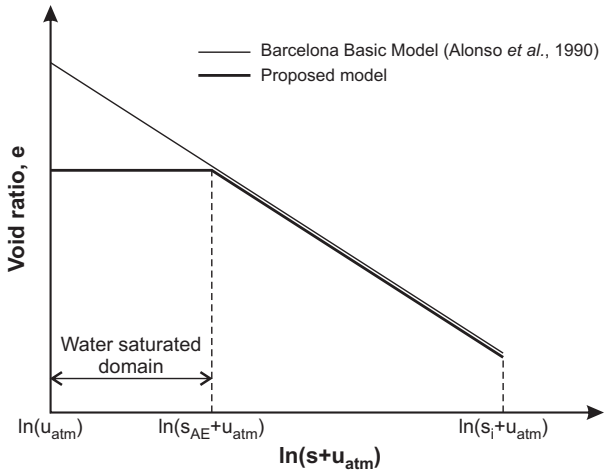

Figure 5.25: Evolution of void ratio along a wetting path under constant mean net stress. Original formulation of the Barcelona Basic Model (Alonso *et al.*, 1990) and proposed model.

8 Experimental validation of the new model

In the previous section, a new extension of the Barcelona Basic Model was suggested to better reproduce the swelling behaviour of compacted bentonites saturated under confined

[8]In order to overcome the issue related to the water density, water densities higher than 1 Mg/m^3 are generally used, or experimental data are reinterpreted using a water density higher than 1 Mg/m^3 in order to find a degree of saturation equal to 1 for a null suction.

conditions. In order to highlight the contribution of the new model, a swelling pressure test is modelled. The parameters considered in the analysis are those determined for the mixture of MX-80 bentonite and sand in Section 6.3 and the threshold degree of saturation S_r^* is chosen equal to 0.96. Indeed the swelling pressure of this material was determined in the framework of the Esdred (Gatabin *et al.*, 2006) and Bentogaz 2 (Dridi *et al.*, 2013) projects.

A sample with an initial dry density of 1.78 Mg/m^3 and an initial water content of 12.4% is considered. The corresponding initial suction of 27.9 MPa is determined from the water retention model developed in Chapter 4. In addition, an initial isotropic stress state is considered with an initial mean net stress of 0.1 MPa. The test that is modelled consists in progressively saturating the material by increasing the water pressure from -27.8 MPa to atmospheric pressure (0.1 MPa). The evolution of the swelling stress is then recorded along this wetting path. For information purpose, the swelling pressure determined experimentally by Gatabin *et al.* (2006) and Dridi *et al.* (2013) is of the order of 6.4 MPa.

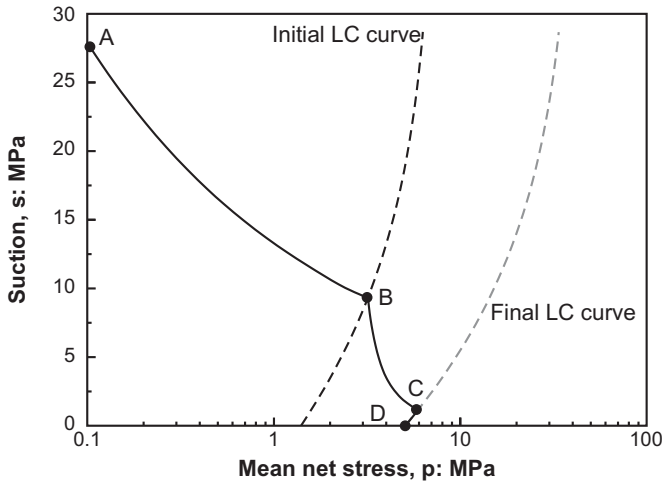

Figure 5.26: Typical stress path in the $(p-s)$ plane followed by a sample wetted under confined conditions.

The behaviour of the tested sample being only volumetric, the results are analysed in the $(p-s)$ plane (Figure 5.26). Let us denote A the initial state of the sample. As hydration of the bentonite sample proceeds, the stress state progressively moves from A to D according to the following sequence:

- **From A to B**: since deformation of the sample is prescribed by the confined conditions, hydration yields an increase of the mean net stress. From A to B, the increase in mean stress p with suction s occurs within the elastic domain and follows the analytical solution

$$p\left(s\right) = p_A \left(\frac{s_A + u_{atm}}{s + u_{atm}} \right)^{\frac{\kappa_s}{\kappa}} \tag{5.64}$$

  where p_A and s_A are the initial mean net stress and suction respectively. Note that

Equation (5.64) is obtained after integrating

$$\mathrm{d}\varepsilon_v = \mathrm{d}\varepsilon^e_{vp} + \mathrm{d}\varepsilon^e_{vs} = \frac{\kappa}{1+e}\frac{\mathrm{d}p}{p} + \frac{\kappa_s}{1+e}\frac{\mathrm{d}s}{s+u_{atm}} = 0. \tag{5.65}$$

- **B**: the stress path reaches the Loading-Collapse yield surface.
- **From B to C**: further decrease in suction comes along with hardening of the yield surface. Owing for the addition plastic component $\mathrm{d}\varepsilon^p_{vp}$ in Equation (5.65), the increase in mean net stress with decreasing suction is less important than in the elastic domain.
- **C**: the threshold degree of saturation S^*_r is reached ($S_r = S^*_r$). The swelling pressure is equal to 5.92 MPa.
- **From C to D**: further decrease in suction does not produce any elastic deformation due to suction changes, so that $\mathrm{d}\varepsilon^e_{vs} = 0$. However, the apparent preconsolidation pressure is still decreasing with decreasing suction. Accordingly, in order to maintain the constant volume conditions without violating the yield criterion, a decrease in mean net stress is observed. For $s = 0$, the swelling pressure is equal to 5.25 MPa. Note that this decrease in swelling pressure between C and D can be avoided by considering that the apparent preconsolidation pressure p_0 is constant for $S_r \geq S^*_r$.

  For the sake of comparison, the swelling pressure predicted by the Barcelona Basic Model is equal to 16.48 MPa which is significantly higher than the 6.4 MPa measured experimentally.

Finally, Gatabin *et al.* (2006) determined the swelling pressure of the compacted mixture as a function of the mixture dry density. Samples were compacted to different dry densities and water contents and saturated under constant volume conditions in order to determine their swelling pressure. The experimental results are presented in Figure 5.27.

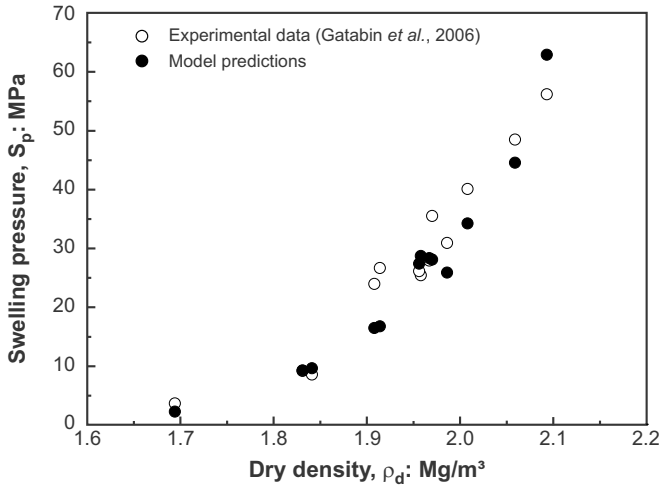

Figure 5.27: Dependency of the swelling pressure on the dry density. Comparison between experimental results (Gatabin *et al.*, 2006) and model redictions.

The sole effect of void ratio in the mechanical model does allow reproducing the increase of swelling pressure observed for increasing dry density. As a matter of fact, according to Equation (5.64), the swelling pressure developed in the elastic domain is independent of the material dry density. In order to model the different swelling pressure tests, the following assumptions are made:

- Knowing the initial water content and the dry density of the mixture, the initial suction is computed using the water retention model developed in Chapter 4. The parameters of the water retention model are given in Table 4.1.
- The position of the Loading-Collapse curve is affected by compaction. It is assumed that only the preconsolidation pressure for saturated conditions p_0^* is modified. Its value is computed so that the point $(p_0 - s)$, where p_0 is the compaction pressure and s is the suction computed thanks to the water retention model, belongs to the LC curve.
- All other parameters (see Table 5.1) remain constant.

Figure 5.27 presents the experimental data together with the model predictions. With a limited number of assumptions, the model reproduces satisfactorily the dependency of the swelling pressure on the initial dry density. The model is thus able to interpret within a unified framework the most important stress path regarding the use of bentonite as engineered barrier.

9 Model parameters: summary

As an extension of the Barcelona Basic Model (Alonso *et al.*, 1990), the model developed in this chapter requires the definition of ten parameters. These parameters include both elastic parameters and plastic and hardening parameters. A summary is presented below.

The elastic behaviour of the material is characterized by the three following parameters

- κ, the elastic compressibility coefficient for changes in mean net stress or, alternatively, the bulk modulus K defined as

$$K = \frac{1+e}{\kappa} p \tag{5.66}$$

- G, the shear modulus, which may be chosen to be constant or to derive from the bulk modulus K by considering a constant Poisson's ratio ν according to

$$G = \frac{3\,(1-2\nu)}{2\,(1+\nu)} K \tag{5.67}$$

- κ_s, the elastic compressibility coefficient for changes in suction or, alternatively, the bulk modulus for changes in suction K_s defined as

$$K_s = \frac{1+e}{\kappa_s} \left(s + u_{atm}\right). \tag{5.68}$$

In the elastic domain, κ and κ_s control the volumetric behaviour of the material while G governs the deviatoric behaviour.

The seven plastic and hardening parameter are

- $\lambda(0)$, the slope of the saturated virgin consolidation line
- r, a parameter defining the minimum soil compressibility in

$$\lambda(s) = \lambda(0)\left[(1-r)\exp(-\omega s) + r\right] \tag{5.69}$$

- ω, a parameter controlling the soil stiffness in Equation (5.69)
- p_0^*, the preconsolidation pressure for saturated state
- p_c, a reference pressure controlling the shape of the LC curve

$$\left(\frac{p_0}{p_c}\right) = \left(\frac{p_0^*}{p_c}\right)^{\frac{\lambda(0)-\kappa}{\lambda(s)-\kappa}} \tag{5.70}$$

- k, a parameter describing the increase of cohesion with suction according to

$$c(s) = c(s) + ks \tag{5.71}$$

- φ, the friction angle.

Finally, the proposed mechanical model considers one additional parameter compared to the Barcelona Basic Model, namely

- S_r^*, the threshold degree of saturation beyond which the volumetric deformation associated with suction changes is null.

10 Conclusions

In the context of deep geological repository for radioactive waste, the swelling capacity of compacted bentonites is one of the most important properties of these materials. Indeed, swelling of the bentonite barrier should ensure an excellent sealing of the technological gaps and fractures, and a good contact between the different materials of the disposal. Yet, from a constitutive point of view, the important swelling strain developed by bentonite-based materials upon wetting under unconfined conditions, as well as the swelling pressure observed under confined conditions, cannot be reproduced using conventional mechanical models. Accordingly, advanced constitutive models should be developed.

In this chapter, the main and relevant experimental observations on the mechanical behaviour of compacted bentonite-based materials are first reviewed. While a relatively large amount of laboratory tests have been performed to determine the swelling pressure of various bentonites compacted at different dry densities, laboratory tests carried out

along well-defined hydromechanical stress paths are still limited. This observation motivated the selection of the Barcelona Basic Model (BBM) developed by Alonso *et al.* (1990) as a *starting point* for modelling the behaviour of compacted bentonites. Indeed, the capacity of the model to reproduce the main features of the behaviour of unsaturated soils is proven. In addition, the model parameters can be relatively easily determined from laboratory tests.

The complete formulation of the Barcelona Basic Model is presented and the contributions of the model are highlighted. In order to study boundary-value problems, the BBM is implemented in the finite element code `LAGAMINE` using an efficient return-mapping algorithm. The model is then validated against experimental data on three different bentonite-based materials. The modelling of various tests shows that the model successfully tackles the effects of suction on the mechanical behaviour of the model. However, the Barcelona Basic Model is not able to satisfactorily reproduce the swelling pressure developed by bentonite samples upon water saturation.

Owing for this observation and a good understanding of the swelling mechanisms at the microscopic scale, a new extension of the original Barcelona Basic Model is proposed. In particular, the new model considers the fact that there is a domain of full saturation with non-null suction. In this domain, the deformations due to suction changes are assumed to be nonexistent. Accordingly, by introducing a threshold degree of saturation beyond which $\kappa_s = 0$, the new model is able to reproduce the swelling pressure of compacted bentonites. The performance of the new model are highlighted by modelling swelling pressure tests on a bentonite-based material compacted to different dry densities and water contents.

Chapter 6

Water transfer mechanisms and permeability evolution

1 Introduction

A proper estimation of the time required to ultimately saturate bentonite buffers under *in situ* conditions is an important stake for the safe design of the repository. Indeed, engineered barriers are designed to work in (almost) fully saturated conditions, meaning that the bentonite buffer should be saturated to perform properly (Sellin & Leupin, 2013). In Chapter 3, the formulation of a classic multiphase flow model for unsaturated porous media was presented. While such a formulation successfully reproduces the flow of water and gas in granular and low-activity clay materials, it has revealed some limitations in the case of very active clays such as bentonites. In particular, the application of such conventional flow model has often resulted in underestimations of the time required to reach full saturation of the barrier (Gerard, 2011; Sánchez *et al.*, 2012b).

This chapter explores the potential role of bentonite microstructure (and its changes along hydromechanical stress paths) on the hydration kinetics of bentonite buffers. As presented in Chapter 2, hydration of bentonite comes along with swelling of the clay particles and important structural changes of the material which are believed to affect the flow properties of the buffer, and in particular its permeability. The stake is thus to better understand the effects of microstructural changes on the hydration kinetics and then, to extend the multiphase flow formulation to take them into account. This chapter is organized as follows. The permeability of saturated bentonites is first considered. Experimental techniques for its determination are presented, together with available experimental data on compacted bentonite-based materials. The factors affecting the saturated permeability are evidenced and existing permeability models are discussed. A new model for the evolution of permeability with the macrostructural void ratio is then presented. In a second step, the permeability of partially saturated bentonites is considered. As for the saturated permeability, experimental techniques, available experimental data and models are presented. Finally, an infiltration test on a compacted bentonite-based material is modelled using the extended flow law. The contributions of the new formulation are highlighted.

2 Water permeability in saturated conditions

2.1 Experimental techniques

Experimental techniques to determine the saturated water permeability K_w in the laboratory are classified into:

- **Direct methods**
  The permeability is directly computed by interpreting experimental data on water flow in terms of Darcy's law. More precisely, saturation of a soil sample is first carried out in an oedometer, triaxial or constant-volume cell. Once that the sample is fully saturated, a pressure gradient is imposed between both sides of the sample. This gradient may either be kept constant (constant-head method) or not (variable-head method). Inflow and outflow water fluxes are then measured, and the permeability of the material is computed according to Darcy's law (3.38). Note that the experimental determination of permeability in compacted bentonites is a critical issue because of the very small fluxes that need to be measured.

- **Indirect methods**
  Indirect methods are based on the analysis of experimental data obtained upon consolidation of the saturated material. For each loading step, the water permeability is computed according to
  $$K_w = \frac{c_v \rho_w g}{E_{oed}} \tag{6.1}$$
  where c_v is the coefficient of consolidation, ρ_w is the water density, g is the gravity acceleration, and E_{oed} is the oedometric modulus. Note that the coefficient of consolidation c_v is determined from the compression – time curve by representing, for each applied stress, the vertical strain in a logarithmic plot of time.

The initial state of the material is different in direct and indirect methods. In direct techniques, the sample is compacted in unsaturated conditions prior to testing. On the other hand, indirect methods consider compression from a slurry state. Marcial *et al.* (2002) and Wang *et al.* (2013c) compared both techniques of permeability determination. As shown in Figure 6.1, the two methods provide consistent results on a mixture of MX-80 bentonite and sand, Kunigel V1 bentonite and Fourges clay.

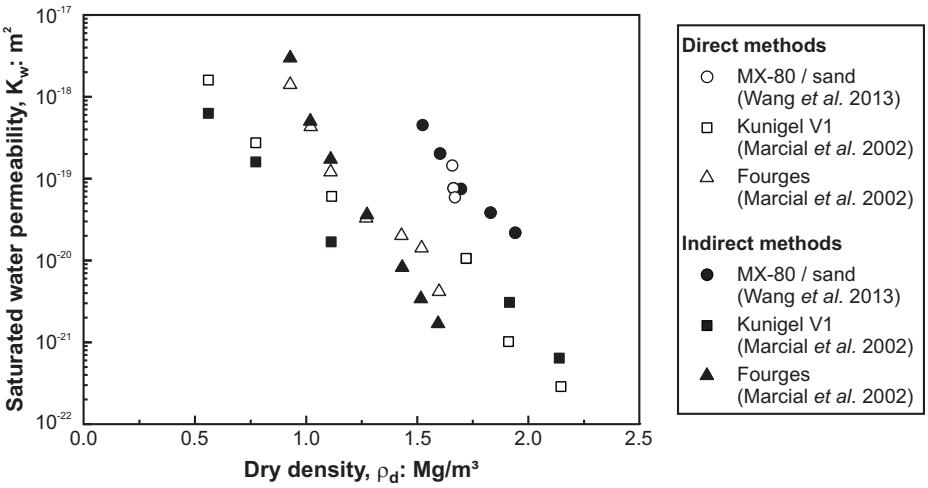

Figure 6.1: Water permeability of a mixture of MX-80 bentonite and sand (Wang *et al.*, 2013c), Kunigel V1 bentonite and Fourges clay (Marcial *et al.*, 2002). Comparison between direct and indirect techniques for permeability measurement.

2.2 Experimental data

Water permeability was determined by Lloret & Villar (2007) on Febex bentonite; by Lajudie *et al.* (1994) on FoCa7 clay; by Sun *et al.* (2014) on GMZ bentonite; by Dixon *et al.* (1996), JNC (2000) and Marcial *et al.* (2002) on Kunigel V1 bentonite; and by Pusch *et al.* (1990); Pusch (2001), Börgesson *et al.* (1996), Rodwell (1999), Karnland *et al.* (2006), Villar (2002) and Imbert *et al.* (2004) on MX-80 bentonite, among others.

Experimental data show that the permeability of compacted bentonite-based materials is affected by a number of factors that are either intrinsic to the material composition or depend on the compaction conditions. These factors are presented in the next subsections.

2.2.1 Influence of the material composition

The factors affecting the water permeability are evidenced by comparing the permeability of different materials. They include the:

- **Montmorillonite content**
  Experimental data show that the higher the montmorillonite content, the lower the permeability of bentonites. According to Lee & Shackelford (2005) and Dananaj *et al.* (2005), the sensitivity of permeability on the montmorillonite content is a consequence of the important swelling capacity of montmorillonite which reduces the volume of macropores upon saturation. Similarly, Dixon *et al.* (1987) compared the water permeability of illite, kaolinite and smectite compacted to different dry densities. The experimental data show that the minerals with low activity (i.e. illite and kaolinite) have similar permeability values while, for a same density, the permeability of more active minerals (such as smectites) is significantly lower.

- **Nature of the exchangeable cations**
  The hydraulic conductivity increases with increasing valency of the exchangeable

cation (Rao & Mathew, 1995; Dananaj *et al.*, 2005; Ahn & Jo, 2009).

- **Sand content**
  The permeability of different bentonite-based mixtures was determined by Borgesson *et al.* (2003), Prikryl *et al.* (2003), Komine (2004), Villar (2005), Gatabin *et al.* (2006), Cui *et al.* (2008), Sun *et al.* (2009) and Komine (2010), among others. Figure 6.2(a) presents the permeability of bentonite/sand mixtures with different proportions of sand. The experimental data show that a higher sand content results in lower water permeability. In addition, the influence of the sand fraction on the permeability is all the more important that the dry density of the mixture is high.

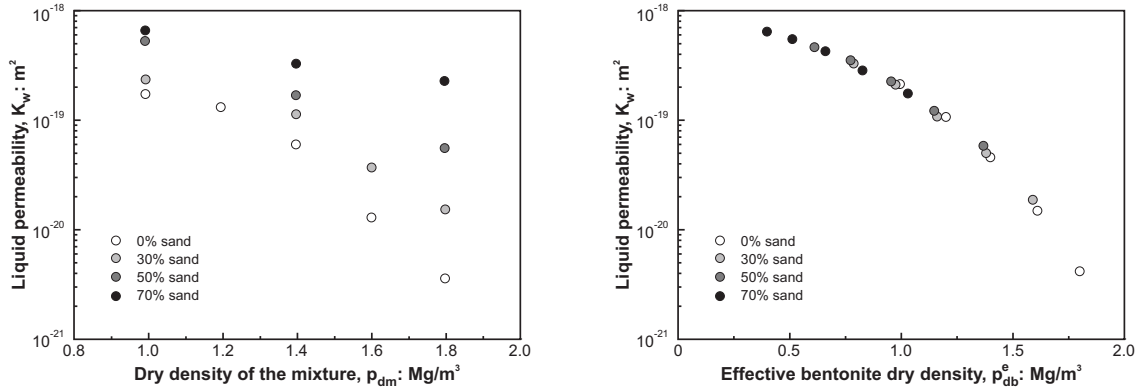

(a) Dependence of water permeability on the dry density of the mixture.

(b) Dependence of water permeability on the effective bentonite dry density.

Figure 6.2: Effect of sand content on the water permeability of bentonite-based materials. Experimental data on mixtures of Kunigel V1 bentonite and sand (JNC, 2000).

In order to interpret all data within a single framework, Dixon *et al.* (1985) defined the effective bentonite dry density ρ^e_{db} of the mixture such as

$$\rho^e_{db} = \frac{m_{sb}}{\Omega_v + \Omega_{sb}} = \frac{f_b \rho_{sm}}{e + f_b \frac{\rho_{sm}}{\rho_{sb}}} \tag{6.2}$$

where m_{sb} is the mass of bentonite solid particles, Ω_v is the porous volume, Ω_{sb} is the volume of bentonite solid particles, e is the void ratio and ρ_{sb} is the density of the bentonite solid particles. The mass fraction of bentonite f_b in the mixture is defined as

$$f_B = \frac{m_{sb}}{m_s} \tag{6.3}$$

where m_s is the total mass of solids. On the other hand, the equivalent solid density of the mixture ρ_{sm} is given by

$$\rho_{sm} = \left(\frac{f_b}{\rho_{sb}} + \frac{1 - f_b}{\rho_{ss}} \right)^{-1} \tag{6.4}$$

with ρ_{ss}, the density of the sand solid grains. Figure 6.2(b) shows that the effective bentonite dry density enables normalizing all experimental data. Accordingly, water permeability becomes a function of the effective bentonite dry density with lower permeabilities observed for higher ρ^e_{db}.

2.2.2 Influence of dry density

Figure 6.3 presents the variation of the saturated water permeability with dry density, for five reference bentonites. For a given material, experimental data show that the water permeability decreases with increasing dry density. These results are interpreted as a consequence of structural changes and reduced porosity through which flow occurs, as the dry density increases. As can be observed in Figure 6.3, the water permeability varies over more than one order of magnitudes over the range of dry densities considered in applications related to the disposal of radioactive waste.

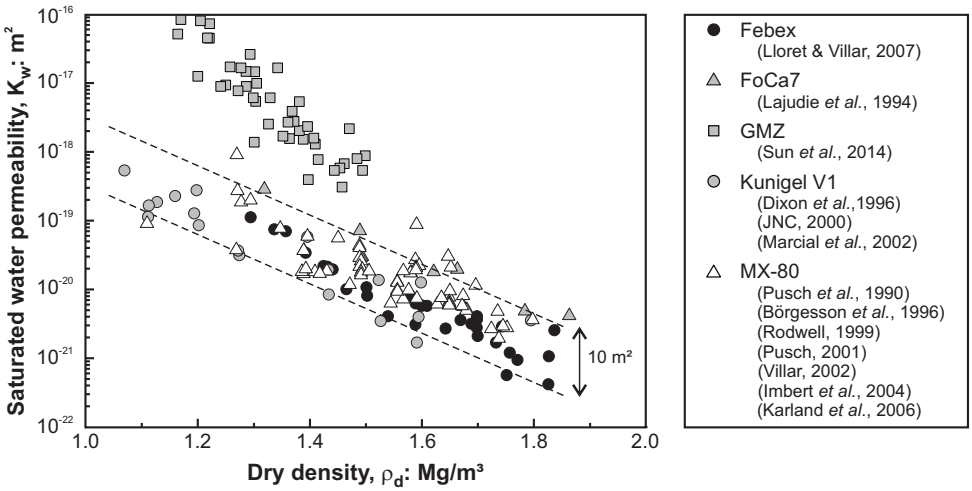

Figure 6.3: Variation of saturated water permeability with dry density. Experimental data for five reference bentonites.

On the other hand, for a given dry density, the permeability of all bentonites, except GMZ bentonite, lies within one order of magnitude, as had already been highlighted by Dixon *et al.* (1987) on sodium bentonites. This relatively low dispersion of experimental data should be compared to the variability of permeabilities of one material. For the sake of comparison, Figure 6.4 gathers the permeability determined on MX-80 bentonite by various authors. One may observe that the data are also spread over one order of magnitude for a given dry density. This dispersion is likely to be due to different mineralogical compositions of the material and different experimental protocols, including compaction procedure.

2.2.3 Influence of the initial water content

Haug & Wong (1992) showed that the initial water content has no significant influence on the saturated water permeability of compacted bentonites.

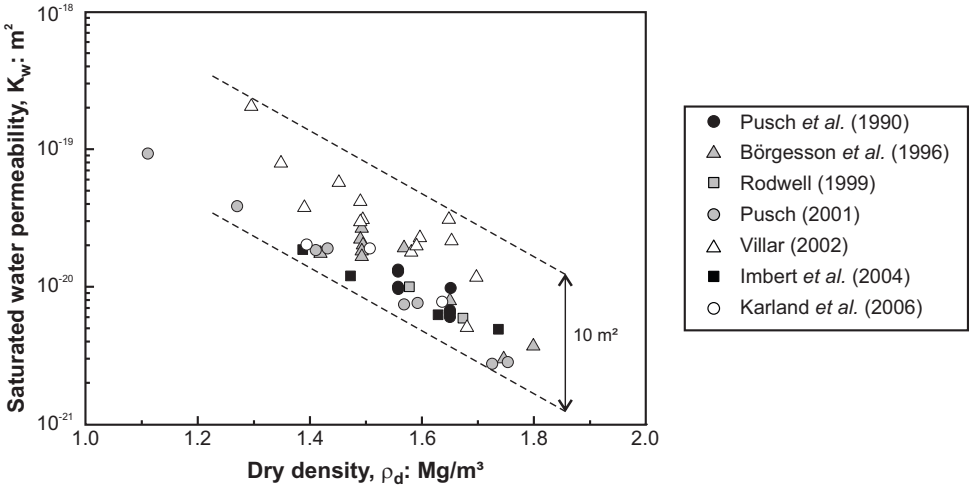

Figure 6.4: Variation of saturated water permeability with dry density. Experimental data for MX-80 bentonite.

2.3 Constitutive models

2.3.1 Formulation for single-porosity porous media

The dependency of water permeability on porosity ϕ or dry density ρ_d has traditionally been modelled using empirical or semi-empirical laws. One of the most famous models is the Kozeny-Carman relationship (Chapuis & Aubertin, 2003). It reads

$$K_w = K_{w0} \frac{\phi^3}{(1-\phi)^2} \frac{(1-\phi_0)^2}{\phi_0^3} \tag{6.5}$$

where K_{w0} is a reference permeability measured at a reference porosity ϕ_0. This law has been widely applied to compacted bentonite-based materials (see Vaunat & Gens, 2005; Akesson *et al.*, 2009; Chen *et al.*, 2009; Gens *et al.*, 2009; Sánchez *et al.*, 2012a, among others). However, Villar (2004b), Dupray *et al.* (2011) and Dupray *et al.* (2013) found out that the original Kozeny-Carman law was not able to reproduce the change is saturated permeability associated to changes in porosity. Indeed, the decrease of permeability with decreasing porosity is higher than predicted by Equation (6.5). Accordingly, the original formulation is sometimes extended to

$$K_w = K_{w0} \frac{\phi^N}{(1-\phi)^M} \frac{(1-\phi_0)^M}{\phi_0^N} \tag{6.6}$$

where N and M are model parameters.

2.3.2 Formulation for double-porosity porous media

Owing to its simplicity, the Kozeny-Carman law does not consider the double structure nature of compacted bentonite-based materials, although the microstructure of bentonites is likely to affect the hydraulic properties. Accordingly, empirical laws relating water permeability to the macrostructural void ratio e_M or macroporosity ϕ_M have been proposed.

In particular, Gens *et al.* (2011) and Sánchez *et al.* (2012b) used

$$K_w = K_{w0} \exp\left[B\left(\phi_M - \phi_{M0}\right)\right] \tag{6.7}$$

with ϕ_{M0} a reference macroporosity for which the intrinsic permeability is K_{w0}.

On the other hand, Romero (2013) extended the Kozeny-Carman equation to account for double-structure of compacted clayey materials and its evolution. In particular, Romero (2013) suggested to express the water permeability as a function of the macrostructural void ratio e_M according to

$$K_w = A \frac{e_M^B}{(1 + e_M)} \tag{6.8}$$

where A and B are model parameters.

2.3.3 Proposed formulation

In this work, the Kozeny-Carman law is extended to better account for the structure of compacted bentonites. The natural extension of the model yields

$$K_w = K_{w0} \frac{\phi_M^N}{\left(1 - \phi_M\right)^M} \frac{\left(1 - \phi_{M0}\right)^M}{\phi_{M0}^N} \tag{6.9}$$

where K_{w0} is a reference permeability measured on a material with a reference macroporosity ϕ_{M0}. According to this relationship, the lowest the macroporosity, the lowest the permeability. However, the use of macroporosity is not suited for expansive soils such as bentonites. Let us remind the definition of the macroporosity ϕ_M

$$\phi_M = \frac{\Omega_{vM}}{\Omega} \tag{6.10}$$

where Ω_{vM} is the volume of the macropores and Ω is the total volume. As underlined by Equation (6.10), the macroporosity is not a measure of the macropores volume, but a measure of their relative volume. Therefore, a formulation in terms of macroscopic void ratio, similar to the one of Romero (2013), is proposed. It reads

$$K_w = K_{w0} \frac{e_M^N}{\left(1 - e_M\right)^M} \frac{\left(1 - e_{M0}\right)^M}{e_{M0}^N} \tag{6.11}$$

where K_{w0} is a reference permeability measured on a material with a reference macroscopic void ratio e_{M0}. The model parameters are determined for a mixture of MX-80 bentonite and sand using experimental data from Gatabin *et al.* (2006): $K_{w0} = 2.5 \times 10^{-20}$ m^2 for $e_{M0} = 0.31$, $N = 2$ and $M = 0.2$ (Figure 6.5).

By using Equation (6.11), one implicitly assumes that water flow takes place essentially in the macropores of the material. Although this hypothesis cannot be directly checked using experimental techniques, some evidences tend to validate it. For instance, the gas permeability determined under unsaturated conditions is up to eight orders of magnitude higher than the water permeability measured under saturated conditions (Villar & Lloret,

2001). This difference in water and gas permeabilities for a same dry density can be explained by the significantly different structures of the material under dry and saturated conditions (Villar, 2004b). Indeed, while the diameter of macropores accessible to gas in dry conditions may reach 10 μm, their diameter is up to three orders of magnitude smaller in saturated conditions (for the same dry density). This decreases in the macropores size is a direct consequence of clay particles and aggregates swelling, as explained in Chapter 2, and is likely to affect fluid flow.

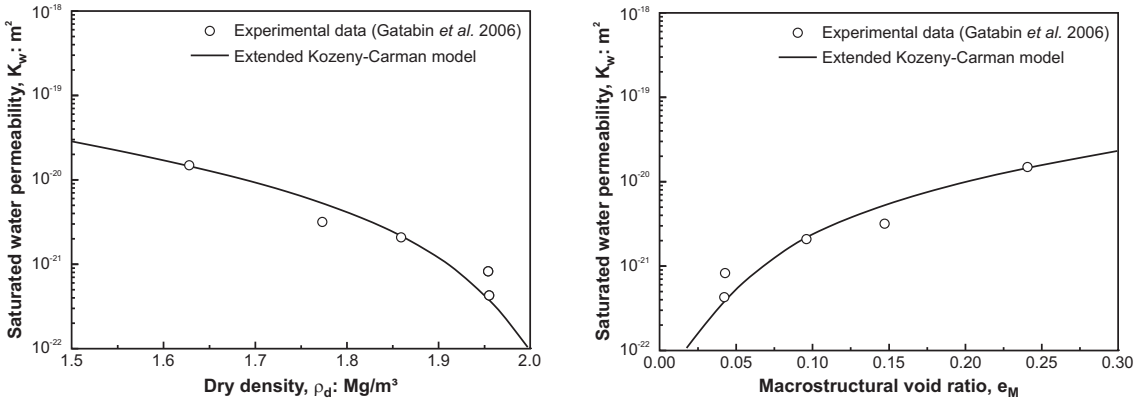

(a) Water permeability as a function of dry density.

(b) Water permeability as a function of the macrostructural void ratio.

Figure 6.5: Variation of saturated permeability with dry density. Comparison between experimental data on a mixture of MX-80 bentonite and sand (Gatabin *et al.*, 2006) and model response.

Finally, Equation (6.11) introduced an additional hydromechanical and multi-scale coupling in the hydromechanical formulation developed in this PhD work. Indeed, the saturated water permeability is now influenced by the mechanical deformation through the void ratio e and by microstructure evolution through e_m (the macrostructural void ratio e_M being computed as $e_m = e - e_m$).

3 Water permeability in unsaturated conditions

3.1 Experimental techniques

The experimental determination of permeabilities in unsaturated conditions is very delicate. The water pressures to be measured are indeed negative and generally very high. Existing experimental techniques include the:

- **Steady-state regime method**
  The test consists in measuring permanent fluxes within a soil when a relative humidity gradient is imposed under constant temperature. However, when imposing on both sides of the sample the relative humidity gradient, liquid and vapour fluxes occur and some difficulties to separate both arise. The permeability determined using this method is thus a global permeability (Loiseau, 2001).

- **Instantaneous profile method**
  In the instantaneous profile method (Daniel, 1982; Cui *et al.*, 2008), a cylindrical sample is wetted from one extremity and the evolution of relative humidity is monitored over time at different heights of the sample. To this end, thermocouple psychrometers are generally used in clays. The obtained results may be plotted in terms of isochrones of suction and water content at different times, knowing the wetting branch of the water retention curve. In order to determine the permeability of the partially saturated porous media, the hydraulic gradient i and the water flux q_w must be computed. The slope of the relative humidity curves at each point provides the water gradient. Using the water retention curve, the relative humidity profile can be converted into a water content profile. Then, considering the profiles at different times, the water flux can be computed as

$$q_w = A\frac{\int_{y_i}^{H}\theta_{t+\Delta t}\mathrm{d}y - \int_{y_i}^{H}\theta_t\mathrm{d}y}{\Delta t} \tag{6.12}$$

  where A is the surface area of the sample face, H is the sample height and θ is the volumetric water content. Knowing the evolution of both hydraulic gradient and water flux with time, the permeability at different degrees of saturation is obtained as (Daniel, 1982)

$$k_w = -\frac{1}{A}\frac{q_w}{\frac{1}{2}\left(i_t + i_{t+\Delta t}\right)}. \tag{6.13}$$

3.2 Experimental data

Experimental data on compacted bentonite-based materials are limited. In granular materials and low-activity clays, experimental data show that the water permeability decreases as the material becomes drier. For example, Figure 6.6 presents the evolution of the water permeability of the Callovo-Oxfordian claystone as a function of the degree of saturation. The dependency of the permeability on the degree of saturation has been widely explained by a decrease in the cross section responsible for water flow as the materials desaturates.

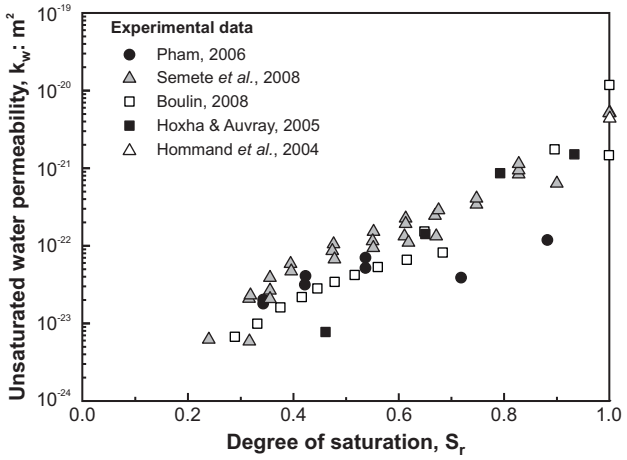

Figure 6.6: Water permeability a a function of the degree of saturation. Experimental data on the Callovo-Oxfordian claystone.

Cui *et al.* (2008) used the instantaneous profile method to investigate the permeability of a partially saturated mixture of Kunigel bentonite and sand. Figure 6.7 presents the evolution of the computed water permeability as a function of suction. The following observations are made from Figure 6.7:

- The permeability does not monotonically decrease with increasing suction. Upon hydration, the hydraulic conductivity decreases first, and after a certain suction threshold, increases.
- The change in permeability is not unique. The curves obtained from sensors located at different heights from the water inlet are different.

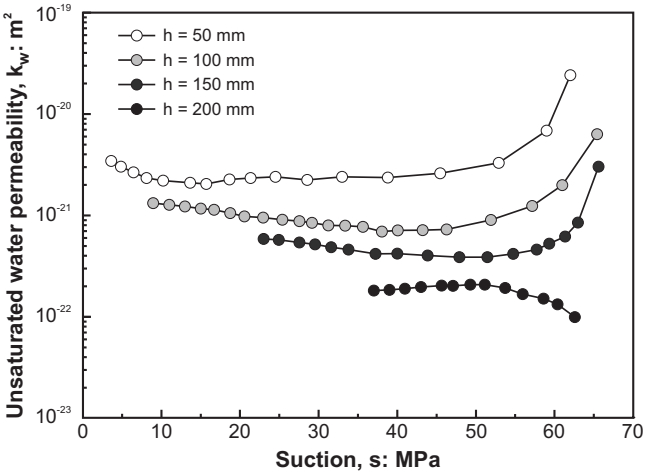

Figure 6.7: Liquid permeability versus suction for a compacted mixture of MX-80 bentonite and sand (Wang *et al.*, 2013a). h is the distance from the wetting face.

These results have been explained by important structural changes experienced by the material upon wetting. In addition, the difference in permeabilities depending on the distance from the wetting face results from different stress paths followed by the material at different heights of the sample. Indeed, as hydration is not uniform within the sample (water is injected from one face), swelling is not uniform over the sample height neither. Similar results were obtained by Ye *et al.* (2009) on GMZ bentonite and Wang *et al.* (2013a) on a mixture of MX-80 bentonite and sand.

3.3 Constitutive models

Experimental data show that the permeability in unsaturated conditions depends on the degree of saturation of the porous medium. Accordingly, the water permeability is generally expressed as

$$k_w = K_w k_{rw}\left(S_r\right) \tag{6.14}$$

where K_w is water permeability in saturated conditions and k_{rw} is the relative permeability which is a function of the degree of saturation. The relative permeability is defined as the ratio between the unsaturated permeability (for a given degree of saturation and

soil structure) and the saturated permeability. It takes a value of 0 for theoretically completely dry conditions and 1 in saturated conditions.

The water relative permeability is often expressed as a power law of the degree of saturation S_r such that

$$k_{rw} = (S_r)^{n_k} \tag{6.15}$$

where n_k is a model parameter, typically considered to vary between 2 and 5. Figure 6.8 highlights the influence of this parameter on the relative permeability function.

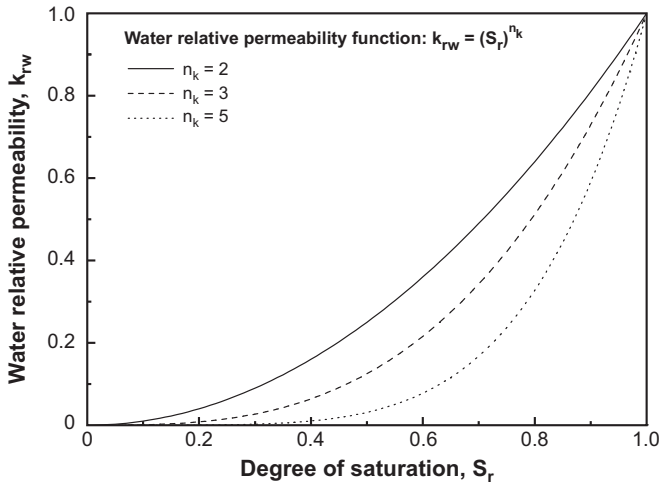

Figure 6.8: Evolution of the relative permeability with the degree of saturation. Influence of the parameter n of the power law.

Note that, in non-swelling porous materials, the relative permeability takes into account the change in cross section responsible for water flow with the amount of water in the porous material. In the case of compacted bentonites, the structure is continuously evolving upon wetting. Yet, in this PhD thesis, structural changes are exclusively taken into account in the saturated water permeability.

4 Numerical modelling of an infiltration test

4.1 Description of the test

Wang *et al.* (2013a) carried out an infiltration test on a compacted mixture of MX-80 bentonite and sand, with respective proportions of 70/30 in dry mass. The specimen (250-mm high and 50 mm in diameter) is compacted to a dry density of 1.67 Mg/m^3 and an initial water content of 11%. In order to favour homogeneity, the sample is compacted in 5 layers of 50 mm each. After compaction, the sample is introduced in a cylindrical cell for the infiltration test. Note that the infiltration cell has the same diameter as the sample. The two ends of the infiltration cell are tightly closed to maintain constant-volume conditions during infiltration. Four relative humidity sensors are installed every 50 mm along the sample height (h = 50, 100, 150 and 200 mm from the wetting end), as shown

in Figure 6.9. The initial relative humidity of the specimen is measured equal to 65 MPa.

Water supply is done at atmospheric pressure from the bottom base. The top cover allows air expulsion but limited water evaporation (a deflated balloon-shaped membrane is used to cover the air outlet and air was released regularly to keep atmospheric pressure). Finally, synthetic water with a similar chemical composition to that of the pore water of the Callovo-Oxfordian claystone from the Andra Underground Research Laboratory in Bure, France, is used.

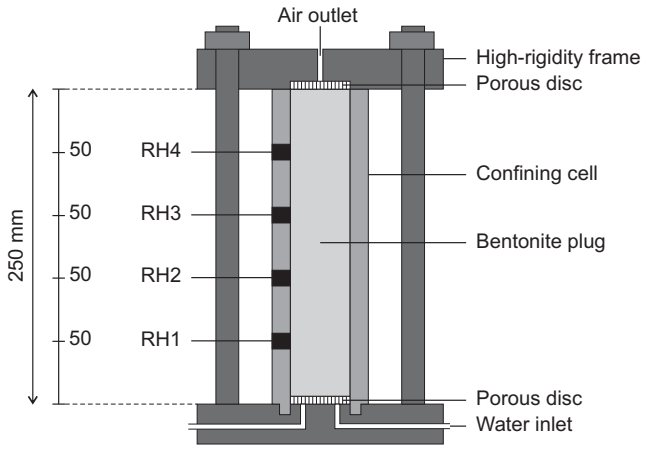

Figure 6.9: Schematic representation of the experimental set-up used for the infiltration test (Wang *et al.*, 2013a). RH1 to RH4 denote the relative humidity sensors.

4.2 Features of the analysis

A hydromechanical model of the infiltration test is realized. The analysis assumes one-dimensional axisymmetric conditions around the longitudinal axis of the sample (Figure 6.10). The soil sample is meshed with 50 eight-noded isoparametric elements. Despite the compaction process, the bentonite sample is assumed homogeneous. An initial isotropic stress state of 0.1 MPa is considered in the whole sample, the effects of gravity being neglected. On the other hand, the initial suction in the sample is equal to 65 MPa, corresponding to water pressures of -64.9 MPa (the gas pressure is assumed constant and equal to atmospheric pressure). Finally, water injection in the bentonite sample is modelled by imposing the water pressures at the bottom of the sample equal to 0.1 MPa. No water flow is allowed at the top of the sample.

The hydromechanical analysis is performed using the water retention model developed in Chapter 4, the model parameters being given in Table 4.1. On the other hand, the mechanical behaviour of the bentonite sample is reproduced by using the Barcelona Basic Model with its proposed extension (see Chapter 5). Water permeability is a function of the macroscopic void ratio according to Equation (6.11). For the investigated material, the model parameters are determined using experimental data from Gatabin *et al.* (2006): $K_{w0} = 2.5 \times 10^{-20}$ m^2 for $e_{M0} = 0.31$, $N = 2$ and $M = 0.2$ (Figure 6.5). Finally, the exponent n_k of the relative permeability law (6.15) is calibrated by best-fitting the

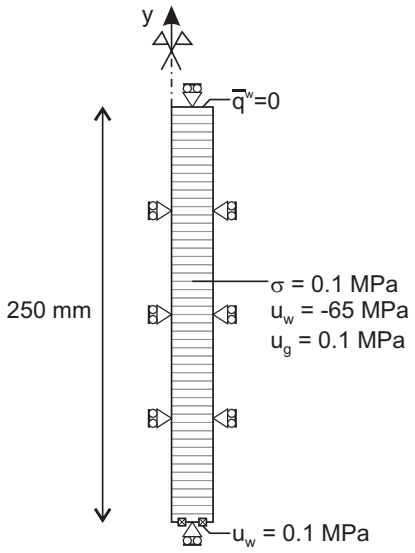

Figure 6.10: Axisymmetric finite element mesh, with initial and boundary conditions, adopted for the analysis of the infiltration test. The y axis is the axis of symmetry of revolution.

responses of two relative humidity sensors, namely RH2 and RH3, located at distances of 100 and 150 mm from the injection front. Consequently, the model is validated by comparing the experimental and numerical results for the two other sensors, namely RH1 and RH4. A value of $n_k = 3.4$ is used in the reference analysis. Its influence on the model response is discussed in the next section.

4.3 Numerical results

Figure 6.11 presents the evolution through of the relative humidity measured at different heights of the sample. The numerical results are compared to the experimental results.

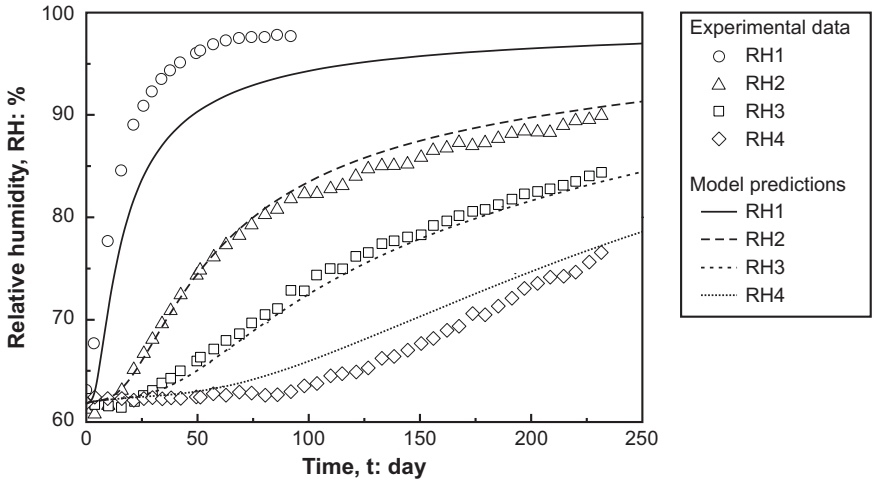

Figure 6.11: Evolution of relative humidity during water infiltration. Comparison between experimental data (Wang *et al.*, 2013a) and model predictions.

As soon as hydration starts, an increase in relative humidity is detected by the sensor RH1, located at a distance of 50 mm from the wetting face. As water injection proceeds, the sensors RH2, RH3 and RH4 located at increasing distances from the bottom progressively exhibit an increase in relative humidity. As observed in Figure 6.11, the hydration rate is all the more important that the considered point is situated close to the injection water face. The progressive increase of relative humidity measured by the different sensors is well captured by the numerical model. However, a somewhat weaker agreement is obtained for RH1 which is located the closest from the injection front. Indeed, the very fast reaction of this sensor is not well reproduced numerically. This discrepancy of the model could be explained by the assumed equilibrium between the microstructural and macrostructural levels. In the constitutive model, it is indeed assumed that swelling strains develop as soon as suction decreases. However, it is likely that at the beginning of injection, the open structure and important porosity of the material let water flow relatively easily through the material, swelling of the structure being then somewhat delayed. While this phenomenon may be neglected at the time scale of the geological repository, it could lead to some discrepancy on the short time. On the other hand, as the infiltration cell is different from the compaction cell, the initial contact between the bentonite sample and the infiltration cell could be locally imperfect and the interface could act a preferential path for water flow. In any case, the difference between the observed and modelled results should be balanced by the accuracy of the relative humidity sensors which is generally of the order of 1 to 3 %.

In order to better understand the coupled hydromechanical processes taking place in the bentonite column, the numerical results are analysed under the form of profiles through the column. Figures 6.12(a) and 6.12(b) show the evolution through time of the suction and degree of saturation profiles in the bentonite column. Water injection yields a progressive decrease of suction and increase of the degree of saturation in the sample, these changes being the most significant at the bottom of the sample where water is injected. After 250 days of injection, saturation of the sample is not achieved (Figure 6.12(b)) and the overall degree of saturation is about 0.66.

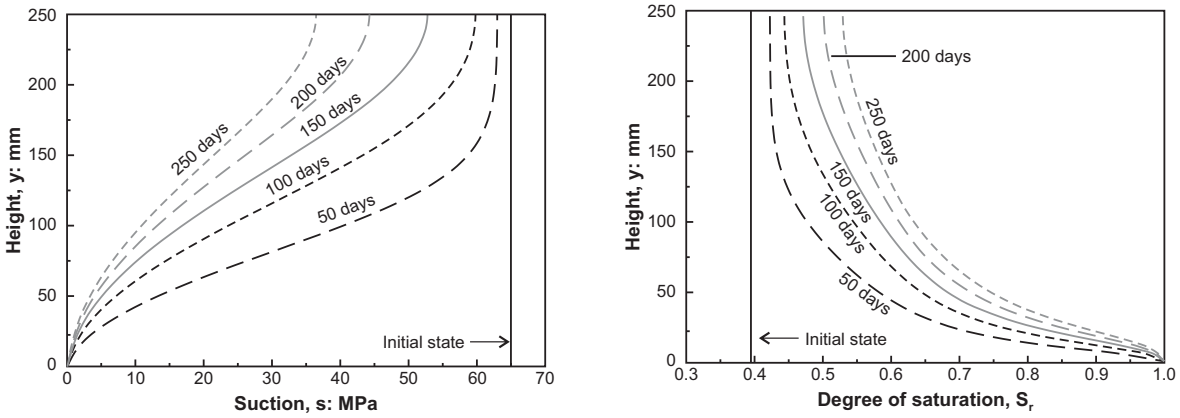

(a) Suction profiles.

(b) Degree of saturation profiles.

Figure 6.12: Evolution through time of suction and degree of saturation in the column during water injection (numerical results).

The progressive hydration of the bentonite sample yields important structural changes (Figure 6.13). Firstly, water injection results in an important increase in void ratio in the lower part of the sample (Figure 6.13(a)). Since global swelling of the sample is prevented, the increase of porosity at the bottom of the sample should be counterbalanced by an increase of porosity at the top of the sample. Accordingly, the upper part of the sample is compressed by the swollen bottom part. As water penetrates within the sample, the transition between the swollen and compressed zones takes away from the injection side.

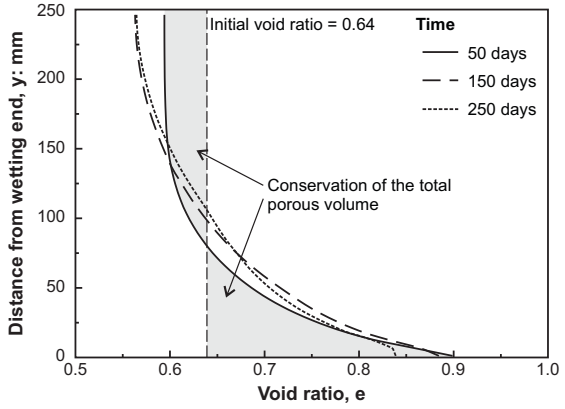

(a) Total void ratio e.

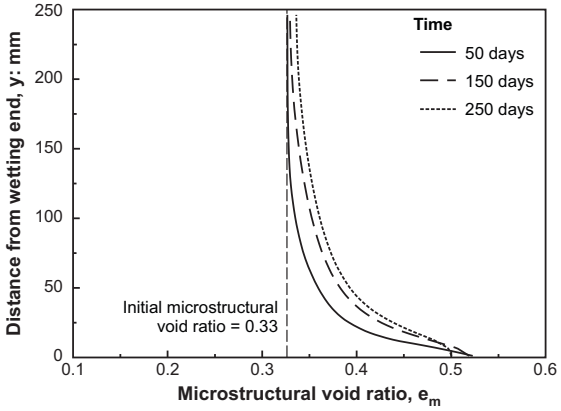

(b) Microstructural void ratio e_m.

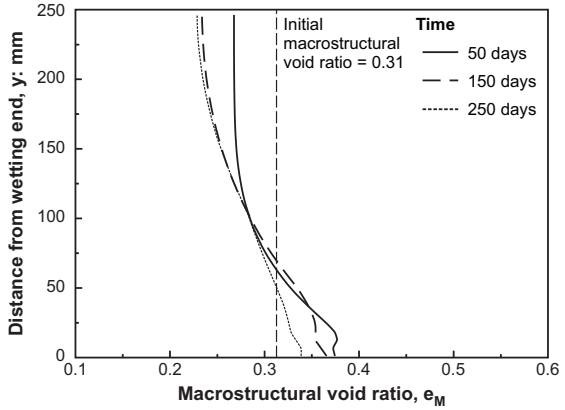

(c) Macrostructural void ratio $e_M = e - e_m$.

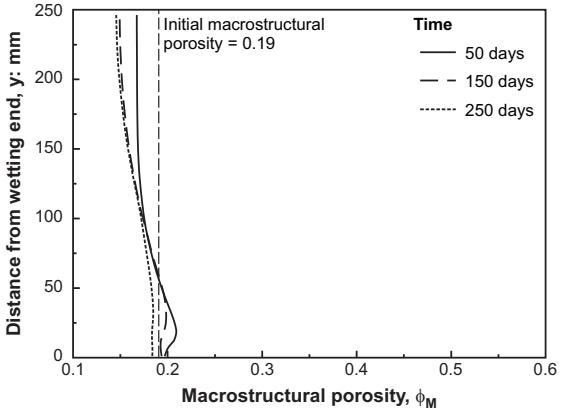

(d) Macrostructural porosity $\phi_M = (e_M/e)\,\phi$.

Figure 6.13: Profiles of (a) total, (b) microstructural and (c) macrostructural void ratios, and of (d) macrostructural porosity after 50, 150 and 250 days of hydration.

On the other hand, bentonite hydration results in an increase of the microstructural void ratio (Figure 6.13(b)). While the initial microstructural void ratio was equal to 0.33, it increases up to 0.52 at the bottom of the sample. Note that, contrary to the total void ratio, the volume of micropores is not conserved during hydration, but increases with increasing water content.

The difference between the total void ratio e and the microstructural void ratio e_m provides the macrostructural void ratio e_M (Figure 6.13(c)). At the beginning of the test (see profiles for days 50), the increase in e is higher than the increase in e_m, so that the

volume of macrovoids increases. However, as hydration proceeds, a redistribution of the void ratio is observed and the microstructural void ratio keeps increasing in the whole sample. Consequently, the macrostructural void ratio progressively decreases. After 250 days of hydration, it remains higher than its initial value at the bottom of the sample (up to a height of 50 mm), but has significantly decreased in the rest of the column. Figure 6.13(d) presents the profiles in terms of macrostructural porosity ϕ_M. A comparison between Figures 6.13(c) and 6.13(d) evidence higher changes in e_M than ϕ_M. In addition, contrary to the macrostructural void ratio, a decrease in the macroporosity is observed in the whole sample after 250 days of water saturation.

These structural changes in the bentonite sample directly affect the permeability of the material. Figure 6.14 shows the evolution through time of the saturated, relative and unsaturated water permeability profiles.

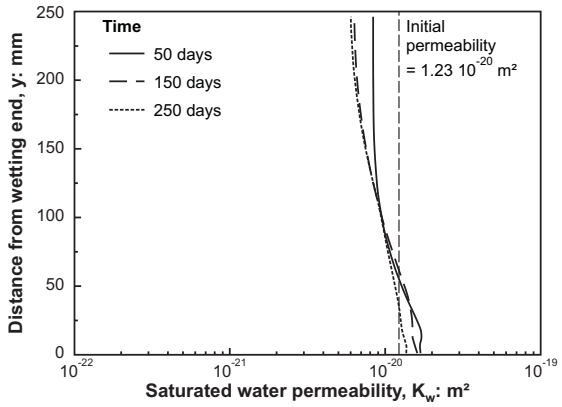

(a) Saturated water permeability.

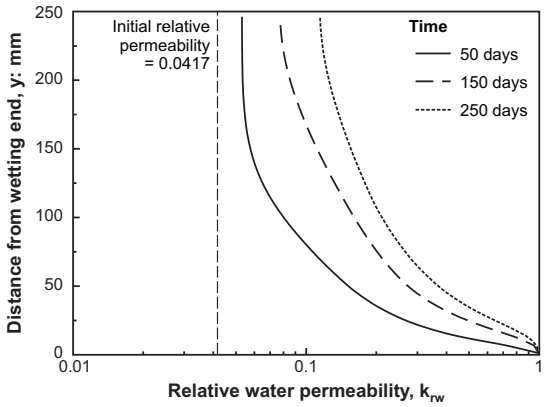

(b) Relative water permeability.

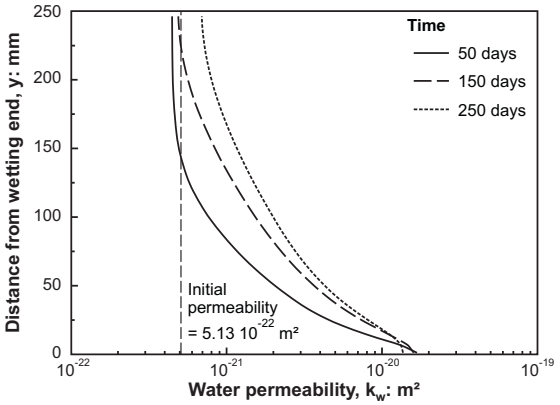

(c) Unsaturated water permeability.

Figure 6.14: Profiles of (a) saturated, (b) relative and (c) unsaturated water permeabilities after 50, 150 and 250 days of hydration.

As can be observed, water injection has opposite effects on the saturated water permeability (Figure 6.14(a)) and relative water permeability (Figure 6.14(b)). Indeed, the saturated water permeability is affected by changes in the macrostructural void ratio. While an increase in e_M is observed locally at the bottom of the column, the macrostruc-

tural void ratio globally decreases in the sample, so that a reduction of the saturated water permeability is predicted. In particular, the saturated permeability value at the top of the sample is divided by two after 250 days of water injection. On the contrary, water saturation enhances the relative permeability, so that the water permeability of the sample increases with time (Figure 6.14(c)).

Taking into account the structural changes in bentonite, and their effects on the water flow properties, is essential for the good reproduction of the hydration kinetics. For the sake of comparison, Figure 6.15 presents the evolution through of the relative humidity measured at different heights of the sample. The experimental results are compared to the numerical results obtained with a constant saturated water permeability. As for the reference case, the exponent n_k is determined by best-fitting the experimental data at RH2 and RH3, so that a value of $n_k = 3.1$ is used in this new modelling. As observed in Figure 6.15, the evolution of the relative humidity is not well captured, neither for RH1 nor RH4. The increase of relative humidity in RH1 is slower than observed experimentally, and even slower than predicted using the developed model (see Figure 6.11). On the other hand, a faster increase of relative humidity is observed for the sensor RH4 located the further from the injection face. The permeability model developed in this chapter allows a better reproduction of the hydration kinetics since

- the saturated water permeability is enhanced at the bottom of the sample due to a local increase in the macrostructural void ratio.
- the saturated water permeability decreases in the upper part of the sample as a result o decreasing void ratio and increasing microstructural void ratio.

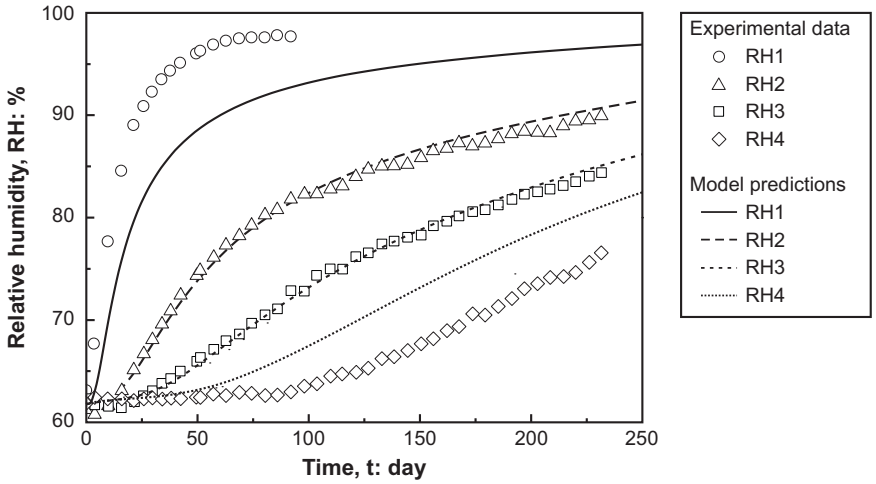

Figure 6.15: Evolution of relative humidity during water infiltration. Comparison between experimental data (Wang *et al.*, 2013a) and model predictions obtained with a constant saturated permeability and $n_k = 3.1$.

4.4 Critical analysis of the instantaneous profile method

The instantaneous profile method (Daniel, 1982) has often been used to interpret infiltration tests and determine the water permeability of unsaturated porous materials. By monitoring of the injected water volume and the evolution of the relative humidity at different distances from the wetting front, the water permeability may be expressed as a function of suction.

Figure 6.16 presents the evolution of the water permeability with suction predicted by the numerical model. Note that the different permeability values are obtained at four different Gauss points of the mesh. For the sake of comparison, the permeabilities computed by Wang *et al.* (2013a) using the instantaneous profile method are also represented.

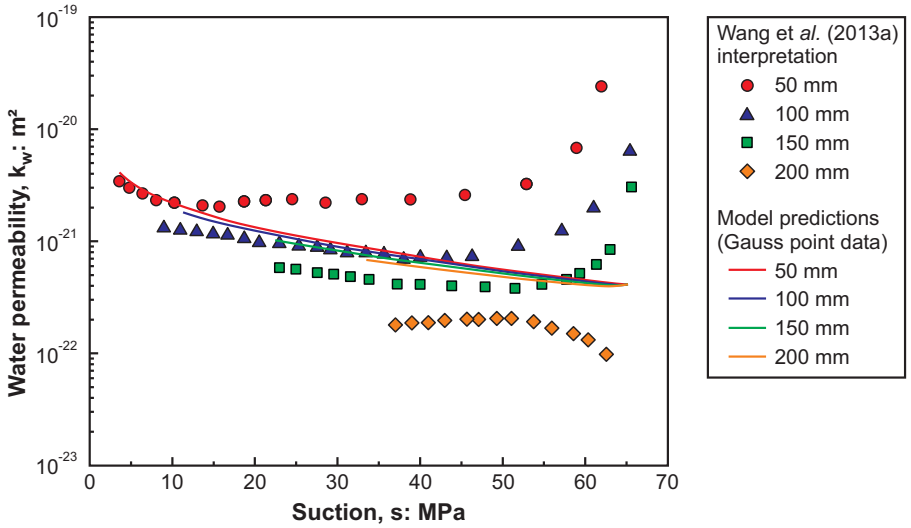

Figure 6.16: Water permeability versus suction at different distances from the wetting end y. Comparison between Wang *et al.* (2013a) interpretation and the values obtained from the numerical model. Water permeabilities are obtained directly at different Gauss points.

Despite the good performance of the numerical model in reproducing the evolution of relative humidity in the sample, a very bad agreement is apparently obtained in terms of unsaturated water permeability. Indeed, Wang *et al.* (2013a) show that the permeability evolution strongly depends on the considered height. At the bottom of the sample, an important decrease in permeability is observed between 65 MPa and 50 MPa of suction. The permeability is then relatively stable with decreasing suctions, although a slight increase is observed below 15 MPa. On the contrary, an increase in permeability is detected in the high suction range for the sensor located the furthest from the injection side. This trend is not reproduced by the numerical model which predicts a continuous increase of the water permeability with suction, regardless the distance from the wetting face. In addition, the evolution of the water permeability is less significant than the one predicted by Wang *et al.* (2013a) using the instantaneous profile method.

In order to better understand the apparent discrepancies between the unsaturated permeability values computed by Wang *et al.* (2013a) and predicted by our model, the evolution of relative permeability modelled at distances of 50, 100, 150 and 200 from the injection side are used to compute the relative permeability according to the instantaneous profile method. In order to determine the permeability of the partially saturated porous media, the hydraulic gradient i and the water flux q_w must be computed. In particular, the hydraulic gradient i is calculated as the slope of the isochrone (the tangent of the suction profile s at a height y and time t). It reads

$$i_t = \left.\frac{\Delta s}{\Delta y}\right|_t \tag{6.16}$$

s and y being expressed in the same length units.

On the other hand, using the water retention curve, the relative humidity profile can be converted into a water content profile. Wang *et al.* (2013a) used the following relationship to compute the gravimetric (w) and volumetric (θ) water content

$$w = -7.26 \log s + 24.102 \tag{6.17}$$

$$\theta = \frac{w \rho_d}{\rho_w} \tag{6.18}$$

where ρ_d is the material dry density (equal to 1.67 Mg/m^3) and ρ_w is the water density. Considering the volumetric water content profiles at different times, the water flux can be determined according to

$$q_w\left(y_i\right) = A \frac{\int_{y_i}^{H} \theta_{t+\Delta t} \mathrm{d}y - \int_{y_i}^{H} \theta_t \mathrm{d}y}{\Delta t} \tag{6.19}$$

where A is the surface area of the sample face, H is the sample height and θ is the volumetric water content. Then, knowing both hydraulic gradient and water flux, the permeability is obtained as (Daniel, 1982)

$$k_w\left(y_i\right) = -\frac{1}{A} \frac{q_w\left(y_i\right)}{\frac{1}{2}\left(i_t + i_{t+\Delta t}\right)}. \tag{6.20}$$

It can be computed as a function of suction at different heights of the sample corresponding to the positions of the relative humidity sensors. In this section, the evolutions of relative humidity at 50 mm, 100 mm, 150 mm and 250 mm from the wetting end are used as input data for the instantaneous profile method (Figure 6.17). The evolutions of water permeability computed in this way are in good agreement with those determined by Wang *et al.* (2013a), both qualitatively and quantitatively. They significantly differ from the permeability values at the Gauss points as shown in Figure 6.16. Consequently, while infiltration column tests provide valuable and necessary data to asses the hydration kinetics of bentonite-based materials, their interpretation using the instantaneous profile method should be taken with caution.

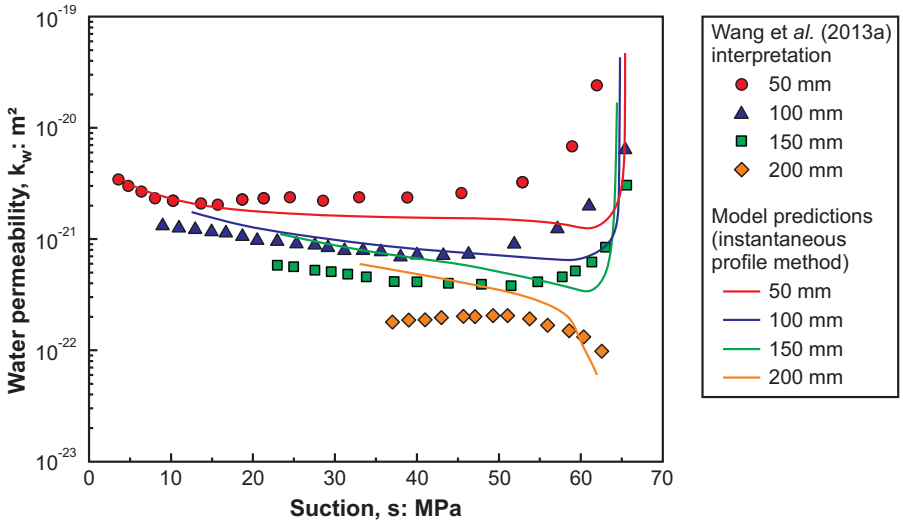

Figure 6.17: Water permeability versus suction at different distances from the wetting end y. Comparison between Wang *et al.* (2013a) interpretation and the reinterpretation of the numerical results.

5 Conclusions

A proper estimation of the time required to ultimately saturate bentonite buffers under *in situ* conditions is an important stake for the safe design of the repository. So far, the application of classic fluid flow model has often resulted in underestimations of the time required to reach full saturation of the barrier. Fore instance, in the case of the Praclay Seal Test conducted in Mol (Chen *et al.*, 2012), Belgium, saturation of the bentonite buffer has appeared to be significantly longer than initially predicted.

The important structural changes observed during hydration constitute one the reasons often mentioned to explain these discrepancies. This chapter focuses on the evolution of water permeability along hydromechanical stress paths and on its influence on the saturation kinetics. Experimental techniques for the determination of both saturated and unsaturated water permeabilities are first reviewed. A synthesis of the available experimental data on bentonite-based materials is proposed. It highlights an important effect of dry density on the saturated permeability values. In this work, the evolution of the saturated permeability with dry density is interpreted in terms of macroporosity accessible to water flow, and a new law, relating the saturated permeability to the macrostructural void ratio $e_M = e - e_m$, is proposed. This law introduces an additional coupling in the hydromechanical formulation developed in this PhD thesis: the water permeability is influenced by the mechanical deformation through the void ratio e and by microstructure evolution through e_m.

The new permeability law is validated by modelling an infiltration test on a compacted bentonite-based material. The evolution of the sample microstructure during hydration is thoroughly analysed and its impact on the hydraulic properties is assessed. Numerical results show that the evolution with time of the relative humidity in the sample is well

captured. In particular, the modelled hydration kinetics is significantly improved compared to the one obtained using classic flow model.

Finally, the estimation of the unsaturated permeability using the instantaneous profile method is criticized. Indeed, the technique significantly overestimates the changes of unsaturated permeability during hydration.

Chapter 7

Hydromechanical behaviour of interfaces and technological gaps

1 Introduction

The laboratory tests designed to study the behaviour of bentonites are generally carried out in ideal conditions: the initial state of the material is known, the environmental conditions are controlled, and the contact between the different materials (the sample, the cell, the porous discs...) can be guaranteed. However, these ideal conditions do not correspond to the reality of the underground structures. In particular, the placement of any engineered barrier in a gallery comes along with unavoidable technological gaps. Figure 7.1 shows some evidence of technological gaps in two large-scale *in situ* experiments, namely the SEALEX experiment carried out in the Tournemire Underground Research Laboratory (URL), France (Barnichon & Deleruyelle, 2009) and the FEBEX experiment realized in the Grimsel Test Site, Switzerland (Alonso *et al.*, 2005a). In Figures 7.1(a) and 7.1(b), gaps are clearly observed between the bentonite buffer and the host rock, as well as between the different blocks of bentonite and between the blocks and the canister in Figure 7.1(b).

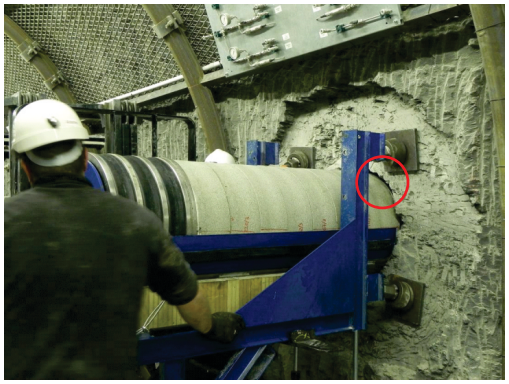

(a) Sealex Experiment in Tournemire URL (Wang *et al.*, 2013b).

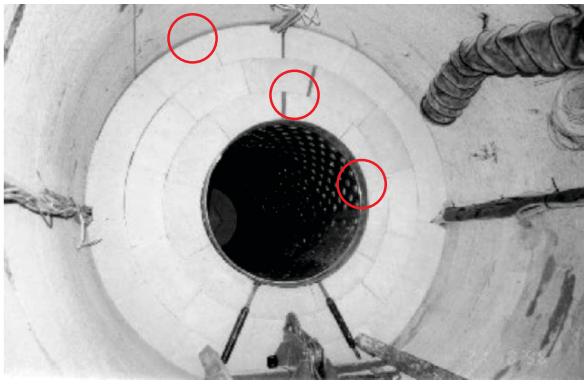

(b) FEBEX Experiment in Grimsel Test Site (Alonso *et al.*, 2005a).

Figure 7.1: Evidence of technological gaps in large-scale *in situ* experiments. Technological gaps and interfaces are highlighted by the red circles.

In the short time, these interfaces and technological gaps represent zones of low mechanical resistance (Wang *et al.*, 2013c; Chen *et al.*, 2014). While bentonite swelling will tend to close the gaps, there is a risk that they remain preferential pathways for the radionuclides migration. When geological disposal in granite formations is considered (where sudden and important water inflow are foreseen), interfaces and technological gaps are also related to the risk of piping and erosion (see Buzzi *et al.*, 2008; Sanden & Börgesson, 2008; Sane *et al.*, 2013; Suzuki *et al.*, 2013, among others). A good understanding of the hydromechanical behaviour of interfaces and their evolution with time is thus a crucial issue regarding the safety functions of the engineered barrier.

While most researchers have traditionally focused on the behaviour of the buffer and the host rock separately, little attention has been paid to the role and influence of technological gaps and interfaces between materials. However, several laboratory experiments have put into evidence the influence of technological gaps on the final swelling pressure developed by a bentonite buffer (Gatabin *et al.*, 2006; Wang *et al.*, 2013a) and the role of interfaces on water flow and gas migration (Buzzi *et al.*, 2008; Van Geet *et al.*, 2008; Zhang, 2013; Liu *et al.*, 2014). Still, the existence of technological gaps is generally neglected in numerical modelling and perfect contact is assumed between the different materials. This strong hypothesis assumes continuity of both mechanical displacements and pore pressures between materials, which is not the case, especially during the first years of the disposal life. Therefore the behaviour of interfaces should be studied and special numerical tools should be employed or developed.

In this chapter, attention is focused on the hydraulic and mechanical behaviours of interfaces and technological gaps. Experimental observations from laboratory, mock-up and large-scale *in situ* tests are presented and analysed in order to highlight the influence and role of both interfaces and initial technological gaps on the overall system behaviour. From the above-described data collection, it appears that little information is available on the normal behaviour of bentonite interfaces and on fluid transfer through interfaces. This observation motivated an experimental characterization campaign carried out at the Technical University of Catalonia (UPC) in Barcelona, Spain, during a three-month research stay. Three types of tests were performed, namely conventional oedometer and oedometric soaking tests, controlled-suction oedometer tests and constant volume swelling pressure tests, with the aims of improving the characterization of the tested material and assessing the role of interfaces. The main outcomes of the experimental campaign are presented in this chapter. In this work, zero-thickness interface elements are adopted to represent interfaces and technological gaps. The equations governing the interface problem are presented and the formulation of the coupled interface element is described. In order to model water flow through and within interfaces, an original three-node formulation is adopted.

2 Experimental observations

2.1 Hydromechanical behaviour of interfaces

The behaviour of interfaces subjected to normal loading has been investigated by a number of authors (see Goodman *et al.*, 1968; Bandis *et al.*, 1983; Barton *et al.*, 1985; Gentier, 1986; Plesha, 1995; Kulatilake *et al.*, 1997; Armand, 2000; Bart *et al.*, 2004; Buzzi *et al.*, 2008; Zhang, 2013, among others). The tests generally consist in loading and unloading uniaxially a rock sample containing a natural or artificially-created joint. The normal displacement, which is assumed to correspond to the gap closure, is then recorded as a function of the applied normal stress p_N. Experimental data show that the mechanical deformation of a fracture under normal loading is generally characterized by a non-linear relationship between the applied normal stress and the interface closure (Figure 7.2), owing for the progressive crushing of the interface asperities. Yet, the interface closure does not decrease indefinitely as the normal stress is increased, but tends to a limit value. Upon unloading, the interface exhibits a higher stiffness and the total normal displacement is not recovered, as a consequence of damage caused to the asperities (Figure 7.2).

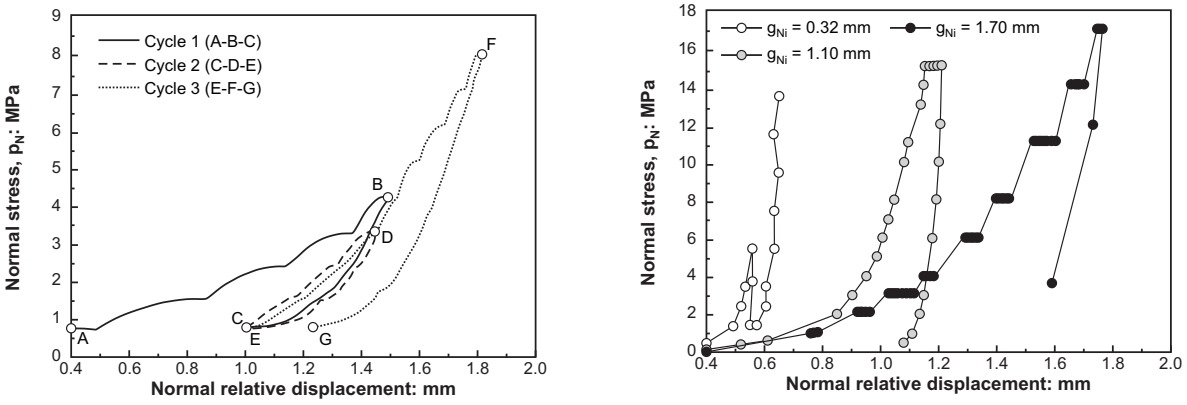

(a) Compacted bentonite (Buzzi *et al.*, 2008). (b) Callovo-Oxfordian claystone (Zhang, 2013).

Figure 7.2: Evolution of the normal relative displacement as a function of the normal applied stress. g_{Ni} denotes the initial gap aperture.

The interpretation of normal loading tests should be moderated when the behaviour of interfaces between compressible materials is considered. Indeed, as already mentioned, it is generally assumed that the normal displacements recorded at the top of the samples correspond to the interface closure. While this hypothesis is reasonably valid in the case of rock or concrete joints, the measured displacements should be corrected accounting for the compressibility of the material in the case of bentonite-based materials. In that case only, it is possible to assess the influence of the interface.

The shear behaviour of joints is generally investigated by performing direct shear test. The test consists in applying a normal stress to a sample containing a natural or artificially-created joint, and shearing the sample under constant normal stress. The experimental results include the evolution of the shear stress τ with the shear relative displacement, and the evolution of the normal relative displacement with the shear relative displacement.

The shear behaviour of interfaces has been investigated by a number of authors (see Barton & Choubey, 1977; Bandis *et al.*, 1983; Barton *et al.*, 1985; Armand, 2000; Seidel & Haberfield, 2002; Alonso *et al.*, 2013; Pellet *et al.*, 2013; Sinnathamby *et al.*, 2015, among others). In the case of plane smooth joints, the shear stress is shown to increase rapidly with the shear displacement, until a maximum value is reached (Figure 7.3). Further shearing of the interface does not affect the shear stress. The maximum shear stress reached upon shear is called the shear strength and is a function of the applied normal stress. A Coulomb failure criterion is generally used to represent such behaviour (Figure 7.3). It is expressed as

$$\tau = (\tan \varphi)\, p_N = \mu p_N \tag{7.1}$$

where φ is the friction angle and the cohesion is assumed equal to 0. The quantity $\mu = \tan \varphi$ is called the friction coefficient.

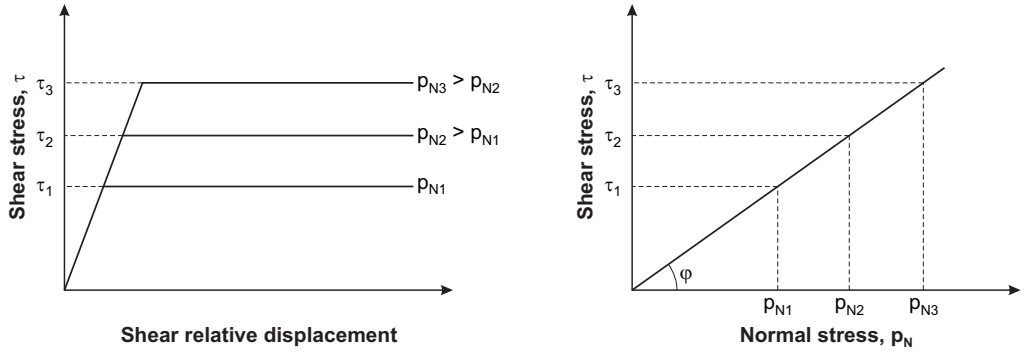

Figure 7.3: Shear behaviour of plane smooth interfaces: stress – displacement diagram and Coulomb failure criterion.

In the case of rough joints, shear-induced dilatancy is often observed (Barton, 1976; Barton & Choubey, 1977; Plesha, 1987; Homand *et al.*, 2001; Zandarin *et al.*, 2013). In addition, upon shearing, the shear stress increases first until reaching a peak value, and then gradually decreases down to a residual value. It is worth mentioning the work of Zandarin *et al.* (2013) on the effects of suction on the shear behaviour of rock joint. Zandarin *et al.* (2013) indeed showed that a decrease in suction leads to a decrease of both shear strength and dilatancy.

Finally, several authors investigated the effect of the joint opening on the (longitudinal) hydraulic conductivity of the interface (see Iwai, 1976; Bandis *et al.*, 1983; Barton *et al.*, 1985; Raven & Gale, 1985; Boulon *et al.*, 1993; Nguyen & Selvadurai, 1998; Pyrak-Nolte & Morris, 2000, among others). The studies show that the permeability of the interface decreases non-linearly as the confining stress increases and the gap aperture decreases. Boussinesq (1868) firstly provided a mathematical law characterising the laminar flow of a viscous incompressible fluid between two smooth parallel plates. Accordingly, the total fluid flow is proven to be proportional to the cube of the aperture between the plates; this is the so-called cubic law. In this case, the longitudinal permeability of the joint k_{wL} is a function of its opening g_N according to

$$k_{wL} = \frac{(g_N)^2}{12}. \tag{7.2}$$

The validity of the cubic law in rock mechanics is proven (Witherspoon *et al.*, 1980; Tsang & Witherspoon, 1981; Oron & Berkowitz, 1998), although improvements are necessary due to the underlying strong hypothesis. In particular, the roughness of the interface is taken into account by considering an hydraulic aperture rather than a mechanical one (Olsson & Barton, 2001). Finally, no dedicated experimental study concerning the normal hydraulic transmissivity of joints and interfaces has been found in the literature.

2.2 Self-sealing

The self-sealing capacity of clay materials is defined as the capacity of these materials to reduce fracture permeability. Contrary to self-healing, which involves loss of memory, the material subjected to self-sealing keeps the memory of the fracture. The processes involved in self-sealing are still far from being fully understood, but probably involve hydromechanical, hydrochemical and hydrobiochemical processes (Bastiaens *et al.*, 2007). At the laboratory scale, the self-sealing capacity of clay soils and rocks has been investigated by a number of authors on different materials: by Van Geet *et al.* (2008) on Boom clay; by Zhang (2011, 2013) and Ghayaza *et al.* (2013) on Callovo-Oxfordian claystone; by Van Geet *et al.* (2008), Cuss *et al.* (2011) and Zhang (2011, 2013) on Opalinus clay; by Horseman *et al.* (1999), Komine *et al.* (2001), Marcial *et al.* (2006) and Liu *et al.* (2014) on bentonite-based materials. In addition, evidences of self-sealing in underground laboratories were noticed by Bastiaens *et al.* (2007) at the HADES underground research facility, Belgium, by Delay *et al.* (2007) and de La Vaissière *et al.* (2014) at the Meuse/Haute-Marne Underground Research Laboratory and by Lanyon *et al.* (2014) at the Mont Terri URL, Switzerland.

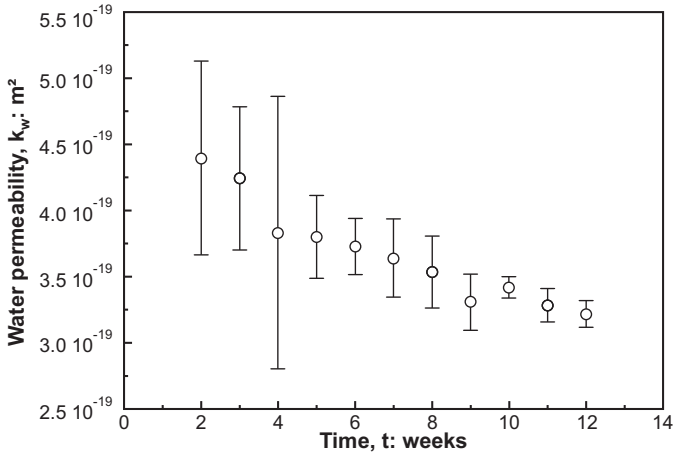

Figure 7.4: Evolution of the water permeability in samples of Boom clay with an initial artificially-created planar fracture (Van Geet *et al.*, 2008). Measured values and 95% confidence intervals.

In the framework of the SELFRAC project, Van Geet *et al.* (2008) investigated the self-sealing capacity of Boom clay and Opalinus clay. Planar fractures of about 300 μm aperture were created through the axis of cylindrical samples. Water was then injected in the samples and the evolution of the hydraulic conductivity was monitored. Figure 7.4 shows that after nine weeks, the water permeability of Boom clay has decreased from

4.4×10^{-19} m^2 to 3.2×10^{-19} m^2, and has reached a value in the accepted range of values for undisturbed Boom clay (Yu *et al.*, 2011). Note that the decrease in water permeability was even more important in samples where initial gaps of 6 mm and 12 mm in diameter were drilled. In that case, the drop in hydraulic conductivity reached indeed more than one order of magnitude (Van Geet *et al.*, 2008). After dismantling the test, the original fissure in the Boom clay sample was not visible with the naked eye. However, after drying under atmospheric conditions, the fracture re-appeared, meaning that the initial cohesion of the sample was not recovered and that self-healing of the sample was not achieved. In addition, μCT scanning of the sample, carried out before and after the hydraulic test, evidenced a decrease in density in the zone where the original fracture was located.

Zhang (2013) investigated the self-sealing capacity of Callovo-Oxfordian claystone under wetted gas flow. During 24 hours, a fractured sample was flowed with dry gas under a confining pressure of 1 MPa. Then, wetted gas with increasing relative humidity of 75% to 100% was injected. As shown in Figure 7.5, the flow of wetted gas caused a progressive radial expansion of the sample, suggesting important local swelling pressures at the interface contact points. Local swelling of the interface is believed to result from the hydration of clay minerals present in the claystone matrix. In the meanwhile, significant permeability decrease is observed. Ghayaza *et al.* (2013) showed that the self-sealing capacity of clay materials was a function of the fracture roughness. In particular, rough interfaces exhibit a better self-sealing capacity, owing for the high surface in contact with water or wetted gas.

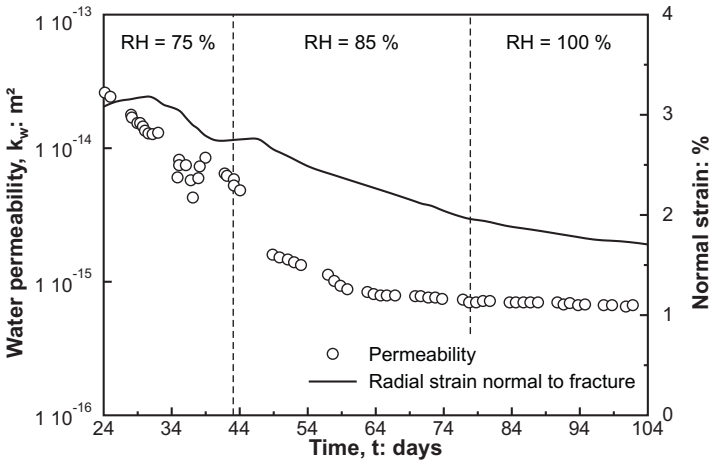

Figure 7.5: Effect of wetted gas flow on fracture sealing in Callovo-Oxfordian claystone (Zhang, 2013).

2.3 Technological gaps

The influence of technological gaps on the hydromechanical behaviour of bentonite-based materials has been investigated by Gatabin *et al.* (2006), de La Vaissière (2013) and Wang *et al.* (2013a) on a compacted mixture of MX-80 bentonite and sand, by Chen *et al.* (2014) on MX-80 bentonite and by Marcial *et al.* (2006) on Kunigel V1 bentonite. The tests generally consist in saturating a bentonite sample whose dimensions are smaller

than the confining cell. Accordingly, the sample will first experience hydration under unconfined (or partly confined) conditions, before reaching full contact with the cell and developing a swelling pressure.

Gatabin *et al.* (2006) studied the influence of technological gaps on the swelling pressure developed by a compacted mixture of MX-80 bentonite and sand. From the experimental data, it appears that the effect of technological gaps is essentially associated to the decrease of the material density (Figure 7.6). Indeed, for a same final value of dry density, the swelling pressure developed by a sample saturated with an initial gap is similar to the one developed by a sample hydrated under constant volume conditions. Similar conclusions were drawn by Wang *et al.* (2013a) on the same material.

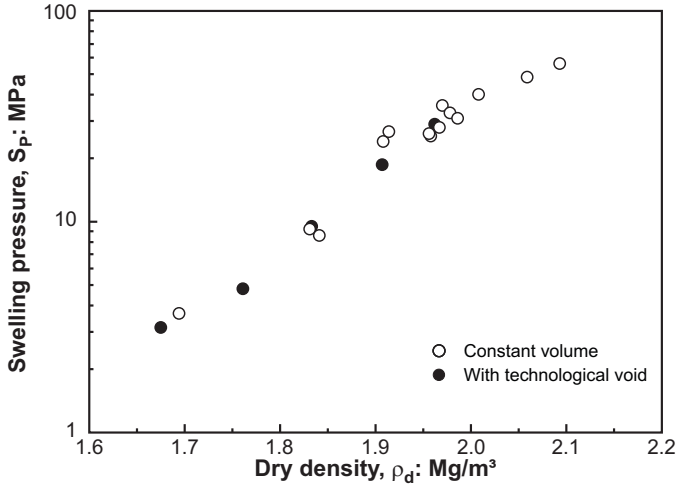

Figure 7.6: Evolution of the swelling pressure with dry density for a compacted mixture of MX-80 bentonite and sand. Comparison between the swelling pressure determined under constant volume conditions and with a technological gap (Gatabin *et al.*, 2006).

Furthermore, Wang *et al.* (2013a) analysed the influence of gaps on the permeability. Bentonite samples were hydrated with an initial radial gap. Once full saturation of the sample was achieved, the hydraulic conductivity was determined. Figure 7.7 shows the experimental results, together with the one obtained by Gatabin *et al.* (2006). Contrary to Wang *et al.* (2013a), the sample used by Gatabin *et al.* (2006) was saturated under confined conditions and the hydraulic conductivity was determined. Then, an axial technological gap was created in order to decrease the dry density, the sample was allowed to fully hydrated and the water conductivity was determined. Figure 7.7 shows that the permeability obtained by Wang *et al.* (2013a) is around one order of magnitude higher than the one determined by Gatabin *et al.* (2006). According to Wang *et al.* (2013a), the filled radial gap represents a discontinuity with lower hydromechanical resistance and triggers a preferential water flow. Such explanation is consistent with the observations made by Chen *et al.* (2014) who investigated the hydraulic resistance of MX-80 bentonite/Boom clay interface using an injection cell. Chen *et al.* (2014) showed indeed that hydraulic fracturing takes place in the interface when water is injected with an increasing pressure, although the technological gap is quickly reduced due to bentonite swelling. However, it should be noted that the data obtained by Gatabin *et al.* (2006) and Wang *et al.* (2013a)

are in the range of permeability variations for a given material (see Chapter 6) and further experimental investigation is probably required to validate the provided explanation.

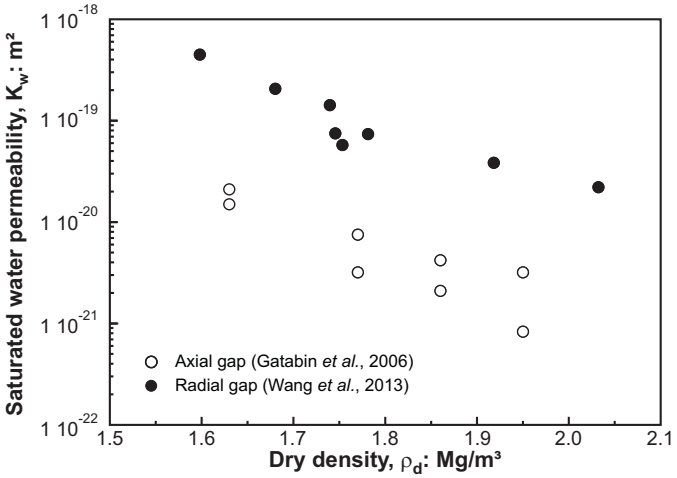

Figure 7.7: Evolution of water permeability with dry density for a compacted mixture of MX-80 bentonite and sand (Gatabin *et al.*, 2006; Wang *et al.*, 2013a). Comparison between sample with initial axial and radial technological gaps.

3 Experimental characterization

3.1 Objectives

The experimental characterization of interfaces behaviour is an important issue towards a better understanding of the role of these interfaces on the overall behaviour of engineered barrier systems, and towards the development of adequate numerical tools and constitutive models. As highlighted in the previous section, existing experimental data on the hydromechanical behaviour of interfaces concern essentially the shear behaviour and the evolution of the conductivity as a function of the joint aperture. On the other hand, there is little information on the normal compressibility behaviour and the normal fluid transfer properties of interfaces, i.e. how fluids flow from one side of a technological gap or interface to the other. These two aspects are investigated in the present work.

Above all, the experimental characterization of interfaces behaviour requires a good knowledge of the behaviour of the material on both sides of the interface. Let us consider a one-dimensional loading test on a bentonite block (Figure 7.8(a)). The measured vertical displacement will characterize the response of the material to loading. On the contrary, if the same test is performed on a vertical assembly of two bentonite blocks (Figure 7.8(b)), the vertical displacement will reflect the compressibility of both the material and the interface, with relative importance depending on the stiffness of the soil and the stiffness of the interface. Indeed in the present case, the soil compressibility cannot be neglected with regards to the compressibility of the interface. Note that this may be different when considering the normal behaviour of rock joints.

(a) Characterization of the material behaviour.

(b) Characterization of the material and the interface behaviours.

Figure 7.8: Principle of the experimental characterization of the interface behaviour. Example for one-dimensional mechanical loading.

Accordingly, the experimental characterization presented in this chapter concerns the hydromechanical behaviour of a bentonite-based material and the behaviour of interfaces. More specifically, the experimental campaign has two main objectives:

(1) **Get an insight into the influence of interfaces on the behaviour of block assemblies.**

In particular, attention is focused on the normal behaviour with regards to mechanical loading and fluid transfer properties.

(2) **Characterize the hydromechanical behaviour of the material upon mechanical and hydraulic loading.**

The tests aim at studying the compressibility and swelling behaviour of the material. In particular, attention is focused on the hydromechanical behaviour in the low-suction domain (suction values up to 1.3 MPa). The tests will be used as references to assess the influence of interfaces.

To achieve these objectives, three types of tests are performed, namely conventional oedometer and oedometric soaking tests, controlled-suction oedometer tests and constant volume swelling pressure tests.

3.2 Soil used in the investigation

3.2.1 Material

The soil used in the investigation is a mixture of Kunigel V1 bentonite (from Japan) and quartz sand with a proportion of 70/30 in dry mass, referred to as K/S mixture hereafter. This mixture is a reference material in the Canadian and Japanese concepts for the geological disposal of radioactive waste. In particular, it was used in the full-scale Tunnel Sealing Experiment (TSX) conducted at Manitoba, Canada (Chandler *et al.*, 1998; Dixon *et al.*, 2002).

Kunigel V1 is classified as a highly plastic clay with a liquid limit w_L ranging from 415 to 474% and a plastic limit w_P between 27 and 32% (Komine & Ogata, 1992; Marcial *et al.*, 2002). In order to identify the mineralogical composition of the Kunigel V1 bentonite, X-ray diffraction (XRD) patterns were obtained on random-oriented powder and on oriented aggregates. The analysis were carried out in the Department of Geology at

the University of Liege, using a Bruker D8-Advance diffractometer with CuKα radiations. The mineralogical composition of the Kunigel V1 bentonite is presented in Table 7.1. The material contains 50% of montmorillonite, 40% of quartz, 4% of K-felspar, 2% of albite, 2% of heulandite and 2% of calcite. For the sake of comparison, existing data from the literature are also presented in Table 7.1.

	Present study	**Literature**[a]
Phyllosicilicate	50% montmorillonite	46–49% montmorillonite
SiO_2	40%	29–38%
K-feldspar	4%	2.7–5.5%
Plagioclase	2%	4%
Other	2% heulandite, 2% calcite	

[a]JNC (2000), Nakashima (2004)

Table 7.1: Mineralogical composition Kunigel V1 bentonite.

3.2.2 Sample preparation

Special attention is given to the procedure of manufacturing soil samples at a dry density of 1.60 ± 0.01 Mg/m^3 and a water content of 16.5 ± 1.5%, in order to obtain an adequate sample homogeneity and repeatability. At these dry density and water content, the degree of saturation is equal to 0.65 and the initial total suction is between 4.7 and 4.9 MPa (as measured by a dew-point chilled-mirror WP4). Note that in this work, the water content is determined after oven-drying at 110°C. Although this temperature is not sufficient to eliminate all interlayer water of smectites, it is used as a reference value. Yet the influence of a higher oven temperature (180°C) on the determination of the water content was evaluated. Figure 7.9 shows that the water content determined at 180°C is in average 0.63% greater than the one measured at 110°C, irrespective of the material dry density.

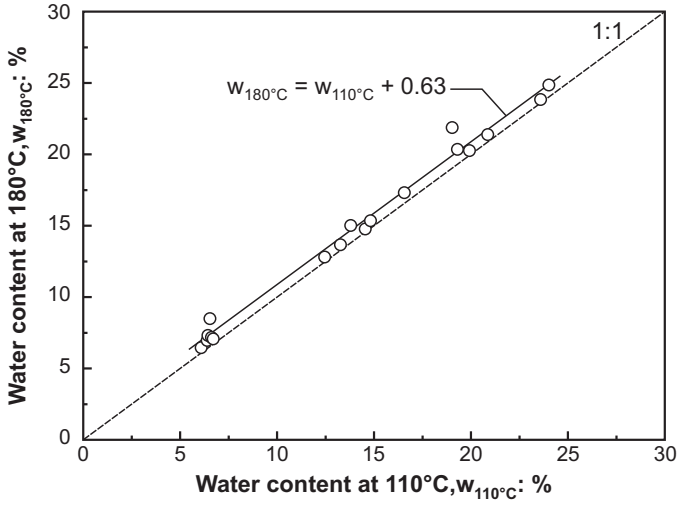

Figure 7.9: Influence of the drying temperature on the measured water content.

Soil specimens (50 mm in diameter, 10 mm high) are compacted in a single layer by means of static compaction. In preparing specimens, the required quantity of water to achieve a starting water content of 16.5% is added to the powder mixture. The required quantity of soil is poured into the assembled oedometer mould (Figure 7.10). The piston is then pushed at a constant rate of 0.50 mm/min axial displacement until reaching contact between the flanges and the rest of the mould wall. During compaction, the entrapped air is progressively released by the air pressure valve. The force of compaction is determined by a load cell during the test. The vertical net stress required to reach the target dry density is of the order of 0.95 MPa. In order to reduce some rebound upon unloading, the piston is blocked for about 30 minutes.

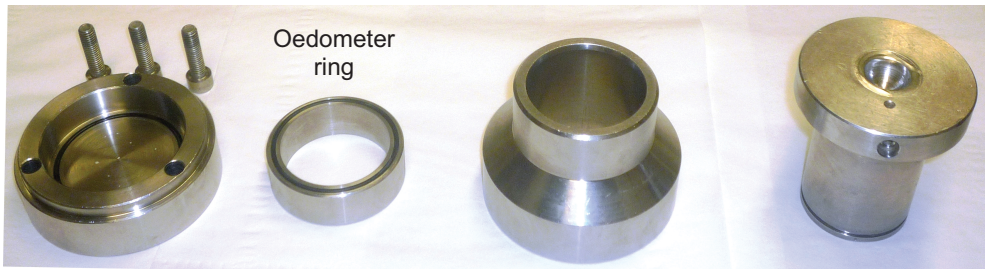

Figure 7.10: Cell used for one-dimensional compaction.

The microstructure of the as-compacted samples is investigated by means of mercury intrusion porosimetry (MIP) after freeze-drying (Delage *et al.*, 1982). As shown in Figure 7.11, the compacted K/S mixture displays a clear bimodal pore size distribution, the two peaks being in the range of pore sizes of 0.03 μm (micropores) and 3 μm (macropores). Compared to a sample of Kunigel V1 bentonite compacted at a dry density of 1.36 Mg/m^3 (i.e. the effective bentonite density of the K/S mixture), the pore size distribution of the K/S mixture defines a peak of macropores at a larger diameter. This larger dominant pore size of the mixture is a consequence of the less developed aggregates and is likely to induce a lower air-entry value of the mixture.

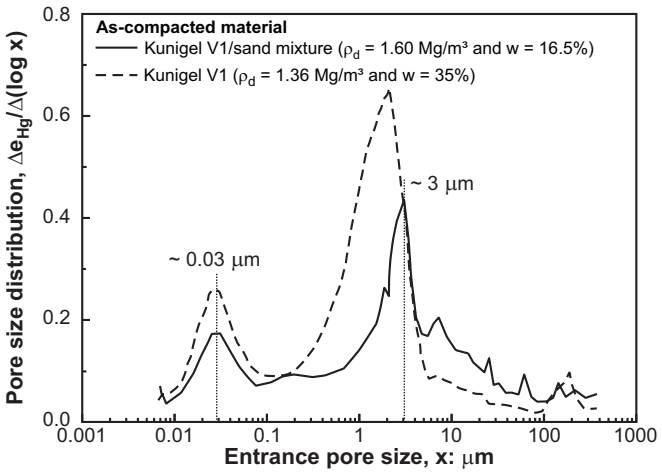

%

Figure 7.11: Pore size distributions of K/S mixture compacted at a dry density $\rho_d = 1.60$ Mg/m^3 and a water content $w = 16.5\%$. Comparison with the pore size distribution of pure Kunigel bentonite compacted at a dry density $\rho_d = 1.36$ Mg/m^3 and a water content $w = 35\%$ (Romero, 2014).

3.2.3 Experimental results from previous investigations

The work presented in this chapter lies in the continuity of past and on-going investigations carried out by CIMNE-UPC-GEOLAB on the behaviour of Kunigel V1 bentonite and the K/S mixture. The characterization of the K/S mixture mainly concerned its water retention behaviour. More specifically, two types of measures were performed, namely controlled-suction oedometer tests and measure of total suction on drying under unconfined conditions. The main experimental results of the past investigations are presented in this section.

Figure 7.12 presents the evolution of void ratio during wetting and drying path under oedometer conditions and a vertical net stress of 0.4 MPa. As observed in Figure 7.12, larger strains are experienced by the sample upon drying than upon wetting. Figure 7.12(b) indicates the changes in water content observed during the wetting and drying paths. Hydraulic hysteresis effects are clearly observed and the air-entry value is significantly higher than the water-entry value. However, the significant shrinkage observed around 0.5 MPa does not induce significant desaturation of the material. As far as the wetting path is concerned, the sample experiences little swelling upon wetting, while the water content significantly increases.

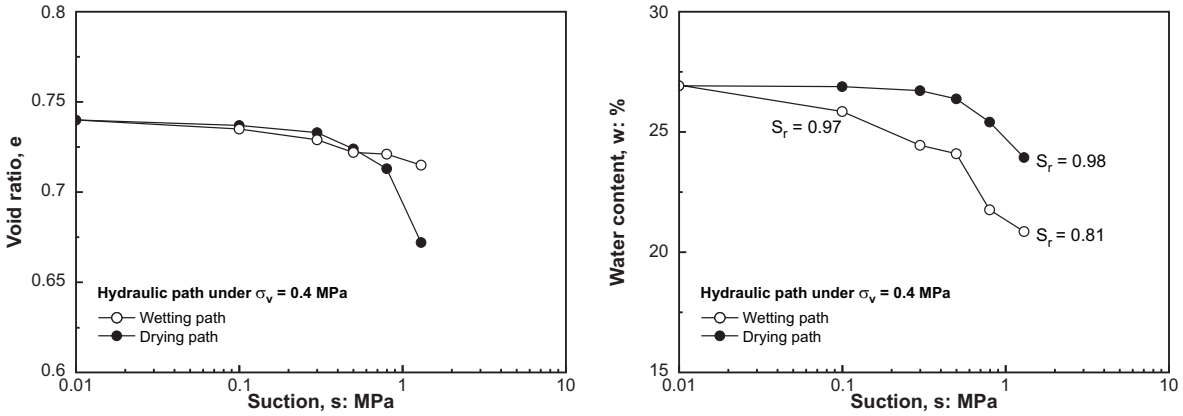

(a) Evolution of void ratio with suction.

(b) Evolution of water content with suction.

Figure 7.12: Controlled-suction oedometer tests on the K/S mixture compacted at $\rho_d = 1.60$ Mg/m^3 (Romero, 2014). Wetting path starts from as-compacted conditions and drying path starts from saturated conditions.

In order to complement the water retention curve in the high suction range, the total suction was measured along a drying path under unconfined conditions. A dew-point chilled-mirror WP4 was used. Figure 7.13(a) presents the evolution of (total) suction upon drying under unconfined conditions. Note that the material was compacted at an initial dry density of 1.60 Mg/m^3 and different water contents. For the sake of comparison, existing data on Kunigel V1 are also represented.

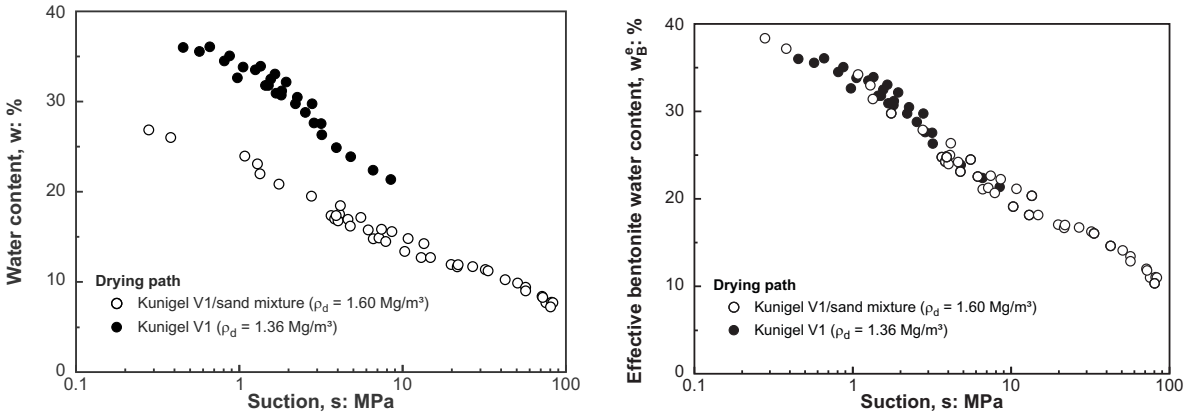

(a) Evolution of water content with suction (Romero, 2014).

(b) Evolution of effective bentonite water content with suction.

Figure 7.13: Water retention curve (drying path) on compacted Kunigel V1 bentonite and the K/S mixture.

By assuming that water is stored in the bentonite aggregates only, an effective bentonite water content w_B^e is defined

$$w_B^e = \frac{m_w}{m_{sb}} = \frac{w}{f_b} \tag{7.3}$$

where m_w is the mass of water, m_{sb} is the mass of bentonite solid particles, w is the water content of the mixture and f_b is the mass fraction of bentonite (equal to 0.7 for the K/S mixture). The effective bentonite water content allows normalizing the water retention curves. As shown in Figure 7.13(b), a good correspondence is obtained between the water retention behaviour of pure Kunigel V1 bentonite and the K/S mixture.

3.2.4 Creation of interfaces

In this work, the hydromechanical behaviour of interfaces is studied by performing tests on vertical assemblies of soil samples. In order to create these assemblies, two samples with a height of 10 mm are compacted separately in two different oedometer rings and then brought in contact in the same oedometer ring (smooth interfaces are considered). This process is a critical issue as it should ensure good contact between the samples while limiting the deformation of the samples. Basically, two strategies exist to bring in contact the soil samples (Figure 7.14). The first one is depicted in Figure 7.14(a). It consists in superposing the two oedometer rings with the soil samples at the bottom of each ring, and pulling down the upper sample. This process limits the deformation of the samples but contact between both samples cannot be guaranteed. Therefore, the final height of the assembly is also measured with a precision calliper. The second strategy is depicted in Figure 7.14(b). This procedure is similar to the first one, except that the soil samples are initially bring into contact and both of them are pulled down into a single oedometer ring. While contact between the samples is ensured, considerable deformation of the samples may be generated. Therefore, the first strategy is adopted in this work. The system used to bring into contact the soil samples is presented in Figure 7.15.

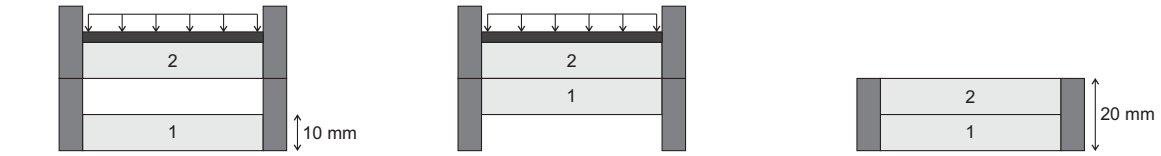

(a) Assembling technique n°1. (b) Assembling technique n°2. (c) Final sample.

Figure 7.14: Compaction process for the creation of interfaces.

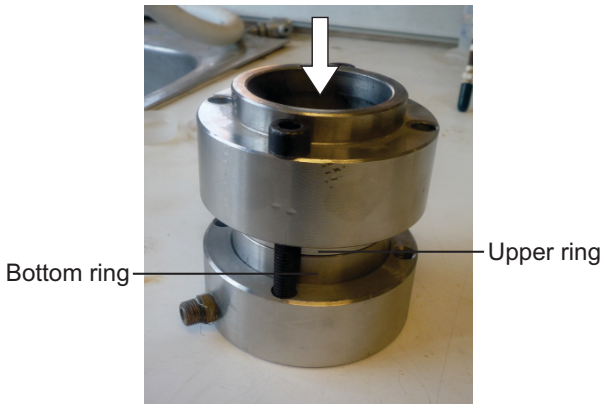

Figure 7.15: System used to bring into contact soil samples.

3.3 Conventional oedometer and oedometric soaking tests

3.3.1 Experimental equipment

Conventional oedometer cells are used to study the one-dimensional compressibility behaviour under constant water content, as well as the swelling behaviour during soaking under constant vertical stress. In these oedometer cells, the soil sample (50 mm in diameter and 10 mm high) rests on a porous disc connected to a water inlet. This inlet allows water supply at atmospheric pressure during inundation stages. The upper part of the sample is in direct contact with the piston. Vertical loads up to 2 MPa are applied with a lever-arm loading mechanism and vertical displacements ΔH are measured using a Linear Variable Differential Transformer (LVDT). The volumetric (vertical) strain ε_v is then computed as

$$\varepsilon_v = \frac{\Delta H}{H_i} \tag{7.4}$$

where H_i is the initial sample height. The volumetric strain is assumed positive during sample compression and negative during swelling. Finally, the current void ratio e is obtained from

$$e = e_i - \varepsilon_v \left(1 + e_i\right) \tag{7.5}$$

where e_i is the initial void ratio.

3.3.2 Experimental programme

Three oedometer tests, referred to as OEDO-01a, OEDO-01b and OEDO-02, are performed on the compacted K/S mixture. One additional test, referred to as OEDO-11, aims at studying the influence of an interface on the compressibility and swelling behaviour. Each test consists in loading incrementally the specimen to a specific level of vertical stress and under constant water content. Once that the target vertical stress is reached, the soil sample is inundated under constant vertical stress (Figure 7.16). Each test is carried out until the stabilisation of the vertical displacement. More precisely, stabilisation is assumed when the rate of vertical deformation of the sample becomes lower than -0.3%/day. In this work, a target vertical stress close to the swelling pressure is selected to limit swelling during the soaking stage. Accordingly, OEDO-01a, OEDO-01b and OEDO-02 are soaked under a vertical stress of 0.4 MPa. A lower vertical stress of 0.24 MPa is adopted for OEDO-11 in order to approach the swelling pressure measured on a vertical assembly of two blocks (see Section 3.5 of this chapter) and remains below the apparent preconsolidation pressure of the material.

In order to study the mechanical compressibility of the material under constant initial water content, two samples (OEDO-01a and OEDO-01b) are loaded up to 1.6 MPa and unloaded to 0.4 MPa prior to soaking. These two tests are also aimed at analysing the repeatability of the results. On the contrary, OEDO-02 aims at studying the influence of the preliminary loading path on the swelling behaviour and is therefore loaded to a maximal vertical stress of 0.4 MPa. Finally, after stabilisation of the vertical strain at 0.4 MPa (soaking stage), OEDO-01a is progressively unloaded to vertical stresses of 0.2 MPa and 0.1 MPa, and allowed to equilibrate under each vertical stress.

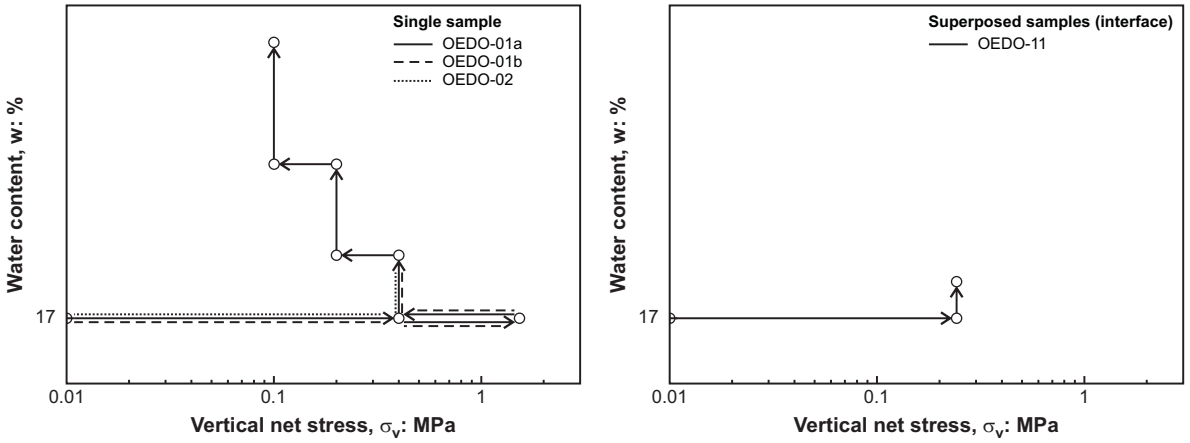

(a) Tests on unique samples.

(b) Test on superposed samples.

Figure 7.16: Stress paths followed in the conventional oedometer cells.

3.3.3 Experimental results

Figure 7.17 shows the variation of void ratio during the initial loading stage of OEDO-01a to a vertical stress of 1.6 MPa and subsequent unloading stage to 0.4 MPa, both carried out under constant water content. On loading, a clear pre- and post-yield response is observed, defining a preconsolidation pressure at around 0.51 MPa. This vertical stress value is significantly lower than the value reached during static compaction, which could be explained by a fast compaction process (during which undrained conditions prevail) and by friction between the soil sample and the compaction mould.

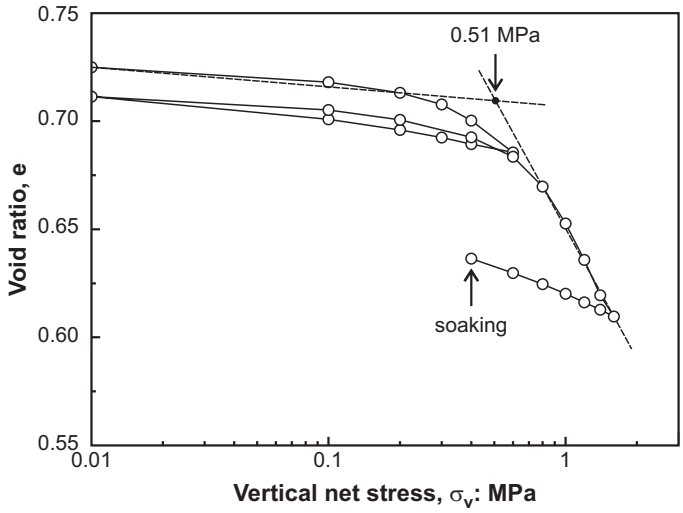

Figure 7.17: Loading - unloading path under oedometer conditions and constant water content (OEDO-01a).

Apparent swelling index and compression index for changes in vertical net stress can be determined from Figure 7.17. The swelling index κ' is measured on an unloading path

from 0.6 MPa to 0.01 MPa and is equal to

$$\kappa' = -\frac{\mathrm{d}e}{\mathrm{d}\left(\ln \sigma_v\right)} = 0.006. \tag{7.6}$$

Note that the unloading path from 1.6 MPa to 0.4 MPa gives a slightly higher value of κ', of the order of 0.02. The apparent compression index λ' is defined as the slope of the normally consolidated line in the $(e - \ln \sigma_v)$ plane. It is equal to

$$\lambda' = -\frac{\mathrm{d}e}{\mathrm{d}\left(\ln \sigma_v\right)} = 0.09. \tag{7.7}$$

Similar values are obtained after loading and unloading OEDO-01b, namely $\kappa' = 0.006$ and $\lambda' = 0.11$. However, the apparent preconsolidation pressure determined from this test is slightly lower (around 0.4 MPa), yielding larger strain and smaller void ratio before soaking (0.60 against 0.63 for OEDO-01a).

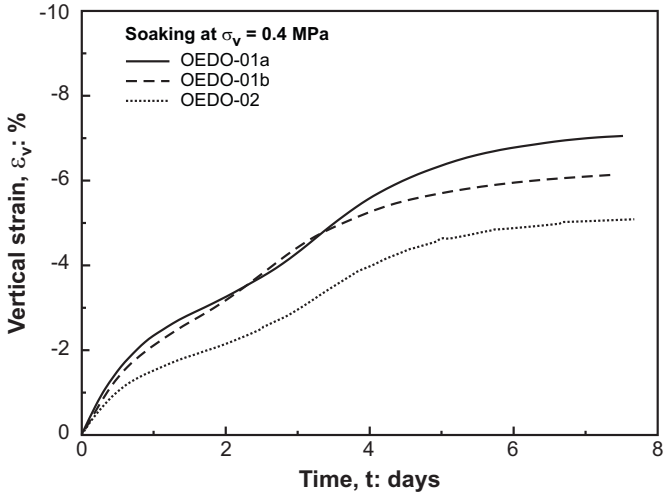

Figure 7.18: Soaking under oedometer conditions at a vertical stress of 0.4 MPa. Comparison between OEDO-01a, OED-01b and OED-02.

After loading (or unloading) to a vertical stress of 0.4 MPa, the samples are inundated under constant vertical stress. Figure 7.18 presents the evolution with respect to time of the vertical strain developed during soaking. For the three tests OED-01a, OED-01b and OED-02, the vertical strain presents an inflexion point after 2 days, with a reduction in the swelling pressure development, followed by a faster increase of displacements, and a final stabilisation after almost 6 days of hydration. This reduction in the swelling pressure development could indicate some collapse of the material, although deeper investigation is required to confirm this hypothesis. Furthermore, the final vertical strain developed by OED-02 (-5.1%), which was not loaded beyond 0.4 MPa, is lower than the vertical strain developed by OED-01a and OED-01b (-6.7% and -5.6% respectively), despite the similar void ratios reached before soaking (0.63, 0.60 and 0.62 for OEDO-01a, OEDO-01b and OEDO-02 respectively). However, it is likely that loading results in a more stable structure that is less sensitive to collapse phenomena, which would explained the observed difference of vertical strain. Finally, comparison between tests OED-01a and OED-01b

indicates a relatively good repeatability of the experimental results, with a difference in the final vertical strain of 1.1%.

Figures 7.19(a) and 7.19(b) show the evolution of vertical strain and void ratio developed on soaking at vertical stresses of 0.4 MPa, 0.2 MPa and 0.1 MPa. For each unloading stage, the vertical load was maintained until stabilisation of the vertical strain. As shown in Figure 7.19, the swelling strain developed on soaking is all the more important that the vertical stress is low. Accordingly, longer equalisation times are required for each unloading stage. The final swelling strain developed by OEDO-01a on soaking under 0.4 MPa is about -6.8% after 7.5 days, while the vertical strains developed under 0.2 MPa and 0.1 MPa are respectively -18.8% after 10 days (since unloading to 0.2 MPa) and -40.0% after 16 days. It is possible to compute an apparent swelling index κ' from this unloading path. Interestingly, this swelling index, equal to 0.4, appears to be significantly higher than the index determined upon loading or unloading under constant water content.

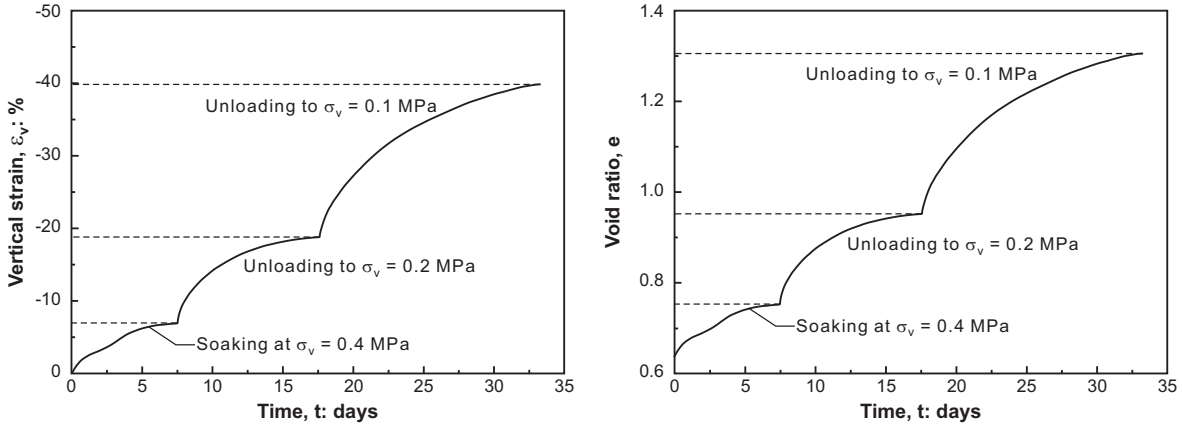

(a) Evolution of vertical strain.

(b) Evolution of void ratio.

Figure 7.19: Soaking under oedometer conditions at vertical stresses of 0.4 MPa, 0.2 MPa and 0.1 MPa (OEDO-01a).

Figure 7.20 presents the experimental results for OEDO-11, which aims at studying the influence of an interface between two soil samples. Figure 7.20(a) depicts the evolution of the vertical strain during the loading and unloading paths to a vertical stress of 0.24 MPa. The total vertical strain after loading to 0.24 MPa reaches 1.15%, which is hardly higher than the strain encountered by OEDO-01a. At the investigated stress level and with the equipment used in this investigation, it is therefore difficult to assess any conclusion concerning the compressibility behaviour of the interface.

Figure 7.20(b) presents the evolution of the vertical strain during soaking of OEDO-11 under a vertical stress of 0.24 MPa. As no soaking test of a single sample under this vertical stress is performed, comparison between OEDO-11 and the previous tests is difficult. Yet two remarks can be made. First of all, the final vertical strain developed by OEDO-11 reaches -3.1%, which is significantly lower than the -5% developed by OEDO-02 after soaking at a vertical stress of 0.4 MPa. This behaviour could either be caused by a higher sensitivity to collapse of the K/S mixture hydrated under low vertical stress,

or a higher compressibility of the interface upon wetting (or a combination of both). In any case, considerably slower hydration kinetics is observed for OEDO-11 compared to the previous tests on a single sample. Indeed, more than 25 days are required before stabilisation of the vertical strain, against 7 days for OEDO-02.

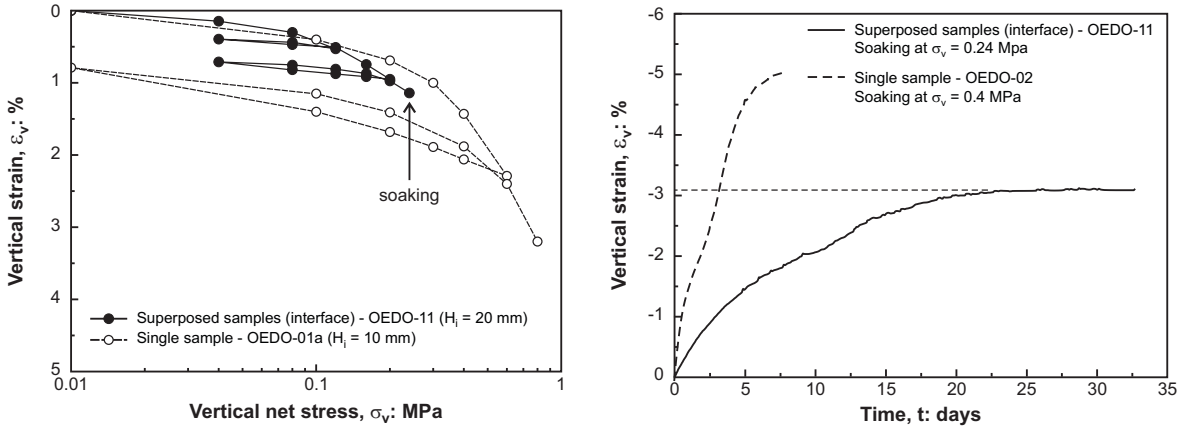

(a) Loading - unloading path under constant water content.

(b) Soaking under a vertical net stress of 0.24 MPa.

Figure 7.20: Influence on the interface on loading – unloading and soaking paths (OEDO-11). Comparison between the responses on a single sample and superposed samples.

3.4 Controlled-suction oedometer tests

3.4.1 Experimental equipment

The basic scheme of the controlled-suction oedometer cell is presented in Figure 7.21. In this cell, matric suction is imposed by means of the axis translation technique (Hilf, 1956). This technique involves the translation of the reference air pressure u_g, which can be viewed as an artificial increase in the atmospheric pressure under which the test is performed. Accordingly, in order to impose a given matric suction s, the water pressure is increased to a (positive) value $u_w = u_g - s$.

Inside the oedometer cell, the soil sample is sandwiched between two porous discs. Pore air pressure is applied to the top of the sample through a coarse porous disc, while the water pressure system is connected to the lower porous disc. A saturated high air-entry value cellulose acetate membrane (Spectra/Pormembrane MWCO: 6000-8000) is used as an interface between the soil specimen and the pore water pressure system (lower porous disc). This membrane acts as a link between the pore water in the soil and water in the measuring system, and avoids the passage of free air into the water compartment. Water pressure, as well as inflow and outflow volume changes, are controlled by a pressure/volume controller (GDS). A vertical pressure is applied to the soil sample by means of compressed air acting on a loading platen. A 1-mm thick rubber membrane separates the diaphragm pressure chamber from the pore air pressure chamber. During the test, the vertical displacement is measured using a LVDT.

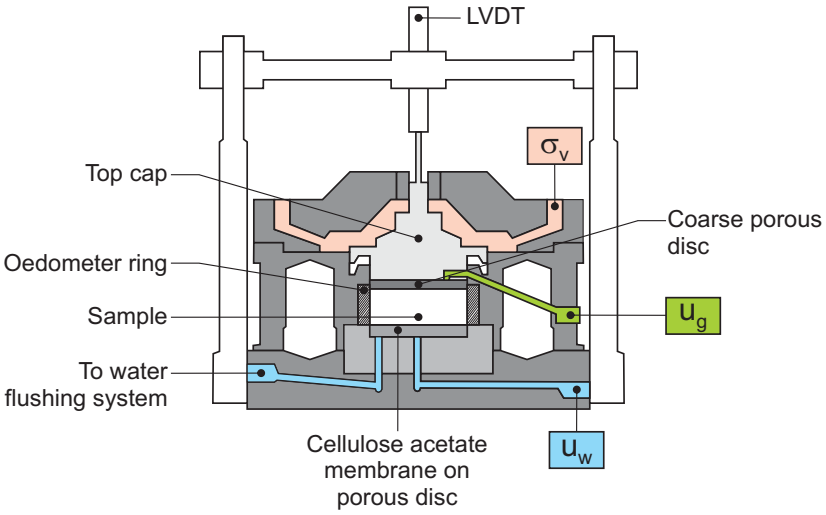

Figure 7.21: Controlled-suction oedometer cell used in the investigation (Romero & Jommi, 2008).

3.4.2 Experimental programme

Three controlled-suction oedometer tests, referred to as CSuc-01, CSuc-02a and CSuc-02b, are performed to characterize the swelling behaviour of the K/S mixture during wetting under vertical load (Figure 7.22). Starting from as-compacted conditions, CSuc-01 and CSuc-02a follow single-step wetting paths to a suction of 0.01 MPa and under net vertical stresses of 0.4 MPa and 0.2 MPa respectively. In order to deeper analyse the swelling process in the low-suction range, CSuc-02b consists in the progressive hydration of the material under a vertical net stress of 0.2 MPa. For this test, six suction steps are considered, namely 1.3 MPa, 0.8 MPa, 0.5 MPa, 0.3 MPa, 0.1 MPa and 0.01 MPa. Each suction step is maintained until reaching steady state conditions from soil volume change readings.

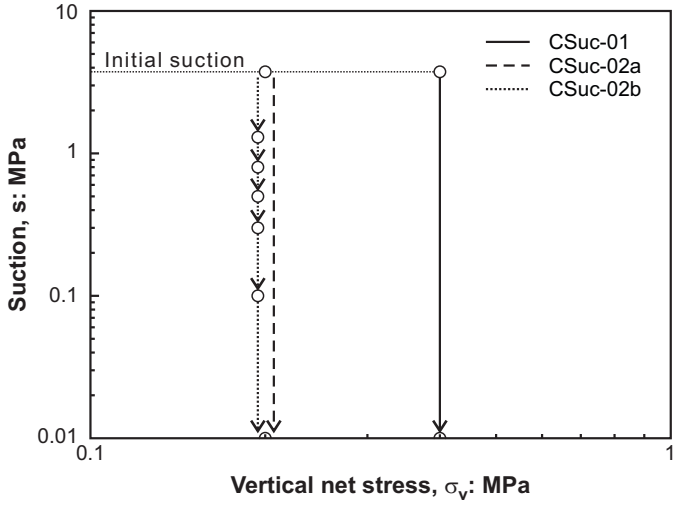

Figure 7.22: Stress paths followed in the controlled-suction oedometer cell.

In order to reach the different suction values, the air overpressure method is followed. Accordingly, the air pressure is increased and maintained constant during the whole test. An air pressure of 1.4 MPa is used together with a total vertical stress (diaphragm pressure) of 1.8 MPa and 1.6 MPa respectively for CSuc-01 (σ_v = 0.4 MPa) and CSuc-02a and CSuc-02b (σ_v = 0.2 MPa). Matric suction is then regulated by changing the pore water pressure.

3.4.3 Experimental results

Figure 7.23 presents the evolution of the vertical swelling strain undergone by the sample during the single-step wetting stage to a suction on 0.01 MPa and at a vertical stress of 0.4 MPa (CSuc-01 test). Six days are considered for matric suction equalisation along the wetting path. The final vertical strain experienced by the material is equal to -4.7%. Figure 7.23 also shows the comparison with the single-step soaking test at the same vertical stress presented in Section 3.3. A good agreement between both results is observed, not only in terms of the final deformation, but also in the shape of the time evolution of the swelling strain. The final water content of the soil sample is determined after oven-drying and is equal to 27.01% which confirms full saturation of the sample.

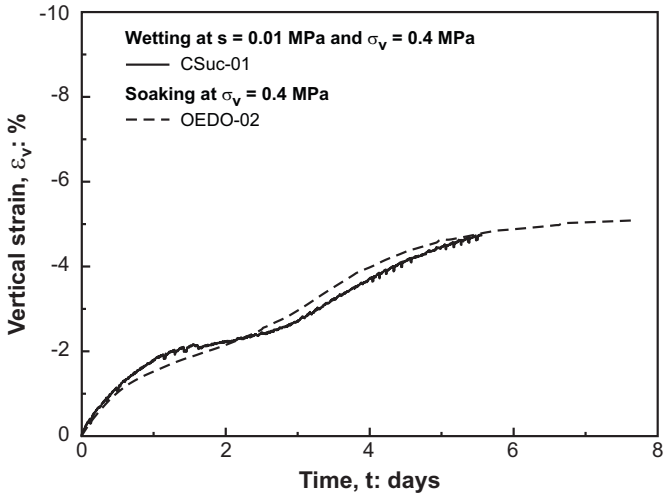

Figure 7.23: Wetting under oedometer conditions at a vertical stress of 0.4 MPa and a suction of 0.01 MPa (CSuc-01). Comparison with the oedometric soaking test OED-02.

Saturation at a lower vertical stress of 0.2 MPa is studied in CSuc-02a and CSuc-02b tests. Figure 7.24 presents the evolution of the vertical swelling strain undergone by the sample during the single-step wetting stage to a suction on 0.01 MPa (CSuc-02a test). The final vertical strain experienced by the material is equal to -11.78% and is thus lower than the strain experienced by OEDO-01a during soaking at 0.2 MPa. Possible explanations for this observation include an incomplete saturation of the material (although the injected water has shown some stabilization), different initial conditions (especially in terms of bentonite content) or the difference of the followed stress path.

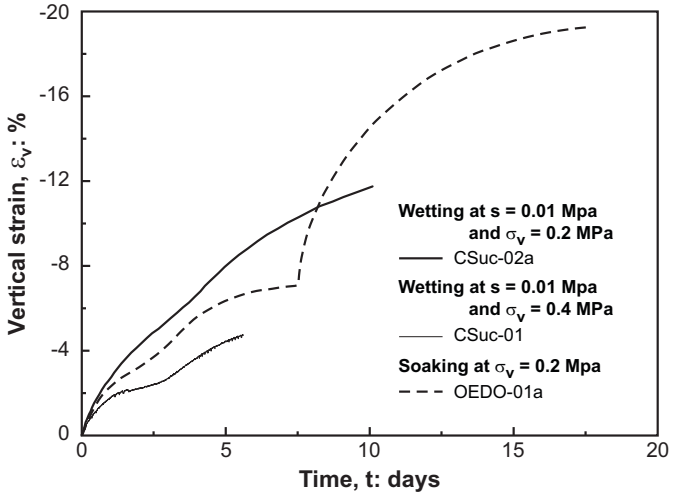

Figure 7.24: Wetting under oedometer conditions at a vertical stress of 0.2 MPa and a suction of 0.01 MPa (CSuc-01). Comparison with CSuc-01 and the oedometric soaking test OED-02.

Figure 7.25 presents the evolution of the vertical strain along the different steps on wetting to a suction of 0.01 MPa at a vertical net stress of 0.2 MPa. The total swelling undergone during this multi-step process was -8.95%, which should be compared to the swelling of -11.78% displayed by CSuc-02a during single-step wetting at the same vertical net stress. A fairly good agreement is thus obtained between the two tests.

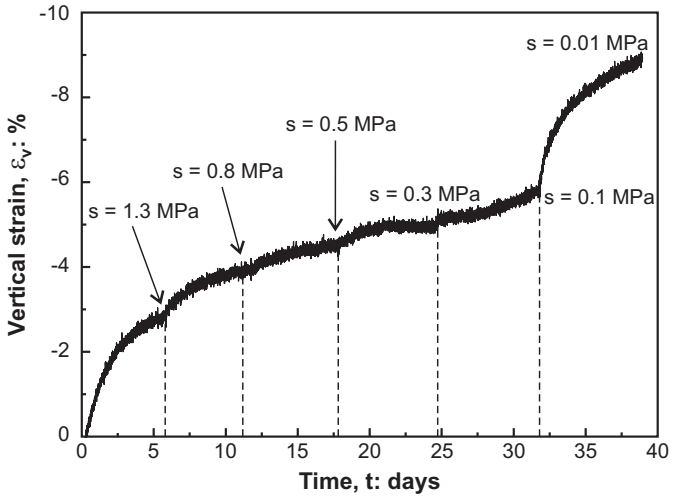

Figure 7.25: Multi-stage wetting under oedometer conditions at a vertical stress of 0.2 MPa (CSuc-02b).

Finally, Figure 7.26 presents the experimental results of CSuc-02b in terms of evolutions of the void ratio and water content with suction. The slope of the $(\ln s - e)$ graph, obtained after linear regression of the experimental data, is equal to -0.014. It can be used as a first estimate of the κ_s parameter of the mechanical model. However, Figure 7.26 does not show stabilization of the void ratio when decreasing suction. Yet stabilization of the water content is not clear neither.

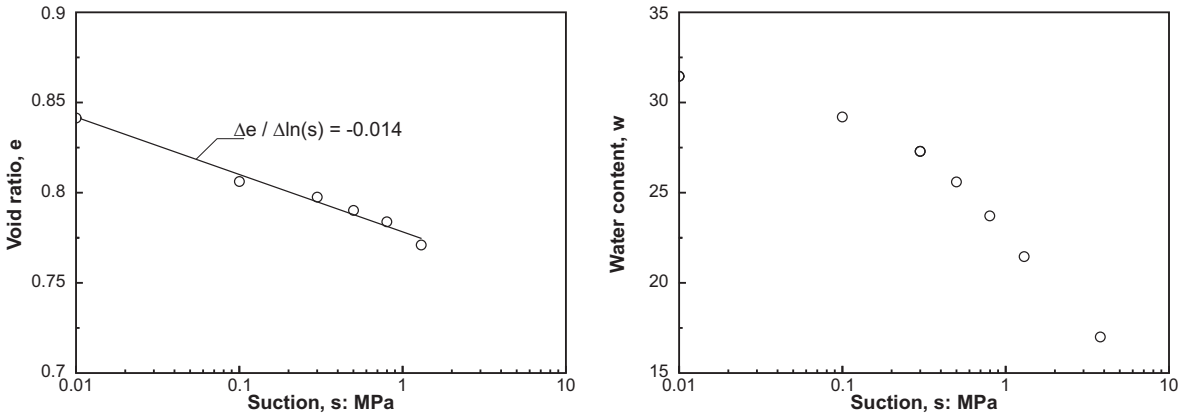

(a) Void ratio.

(b) Water content.

Figure 7.26: Multi-stage wetting under oedometer conditions at a vertical stress of 0.2 MPa (CSuc-02b). Evolution of void ratio and water content with decreasing suction.

3.5 Swelling pressure tests

3.5.1 Experimental equipment

Single-step soaking tests under constant volume conditions are performed to complement the information of swelling pressure development starting from as-compacted conditions. A special isochoric cell (Hoffmann, 2005) is used for these tests. It is constituted by top and bottom caps with fixed porous discs, and an oedometer ring (50 mm in diameter, 20 mm high) in which the soil is compacted. Both top and bottom caps have water inlet/outlet, and sealing between the oedometer ring and the caps is ensured by rubber Viton O-rings. Injection water pressure, as well as inflow volume changes, are controlled by a pressure/volume controller (GDS).

In order to record the swelling pressure developed on soaking, a load cell is placed between the isochoric cell and a high rigidity frame (Figure 7.27). To ensure good contacts between the different elements (the load cell, the top cap, the cell and the bottom cap), a small initial vertical stress is applied before hydration.

3.5.2 Experimental programme

One swelling pressure test, referred to as SP-01, is performed on the bentonite/sand mixture compacted at a dry density of 1.60 Mg/m^3 and an initial water content of 16.5%. Two additional tests, referred to as SP-02a and SP-02b, are carried out to analyse the influence of an interface between two superposed samples and verify the repeatability of the measurements. A low back-pressure of 0.04 MPa at the bottom end was used.

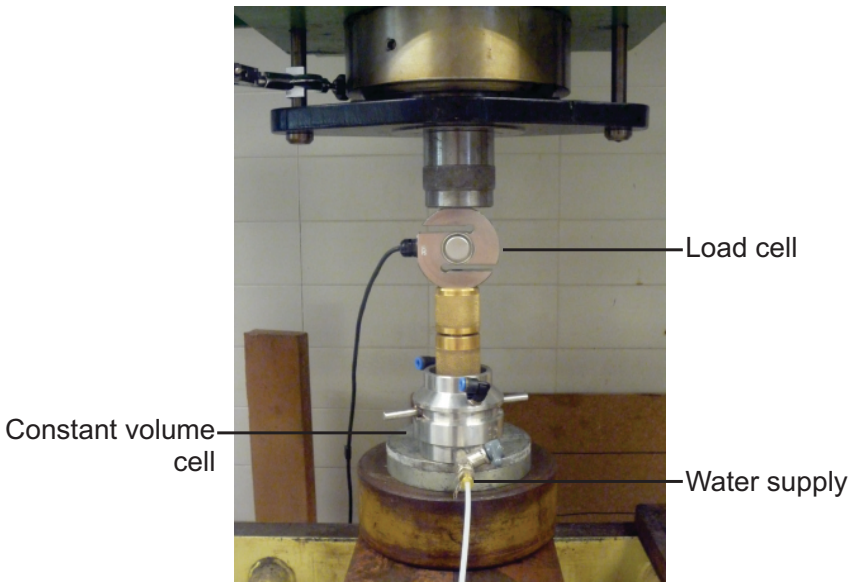

Figure 7.27: Experimental equipment used for the swelling pressure tests.

3.5.3 Experimental results

Figure 7.28 presents the evolution of the swelling pressure during water infiltration for the different swelling pressure tests. For the three samples, the swelling pressure increases rapidly, with more than 90% of the final swelling pressure developed during the first half day. After 4 days of hydration, the swelling pressure of the bentonite-based material compacted at a dry density of 1.60 Mg/m^3 is equal to 0.42 MPa.

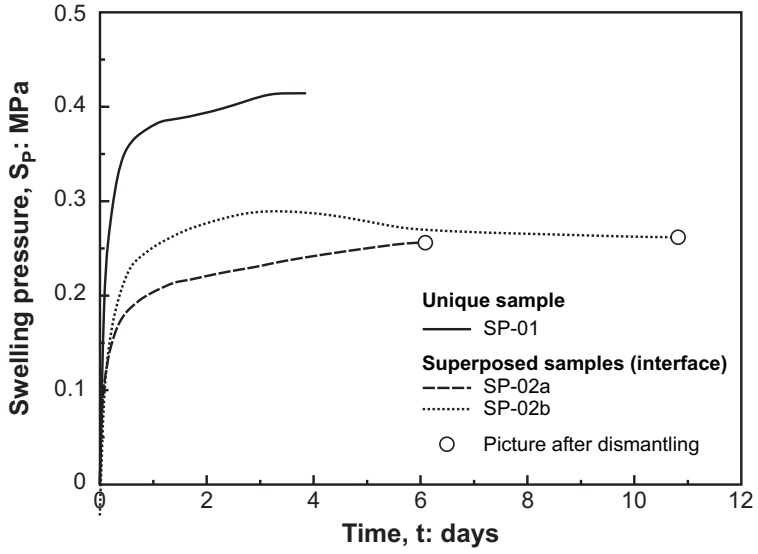

Figure 7.28: Evolution of the swelling pressure during soaking under constant volume conditions.

The swelling pressures developed by SP-02a (superposed samples) during hydration is significantly lower than the one measured on the unique sample SP-01. After 6 days of hydration, a swelling pressure 0.256 MPa is measured on SP-02a. After dismantling of the

test, it appears that the sample assembly is not fully saturated. Figure 7.29(a) shows the state of the sample. A clear difference is observed between the bottom part of the sample, which was in direct contact with the saturated porous stone, and the upper part of the sample. Sealing between both samples of the assembly is not fully achieved and they can be separated manually. In order to quantify the state of hydration of the assembly, small samples are taken at the bottom and top of the assembly, and their water content and total suction are measured. Total suction was measured using a dew-point chilled-mirror WP4 while the water content was determined after oven-drying. For the lower part of the sample, a water content of 39.3% and a total suction of 0.9 MPa indicate full saturation of the material. However, lower water content and higher total suction are measured at the upper part of the sample, pointing out that the sample is not yet saturated.

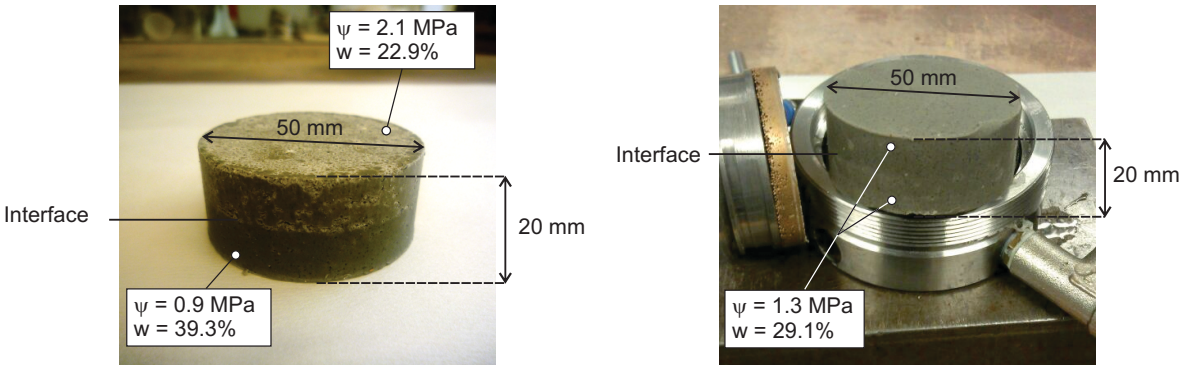

(a) SP-02a. (b) SP-02b.

Figure 7.29: SP-02a and SP-02b samples after dismantling.

In order to better analyse the influence of the interface between the blocks of the assembly, the swelling pressure test is repeated and the sample (SP-02b) is allowed to hydrate during a longer time. Figure 7.28 presents the evolution the swelling pressure during hydration. The experimental data shows a clear stabilisation of the swelling pressure to 0.261 MPa after 6 days, but hydration was maintained during a total of 11 days. Figure 7.29(b) shows the state of the sample after 11 days of hydration. Rather good sealing of the interface is observed. Small samples from the upper and bottom part of the assembly are taken and their water content and suction are measured together. An average water content of 29.1% is measured, corresponding to a total suction of 1.3 MPa, and indicates saturation of the assembly.

3.6 Synthesis of the experimental results

In this chapter, the results of an experimental campaign, carried out at the Technical University of Catalonia, were presented. The different types of tests were performed in order to get a better understanding of the role and influence of interfaces in underground structures. In this section, the main outcomes of the experimental campaign are presented, with a focus on the swelling behaviour of the K/S mixture and the role of interfaces on the normal hydromechanical behaviour of assemblies.

3.6.1 Swelling behaviour

Figure 7.30 presents the results of the different hydration tests under oedometer and constant-volume conditions in a vertical stress - void ratio plot. Complementary data on controlled-suction tests presented in Section 3.4 are also included. A good agreement is obtained for the different tests performed, although a higher discrepancy is observed at lower stresses. For a dry density of 1.60 Mg/m^3 (e = 0.71), the swelling pressure of the K/S mixture is of the order of 0.42 MPa. A relationship between the vertical strain (swelling) and the vertical stress σ_v may be found within the vertical stress range investigated

$$\varepsilon_v = 0.125 \ln \left(\frac{\sigma_v}{S_{P(\varepsilon_v=0)}} \right) \tag{7.8}$$

where $S_{P(\varepsilon_v=0)}$ = 0.42 MPa is the estimated swelling pressure to ensure no expansion on soaking at constant vertical stress.

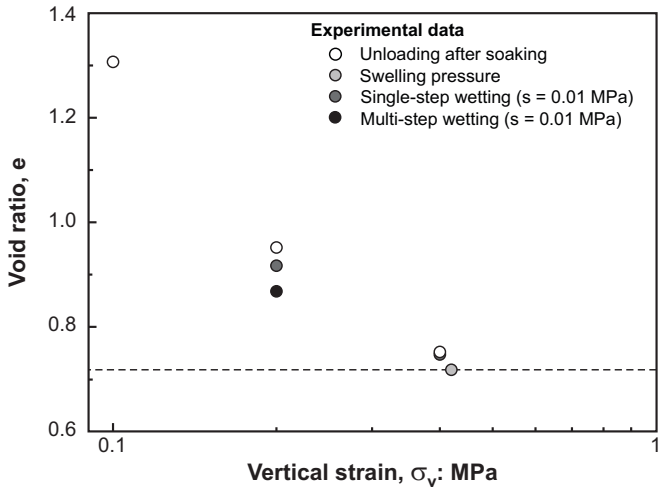

Figure 7.30: Vertical stress - void ratio relationship for the different tests performed.

The experimental results are also represented in the dry density – swelling pressure plane (Figure 7.31). For the sake of comparison, the data obtained by Dixon *et al.* (1996) are also represented. As shown in Figure 7.31, the experimental data of the present study are in the expected range of swelling pressure for the corresponding dry densities.

Finally, Table 7.2 presents a synthesis of the parameter values that can be used as first approximations in the mechanical model.

κ	κ_s	λ	p_0 (MPa)
0.006–0.02	0.014	0.09	0.51

Table 7.2: Parameters of the mechanical model for the K/S mixture.

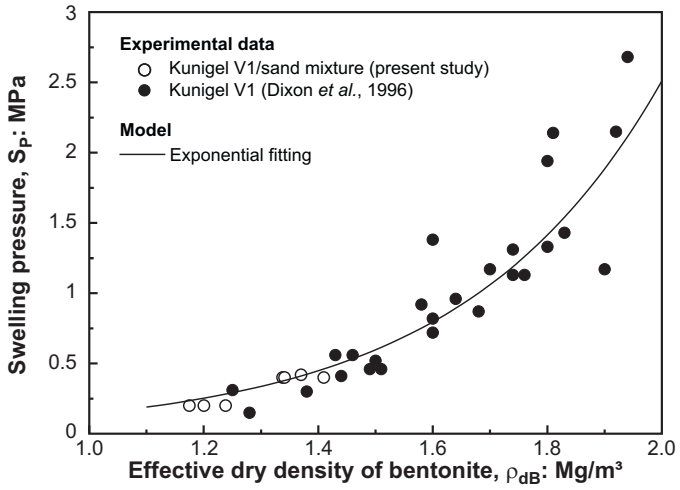

Figure 7.31: Evolution of the swelling pressure of the K/S mixture. Comparison with the experimental data of Dixon *et al.* (1996).

3.6.2 Influence of interfaces

Insights into the influence of interfaces on the hydromechanical behaviour of bentonite blocks were obtained from the soaking test OEDO-11 carried out under oedometric conditions, and from the swelling pressure tests SP-02a and SP-02b. From these tests results, the following conclusions can be drawn:

- **Swelling behaviour**: lower swelling strains and swelling pressures were detected in OEDO-11, SP-02a and SP-02b, compared to the reference tests. While this observation is in disagreement with a unique relationship between the swelling pressure and the dry density, similar observations were made by Dridi *et al.* (2013) on a compacted mixture of MX-80 bentonite and sand.

- **Saturation kinetics**: a considerably slower hydration process was observed in both soaking and swelling pressure tests. Observations from SP-02 dismantling show that the interface acts as a barrier for water flow. Indeed, the interface is likely to represent a zone of larger pores where the retention properties are modified.

While the results of the experimental campaign should be considered as preliminary results - the tests are far from being perfect -, they at least provide motivation for further investigation. The control of the initial conditions of the sample is a major issue to assess the role of interfaces. However, these conditions are not easily controlled, especially when working with a mixture of bentonite and sand. Indeed, the good and identical proportions of each material cannot be guaranteed. Further investigations should therefore preferably be carried out on a *pure* bentonite. A second major issue concerns the initial state of the contact between the samples which cannot be estimated, unless by direct measure of the assemblies height.

4 Governing equations of the interface problem

The interfaces and technological gaps observed in underground structures may be considered as geometrical discontinuities, besides material discontinuities. The mechanical displacements, water pressure and gas pressure on each side of the interface may indeed differ. However, their mechanical and hydraulic evolution cannot be considered independently and each side of the interface interacts with each other. Consequently, specific numerical tools should be employed to incorporate interfaces and technological gaps in finite element models. Indeed, when classic solid elements are used, the displacement, water pressure and gas pressure fields are implicitly assumed to be continuous between elements.

Various approaches exist for the representation of interfaces and technological gaps. A first approach consists in representing the interface zone by an equivalent continuum and using classic solid elements (Toprak *et al.*, 2013; Mokni & Barnichon, 2016) or special thin layer elements (Sharma & Desai, 1993; Wang & Wang, 2006; Wriggers *et al.*, 2013). In a second approach, which is adopted here, interfaces between materials as well as technological gaps are modelled using zero-thickness interface finite elements. While these types of elements are common in mechanics (see Goodman *et al.*, 1968; Charlier & Cescotto, 1988; Day & Potts, 1994; Habraken *et al.*, 1998; Wriggers, 2006, among others), the originality of the element used in this work is its coupled hydromechanical formulation.

The hydromechanical zero-thickness element is briefly described in this section, further description being found in Cerfontaine *et al.* (2015). As for solid elements, different types of equations govern the hydromechanical problem. They are presented in this section. Note that the description of the element is restricted to two-dimensional analysis under isothermal conditions.

4.1 Mechanical problem

4.1.1 Kinematics at the interface

The mechanical problem is a problem of contact between two deformable bodies and the evolution of their relative displacement once in contact with each other. Let us consider two deformable porous media $\mathcal{B}^1$ and $\mathcal{B}^2$ in their current configurations at time t. Their kinematics was described in Chapter 3. The boundaries of the two bodies in the current configuration are denoted $\partial\mathcal{B}^1$ and $\partial\mathcal{B}^2$ and, for each solid body ($i = 1, 2$), the Dirichlet and Neumann boundary conditions are denoted respectively $\partial\mathcal{B}^i_{\bar{x}}$ and $\partial\mathcal{B}^i_t$. The problem of contact introduces a new non-classic boundary condition on $\partial\mathcal{B}^1_c$ and $\partial\mathcal{B}^2_c$ of each solid where contact is likely to happen (Figure 7.32). According to the terminology adopted by Belgacem *et al.* (1998) and Cerfontaine *et al.* (2015), $\partial\mathcal{B}^1_c$ and $\partial\mathcal{B}^2_c$ define respectively the mortar side and the non-mortar side of the interface. A local system of coordinates $(\boldsymbol{e}_1, \boldsymbol{e}_2)$ is defined along the mortar side $\partial\mathcal{B}^1_c$, where $\boldsymbol{e}_1$ represents the normal to the surface.

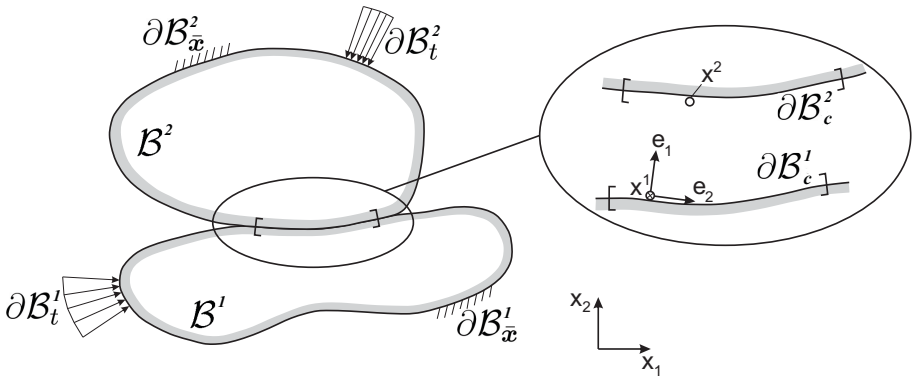

Figure 7.32: Statement of the mechanical problem.

The gap function g_N measures the distance between the two bodies $\mathcal{B}^1$ and $\mathcal{B}^2$. It is defined as

$$g_N = \left(\boldsymbol{x}^2 - \bar{\boldsymbol{x}}^1\right) \cdot \bar{\boldsymbol{e}}_1 \tag{7.9}$$

where $\bar{\boldsymbol{x}}^1$ is the closest point projection of a point of $\boldsymbol{x}^2$ of the boundary $\partial\mathcal{B}^2_c$ onto $\partial\mathcal{B}^1_c$, and $\bar{\boldsymbol{e}}_1$ is a unit normal vector at point $\bar{\boldsymbol{x}}^1$. If g_N is positive, the two bodies $\mathcal{B}^1$ and $\mathcal{B}^2$ are not in contact. Contact between the two bodies occurs once that g_N becomes null or negative. In particular, if $g_N = 0$, the contact is said to be ideal. If g_N is negative, the gap function g_N defines an interpenetration distance.

The definition of a relative tangential displacement between two points in the plane of contact has no meaning in the field of large displacement (Habraken *et al.*, 1998; Cerfontaine *et al.*, 2015). Instead normal and tangential velocities are defined in the local system of coordinates. For frictional contact, the relative tangential velocity $\dot{g}_T$ at the contact interface between the to bodies is defined as

$$\dot{g}_T = \frac{\mathrm{d}}{\mathrm{d}t}\left[\bar{\boldsymbol{e}}_2 \cdot \left(\boldsymbol{x}^2 - \bar{\boldsymbol{x}}^1\right)\right] \tag{7.10}$$

where the superior dot denotes a time derivative and $\bar{\boldsymbol{e}}_2$ is a tangential unit vector at point $\bar{\boldsymbol{x}}^1$. The normal and tangential velocities can be gathered into the vector $\dot{\boldsymbol{g}}$ such that

$$\dot{\boldsymbol{g}} = \dot{g}_N \boldsymbol{e}_1 + \dot{g}_T \boldsymbol{e}_2 = \begin{bmatrix} \dot{g}_N & \dot{g}_T \end{bmatrix}^T \tag{7.11}$$

where the superscript T stands for the transpose operator.

4.1.2 Contact constraint and regularization technique

Contact between two solid bodies comes along with a contact stress vector $\boldsymbol{\sigma_c}$ along the common boundary of the two bodies. The vector $\boldsymbol{\sigma_c}$ is described in the local system of coordinates such that

$$\boldsymbol{\sigma_c} = -p_N \boldsymbol{e}_1 + \tau \boldsymbol{e}_2 = \begin{bmatrix} -p_N & \tau \end{bmatrix}^T \tag{7.12}$$

where p_N is the normal pressure and τ is the shear stress in the plane of the interface. The normal contact constraint ensures that two solids in contact do not overlap each other.

The ideal contact constraint is summarized into the Hertz-Signorini-Moreau condition (Wriggers, 2006) given by

$$g_N \geq 0 \qquad \text{and} \qquad p_N \geq 0 \qquad \text{and} \qquad p_N g_N = 0. \tag{7.13}$$

If there is no contact, the gap function g_N is positive and the contact pressure p_N is null. On the other hand, when contact arises, the gap function is null and the contact pressure is positive.

From a computational point of view, the preceding relationship may be difficult to ensure. Furthermore, when dealing with geomaterials, the interpenetration of two bodies has a physical basis, which is the progressive crushing of the interface asperities. Therefore, the penalty method (Habraken *et al.*, 1998) is used to regularize the constraint by authorizing an interpenetration of the solids in contact independently on the roughness of the surfaces. The related pressure p_N is a function of the interpenetration through the penalty coefficient K_N

$$\dot{p}_N = -K_N \dot{g}_N \tag{7.14}$$

where the minus sign ensures the contact pressure is positive when interpenetration increases, i.e. $g_N < 0$ and $\dot{g}_N < 0$. If the penalty method is employed, interpenetration is necessary to generate contact pressure and the gap function becomes negative. The law may thus be considered as a constitutive law (Gens *et al.*, 1990) where the penalty coefficient plays the role of a constitutive parameter. Note that the penalty coefficient may either be chosen constant or expressed as a function of the stress state or interface opening (Gens *et al.*, 1990; Bart, 2000; Alonso *et al.*, 2013) (Figure 7.33).

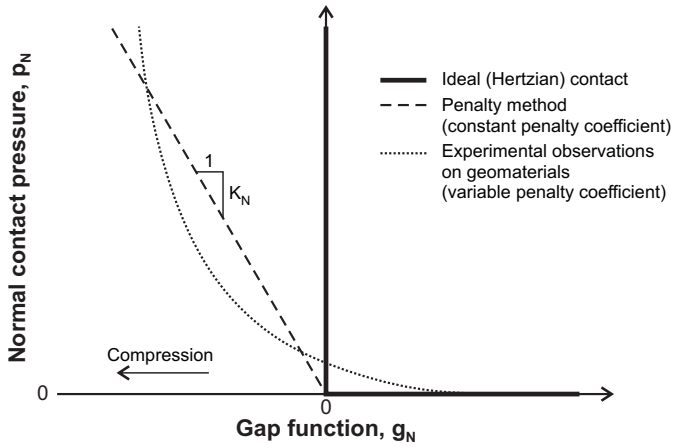

Figure 7.33: Relationship between the gap function g_N and the normal contact pressure p_N.

When both sides of an interface are in contact, two situations should be considered from a frictional point of view, namely the stick and the slip states. In the stick state, two points in contact are not allowed to move in the tangential direction, so that $\dot{g}_T = 0$. On the other hand, in the slip state, a relative tangential displacement exists between both sides of the interface. Mathematically, this condition can be expressed as

$$\dot{g}_T^{sl} \geq 0 \qquad \text{and} \qquad f_c(\boldsymbol{\sigma_c}) \leq 0 \qquad \text{and} \qquad \dot{g}_T^{sl} f_c(\boldsymbol{\sigma_c}) = 0 \tag{7.15}$$

where $\dot{g}_T^{sl}$ is the variation of the non-recoverable displacement in the tangential direction. It is related to the variation of tangential displacement

$$\dot{g}_T = \text{sign}\,(\dot{\tau})\,\dot{g}_T^{sl} \tag{7.16}$$

with $\text{sign}\,(\dot{\tau})$ the sign function of $\dot{\tau}$.

The transition from stick to slip state is ruled by a criterion $f_c(\boldsymbol{\sigma_c})$ defining a threshold of admissible shear stress. The slip state involves a relative tangential displacement in the plane of the interface. In this work, the Coulomb criterion is adopted as relatively smooth interfaces are considered (see Section 2.1). It reads

$$f_c(\boldsymbol{\sigma_c}) = |\tau| - \mu p_N \tag{7.17}$$

where $|\tau|$ is the norm of the shear stress τ and μ is the friction coefficient. Perfect plasticity is considered. Accordingly, once that the Coulomb criterion is reached, relative displacement of the interfaces continues without any further increase of the shear stress, unless the normal stress is increased. In addition, a non-associated flow rule ($g_c(\boldsymbol{\sigma_c}) = 0$) is assumed, so that dilatancy of the interface is disregarded.

Finally, the ideal stick state $\dot{g}_T = 0$ is also regularised by the penalty method, i.e. a relative displacement is allowed. Thence, the relation between the shear stress and the tangential variation of displacement reads

$$\dot{\tau} = K_T \dot{g}_T \tag{7.18}$$

where K_T is a penalty coefficient.

Consequently, the mechanical behaviour of the interface is described by the incremental relationship between stress and displacements

$$\dot{\boldsymbol{\sigma}}_c = \dot{\boldsymbol{\sigma}}_c\,(\boldsymbol{g}, \dot{\boldsymbol{\sigma}}_{\boldsymbol{c}})\,. \tag{7.19}$$

The constitutive behaviour at the interface between two bodies can be split into constitutive relations for the normal and the tangential directions and written in the form

$$\dot{\boldsymbol{\sigma}}_c = \begin{bmatrix} -K_N & 0 \\ 0 & K_T \end{bmatrix} \cdot \dot{\boldsymbol{g}} = \boldsymbol{D_c^e} \cdot \dot{\boldsymbol{g}} \tag{7.20}$$

where $\boldsymbol{D_c^e}$ is equivalent to the elastic compliance tensor. When the interface reaches the slip state, an elastoplastic compliance tensor $\boldsymbol{D_c^{ep}}$ is defined such that

$$\dot{\boldsymbol{\sigma}}_c = \begin{bmatrix} -K_N & 0 \\ -\mu K_N \frac{\tau}{|\tau|} & 0 \end{bmatrix} \cdot \dot{\boldsymbol{g}} = \boldsymbol{D_c^{ep}} \cdot \dot{\boldsymbol{g}} \tag{7.21}$$

where $|\tau|$ is the absolute value of τ.

4.1.3 Continuum formulation

Each solid body $\mathcal{B}^i$ satisfies the balance of momentum equation (3.20) and the boundary conditions (3.66) and (3.67). The solution to the mechanical contact problem consists in finding the field of displacement $\boldsymbol{u}$ for all points $\boldsymbol{x} \in \mathcal{B}^i$ verifying these equations and subjected to the contact constraints (7.13) and (7.15).

For any kinematically admissible virtual velocity field $\delta\dot{\boldsymbol{u}}$ on $\mathcal{B}^i$, Equation (3.71) becomes

$$\sum_{i=1}^{2}\left[\int_{\mathcal{B}^i}\boldsymbol{\sigma_t}\cdot\nabla\left(\delta\dot{\boldsymbol{u}}\right)\mathrm{d}\Omega\right]=\sum_{i=1}^{2}\left[\int_{\mathcal{B}^i}\boldsymbol{b}\cdot\delta\dot{\boldsymbol{u}}\mathrm{d}\Omega+\int_{\partial\mathcal{B}_t^i}\bar{\boldsymbol{t}}\cdot\delta\dot{\boldsymbol{u}}\mathrm{d}\Gamma+\int_{\partial\mathcal{B}_c^i}\boldsymbol{\Sigma}_{\boldsymbol{c}}^i\cdot\delta\dot{\boldsymbol{u}}\mathrm{d}\Gamma\right] \quad (7.22)$$

where $\boldsymbol{b}$ are the body forces, $\bar{\boldsymbol{t}}$ are the imposed tractions and $\boldsymbol{\Sigma}_{\boldsymbol{c}}^i$ is the projection of the local stress vector $\boldsymbol{\sigma}_{\boldsymbol{c}}^i$ in the global coordinates. The equality of Equation (7.22) is enforced when the contact area $\partial\mathcal{B}_c^i$ is known. The last term on the right hand side of Equation (7.22) is the mechanical contact contribution to external virtual power.

4.2 Multiphase flow problem

4.2.1 Kinematics at the interface

Let us consider a discontinuity between two porous media in its current configuration (Figure 7.34). This could represent for example an interface between bentonite blocks or a technological gap between a bentonite buffer and the host rock. This discontinuity creates a preferential pathway for longitudinal fluid flow and a volume for fluid storage. Moreover, there is a transversal fluid flow between the bentonite and the discontinuity.

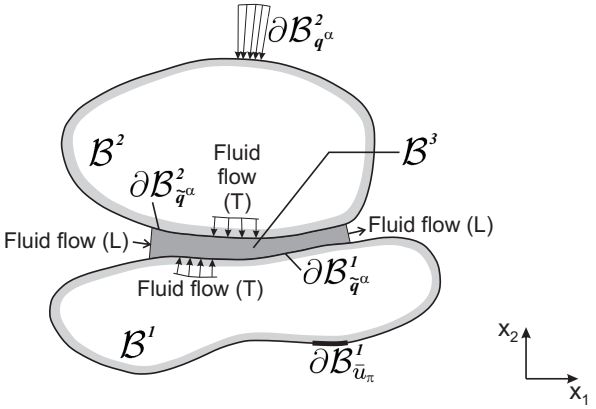

Figure 7.34: Statement of the multiphase flow problem. u_π denotes the water or gas pressure and q^α, the total water or air mass flux.

There is a conceptual difference between the treatment of the mechanical and flow contact problems. The mechanical contact constraint consists of a non-zero pressure p_N applied along the contact zone between two solids. On the other hand, the opening of the discontinuity creates a gap g_N filled with water and air. This gap creates a new volume $\mathcal{B}^3$ in which fluid flow takes place. It is bounded by the two porous media. Their boundary

are termed $\mathcal{B}^1_{\tilde{q}^\alpha}$ and $\mathcal{B}^2_{\tilde{q}^\alpha}$ with $\tilde{q}^\alpha$ denotes the total water or air mass flux on the boundary. Therefore $\mathcal{B}_{\tilde{q}^\alpha}$ represents a boundary where the solids are close enough, fluid interaction holds and mechanical contact is likely to happen. It always includes the contact zone $\partial\mathcal{B}_c$.

$\mathcal{B}^3$ is modelled as an equivalent porous medium. Flows of water and air exist both longitudinally (L) and transversally (T) between the inner volume $\mathcal{B}^3$ and both adjacent porous media $\mathcal{B}^1$ and $\mathcal{B}^2$ (Figure 7.35). This transversal flow is a function of the difference of pressure between them. It introduces a non-classic boundary condition on $\mathcal{B}_{\tilde{q}^\alpha}$ since neither the pressure nor the flux is imposed.

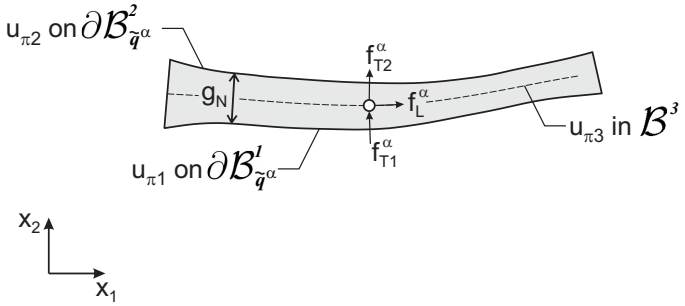

Figure 7.35: Definition of the longitudinal and transversal water and air fluxes.

4.2.2 Fluid flow formulation

As mentioned in the previous section, longitudinal and transversal fluid flows, as well as fluid storage, take place in the interface. In order to describe these phenomena, a three-node formulation is adopted. Accordingly, the fluid pressures on each side of the interface (u_{w1} and u_{w2} for water, u_{g1} and u_{g2} for gas) and the inner fluid pressure (u_{w3} and u_{g3} for water and gas respectively) are the fluid variables. The underlying hypothesis is that the field of pressure is homogeneous inside the interface.

At each point within the interface, three mass fluxes of water are defined (Figure 7.35), namely

- one longitudinal flux f^w_L in the local tangential direction of the interface,
- two transversal fluxes f^w_{T1} and f^w_{T2} in the local normal direction.

The longitudinal flux f^a_L and transversal fluxes f^a_{T1} and f^a_{T2} are defined accordingly for air.

4.2.2.1 Longitudinal fluxes

A combination of advective and non-advective fluxes is considered in both liquid and gas phases of the interface. Advective fluxes are associated to the phase movements, while non-advective fluxes are associated to the motion of species within phases. The total longitudinal mass fluxes of water and air are given respectively by

$$f^w_L = \rho_w q_{lL} + \rho_v q_{gL} + i^w_{gL} \tag{7.23}$$

$$f_L^a = \rho_a q_{gL} + \rho_l^a q_{lL} + i_{gL}^a + i_{lL}^a \tag{7.24}$$

where ρ_w, ρ_v, ρ_a and ρ_l^a are the densities of liquid water, water vapour, dry air and dissolved air respectively. q_{lL} and q_{gL} are the longitudinal advective fluxes of the liquid and gas phases respectively, and i_{gL}^w, i_{gL}^a and i_{lL}^a are the longitudinal diffusive fluxes of water vapour, dry air and dissolved air. Note that, as for the formulation of fluid flow in the solid elements, water diffusion in the liquid phase is neglected due to the small amount of dissolved air.

The generalized Darcy's law is assumed to reproduce the local longitudinal advective fluid flow of both liquid and gas phases in the interface. The longitudinal mass fluxes of the liquid and gas phases are given by

$$q_{lL} = -\frac{k_{wL}}{\mu_w} \left(\nabla_{\boldsymbol{e}_2} u_w - \rho_w g \nabla_{\boldsymbol{e}_2} x_2 \right) \tag{7.25}$$

$$q_{gL} = -\frac{k_{gL}}{\mu_g} \left(\nabla_{\boldsymbol{e}_2} u_g - \rho_g g \nabla_{\boldsymbol{e}_2} x_2 \right) \tag{7.26}$$

where k_{wL} and k_{gL} are the water and gas longitudinal permeabilities of the partially saturated interface, μ_w and μ_g are the dynamic viscosities of liquid water and the gas phase respectively, ρ_g is the density of the gas phase, g is the gravity acceleration and $\nabla_{\boldsymbol{e}_2}$ is the gradient in the direction $\boldsymbol{e}_2$. In these equations, the water and gas longitudinal permeabilities may be expressed as the product of a relative water or gas permeability and a permeability for saturated or dry conditions.

The longitudinal diffusive fluxes are governed by Fick's law. The diffusive fluxes of water vapour and dissolved air read

$$i_{gL}^w = -D_g^{w*} \rho_g \nabla_{\boldsymbol{e}_2} \left(\frac{\rho_v}{\rho_g} \right) = -i_{gL}^a \tag{7.27}$$

$$i_{lL}^a = D_l^{a*} \rho_w \nabla_{\boldsymbol{e}_2} \left(\frac{\rho_l^a}{\rho_w} \right) \tag{7.28}$$

where D_g^{w*} and D_l^{a*} are the effective diffusion coefficients of water vapour and dissolved air in the interface.

4.2.2.2 Transversal fluxes

The interface element used in this work belongs to the family of zero-thickness elements. Accordingly, the concept of pressure gradient through the interface is meaningless and the notion of pressure drop should be used instead. By analogy with the generalized Darcy's law, the transversal mass fluxes of water are assumed to be proportional to the drop of pressure between each side of the interface and the inside. They are expressed as

$$f_{T1}^w = t_{wT1} \left(u_{w1} - u_{w3} \right) \rho_w \tag{7.29}$$

$$f_{T2}^{w} = t_{wT2}\left(u_{w3} - u_{w2}\right)\rho_{w} \tag{7.30}$$

where t_{wT1} and t_{wT2} are the transversal transmissivities for water flow through the partially saturated interface.

Accordingly, the transversal mass fluxes of air are given by

$$f_{T1}^{a} = t_{gT1}\left(u_{g1} - u_{g3}\right)\rho_{a} \tag{7.31}$$

$$f_{T2}^{a} = t_{gT2}\left(u_{g3} - u_{g2}\right)\rho_{a} \tag{7.32}$$

where t_{wT1} and t_{wT2} are the transversal transmissivities for gas flow through the partially saturated interface.

4.2.3 Continuum formulation

Each porous medium verifies the classic hydraulic equilibrium equations. Solving the contact problem consists in finding the water and gas pressure distributions on $\mathcal{B}^i$ verifying the equilibrium equations and satisfying the non-classic boundary conditions (7.29) to (7.32) over $\mathcal{B}^i_{\tilde{q}^\alpha}$. Considering a field of admissible virtual water pressure δu_w on $\mathcal{B}$, the weak formulation of the virtual power principle reads

$$\sum_{i=1}^{3}\int_{\mathcal{B}^i}\left[\dot{m}^w\delta u_w - \boldsymbol{f^w}\cdot\nabla\left(\delta u_w\right)\right]\mathrm{d}\Omega = \sum_{i=1}^{3}\left[\int_{\mathcal{B}^i} Q^w\delta u_w\mathrm{d}\Omega - \int_{\partial\mathcal{B}^i_{q^w}}\bar{q}^w\delta u_w\mathrm{d}\Gamma - \int_{\partial\mathcal{B}^i_{\tilde{q}^w}}\tilde{q}^w\delta u_w\mathrm{d}\Gamma\right] \tag{7.33}$$

where $\boldsymbol{f^w}$ is the water flux at point $\boldsymbol{x}$, $\dot{m}^w$ is the total mass of water inside the current configuration $\mathcal{B}^i$, Q^w is the water source term and $\bar{q}^w$ is the total water flux imposed at the surface $\mathcal{B}^i_{q^w}$. In the previous equation, $i = 1, 2$ corresponds to the two porous media in contact and $i = 3$ to the volume of the interface. The water flow $\tilde{q}^w$ along the boundary corresponds to the transversal fluid flows f^w_{Ti} defined in Equations (7.29) and (7.30).

Similarly, the air mass balance equations reads in a weak form

$$\sum_{i=1}^{3}\int_{\mathcal{B}^i}\left[\dot{m}^a\delta u_g - \boldsymbol{f^a}\cdot\nabla\left(\delta u_g\right)\right]\mathrm{d}\Omega = \sum_{i=1}^{3}\left[\int_{\mathcal{B}^i} Q^a\delta u_g\mathrm{d}\Omega - \int_{\partial\mathcal{B}^i_{q^a}}\bar{q}^a\delta u_g\mathrm{d}\Gamma - \int_{\partial\mathcal{B}^i_{\tilde{q}^a}}\tilde{q}^a\delta u_g\mathrm{d}\Gamma\right] \tag{7.34}$$

where $\boldsymbol{f^a}$ is the air flux at point $\boldsymbol{x}$, $\dot{m}^a$ is the total mass of air inside the current configuration $\mathcal{B}^i$, Q^a is the air source term and $\bar{q}^a$ is the total air flux imposed at the surface $\mathcal{B}^i_{q^a}$. The air flow $\tilde{q}^a$ along the boundary corresponds to the transversal fluid flows f^a_{Ti} defined in Equations (7.31) and (7.32).

The integrals over $\mathcal{B}^3$ are transformed into a surface integral over $\partial\mathcal{B}^1_{\tilde{q}^w}$ and $\partial\mathcal{B}^1_{\tilde{q}^a}$. This hypothesis is valid since it is assumed that the inner fluid pressures are constant over the aperture g_N of the interface. For $i = 3$, Equations (7.33) and (7.34) become respectively

$$\int_{\partial\mathcal{B}^1_{\tilde{q}^w}} \left[\dot{m}^w \delta u_w - f^w_L \nabla_{\boldsymbol{e}_2}(\delta u_w)\right] g_N \mathrm{d}\Gamma = \int_{\partial\mathcal{B}^1_{\tilde{q}^w}} t_{wT1}(u_{w1} - u_{w3})\rho_w \delta u_w - t_{wT2}(u_{w3} - u_{w2})\rho_w \delta u_w \mathrm{d}\Gamma \quad (7.35)$$

and

$$\int_{\partial\mathcal{B}^1_{\tilde{q}^a}} \left[\dot{m}^a \delta u_g - f^a_L \nabla_{\boldsymbol{e}_2}(\delta u_g)\right] g_N \mathrm{d}\Gamma = \int_{\partial\mathcal{B}^1_{\tilde{q}^a}} t_{gT1}(u_{g1} - u_{g3})\rho_a \delta u_g - t_{gT2}(u_{g3} - u_{g2})\rho_a \delta u_g \mathrm{d}\Gamma \quad (7.36)$$

where the terms $\dot{m}^w$ and $\dot{m}^a$ correspond to storage of water and air in the interface. They may either be considered null, or expressed as a function of the interface aperture, so that

$$\dot{m}^w = \dot{\rho}_w S_r g_N + \rho_w \dot{S}_r g_N + \rho_w S_r \dot{g}_N \quad (7.37)$$

and

$$\dot{m}^a = \dot{\rho}_a (1 - S_r) g_N - \rho_w \dot{S}_r g_N + \rho_w (1 - S_r) \dot{g}_N \quad (7.38)$$

with S_r the degree of saturation of the interface. The water density ρ_w and the air density ρ_a are expressed as functions of the water and air pressures according to Equations (3.50) and (3.53) respectively. Equations (7.37) and (7.38) introduce a coupling term between the hydraulic and mechanical problems.

5 Finite element formulation

The discretization of the governing equations is based on a segment-to-segment approach (Habraken *et al.*, 1998; Fischer & Wriggers, 2004; Puso & Laursen, 2004). In this approach, the contact constraint is applied in a weak sense over the element and the gap function is computed through the closest-point projection of a point of the non-mortar surface onto the mortar one which is given more importance. It is then extrapolated over the element by the means of interpolation functions. In addition, as already mentioned, fluid flows are discretized according to the three-node approach.

In this work, the coupled finite element `FAIF 2D` is used to model interfaces and technological gaps between solid bodies. This element is an isoparametric element with nine nodes and three integration points (Figure 7.36). As for the solid element `MWAT 2D`, each node has five degrees of freedom, namely the spatial coordinates, water pressure, gas pressure and temperature[1]. Interface elements are merged with the external segments of the surrounding volume elements. Consequently they use the same nodal unknowns and create a coupling between both solids.

[1]The developments presented in this chapter are restricted to isothermal conditions, i.e. as if there were only four degrees of freedom.

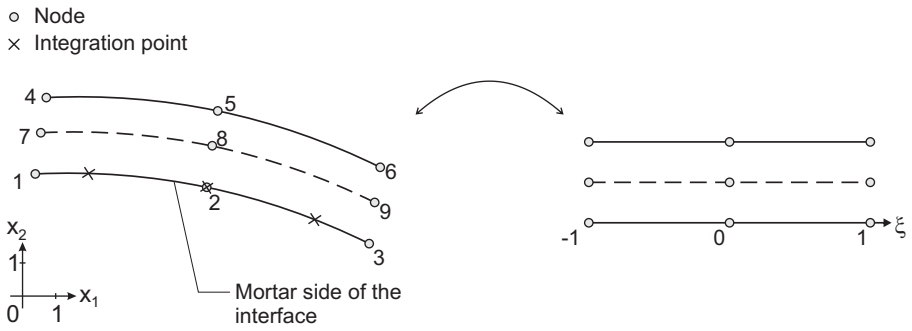

Figure 7.36: One-dimensional finite element `FAIF 2D` with nine nodes and three integration points (left) and its corresponding parent element (right).

Let us define the vector or nodal unknowns $\boldsymbol{U_{Nc}}$

$$\boldsymbol{U}_{\boldsymbol{Nc}}^{T(1\times 36)} = [\boldsymbol{U_{Nc1}}\ \boldsymbol{U_{Nc2}}\ \boldsymbol{U_{Nc3}}\ \boldsymbol{U_{Nc4}}\ \boldsymbol{U_{Nc5}}\ \boldsymbol{U_{Nc6}}\ \boldsymbol{U_{Nc7}}\ \boldsymbol{U_{Nc8}}\ \boldsymbol{U_{Nc9}}] \tag{7.39}$$

with

$$\boldsymbol{U}_{\boldsymbol{Nci}}^{T} = [u_{1i}\ u_{2i}\ u_{wi}\ u_{gi}] \qquad \text{for } i = 1, 9 \tag{7.40}$$

9 being the number of nodes.

Nodal unknowns are interpolated over each side of the element using quadratic serendipity shape functions $\boldsymbol{N}_{(\xi)}$ (Zienkiewicz & Taylor, 2000).

As expressed by Equation (7.22), the contact between two solid bodies yields an additional term in the expression of the external virtual power and modifies the balance of momentum equation. Accordingly, an additional contribution to the energetically equivalent nodal forces associated to the nodes of the interface element should be considered. For the boundary of $\mathcal{B}^1$, this expression is given by

$$\boldsymbol{f}_{\boldsymbol{E}}^{i} = \sum_{IP=1}^{3} \left[\boldsymbol{R} \cdot \boldsymbol{\sigma_c} N_{(\xi)i} \det \boldsymbol{J}^{c} W\right]_{IP} \tag{7.41}$$

where the expression between brackets is evaluated for each integration point. In this equation, $\boldsymbol{R}$ is the rotation matrix relating the global system of coordinates $(\boldsymbol{x}_1, \boldsymbol{x}_2)$ to the local system of coordinates $(\boldsymbol{e}_1, \boldsymbol{e}_2)$, such that

$$\dot{\boldsymbol{g}} = \begin{bmatrix} \dot{g}_N \\ \dot{g}_T \end{bmatrix} = \boldsymbol{R}^T \cdot \begin{bmatrix} \dot{x}_1^2 - \dot{x}_1^1 \\ \dot{x}_2^2 - \dot{x}_2^1 \end{bmatrix} = \boldsymbol{R}^T \cdot \Delta\dot{\boldsymbol{x}} \tag{7.42}$$

with the exponent indicating either the side 1 or side 2 of the interface, $\boldsymbol{J}^c$ is the Jacobian of the corresponding transformation, and W is weight of the considered Gauss point.

Let us now consider the hydraulic problem. Fluid flow inside the equivalent porous medium $\mathcal{B}^3$ along the interface involves energetically equivalent internal forces. The contributions of the interface are derived from Equations (7.35) and (7.36) for water and air

respectively. They are expressed as

$$f_I^{wi} = \sum_{IP=1}^{3} \left[\left(\dot{m}^w N_{(\xi)i} - f_L^w \nabla_{\boldsymbol{e}_2} N_{(\xi)i} \right) \det \boldsymbol{J}^c g_N W \right]_{IP} \tag{7.43}$$

$$f_I^{ai} = \sum_{IP=1}^{3} \left[\left(\dot{m}^a N_{(\xi)i} - f_L^a \nabla_{\boldsymbol{e}_2} N_{(\xi)i} \right) \det \boldsymbol{J}^c g_N W \right]_{IP} \tag{7.44}$$

for water and air respectively.

On the other hand, transversal fluxes between $\mathcal{B}^1$, $\mathcal{B}^2$ and $\mathcal{B}^3$ provides energetically equivalent external nodal forces related to the fluid degrees of freedom. The contribution to the external virtual power corresponding to $\mathcal{B}^3$ is derived from Equations (7.35) and (7.36) for water and air respectively. It yields

$$f_E^{wi} = \sum_{IP=1}^{3} \left[\left(t_{wT1} \left(u_{w1} - u_{w3} \right) \rho_w N_{(\xi)i} - t_{wT2} \left(u_{w3} - u_{w2} \right) \rho_w N_{(\xi)i} \right) \det \boldsymbol{J}^c W \right]_{IP} \tag{7.45}$$

and

$$f_E^{ai} = \sum_{IP=1}^{3} \left[\left(t_{gT1} \left(u_{g1} - u_{g3} \right) \rho_a N_{(\xi)i} - t_{gT2} \left(u_{g3} - u_{g2} \right) \rho_a N_{(\xi)i} \right) \det \boldsymbol{J}^c W \right]_{IP}. \tag{7.46}$$

Finally, internal and external nodal forces are gathered into the global vector $\boldsymbol{f}_I$ and $\boldsymbol{f}_E$. Thence the vector of out of balance forces $\boldsymbol{f_{OB}}$ is defined according to

$$\boldsymbol{f_{OB}} = \boldsymbol{f}_I - \boldsymbol{f}_E. \tag{7.47}$$

The stiffness matrix $\boldsymbol{k}$ related to the interface element is computed analytically by derivation of out of balance forces related to node i with respect to generalised degree of freedom j.

6 Conclusions

Interfaces and technological gaps are unavoidable features of underground structures. This chapter aimed at investigating their influence on the hydromechanical behaviour of engineered barrier system. To this aim, a literature review of the available experimental data was realized. While the behaviour of rock joints is relatively well known, the hydromechanical behaviour of clayey interfaces, including the self-sealing capacity of bentonites, is still not very well known and understood. In addition, the role of interfaces on transversal water flow lacks of experimental characterization. Based on these observations, an experimental characterization campaign was realized with the aim of assessing the role of interfaces on the normal behaviour of block assemblies. The experimental data tend to show an influence of the interface on the swelling strain and swelling pressure developed by bentonite samples upon soaking under oedometer and constant-volume conditions respectively. In addition, a considerably slower hydration kinetics was detected when an

interface was present in the bentonite sample. While the results of the experimental campaign should be considered as preliminary results, they provide motivation for further investigation.

The existence of technological gaps is generally neglected in numerical modelling and perfect contact is assumed between the different materials. This strong hypothesis assumes continuity of both mechanical displacements and pore pressures between materials, which is not the case, especially during the first years of the disposal life. In order to overcome the limitations of continuous approaches, the formulation of a zero-thickness hydromechanical interface element is presented. This element allows accounting for the presence or absence of contact between materials, flow within the interface, as well as flow through the interface. The modelling capacity of this formulation will be validated in Chapter 8.

Chapter 8

Applications to some problems of nuclear waste disposal

1 Introduction

The behaviour of an engineered barrier under *in situ* conditions is complex, owing for the strongly coupled processes taking place. In order to improve our comprehension of the processes, various laboratory and *in situ* tests have been carried out in the past years. In France, the Meuse/Haute-Marne Underground Research Laboratory (URL) is excavated 500 meters deep in the Callovo-Oxfordian (COx) claystone (Figure 8.1). Managed by the French national radioactive waste management agency (Andra), the laboratory aims at evaluating the feasibility of geological disposal of radioactive wastes in the COx formation. Accordingly, a number of *in situ* experiments have been performed to study the thermo-hydro-mechanical behaviour of the potential host rock, characterize the excavation damaged zone (EDZ), study the sealing capacity of bentonite-based materials and investigate the impact of gas transfer on the rock/EDZ/bentonite system (Armand *et al.*, 2014).

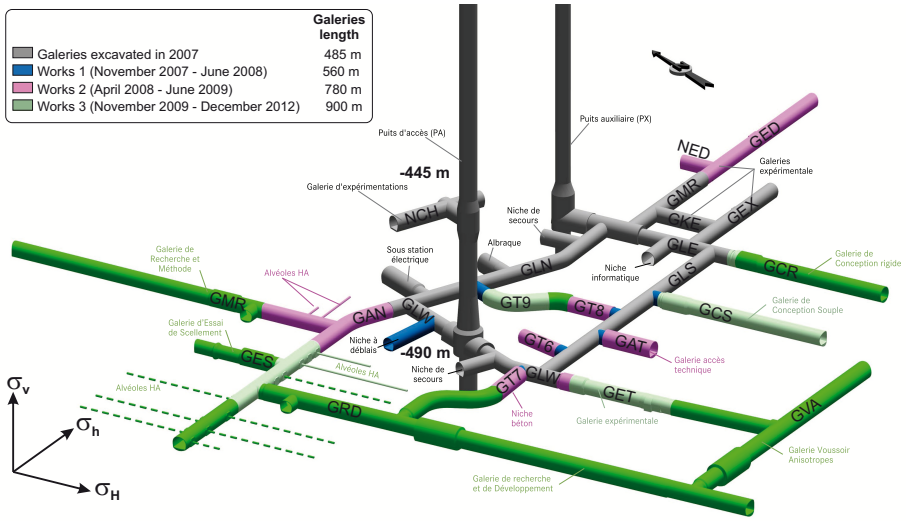

Figure 8.1: Architecture of the Meuse/Haute-Marne Underground Research Laboratory (Andra, 2016).

Among these experiments, the PGZ2 tests were designed to study the saturation process of a bentonite-based material and the impact of gas production on the hydromechanical behaviour of the engineered barrier (de La Vaissière, 2013). Cores of highly compacted bentonite are placed in small-diameter drifts and their progressive saturation is monitored. While monitoring data highlights a complex behaviour of the bentonite behaviour that is not fully understood, this chapter aims at providing clues for a better comprehension of the PGZ2 *in situ* tests.

The experimental data on the investigated mixture of MX-80 bentonite and sand are first summarized. In addition, the different hydromechanical parameters determined from laboratory tests in the previous chapters are presented. The Bentogaz 2 laboratory test, performed on the same material, is then modelled. The experiment consists in an extensively monitored saturation test performed under constant volume conditions. The laboratory experiment is thoroughly analysed. Then, one-dimensional and two-dimensional analyses of the PGZ2 experiments are carried out, with a special attention paid to the influence of technological gaps.

2 Material

Attention is focused on the hydromechanical behaviour of a mixture of MX-80 bentonite and quartz sand, with respective proportions of 70/30 in dry mass. This mixture is considered by the Andra as a potential sealing and backfilling material for the geological disposal of high-activity and medium-activity nuclear waste. In addition, it has been used in several *in situ* tests, including the PGZ2 experiments conducted in Bure and the SEALEX test carried out in the Underground Research Laboratory of Tournemire, both France.

Experimental investigations on the considered mixture have been carried out for several years by the French Atomic Energy Commission (CEA), the Navier Laboratory of Ecole des Ponts ParisTech (see the PhD thesis of Wang, 2012; Saba, 2013), both in Paris, and Ecole Centrale de Lille (see the PhD thesis of Liu, 2013). In this section, the existing experimental data on the hydromechanical behaviour of the material are summarized. Note that, for the sake of completeness, some data presented in the previous chapters are also included. Finally, the parameters of the water retention model, mechanical model and fluid flow law that have been developed in this work are summarized.

2.1 Water retention behaviour

Wang *et al.* (2013c) and Gatabin *et al.* (2016) used the vapour equilibrium technique to investigate the water retention properties of the mixture under both confined and unconfined conditions. Wang *et al.* (2013c) determined the water retention properties of the mixture initially compacted to a dry density of 1.67 Mg/m^3 and a water content of 11%. These conditions are similar to the initial state of the material used in the Bentogaz 2 experiment. On the other hand, the material studied by Gatabin *et al.* (2016) was compacted to a dry density of 2.03 Mg/m^3 and at a water content of 7.08%. These conditions

correspond to the initial conditions of the material used in the PGZ2 *in situ* experiment.

The experimental data obtained by Wang *et al.* (2013c) and Gatabin *et al.* (2016) during wetting under confined conditions are presented in Figure 8.2. They were used to calibrate the water retention model developed in Chapter 4. This model is expressed in terms of water ratio e_w and reads

$$e_w = \underbrace{e_m \exp\left[-\left(C_{ads} s\right)^{n_{ads}}\right]}_{\text{Microstructral water ratio}} + \underbrace{(e - e_m)\left\{1 + \left[(e - e_m)\,\frac{s}{A}\right]^n\right\}^{-m}}_{\text{Macrostructral water ratio}} \tag{8.1}$$

where e and e_m are respectively the total and microstructural void ratios, n_{ads} and C_{ads} are parameters controlling water retention in the microstructure, n and m are parameters controlling water retention in the macrostructure, and A controls the dependence of the air-entry pressure on the macrostructural void ratio. In Equation (8.1), the microstructural water is assumed to evolve with the water ratio e_w according to

$$e_m = e_{m0} + \beta_0 e_w + \beta_1 e_w^2 \tag{8.2}$$

where e_{m0} is the microstructural void ratio for the dry material, and β_0 and β_1 are parameters quantifying the swelling potential of the microstructure. The parameters of the microstructure evolution law and water retention model are given in Table 8.1.

Microstructure evolution			**Water retention**				
			Microstructure		**Macrostructure**		
e_{m0}	β_0	β_1	C_{ads} (MPa^{-1})	n_{ads}	A (MPa)	n	m
0.29	0.1	0.18	0.0053	0.79	0.2	3	0.15

Table 8.1: Parameters of the microstructure evolution law and water retention model for the mixture of MX-80 bentonite and sand.

Finally, the model responses for wetting paths under confined conditions are shown in Figure 8.2 for three dry densities corresponding to the initial conditions of three laboratory and *in situ* tests, namely the Bentogaz 2 and PGZ2 experiments presented in this chapter and the infiltration test described and modelled in Chapter 6.

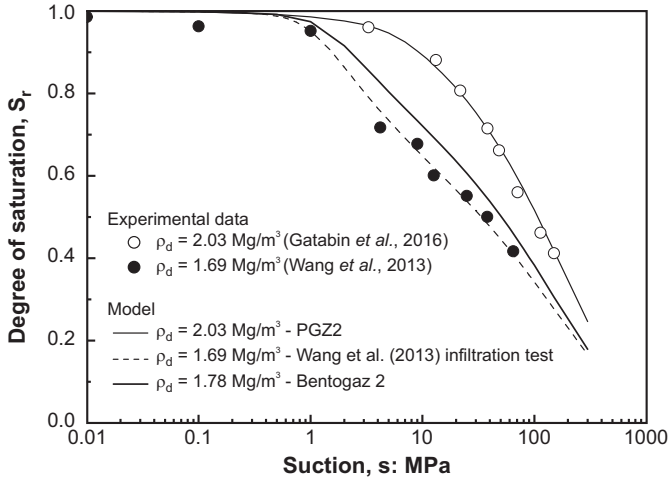

Figure 8.2: Water retention curves of the mixture of MX-80 bentonite and sand. Experimental data (Wang *et al.*, 2013c; Gatabin *et al.*, 2016) and model calibration.

2.2 Mechanical behaviour

Wang *et al.* (2013c) studied the mechanical behaviour of the mixture compacted at an initial dry density of 1.67 Mg/m^3. Controlled-suction oedometer tests were performed at three different suction values and an oedometer test was realized on the saturated material. In addition, Gatabin *et al.* (2006) measured the swelling pressure of the mixture compacted to different dry densities.

The mechanical behaviour of the bentonite/sand mixture is reproduced using the mechanical model developed in Chapter 5. The model extends the Barcelona Basic Model of Alonso *et al.* (1990) in order to better reproduce the swelling pressure developed by bentonites upon saturation under confined saturation. The values of the ten model parameters are presented in Table 8.2. Note that due to the lack of data, the values of some parameters (especially the shear strength parameters) are assumed from a review of the literature. In addition, the threshold degree of saturation S_r^* limiting the saturated water retention domain is assumed equal to 0.96. The influence of this parameter is analysed in Section 3.4.1.

κ	κ_s	ν	$c\,(0)$ (MPa)	k	ϕ (°)	$\lambda\,(0)$	p_0^* (MPa)	p_c (MPa)	r	ω (MPa^{-1})
0.025	0.073	0.35	0.1	0.046	25	0.12	1.40	0.01	0.8	0.09

Table 8.2: Parameters of the mechanical model for the mixture of MX-80 bentonite and sand.

2.3 Flow properties

The flow of water in saturated and partially saturated bentonite is modelled using the flow law presented in Chapter 3 and later extended in Chapter 6. In particular, the saturated water permeability K_w is expressed as a function of the macrostructural void ratio according to

$$K_w = K_{w0} \frac{e_M^N}{(1-e_M)^M} \frac{(1-e_{M0})^M}{e_{M0}^N} \tag{8.3}$$

where K_{w0} is a reference permeability measured on a material with a reference macroscopic void ratio e_{M0}, and N and M are model parameters. These parameters are determined using the experimental data from Gatabin *et al.* (2006) (Figure 8.3).

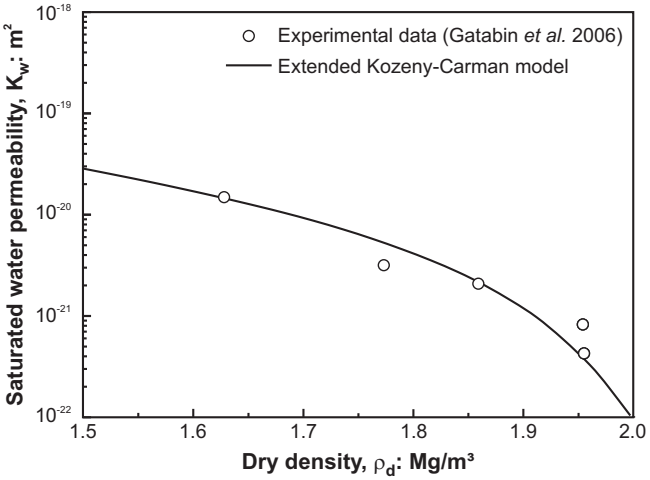

Figure 8.3: Evolution of the water permeability of the MX-80 bentonite/sand mixture with dry density. Experimental data (Gatabin *et al.*, 2006) and model calibration.

Finally, an exponential law is used for the relative permeability. The value of the exponent n_k is determined through back-analysis of the hydration test presented in Chapter 6. The different hydraulic parameters are determined given in Table 8.3.

Saturated permeability				**Relative permeability**
K_{w0} (m^2)	e_{M0}	N	M	n_k
2.5×10^{-20}	0.31	2	0.2	3.4

Table 8.3: Parameters of the water flow model for the mixture of MX-80 bentonite and sand.

3 Bentogaz 2 experiment

3.1 Description of the test

The Bentogaz 2 experiment is a laboratory test, carried out by the French Atomic Energy Commission (CEA), in order to study the water saturation and gas migration processes in compacted bentonite (Gatabin & Guillot, 2008; Gatabin *et al.*, 2011). The main originality of the test is its extensive instrumentation, making possible the complete monitoring of the hydromechanical state of the sample.

The mixture used for the Bentogaz 2 experiment has an initial water content of 12.4%. The sample (100 mm high, 120 mm in diameter) is compacted with an isostatic press at a pressure of 30 MPa, corresponding to a dry density of 1.78 Mg/m^3. The characteristics of the sample are summarized in Table 8.4.

Compaction pressure (MPa)	**Height** (mm)	**Diameter** (mm)	**Dry density** (Mg/m^3)	**Water content** (%)
30	100	120	1.78	12.4

Table 8.4: Characteristics of the as-compacted sample used for the Bentogaz 2 experiment.

The Bentogaz 2 test is performed under constant volume conditions using the experimental set-up presented in Figure 8.4. The bentonite sample is placed in a confining cell made of stainless steel and is sandwiched between two stainless steel porous discs. The upper disc allows fluid exchanges with the ambient controlled atmosphere, while the lower one is used for water supply. The piston is then placed and the whole assembly is fixed in a high-rigidity frame. Finally, a preload of 0.2 MPa is applied to ensure a good contact between the materials.

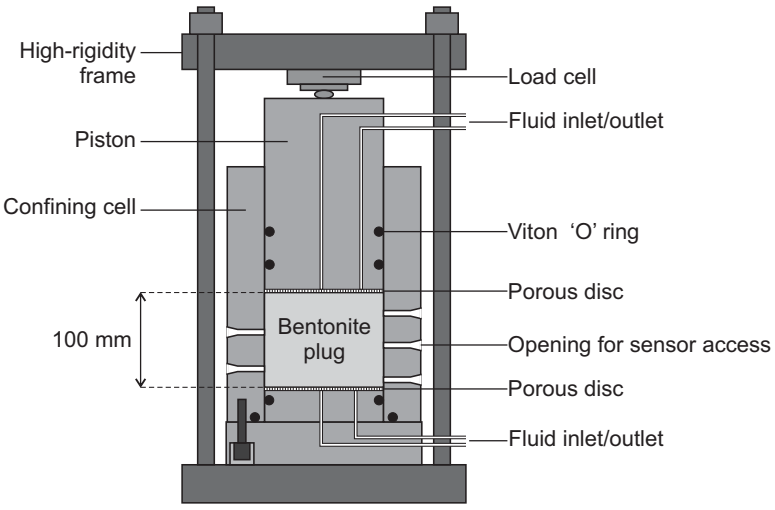

Figure 8.4: Schematic representation of the experimental set-up used for the Bentogaz 2 experiment.

In order to follow the hydromechanical state of the sample during hydration, the total vertical pressure and the injected water volume are recorded through time. In addition, the cell is equipped with four total radial pressure sensors, named PT1 to PT4, and placed at different heights of the sample. These sensors are directly drilled in the wall of the cell. Their positions are given in Table 8.5.

Reference	**Angle** (°)	**Height** (mm)	**Representation**
PT1	0	12.5	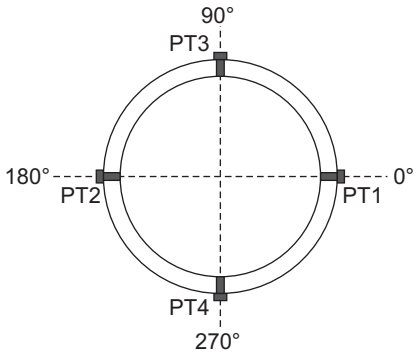
PT2	180	37.5	
PT3	270	50	
PT4	90	75	

Table 8.5: Position of the total radial pressure sensors. Height is measured from bottom (injection) end of the sample.

The Bentogaz 2 experiment was launched on July 8, 2008. The water used for hydration was a synthetic water representative of the site of Bure. Until July 8, 2009, hydration was performed from the bottom end at a water pressure of 0.11 MPa. In order to allow degassing, the circuits in contact with the upper face were maintained opened. Then, a water pressure of 0.5 MPa was applied on the upper face of the sample in order to ensure full saturation of the sample. This pressure was maintained during two months. Once that full saturation of the sample was ensured, several gas injection stages were carried out in order to investigate gas breakthrough and migration processes, as well as the self-sealing capacity of the material. However, these stages are not detailed nor modelled in this work.

3.2 Features of the analysis

The analysis of the problem assumes one-dimensional axisymmetric conditions around the longitudinal axis of the sample. The soil sample is meshed with 120 eight-noded isoparametric elements (Figure 8.5). Gravity is not considered. An initial isotropic stress state is considered, the total stress being equal to the preload of 0.2 MPa. The initial suction in the sample is estimated from the water retention model, assuming an initial water content of 12.4% and a dry density of 1.78 Mg/m^3. The water pressures are set equal to -27.8 MPa, while the gas pressures are fixed equal to atmospheric pressure. Since air is allowed to escape from the upper part of the sample, gas pressures are maintained fixed during the entire analysis.

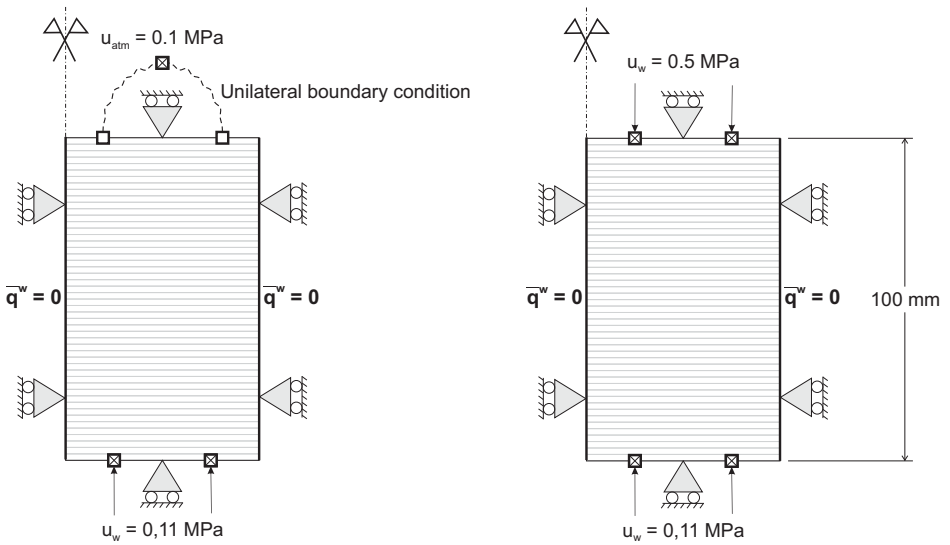

(a) First stage: injection from the bottom.

(b) Second stage: injection from the top.

Figure 8.5: One-dimensional finite element mesh and boundary conditions.

The first stage of the Bentogaz 2 experiment consists in the injection of water from the bottom face of the sample. Accordingly, the water pressure is imposed at 0.11 MPa at the bottom of the sample (Figure 8.5(a)). In addition, it is assumed that water can escape the sample from the upper boundary, but only if the sample is fully saturated. Therefore, water flux $\bar{q}^w$ exists when the water pressure at the top of the sample exceeds atmospheric pressure. Such a condition is modelled through a unilateral boundary condition on the water pressure. It is expressed as

$$\bar{q}^w = \begin{cases} 0, & \text{if } u_w \leq u_{atm} \\ K_{pen}\left(u_{atm} - u_w\right) & \text{otherwise} \end{cases} \tag{8.4}$$

where K_{pen} is a numerical penalty coefficient ruling the water outflow.

During the second stage of the test, water is injected from the top to ensure full saturation of the sample. Water pressures equal to 0.5 MPa are imposed at the top of the sample, while the pressure is maintained at 0.11 MPa at the bottom of the sample (Figure 8.5(b)).

3.3 Experimental and numerical results

3.3.1 Injected water volume

Figure 8.6 presents the evolution of the injected water volume through time. The experimental curve is characterized by a rapid increase of the injected water volume, corresponding to water filling of the dead volume (tubing) and saturation of the bottom porous disc. This volume was measured equal to 20 cm^3 prior to the test and is used to correct the numerical curve. As observed in Figure 8.6, the numerical model compares remarkably well with the experimental curve. As water injection proceeds, the injection

rate becomes lower and lower, mainly as a result of the smaller pressure gradient. The injected water volume reaches 188.5 cm^3 at the end of the first injection stage.

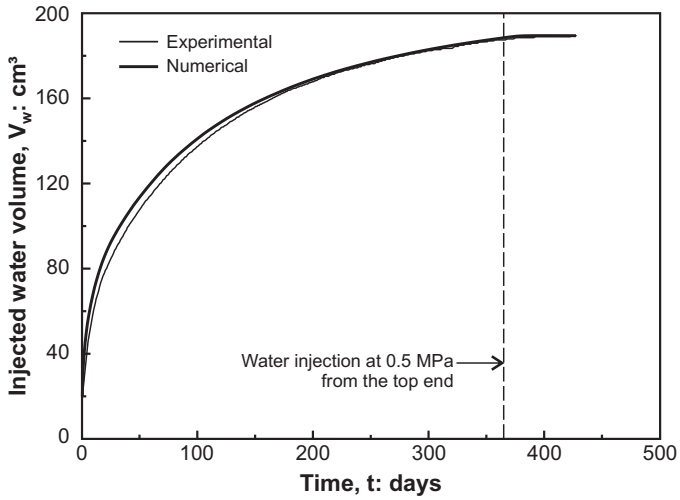

Figure 8.6: Water volume injected from the bottom end. Comparison between experimental data and model predictions.

Figures 8.7(a) and 8.7(b) show the evolution through time of the suction and degree of saturation profiles. Water injection yields a progressive decrease of suction and increase of degree of saturation in the sample, which are the most significant at the bottom of the sample where water is injected. After one year of injection, the sample is not fully saturated (Figure 8.7(b)) and the overall degree of saturation is equal to 0.96. In order to ensure full saturation of the sample, water is injected at 0.5 MPa from the top during two months. Figures 8.7(a) and 8.7(b) confirm that full saturation of the sample is reached by the end of this stage (full saturation is actually reached after one week of injection from the top end).

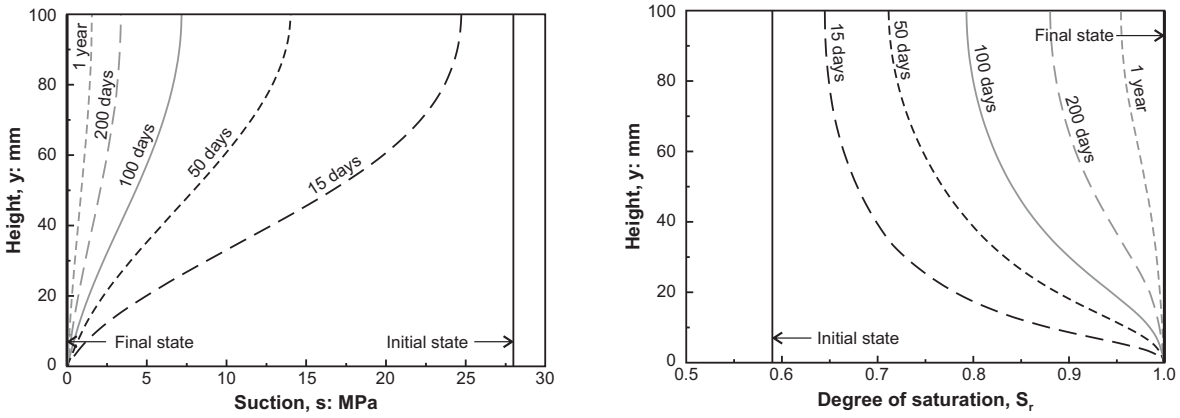

(a) Suction profiles.

(b) Degree of saturation profiles.

Figure 8.7: Evolution through time of suction and degree of saturation in the sample during water injection (numerical results).

3.3.2 Typical stress and strain paths

Before proceeding any further with the comparison between experimental data and numerical results, the stress and strain paths undergone by the sample are detailed. In Chapter 5, the global stress path followed by a sample wetted under confined conditions was thoroughly described. Yet, if boundary-value problems are considered, as it is the case in this chapter, the stress and strain paths undergone by one given point of the sample may significantly differ from the paths globally followed by the sample. Indeed, while constant volume conditions are prescribed at the global scale, volume changes are locally allowed. In addition, since hydration is not uniform with the sample, the followed stress and strain paths will differ from one point of the sample to another. Yet, one can identify common features and trends in these paths.

In the following, the paths followed by a point located at a height of 37.5 mm from the bottom end are thoroughly described. Note that this point corresponds to the location of the total radial stress sensor PT2. The stress and strain paths followed by the considered point are represented in Figures 8.8 and 8.9 respectively. Let A be the initial state of the material at time $t = 0$. As hydration of the bentonite sample proceeds ($t > 0$), the stress and strain states move progressively from A to H according to the following sequence:

- **From A to B**: the suction decrease imposed at the bottom of the sample has hardly reached the considered point (Figure 8.8(d)). However, as a result of hydration and swelling of the lower elements, the vertical stress increases and the point undergoes elastic loading (Figure 8.8(a)). As a result, the void ratio decreases, with a slope in the $(\ln p - e)$ plane ($= 0.021$) close to the elastic compressibility $\kappa = 0.025$ (Figure 8.9(a)). In addition, the increase in vertical stress comes with an increase in deviatoric stress (Figure 8.8(a)). In particular, the slope of the path in the $(p - q)$ plane is equal to 0.58, which is hardly lower than the $3\,(1 - 2\nu)\,/\,(1 + \nu) = 2/3$ slope of oedometer loading. Finally, the decrease in void ratio at almost constant suction yields an increase of the degree of saturation (Figure 8.8(d)).

- **From B to C**: the effects of hydration become prominent and control the compressibility behaviour. The considered point undergoes elastic swelling due to the suction decrease. The swelling entails an increase in both void ratio (Figure 8.9) and mean net stress (Figure 8.8(b)). Indeed, while swelling is prevented at the global scale (as a result of the imposed confined conditions), local swelling within the sample is possible. Yet, radially, the sample is not able to swell. It yields an increase of the radial stress which becomes higher than the vertical stress, and thus a decrease of the deviatoric stress (Figure 8.8(a)). Finally, since the behaviour is elastic, the preconsolidation pressure for saturated conditions remains constant (Figure 8.8(c)). However, the decrease in suction leads to an important decrease of the apparent preconsolidation pressure and a reduction of the elastic domain.

- **C**: the decrease of the apparent preconsolidation pressure is such that the stress path reaches the Loading-Collapse (LC) curve (Figure 8.8(a)). Note that, in Figure 8.8(b), the LC curve is plotted for a deviatoric stress equal to 0, which is the reason why the point C is apparently not on the yield surface.

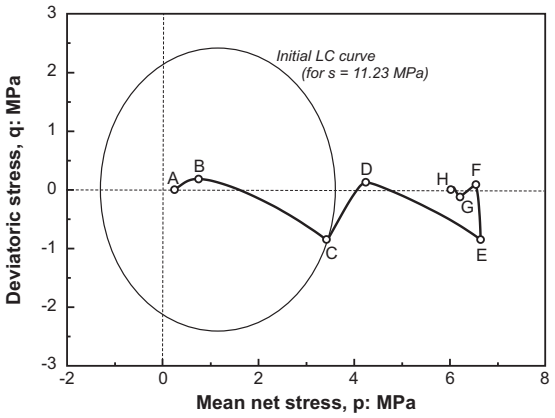

(a) Stress path in the $(p-q)$ plane.

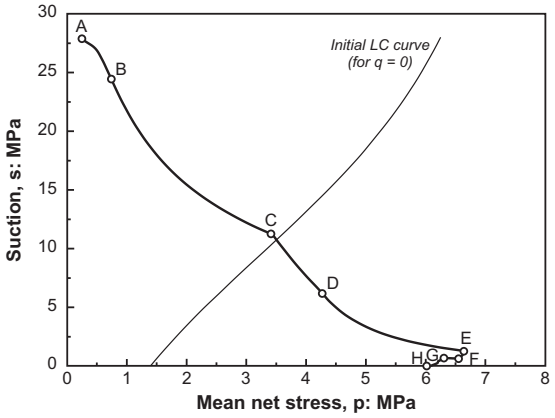

(b) Stress path in the $(p-s)$ plane.

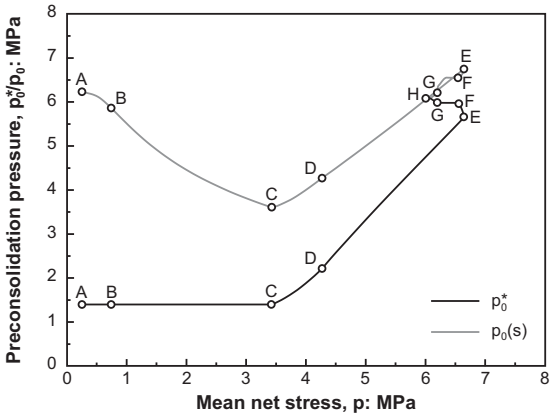

(c) Evolutions of the apparent and saturated preconsolidation pressures.

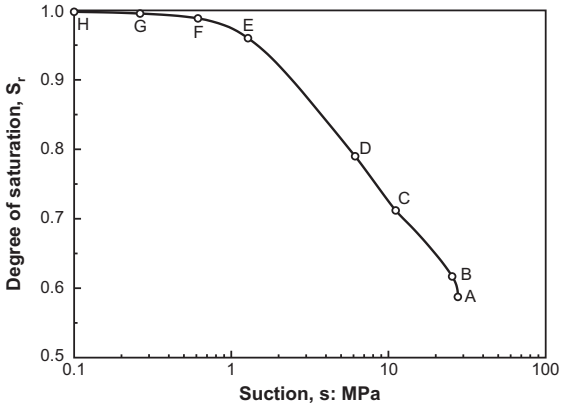

(d) Stress path in the $(s-S_r)$ plane.

Figure 8.8: Stress paths followed by a point located at a distance of 37.5 mm from the bottom face.

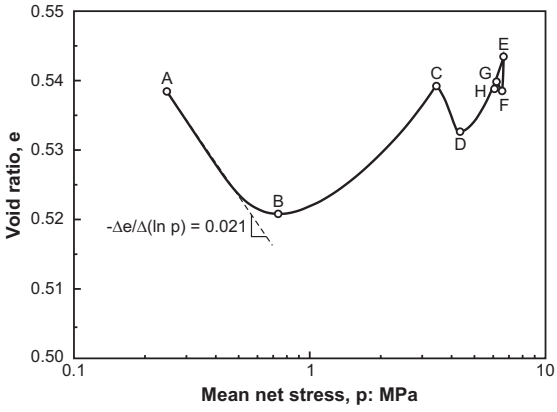

(a) Evolution of the void ratio with the mean net stress.

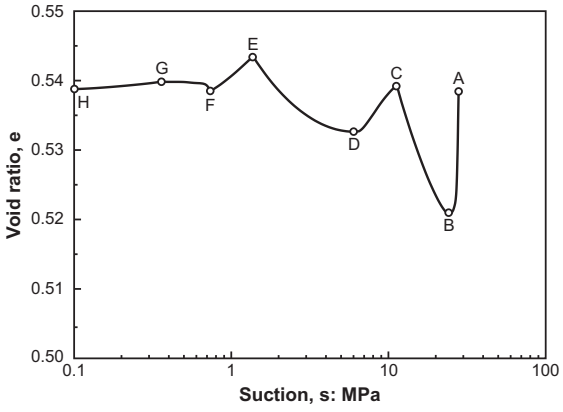

(b) Evolution of the void ratio with suction.

Figure 8.9: Strain paths followed by a point located at a distance of 37.5 mm from the bottom face.

- **From C to D**: the behaviour is now elastoplastic. While hydration continues (Figure 8.8(d)), plastic collapse is observed and the void ratio at the considered point decreases (Figure 8.9(b)). The vertical stress, hence mean stress, remains increasing as hydration and swelling of the sample proceeds. However, laterally, the stress increases at a lower rate due to collapse, so that the deviatoric stress increases (Figure 8.8(a)). Finally, yielding comes along with hardening of the LC curve and increase of the preconsolidation pressure (Figure 8.8(c)).

- **From D to E**: hydration continues and the behaviour is still elastoplastic. However, from point D on, elastic swelling due to suction decrease becomes more important than the plastic collapse and the void ratio increases again (Figure 8.9). In addition, the radial stress raises and the deviatoric decreases to become negative.

- **E**: the threshold degree of saturation $S_r^* = 0.96$ is reached and any further decrease in suction does not produce volumetric strain.

- **From E to F**: swelling of the upper elements leads to compressive strain at the considered point (Figure 8.9). Moreover, the stiffness loss associated to the absence of elastic swelling, yields a decrease of the mean net stress. In Figure 8.8(c), the difference between the apparent and saturated preconsolidation pressures becomes smaller as suction decreases.

- **From F to G**: water is injected from the top side of the sample and hydration of the material proceeds. The decrease in mean stress is such that the point behaves elastically. The saturated preconsolidation pressure is constant, while the apparent preconsolidation stress decreases as suction reduces.

- **G**: the decrease in the apparent preconsolidation pressure is more important than the decrease in mean stress. The LC curve is activated once more and the behaviour is elastoplastic.

- **From G to H**: hydration of the material proceeds without much volume changes at the considered point.

- **H**: the material has reached full saturation at the considered point.

The different stages of the stress and strain paths described above are summarized in Table 8.6.

Stage	**Time** (days)	e	p (MPa)	q (MPa)	s (MPa)	S_r	**Physical process**
A	0	0.538	0.25	0	27.88	0.59	Initial state.
		↘	↗	↗	↘	↗	Compression due to swelling of the lower elements.
B	3.4	0.521	0.74	0.184	24.4	0.62	
		↗	↗	↘	↘	↗	Elastic swelling due to hydration.
C	17.6	0.539	3.42	-0.854	11.23	0.71	Activation of the LC yield surface.
		↘	↗	↗	↘	↗	Plastic collapse due to hydration.
D	44.3	0.533	4.27	0.126	6.17	0.79	
		↗	↗	↘	↘	↗	Elastoplastic swelling due to hydration.
E	234	0.544	6.65	-0.86	1.28	0.96	Threshold degree of saturation S_r^* reached.
		↘	↗	↗	↘	↗	Compression due to hydration and swelling of the upper elements.
	365	0.538	6.55	0.095	0.63	0.99	Water injection from the top side of the sample.
F	367.3	0.538	6.55	0.095	0.63	0.99	
		↗	↘	↘	↘	↗	Elastic swelling due to decrease in mean stress (collapse of the upper elements).
G	378.4	0.540	6.20	-0.134	0.26	0.996	Activation of the LC yield surface.
		↘	↘	↗	↘	↗	Plastic collapse
H	378.5	0.539	6.08	0.042	0	1	Final saturated state.

Table 8.6: Description of the stress, suction and saturation paths for a point located at a height of 37.5 mm from the bottom end.

As already discussed, the stress and strain paths at a given point of the sample are strongly dependent on the behaviour of the surrounding elements. Interestingly, one observes that the hydration process leads to a non-homogeneous final distribution of dry density within the sample (Figure 8.10). As soon as hydration starts, important decrease of the dry density is observed at the bottom of the sample. Accordingly, the dry density increases in the upper part of the sample as global swelling of the sample is prevented (swelling at the bottom of the sample yields compressive strains in the upper part). However, as hydration proceeds and suction decreases within the sample, elements more and more distant from the wetting end tends to swell and an important redistribution of the dry density is noticed.

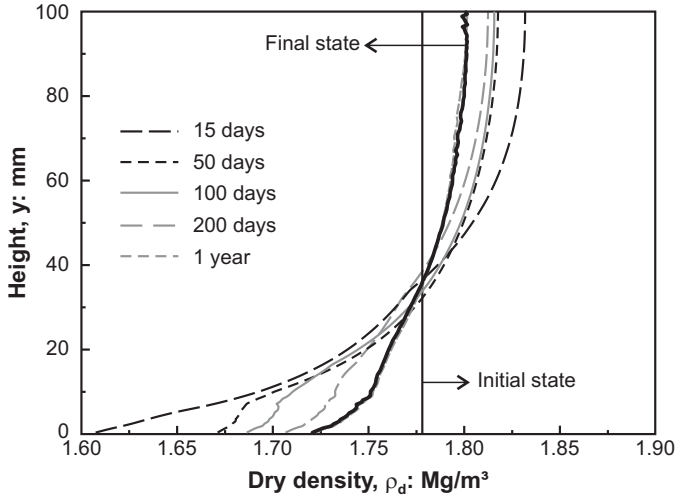

Figure 8.10: Evolution through time of the sample dry density.

Figure 8.10 shows that the area around the total radial pressure sensor PT2, for which the stress and strain paths were described, experiences little changes in dry density. For the sake of completeness, Figures 8.11 and 8.12 show therefore the stress and strain paths followed by three additional points located at distances of 12.5 mm, 50 mm and 75 mm from the sample bottom face corresponding to the position of the total radial pressure sensors PT1, PT3 and PT4. The figures show that, from a qualitative point of view, the stress and strain paths do not vary much from one point of the sample to another.

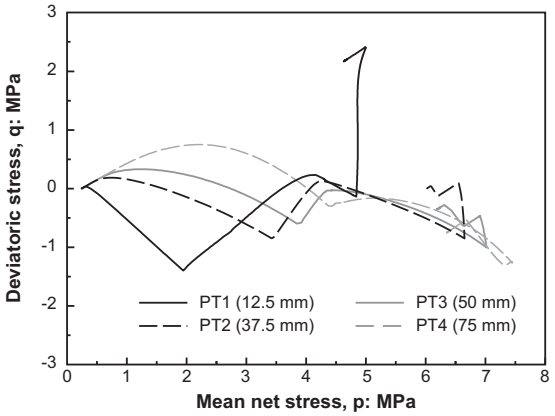

(a) Stress path in the $(p-q)$ plane.

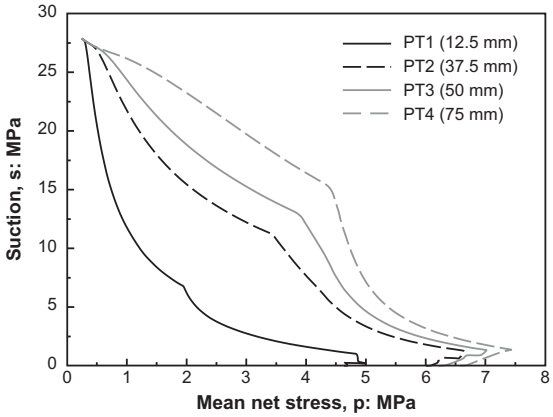

(b) Stress path in the $(p-s)$ plane.

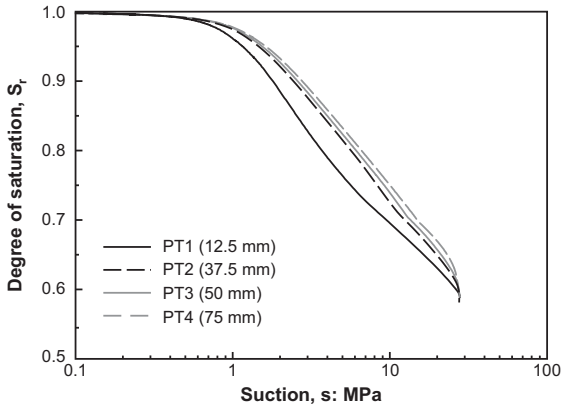

(c) Stress path in the $(s-S_r)$ plane.

Figure 8.11: Stress paths followed by four points located at distances of 12.5 mm, 37.5 mm, 50 mm and 75 mm from the bottom face.

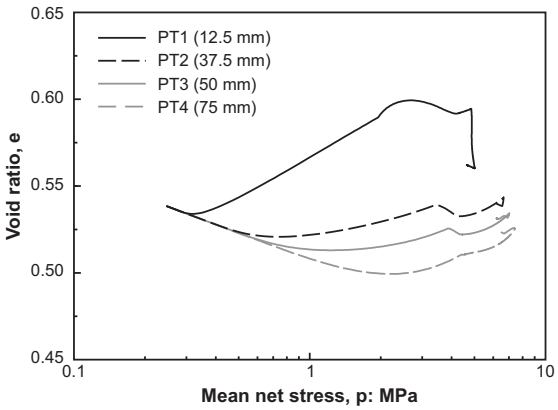

(a) Evolution of the void ratio with the mean net stress.

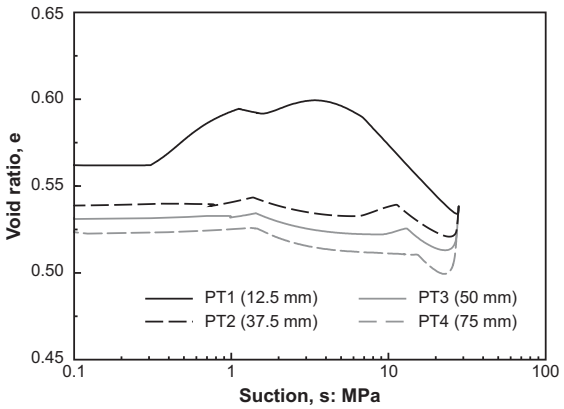

(b) Evolution of the void ratio with suction.

Figure 8.12: Strain paths followed by four points located at distances of 12.5 mm, 37.5 mm, 50 mm and 75 mm from the bottom face.

3.3.3 Total vertical stress

The evolution of the total vertical pressure developed upon hydration is presented in Figure 8.13. An excellent agreement is observed between the experimental results and the model predictions. The development of the vertical swelling pressure exhibits a first stage (until day 70 on the experimental curve and day 43 on the numerical one) of high swelling rate. After that, a significant change of the slope occurs and a lower swelling rate is observed on both experimental and numerical curves. Between days 100 and 250, a slight change in curvature is observed on the experimental curve. As hydration proceeds and the rate of water injection decreases, a progressive stabilization of the swelling pressure is observed. After one year of water injection, the total vertical pressure developed by the sample is equal to 6.42 MPa, which is in agreement with the swelling pressure determined on smaller samples by Gatabin *et al.* (2006). Water is then injected from the top end to ensure full saturation of the sample. From an experimental point of view, water injection from the top face yields an increase of the total vertical pressure, the vertical pressure reaching a value of 6.75 MPa. On the other hand, the numerical curve shows a decrease of the vertical pressure with stabilization at 6.26 MPa.

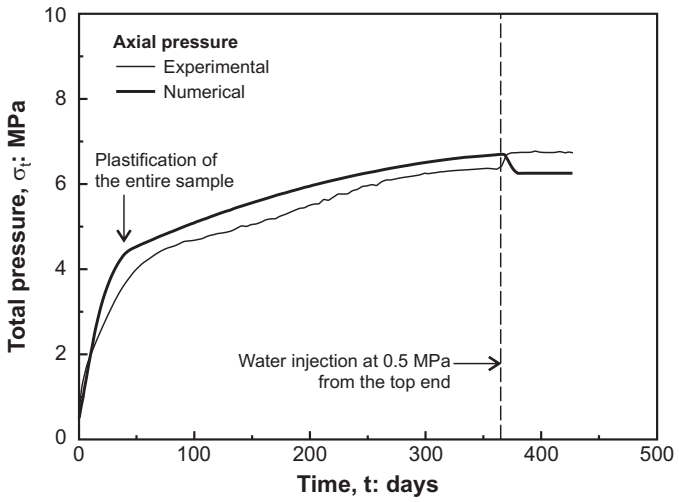

Figure 8.13: Total vertical pressure. Comparison between experimental data and model predictions.

As discussed above, the development of the total vertical pressure during hydration of the bentonite sample is marked by two main events: firstly, a change of slope at the beginning of the first hydration stage and secondly, an increase or decrease of the swelling pressure as soon as water is injected from the top face. In order to understand these two events, the evolution of the preconsolidation pressure profiles is given in Figure 8.14. The preconsolidation pressure p_0^* is the hardening variable of the mechanical model. Accordingly, an increase of p_0^* indicates an increase of the plastic volumetric deformation of the sample. As evidenced in Figure 8.14(a), hydration of the sample leads to a progressive yielding of the material and the change of swelling rate observed on day 43 in Figure 8.13 corresponds to the plastification of the entire bentonite sample. On the other hand, water injection from the top face generates additional plastic strains whose magnitude is the highest at the top of the sample. A reason for the decrease in the total vertical stress is the shape of

the Loading-Collapse curve in the low suction range. Indeed, although no elastic swelling is considered in the quasi-saturated domain (according to the mechanical model developed in Chapter 5), the apparent preconsolidation pressure still decreases with decreasing suction (according to the expression of the LC curve) and the ultimate suction decrease follows an elastoplastic stress path.

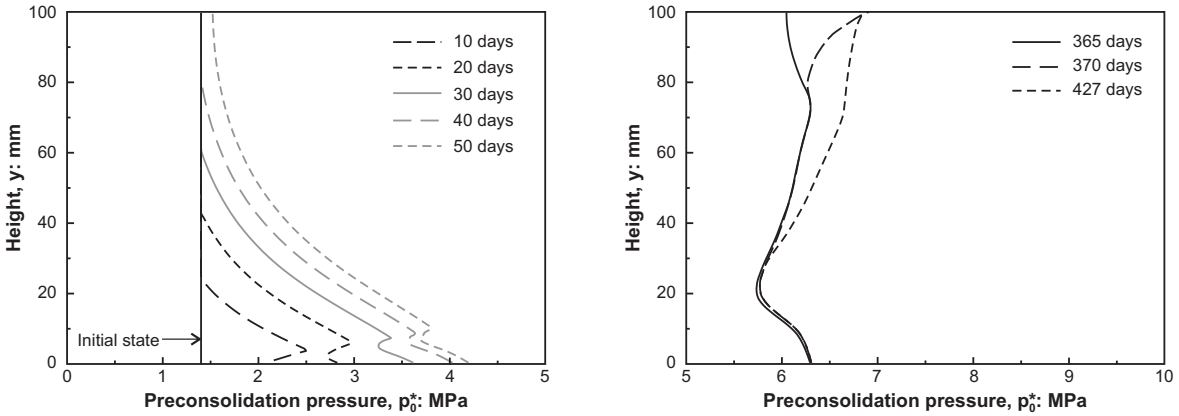

(a) Stage 1: injection from the bottom.

(b) Stage 2: injection from the top.

Figure 8.14: Evolution through time of the preconsolidation pressure p_0^* in the sample during water injection (numerical results).

3.3.4 Total radial stress

The radial total pressure developed by the sample during hydration is measured at different heights. Figures 8.15 compare the experimental and numerical results in terms of total lateral stress. As soon as hydration started, the total pressure sensors exhibited a signal response (thin continuous curves in Figures 8.15). Therefore, the experimentalists of the French Atomic Energy Commission corrected the rough data by subtracting the initial pressure measured by the sensors (dash curves in Figures 8.15). The corresponding shifts are equal to 3.65 MPa for PT1, 2.8 MPa for PT2, 4 MPa for PT3 and 1.4 MPa for PT4. However, it should be noted that some degree of uncertainty remains on the applied correction, which is the reason why both rough and corrected data are represented in Figures 8.15. As shown in the figures, the numerical model represents well the experimental data, both qualitatively and quantitatively. The evolution of the radial pressure follows a trend which is different from the vertical pressure. The total radial stress reached after full saturation of the sample is different from one height to another. While that was initially attributed to friction between the sample and the cell, the numerical model is able to reproduce the observed features. As soon as injection from the top started, the total radial pressures exhibited decrease, contrary to the vertical pressure. This decrease is all the most important that the sensor is close to the top injection front.

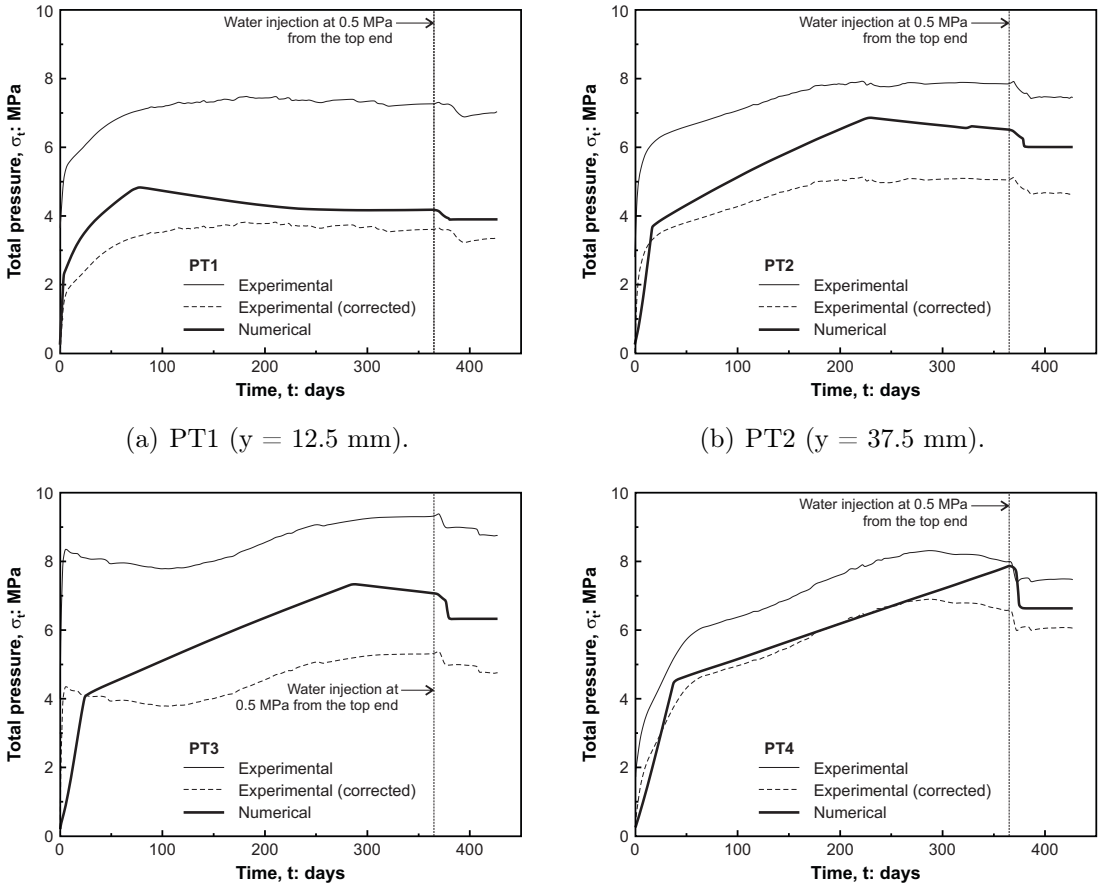

(a) PT1 (y = 12.5 mm).

(b) PT2 (y = 37.5 mm).

(c) PT3 (y = 50 mm).

(d) PT4 (y = 75 mm).

Figure 8.15: Total radial pressure along the sample. Comparison between experimental results and numerical predictions.

A common trend is observed for all radial sensors. The analysis is carried out for the sensor PT2 located at 37.5 mm from the bottom end of the sample (Figure 8.16). The radial pressure is first marked by a rapid elastic increase (1). Then, the point reaches the LC curve and elastoplastic deformations are generated (2). The curve is marked by a peak corresponding to the reaching of the threshold degree of saturation $S_r^* = 0.96$. As a consequence of the loss of rigidity, the pressure decreases (3). After one year of hydration from the bottom end, water is injected from the top at 0.5 MPa. Accordingly, the water pressure increases and plastic deformation are created (4). Finally, full saturation is quickly attained and the total radial pressure stabilizes (5).

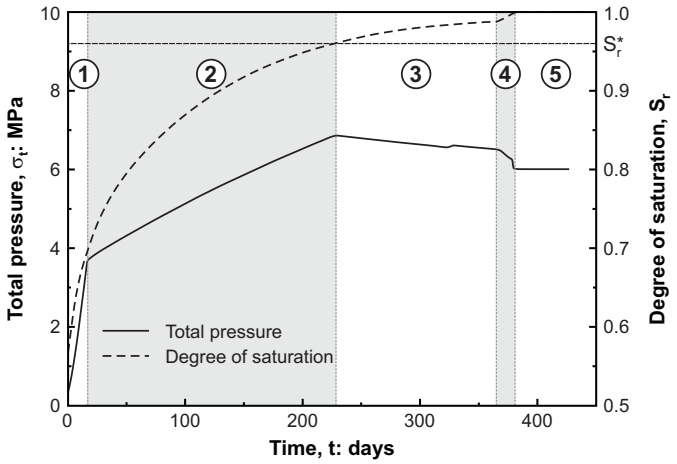

Figure 8.16: Evolution of the total radial pressure at a distance of 37.5 mm from the bottom face.

3.4 Sensitivity analysis

The sensitivity analysis performed in this section has two main objectives. First of all, it aims at highlighting the contributions of the developed model and new hydromechanical coupling that are introduced. Secondly, uncertainty accompanies some model parameters. The influence of these parameters on the model response is evaluated.

3.4.1 Influence of the threshold degree of saturation S_r^*

In the reference model, a threshold degree of saturation S_r^* equal to 0.96 was assumed. This parameter is introduced in the mechanical model to limit swelling due to hydration in the zone of partial saturation. Indeed, since the water retention model has no real air-entry value, the threshold parameter is introduced to delimit the partially saturated domain from the saturated domain. Figure 8.17 compares the response of the model for five different values of S_r^*, namely 0.96 (reference model), 0.97, 0.98, 0.99 and 1 (original Barcelona Basic Model). As far as the degree of saturation within the sample remains below the threshold degree of saturation, all models predict the same response. On the other hand, once that the degree of saturation reaches locally S_r^*, the model responses differ and the rate of total pressure increase is all the more important that S_r^* is high. Accordingly, the highest S_r^*, the largest the final swelling pressure. In particular, the highest swelling pressure is attained with the original Barcelona Basic Model formulation. After 365 days of hydration, the swelling pressure is of the order of 11.5 MPa and has not stabilized, although the injected water volume has almost. Figure 8.17 highlights thus the important contribution of the mechanical model developed in this work.

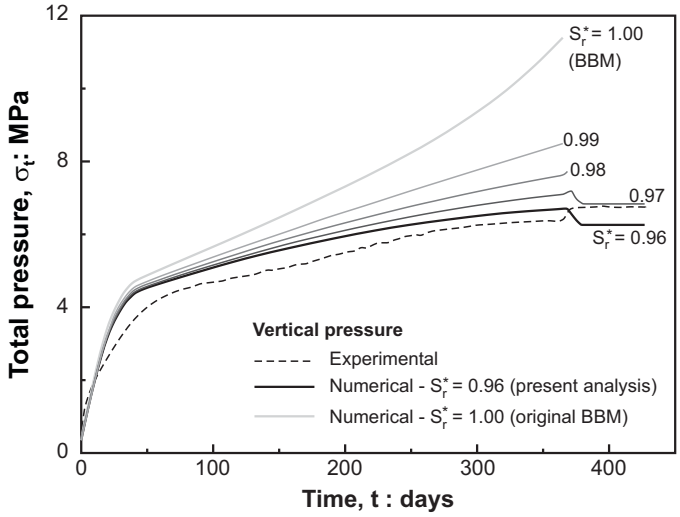

Figure 8.17: Influence of the threshold degree of saturation S_r^* on the total vertical pressure.

3.4.2 Influence of the water retention model

To assess the influence of the water retention model adopted in the reference case, a simulation is performed with a *fixed* water retention curve corresponding to a constant initial dry density. At the global scale, the developed water retention model allows a better reproduction of the hydration kinetics, as demonstrated in Section 4.3 of Chapter 6.

Yet, the water retention model also affects the mechanical behaviour of the bentonite sample since it determines the moment when the criterion $S_r = S_r^*$ is reached. Figures 8.18(a) to 8.18(d) present the evolutions of the total radial pressure at different heights of the sample, both for a *fixed* water retention curve ("constant WRC") and the reference case ("present analysis"). The different figures show that the water retention model influences the time when the maximum total pressure is reached. In particular, for the sensor PT1 located the closer from the bottom face, the peak pressure predicted with a constant water retention curve takes place before the one predicted with the water retention model developed in Chapter 4. Indeed, this sensor is located in the zone where the sample experiences swelling strain (see Figure 8.10). Accordingly, for a given suction value, the degree of saturation will be higher with the constant water retention curve than with the new model. In this case, the criterion $S_r = S_r^*$ is thus reached before. The opposite phenomena are observed for the sensors PT2, PT3 and PT4 which are located in compressed zones.

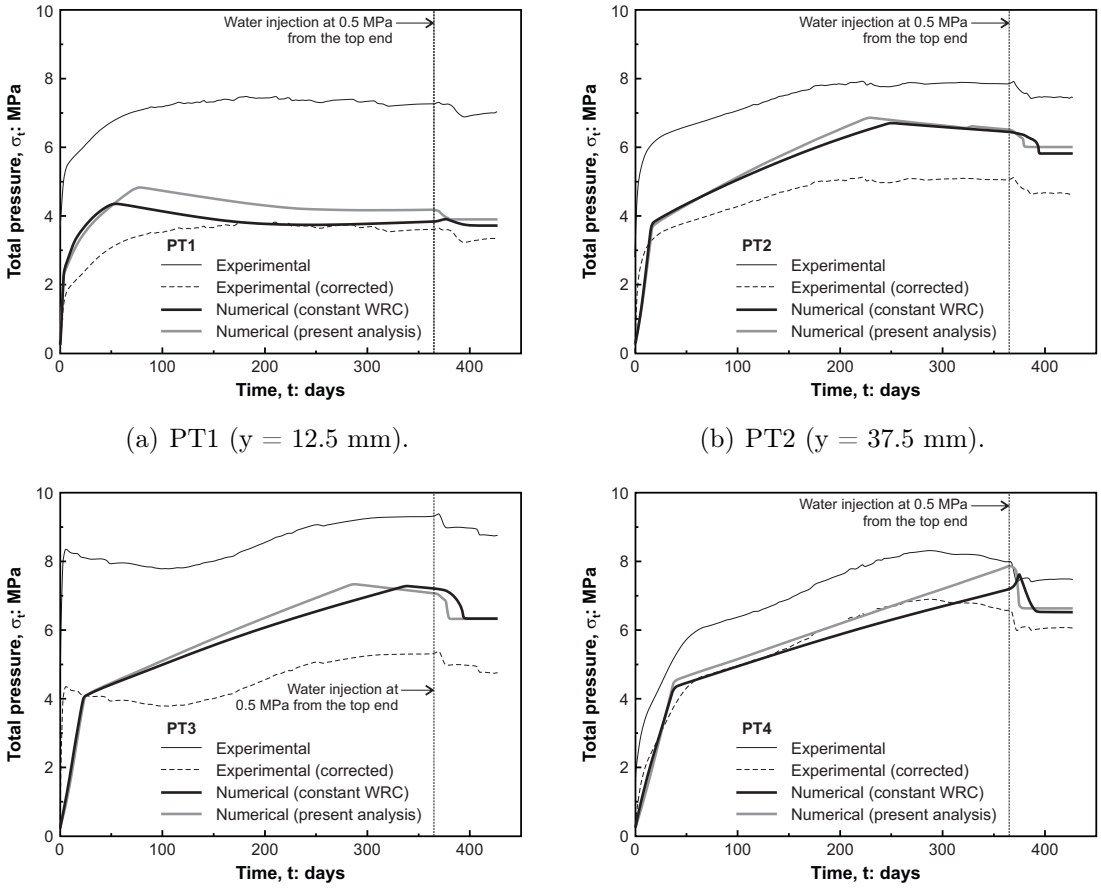

(a) PT1 (y = 12.5 mm).

(b) PT2 (y = 37.5 mm).

(c) PT3 (y = 50 mm).

(d) PT4 (y = 75 mm).

Figure 8.18: Influence of the water retention model on the total radial pressure along the sample.

3.4.3 Influence of the initial void ratio

Because it will be difficult to ensure the exact target dry density under *in situ* conditions, and especially at the industrial scale, it is essential to study the influence of the initial void ratio on the model response. However, the only modification of the initial void ratio in the mechanical model parameters does not yield any significant change of the mechanical response. As a matter of fact, in the elastic domain of the Barcelona Basic Model, the swelling pressure S_P developed under constant volume conditions is given by

$$S_P = p_i \left(\frac{s_i + u_{atm}}{u_{atm}} \right)^{\frac{\kappa_s}{\kappa}} \tag{8.5}$$

where p_i and s_i are the initial mean net stress and suction, u_{atm} is the atmospheric pressure, and κ_s and κ are the elastic parameters related to suction and mean net stress changes respectively (see Chapter 5). The previous equation highlights the fact that, in the elastic domain at least, the swelling pressure is not influenced at all by the void ratio.

However, changes in void ratio are likely to affect at least two parameters of the mechanical

model, namely the elastic stiffness κ_s related to suction changes and the preconsolidation pressure p_0^*. Their influence of the model response is discussed in the next two sections.

3.4.4 Influence of the elastic stiffness κ_s

The elastic stiffness κ_s is very much dependent on the material dry density. Indeed, an increase in the dry density enhances the swelling capacity of the compacted material (see Chapter 5). In order to assess the influence of κ_s on the model response, two additional simulations are performed with values of 0.063 and 0.083. Figure 8.19 presents the evolution of the vertical pressure developed by the sample during hydration for the three different values of the parameter κ_s. As shown in Figure 8.19, the elastic stiffness κ_s affects both the swelling rate and the final swelling pressure. A higher κ_s yields a higher swelling rate, hence a higher total pressure.

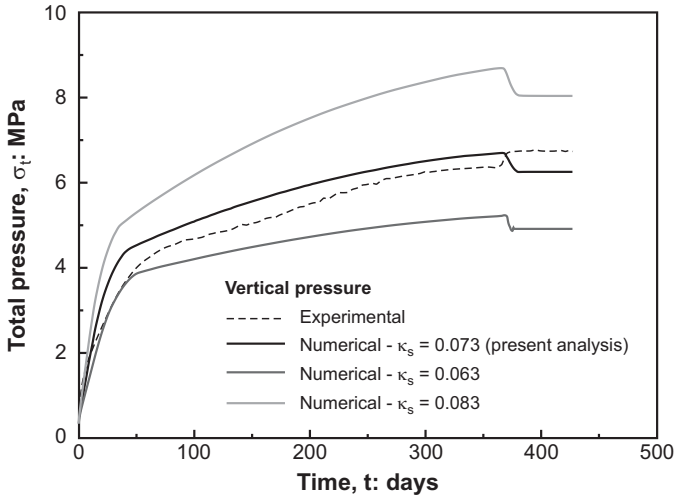

Figure 8.19: Influence of the elastic stiffness κ_s on the total vertical pressure.

3.4.5 Influence of the preconsolidation pressure p_0^*

The preconsolidation pressure p_0^* is an important parameter of the mechanical model since it determines the size of the elastic domain. Accordingly, a smaller value of the preconsolidation pressure yields a smaller elastic domain, and vice versa. In the framework of elastoplasticity, the apparent preconsolidation pressure is interpreted as the higher stress state encountered by the material. For compacted materials, this stress value is the compaction pressure. Yet, in practice, the compaction method is also likely to influence the behaviour of the material. Figure 8.19 presents the evolution of the vertical pressure developed by the sample during hydration for the three different values of the preconsolidation pressure for saturated states p_0^*, namely 1.4 MPa, 1.6 MPa and 1.8 MPa. As can be observed in Figure 8.20, the preconsolidation pressure does not change the evolution of the total pressure with time, but its amplitude.

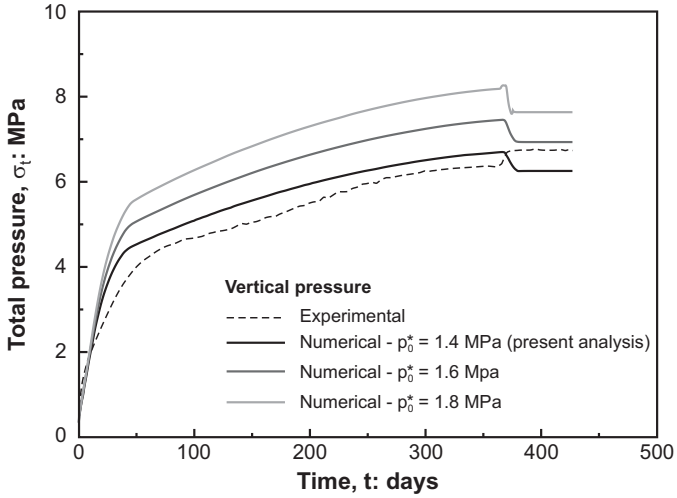

Figure 8.20: Influence of the preconsolidation pressure p_0^* on the total vertical pressure.

3.5 Conclusions

The Bentogaz 2 test was realized at the laboratory scale by the French Atomic Energy Commission. It consisted in the hydration of a compacted sample under constant volume conditions. The main originality of the test is its extensive instrumentation, making possible the complete monitoring of the hydromechanical state of the sample. Yet, the complex responses of the sensors made difficult a good and comprehensive understanding of the material. In this section, the Bentogaz 2 test was modelled using an advanced constitutive framework that supplies new explanations allowing a better understanding of the material behaviour and of the experimental data. In particular, the complex evolution of the total axial and radial pressure sensors with time could be explained by an advancing hydration and swelling front in the bentonite sample. The good agreement between the numerical results and the experimental data, both qualitatively and quantitatively, allowed validating the developed framework.

4 PGZ2 *in situ* test

4.1 Description of the test

The PGZ2 experiment[1] is an *in situ* test carried out by the French national radioactive waste management agency (Andra) in its Meuse/Haute-Marne Underground Research Laboratory located in Bure, France. Initiated in 2009, the test aims at studying the impact of gas production on the hydromechanical behaviour of an engineered barrier. More specifically, two different tests are carried out in order to investigate the competing effects of hydration from the host rock and gas injection. In a first borehole, a plug is inserted and allowed to hydrate naturally. The hydration kinetics and the time required to reach full saturation are determined. In a second borehole, a plug is also inserted and allowed to hydrate, but gas is injected before full saturation of the material is achieved. The measurements of the total swelling pressure and pore pressure in the two boreholes are then compared in order to assess the impact of gas on the hydromechanical behaviour of the plug.

Figure 8.21 presents the overall layout of the PGZ2 experiment. Three boreholes, named PGZ1001, PGZ1011 and PGZ1013 are drilled within the Callovo-Oxfordian host rock. The PGZ1013 borehole is used to monitor bentonite hydration while PG1011 is used to study gas injection during hydration. These boreholes, drilled between the GEX and GMR/GED galleries, are parallel, 20 meters long and 9 meters distant from each other. In order to reduce the investigation time, their diameter is limited to 101.3 mm. Finally, the PGZ1001 borehole is drilled from the GMR gallery parallel to the two first boreholes. It is used to measure the hydraulic head gradient between the GEX and GMR galleries by means of five measurement chambers. This last borehole has a diameter of 76 mm.

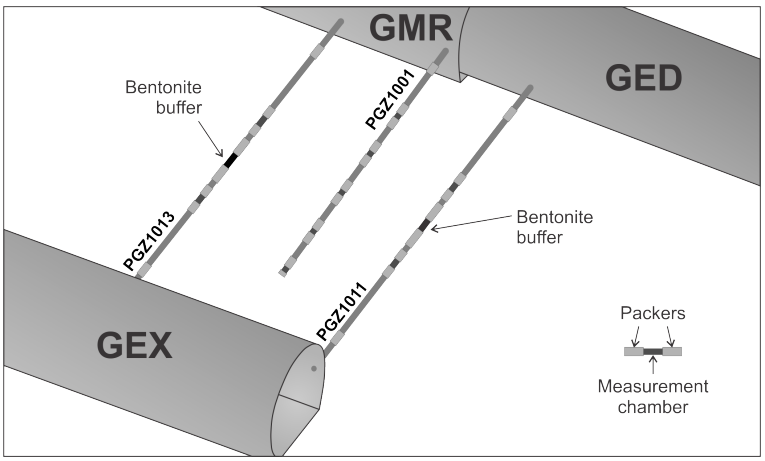

Figure 8.21: Layout of the PGZ2 experiment (de La Vaissière, 2013).

The material used for the plug is a compacted mixture of MX-80 bentonite and quartz sand with a respective proportion of 70/30 in dry mass. The initial dry density of the mixture is about 2.06 g/cm^3 and its initial water content, about 8.8%. The plug has a

[1] A more complete description of the experiment can be found in de La Vaissière (2013).

diameter of 94 mm and a total length of 400 mm. Two seats are inserted at both ends of the cylindrical sample (Figure 8.22). Each of them is equipped with two total pressure sensors (PRT), two interstitial pressure sensors (PRE), one temperature sensor and three hydraulic lines that are used for gas injection.

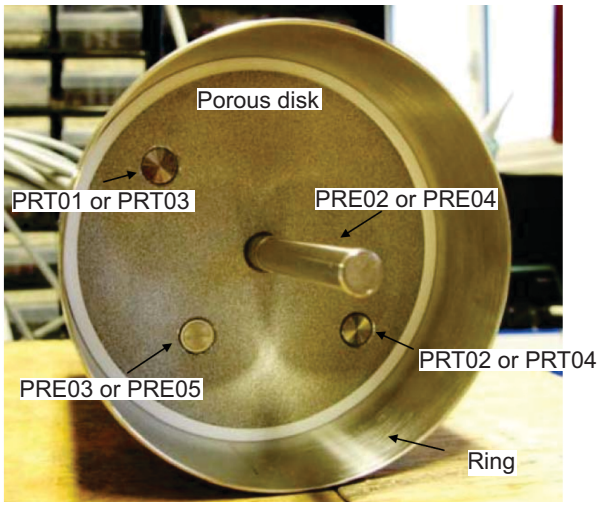

Figure 8.22: Seats composed of a porous disk, total pressure (PRT) and interstitial pressure (PRE) sensors and metal ring (de La Vaissière, 2013).

The initial radial technological gap between the bentonite buffer and the host rock is about 381 cm^3, which represents 14% of the total volume of the borehole section under consideration (Figure 8.23). In addition, technological gaps exist longitudinally between the sleeves of the seats and the host rock (de La Vaissière, 2013). Their volume reaches (2 x 419) cm^3 = 838 cm^3, which should be compared to the initial bentonite volume of 2776 cm^3. The total volume of technological gaps represents therefore more than 30% of the volume of the borehole under consideration.

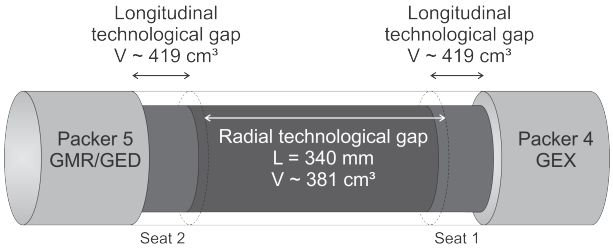

Figure 8.23: Volumes of technological gaps in the PGZ2 *in situ* test.

An important decrease in the buffer density is associated to the progressive filling of technological voids. Yet, for the design of the PGZ2 experiment, only the radial technological was taken into account, based on observations made on mock-up tests (de La Vaissière, 2013). Indeed, these mock-up tests showed that friction between the material, containing 30% sand, and the external and internal walls of the experimental set-up was sufficient to limit the extrusion. Consequently, accounting for the radial gaps only, the expected final dry density of the mixture is 1.81 Mg/m^3.

4.2 Callovo-Oxfordian claystone

The Callovo-Oxfordian claystone (COx) is an indurated clay-rich formation of marine origin, deposited 160 million years ago (between the Callovian and Oxfordian ages) in the western area of the Paris Basin. At the level of the Underground Research Laboratory of Bure, the formation is composed of 40 to 50% of interstratified illite/smectite and illite, kaolinite and chlorite (Gaucher *et al.*, 2004).

Furthermore, at the level of the URL, the initial stress in the COx formation is anisotropic, with the minor horizontal principal total stress $\sigma_{t,h}$ oriented in the axis of the GED and GEX galleries (Figure 8.1) and

$$\begin{aligned} \sigma_{t,h} &= 12 \text{ MPa} \\ \sigma_{t,H} &= 15.6 \text{ MPa} \\ \sigma_{t,v} &= 12 \text{ MPa} \end{aligned} \tag{8.6}$$

with $\sigma_{t,H}$ and $\sigma_{t,v}$, the major horizontal and vertical principal total stresses respectively. The undisturbed water pressure is equal to 4.5 MPa. Yet, Figure 8.24 shows the profile of pseudo-stabilised pressures between the GEX and GMR/GED galleries as measured in the PGZ1001 borehole. The experimental data show that ventilation in the GEX and GMR/GED galleries impacts the pore water profile. The maximum water pressure (equal to 3.68 MPa) is reached at the centre of the borehole.

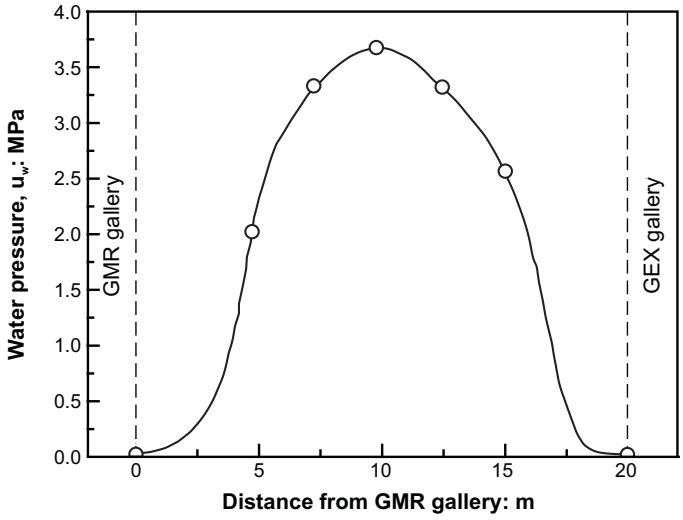

Figure 8.24: Profile of pseudo-stabilised water pressures between the GEX and GMR/GED galleries.

In this work, attention is focused on the behaviour of the bentonite buffer. Accordingly, simple constitutive laws, based on the work of Charlier *et al.* (2013), are adopted to reproduce the hydromechanical behaviour of the Callovo-Oxfordian claystone[2]. In particular, an isotropic linear elastic–perfectly plastic model (with Van Eekelen yield surface) is

[2]Further information on the behaviour of Callovo-Oxfordian claystone and its constitutive modelling can be found in Pardoen (2015).

adopted to reproduce the mechanical behaviour of the Callovo-Oxfordian claystone. The mechanical model is written in terms of the Bishop's definition of the effective stress $\boldsymbol{\sigma'}$ (Bishop, 1959)

$$\boldsymbol{\sigma'} = \boldsymbol{\sigma_t} - b\left[u_w S_r + u_g\left(1 - S_r\right)\right]\boldsymbol{I} \tag{8.7}$$

where $\boldsymbol{\sigma_t}$ is the total stress tensor, b is the Biot coefficient, u_w and u_g are the water and gas pressures, S_r is the corresponding degree of saturation of the porous medium and $\boldsymbol{I}$ is the identity tensor. The Van Eekelen yield surface f_{VE} reads

$$f_{VE} \equiv \frac{J_2}{3} + M_\theta\left(p' - \frac{c}{\tan\varphi}\right) = 0 \tag{8.8}$$

where p' and J_2 are the mean effective stress and the second invariant of the deviatoric stress tensor respectively, M_θ is a depends on the Lode's angle θ according to Equation (5.29), c is the cohesion and φ is the friction angle. Table 8.7 presents the mechanical parameters used to model the behaviour of the Callovo-Oxfordian claystone.

b	E (MPa)	ν	c (MPa)	φ (°)
0.6	4000	0.3	3	20

Table 8.7: Mechanical parameters of the Callovo-Oxfordian claystone (Charlier *et al.*, 2013). E denotes Young's Modulus and ν is the Poisson's ratio.

To reproduce the unsaturated behaviour of the Callovo-Oxfordian claystone, a water retention curve $S_r\left(s\right)$ and a water permeability curve $k_{rw}\left(S_r\right)$ are defined. These relationships are based on the van Genuchten's equation (van Genuchten, 1980), with parameters calibrated in order to reproduce at best the experimental data available (Charlier *et al.*, 2013). The water retention curve and relative permeability law are respectively expressed as

$$S_r = \left[1 + \left(\frac{s}{\alpha}\right)^n\right]^{\frac{1}{n}-1} \tag{8.9}$$

$$k_{rw} = \sqrt{S_r}\left[1 - \left(1 - S_r^{1/m}\right)^m\right]^2 \tag{8.10}$$

where α is a parameter associated with the air-entry pressure, and n and m are model parameters. The different hydraulic parameters of the Callovo-Oxfordian claystone are presented in Table 8.8.

K_w (m^2)	α (MPa)	n	m
4×10^{-20}	15	1.49	0.55

Table 8.8: Hydraulic parameters of the Callovo-Oxfordian claystone (Charlier *et al.*, 2013).

4.3 One-dimensional model

The real geometry of the PGZ2 experiment is complex and the three-dimensional effects are expected to be high: transversally, the gap between the host rock and the bentonite buffer is not uniformly distributed (due to gravity) and longitudinally, the behaviour of the bentonite plug is affected by the presence of the seats. In order to highlight the different coupled hydromechanical processes, the problem is first treated as a one-dimensional idealization of the PGZ2 experiment.

4.3.1 Features of the analysis

A one-dimensional axisymmetric model of the central section of the bentonite buffer is performed. As a consequence of this simplification, the technological void is homogeneously distributed around the bentonite buffer so that there is no initial contact between the buffer and the host rock. The initial gap between the materials is equal to 3.65 mm (Figure 8.25). The radial extension of the model is 10 meters, i.e. more than the distance separating the boreholes PGZ1013 and PGZ1011.

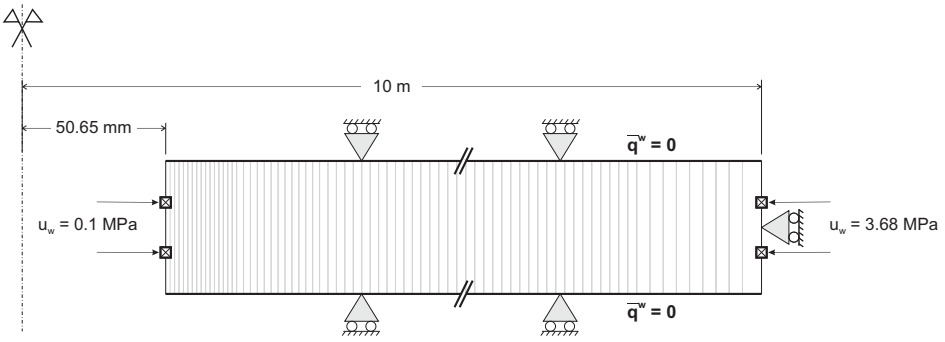

(a) Phase 1: drift excavation.

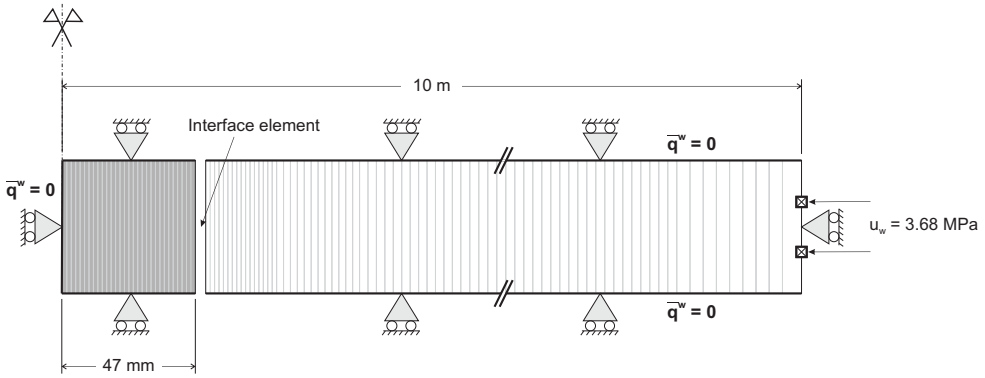

(b) Phase 2: buffer saturation.

Figure 8.25: Geometry of the one-dimensional problem.

The initial total stress in the Callovo-Oxfordian claystone is assumed to be isotropic and equal to 12 MPa, which corresponds to the value of the minor stress. The influence of rock anisotropy is not taken into account in this modelling due to the axisymmetric conditions.

In addition, the water pressure measured at the centre of the PGZ1001 borehole, equal to 3.68 MPa, is considered as initial and natural value of the water pressure field in the Callovo-Oxfordian claystone. The bentonite buffer has an initial suction of 56 MPa which was determined through the water retention curve, knowing the initial dry density and water content. This initial suction corresponds to an initial degree of saturation of 0.66.

The modelling comprises two successive stages. The first stage consists in the excavation of the borehole and the drainage of the water pressure. The excavation is modelled as a progressive reduction (in 1 hour) of the total radial stress at the gallery wall (Figure 8.25(a)). Due to the small diameter of the borehole, and because the borehole was not ventilated, the initial water pressures at the gallery wall are decreased up to atmospheric pressure and maintained constant during 1 day. The bentonite buffer is then placed in the borehole and allowed to hydrate (Figure 8.25(b)).

4.3.2 Parameters of the buffer and the interface

In the PGZ2 test, a technological gap exists between the host rock and the buffer. Consequently, at the beginning of the test, the buffer swelling yields a decrease in dry density. Gatabin *et al.* (2006) evaluated the influence of technological gaps on the swelling pressure. In particular, they determined the swelling pressure of samples compacted to an initial dry density of 2.03 Mg/m^3 and saturated in constant volume cells with an initial technological gap, so as to reach final dry densities as small as 1.67 Mg/m^3. Gatabin *et al.* (2006) showed that the lowest the final dry density, the lowest the swelling pressure (Figure 8.26).

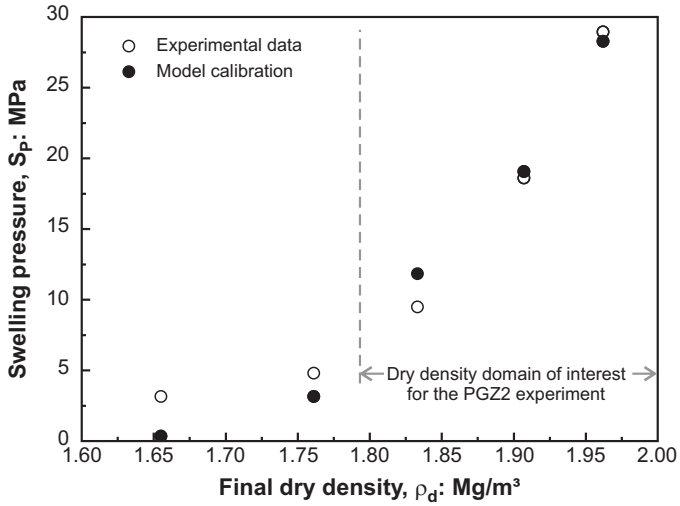

Figure 8.26: Evolution of the swelling pressure with dry densities. Comparison between experimental data (Gatabin *et al.*, 2006) and model calibration.

The mechanical parameters of the MX-80 bentonite/sand mixture were calibrated in Chapter 5 where the developed model has shown good abilities to reproduce the swelling behaviour of bentonites under both oedometer and confined conditions. Yet, one limitations of our mechanical model is the impossibility of reproducing the behaviour of bentonite-based materials under both confined and unconfined conditions. As a matter

of fact, experimental data have shown that the slope of the reversible wetting–drying line for changes in suction, κ_s, was dependent on the dry density of the material, which is not considered in our model. Accordingly, the experimental data presented in Figure 8.26 cannot be reproduced with the developed hydromechanical model and the parameters previously calibrated on the mixture compacted to an initial dry density of 1.67 Mg/m^3.

Considering the very high initial dry density of the material, two model parameters previously calibrated, namely the initial preconsolidation pressure and the elastic slope κ_s, are modified to reproduce the evolution of the swelling pressure as depicted in Figure 8.26. The modification of these parameters is justified by the facts that

- in order to reach a higher dry density, the material needs to be compacted to a higher pressure, so that the apparent preconsolidation stress is higher. Accordingly, the preconsolidation pressure for saturated states p_0^* is likely to increase with increasing density.
- experimental data show that κ_s is enhanced for a higher dry density (see Section 2.2 of Chapter 5).

The values of p_0^* and κ_s are determined by best-fitting the experimental data presented in Figure 8.26. The calibration of the model is shown in the same figure for $p_0^* = 8.81$ MPa and $\kappa_s = 0.148$.

Finally, the existence of technological gaps between he bentonite buffer and the hos rock is explicitly taken into account. It is modelled using the zero-thickness interface element presented in Chapter 7. A penalty coefficient K_N of 10 GPa/m is selected, and the transversal transmissivity t_{wt} between the host rock and the bentonite buffer is first assumed equal to 10^{-12} m/Pa·s. It is considered identical when the technological gap is open and when it is closed.

4.3.3 Numerical results

4.3.3.1 PGZ1013 borehole excavation

The first stage of the modelling consists in the excavation of the PGZ1013 borehole and the drainage of the water pressures. By the end of this stage, the convergence of the Callovo-Oxfordian host rock is small as the displacement of the wall is of only 0.28 mm. However, the Callovo-Oxfordian host rock has reached plasticity and an excavation damaged zone of 2.3 cm thickness is created around the borehole (Figure 8.27(a)). The pore water profile is presented in Figure 8.27(b). The gallery drainage modifies the water pressure profiles on around 0.4 m.

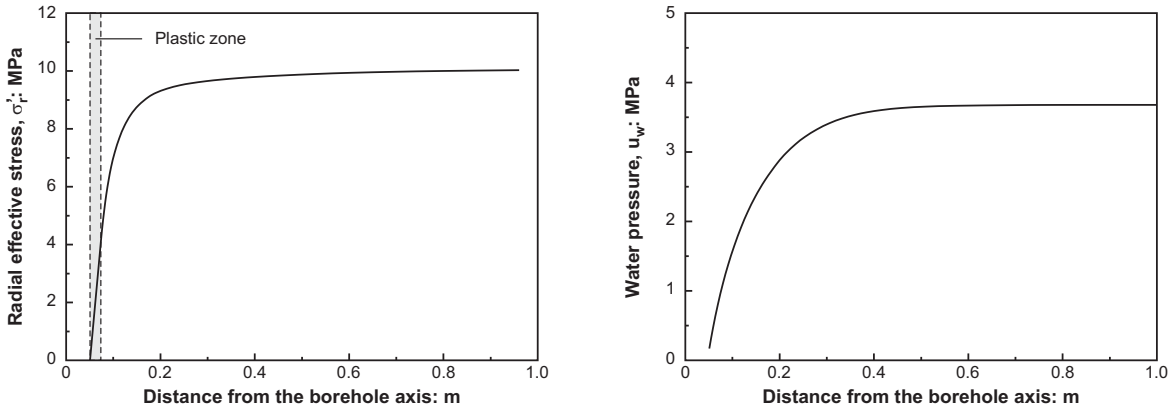

(a) Water pressure.

(b) Radial effective stress.

Figure 8.27: Profiles of water pressure and radial effective stress in the Callovo-Oxfordian claystone at the end of the excavation (1 day).

4.3.3.2 Bentonite hydration: buffer behaviour

In a second phase, the bentonite buffer is placed into the borehole and allowed to hydrate. Figures 8.28(a) and 8.28(b) present the evolution of the water pressure and degree of saturation profiles in bentonite. Despite the very low permeabilities of the bentonite buffer and of the Callovo-Oxfordian host rock (supplying water), the hydration of the buffer is relatively fast, owing for the large contact surface and the important water pressure gradient between the materials. Yet, 12 years are necessary to recover the natural water pressure field of the Callovo-Oxfordian claystone. Indeed, as time passes, the hydraulic gradient between the bentonite plug and the host rock decreases, so that the water fluxes become lower and lower.

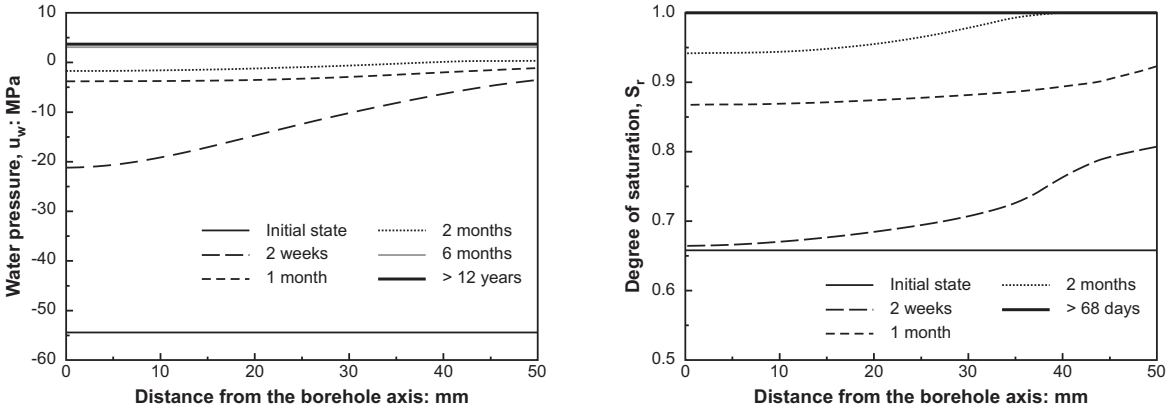

(a) Water pressure.

(b) Degree of saturation.

Figure 8.28: Evolution through time of water pressure in the bentonite buffer during hydration (numerical results).

Figures 8.29(a) and 8.29(b) show the evolutions with time of the global degree of saturation[3] of the buffer and of the total contact pressure between the buffer and the host rock, respectively. The hydration of the buffer first occurs under almost free swelling conditions, the contact pressure between bentonite and the host rock being null (Figure 8.29(b)). Accordingly, swelling leads to the progressive filling of the technological void. During this stage, the global degree of saturation of the buffer does not increase significantly because the volume of the buffer increases (Figure 8.29(a)). Contact between bentonite and the Callovo-Oxfordian formation is reached 10.3 days after the buffer installation (Figure 8.29(b)). From that time on, the contact pressure increases progressively as a consequence of the progressive hydration of the buffer. Contrary to the first free swelling phase, bentonite saturation takes place at a higher rate (Figure 8.29(a)). After 68 days of hydration, the buffer is fully saturated and the total contact pressure at the host rock/bentonite buffer contact is of the order of 10.4 MPa. This duration of 68 days should be compared, on one hand, to the one-year long hydration process of the Bentogaz 2 experiment and, on the other hand, to the considerably lower values predicted by Gerard (2011). Indeed, using a classic hydromechanical framework for partially saturated porous media (see Chapter 3), Gerard (2011) predicted full saturation of the buffer within less than one month.

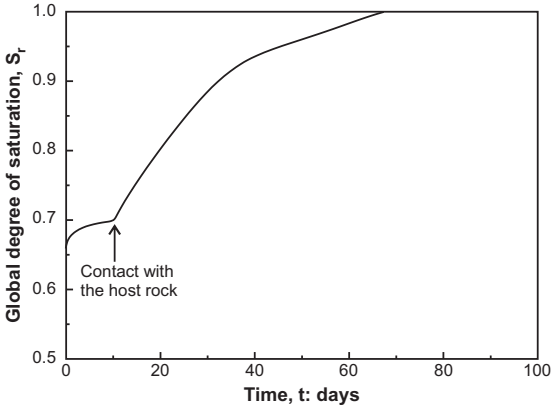

(a) Global degree of saturation.

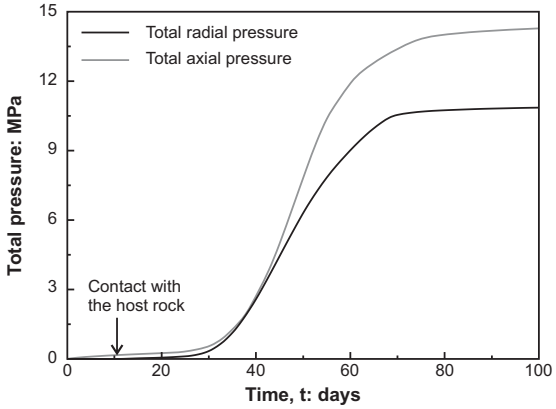

(b) Total contact (radial) pressure and out-of-plane (axial) pressure.

Figure 8.29: Evolutions through time of the global degree of saturation of the buffer, of the total contact pressure between the buffer and the host rock and of the total out-of-plane (axial) pressure.

Finally, the final total (radial) pressure between the buffer and the host rock is equal to 11.0 MPa. Yet, under *in situ* conditions, this contact pressure is not always accessible. As a matter of fact, only the axial total pressure is measured in the PGZ2 experiments, using the total pressure sensors placed in the seats (Figure 8.22). Figure 8.29(b) shows that, in the present analysis, the final axial pressure is equal to 14.3 MPa, which is slightly higher than the contact pressure, owing for the plane strain conditions. For the sake of comparison, Figure 8.30 presents the evolution with time of the total axial

[3]The global or overall degree of saturation of the buffer is defined as the total volume of water in the buffer over its total volume.

pressure recorded in the different boreholes (and by the two seats of each buffer) during the PGZ2 experiments. Figure 8.30 shows an increase in total pressure that is difficult to fully interpret using a simple one-dimensional analysis. Yet, one observes that the total pressures tend to reach values between 8 and 9.5 MPa that are thus lower than predicted by the model. However, the model does not take into account the axial technological gap between the seats and the host rock. Bentonite extrusion in this zone is indeed likely to yield a decrease of the measured pressure.

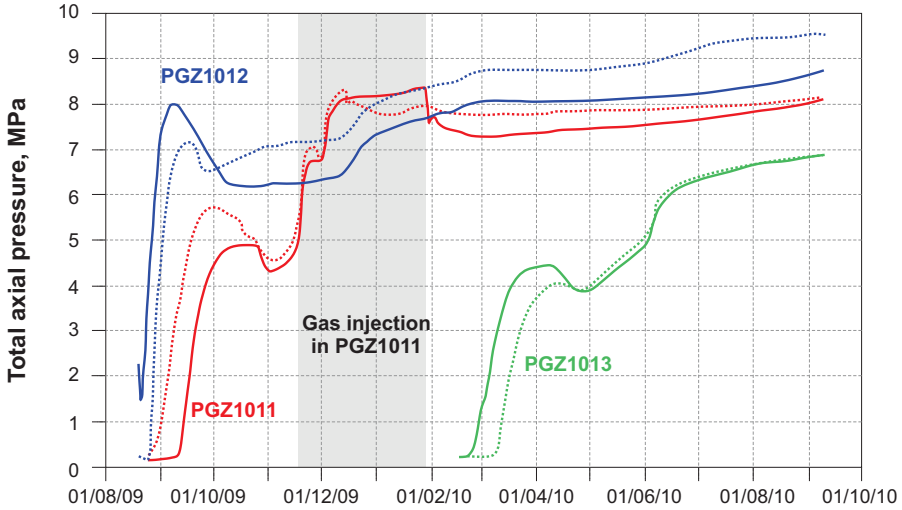

Figure 8.30: Total axial pressure recorded in the different boreholes (different colours) during the PGZ2 experiments. For a same colour, the two lines represent the evolution measured at the two seats.

The stress path of two points located at the centre of the bentonite buffer and on its border can be tracked in the $(s - S_r)$ plane (Figure 8.31). For the point located on the border of the plug, the first part of the path is characterized by a decrease in suction maintaining the degree of saturation almost constant. Indeed, the important swelling of the material leads to an increase of its porosity. Once that contact between the host rock and the buffer is reached, the degree of saturation increases more rapidly, owing for the almost constant-volume conditions. On the other hand, as far as the central part of the bentonite buffer is concerned, the path in the $(s - S_r)$ plane is first characterized by a slight decrease of the the degree of saturation, as a consequence of the material swelling. This swelling is itself a consequence of the decrease in suction and expansion of the material at the border of the buffer. Yet, this decrease is limited and the degree of saturation increases rapidly. Figure 8.31 highlights the significantly different stress paths experienced by the material depending on the considered point. For the sake of completeness, the initial water retention curve, corresponding to a constant porosity of 0.25, is also represented.

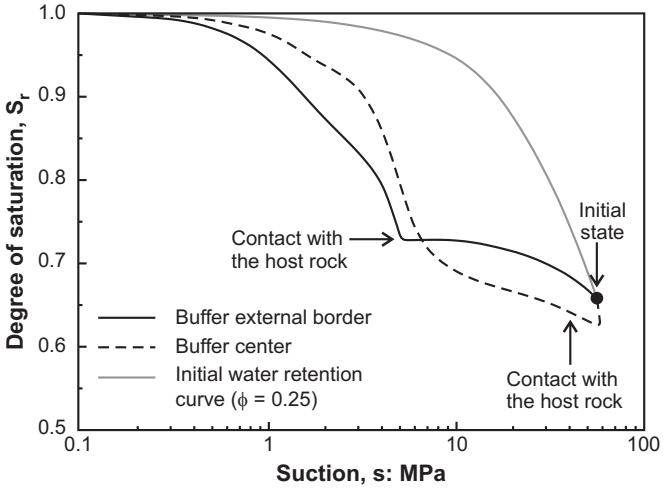

Figure 8.31: Stress path in the $(s - S_r)$ plane followed by two points located at the centre and on the border of the bentonite buffer. Comparison with the water retention curve for a constant initial porosity ($\phi = 0.25$).

Finally, Figure 8.32 shows the evolution with time of the dry density in the bentonite buffer. As the material swells and the technological void is filled, the dry density of the plug decreases progressively. This decrease in dry density is higher close to the drift wall where the suction changes, hence swelling strains, are the largest. Once that contact between the Callovo-Oxfordian claystone and the buffer is reached, the global volume changes become smaller because of the restrained volume conditions. As a matter of fact, at the time when contact is reached, the average dry density of the buffer is equal to 1.79 Mg/m^3 while it was equal to 2.06 Mg/m^3 initially. On the other hand, once that the material is fully saturated, the average dry density is equal to 1.71 Mg/m^3, owing for the progressive increase of the swelling pressure and compression of the surrounding rock. Once that the natural water pressure field is recovered, a higher porosity is found close to the Callovo-Oxfordian host rock. Such distribution of dry density has been observed after dismantling different *in situ* test such as the FEBEX experiment (Villar *et al.*, 2005).

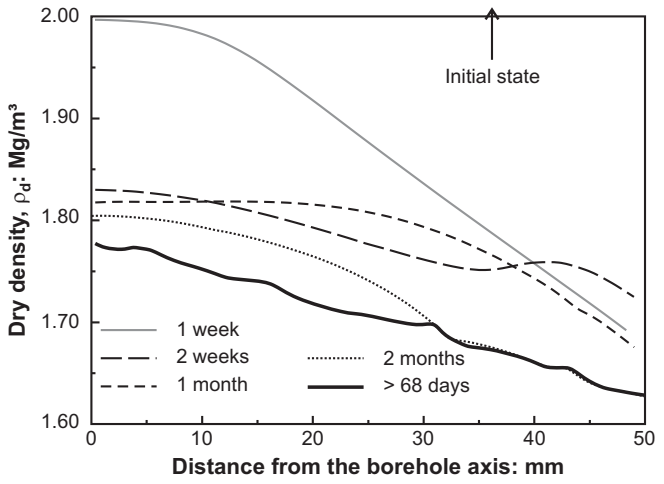

Figure 8.32: Evolution through time of the bentonite dry density.

4.3.3.3 Bentonite hydration: Callovo-Oxfordian claystone behaviour

Figure 8.33 presents the evolution of the water pressure profile in the Callovo-Oxfordian claystone. The initial very high suction in the bentonite buffer leads to the desaturation of the Callovo-Oxfordian claystone in the early saturation process. However, the very high air-entry pressure of the host rock (around 6 MPa) quickly limits the desaturation. As for the bentonite plug, 12 years are necessary to recover the natural water pressure field that existed in the Callovo-Oxfordian claystone prior to the excavation.

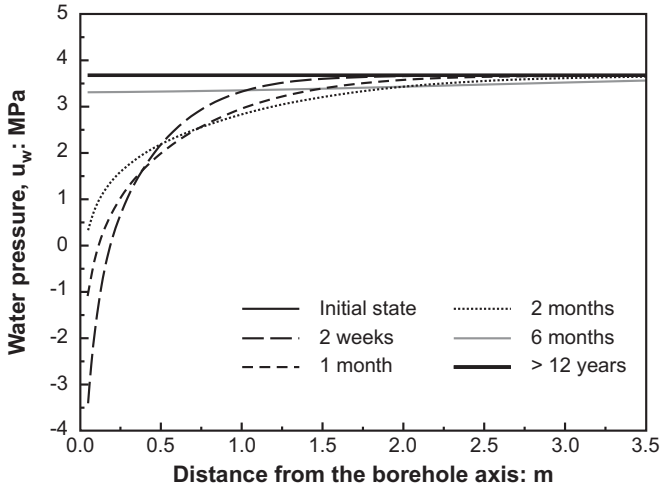

Figure 8.33: Evolution through time of water pressure and degree of saturation in the Callovo-Oxfordian formation during bentonite hydration (numerical results).

4.3.4 Comparison with mock-up tests

In order to better understand the hydration process and kinetics of the bentonite buffer, the French Atomic Energy Commission carried out a series of mock-up tests of the PGZ2 *in situ* experiments (de La Vaissière, 2013). The bentonite plugs were prepared in the same conditions as for the *in situ* tests. Different scenarios for supplying water to the bentonite were reproduced with the aim of explaining how the bentonite plug saturates. The bentonite cores have the same dimensions as the core of the PGZ2 experiment, are placed horizontally and, for the sake of observation, placed in a Pyrex glass tube of larger diameter (Figure 8.34). A total pressure and a force gauges were used to monitor the swelling pressure. The tests were carried out until the glass tube broke due to excessive bentonite swelling.

Five scenarios of hydration were studied, including slow ($>$ 20 days), fast ($\sim$ 2 days) and very fast hydration by liquid water flowing into the technological gap between the buffer and the glass tube at a slow rate (scenarios 1 to 3), slow and occasional hydration (10 cm^3/day) along one and then two horizontal edges and following the vertical axis (scenario 4) and hydration by water vapour (relative humidity of the air $>$ 80%) in the technological gap (scenario 5). Regardless the hydration scenario, the bentonite sample was found to swell extremely quickly (within a few days). In particular, in scenario 4, the glass tube broke after 9 days, but bentonite had not filled the technological gap over

the entire circumference. On the other hand, the technological gap was filled after 4 days of hydration in scenario 5. The numerical results, predicting contact after 10.3 days of hydration, are thus consistent with the observations made of the mock-up tests.

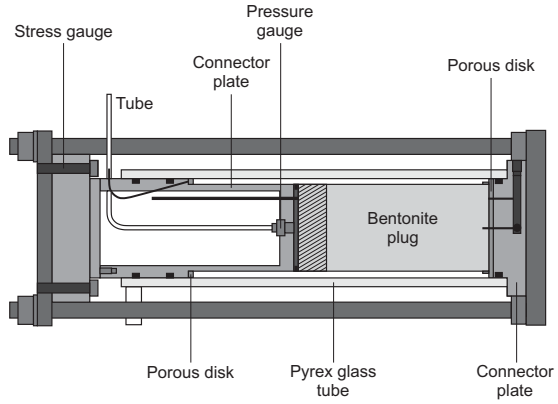

(a) Schematic layout of the cell.

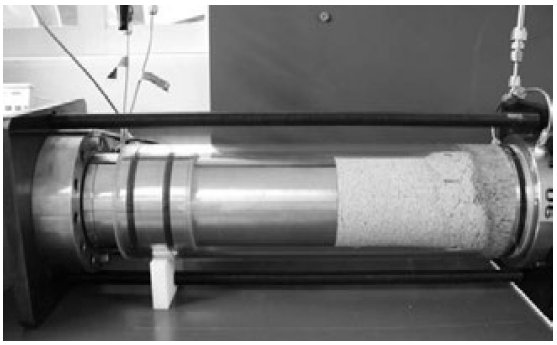

(b) Bentonite sample upon hydration by liquid water.

Figure 8.34: Mock-up cell of the PGZ2 experiment developed by the CEA (de La Vaissière, 2013).

4.3.5 Influence of the water retention model

In order to assess the influence of the developed water retention model on the hydration and swelling kinetics of the buffer, a new modelling is carried out using a *fixed* (constant) water retention curve corresponding to the initial porosity of the material. Figures 8.35(a) and 8.35(b) present the evolution with time of the total contact pressure between the buffer and the host rock and global degree of saturation of the buffer respectively.

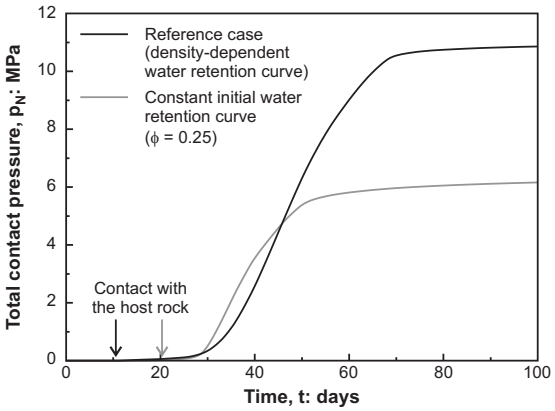

(a) Total contact pressure.

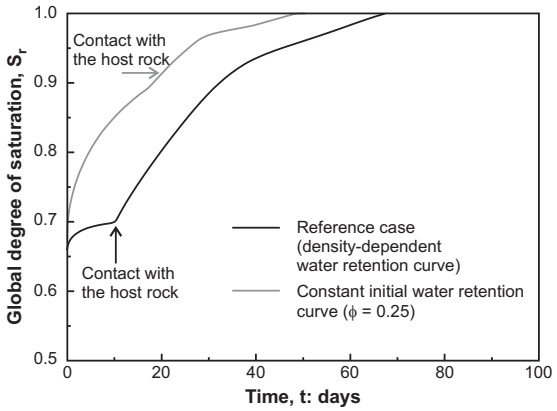

(b) Global degree of saturation.

Figure 8.35: Evolution through time of the total contact pressure between the buffer and the host rock and global degree of saturation of the buffer. Influence of the water retention model on the hydration and swelling kinetics.

As observed in Figure 8.35(a), the swelling pressure developed by the bentonite buffer is considerably lower when the water retention curve is maintained fixed. Indeed, the threshold degree of saturation S_r^* is reached sooner. However, the parameters of the mechanical model were calibrated considering the developed water retention model, so that conclusions on the swelling behaviour cannot legitimately be drawn. On the other hand, the influence of the water retention model on the bentonite saturation is considerable. Indeed, a significantly faster hydration kinetics is predicted when the water retention curve is maintained fixed (Figure 8.35(b)). As a matter of fact, full saturation of the buffer is reached after 48 days, while 68 days were necessary in the reference simulation.

4.3.6 Influence of the gap and interface properties

Due to limited experimental data and a difficult characterization, the hydraulic properties of the gap and interface are subject to important uncertainties. In the reference analysis, a very high transversal transmissivity equal to 10^{-12} m/Pa·s was used. In this section, different values of transversal transmissivity are used and their influence on the swelling and hydration kinetics is analysed.

Figures 8.36(a) and 8.36(b) present the evolution with time of the total contact pressure between the buffer and the host rock and global degree of saturation of the buffer for four different values of transversal transmissivity, namely 10^{-12} m/Pa·s, 10^{-14} m/Pa·s, 10^{-15} m/Pa·s and 10^{-16} m/Pa·s. The two figures show that for transversal transmissivities higher than 10^{-14} m/Pa·s, the interface does not impact the hydration kinetics. Indeed, the hydration kinetics of the buffer is only controlled by the water supply from the host rock and its capacity to receive this water, and the interface has no impedance role. On the other hand, when the transmissivity is decreased below 10^{-14} m/Pa·s, the hydraulic behaviour of the interface delays the saturation of the bentonite buffer and the development of the swelling strain and stress.

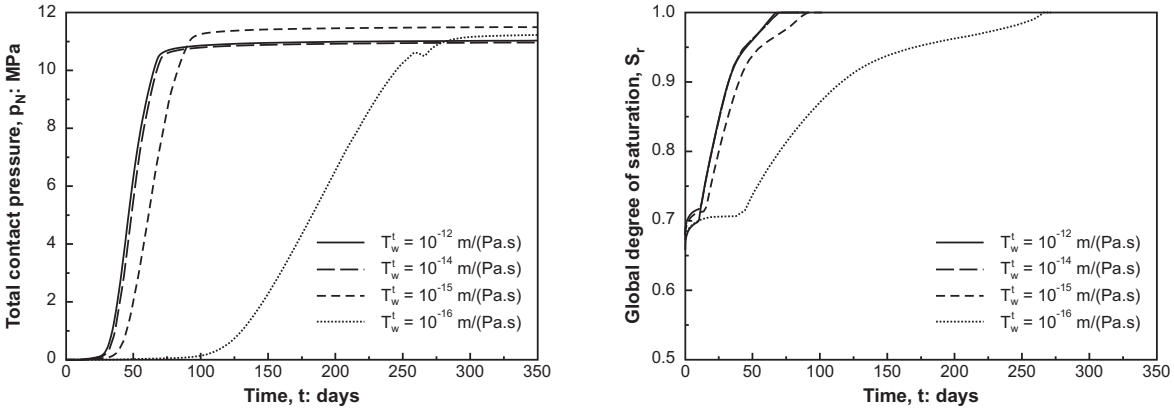

(a) Total contact pressure.

(b) Global degree of saturation.

Figure 8.36: Evolution through time of the total contact pressure between the buffer and the host rock and global degree of saturation of the buffer. Influence of the transversal transmissivity of the gap.

A more realistic situation is to consider a low transmissivity (equal to 10^{-16} m/Pa·s) as

long as there is no contact between the buffer and the host rock, and a higher transmissivity (equal to 10^{-12} m/Pa·s) when contact is achieved. Indeed, the technological gap is likely to modify the transfer mechanisms and delay the saturation process. This situation is considered in Figures 8.37(a) and 8.37(b). One observes that, as long as a technological gap exists, the evolution of the global degree of saturation follows the one predicted for a constant transmissivity of 10^{-16} m/Pa·s. Once that contact is reached between the two materials, water flow is enhanced and the degree of saturation increases rapidly. Full saturation of the bentonite buffer is reached after 94 days, corresponding to an increase of 38% compared to the reference situation.

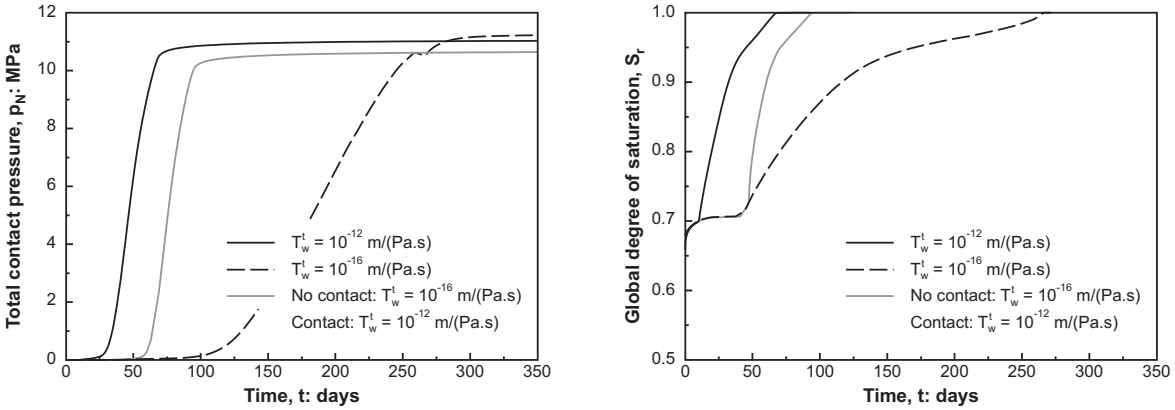

(a) Total contact pressure.

(b) Global degree of saturation.

Figure 8.37: Evolution through time of the total contact pressure between the buffer and the host rock and global degree of saturation of the buffer. Influence of the transversal transmissivity of the gap.

4.4 Two-dimensional model of the central section

4.4.1 Features of the analysis

The problem is now studied in two dimensions and the central section of the bentonite buffer is modelled assuming plane strain conditions. Due to gravity, contact initially occurs at the bottom of the drift, so that the technological gap between bentonite and the host rock is non-uniformly distributed around the buffer (it is maximum in the upper part of the excavation). The first objective of the two-dimensional analysis is to investigate the impact of gravity on the saturation process and swelling pressure development. In a second step, the effects of the host rock anisotropy (initial stress state and permeability) are studied.

The geometry and mesh of the two-dimensional model are shown in Figure 8.38. In a first reference case, the initial and boundary conditions, as well as modelling stages and material parameters, are similar to those described in Section 4.3.1 for the one-dimensional problem.

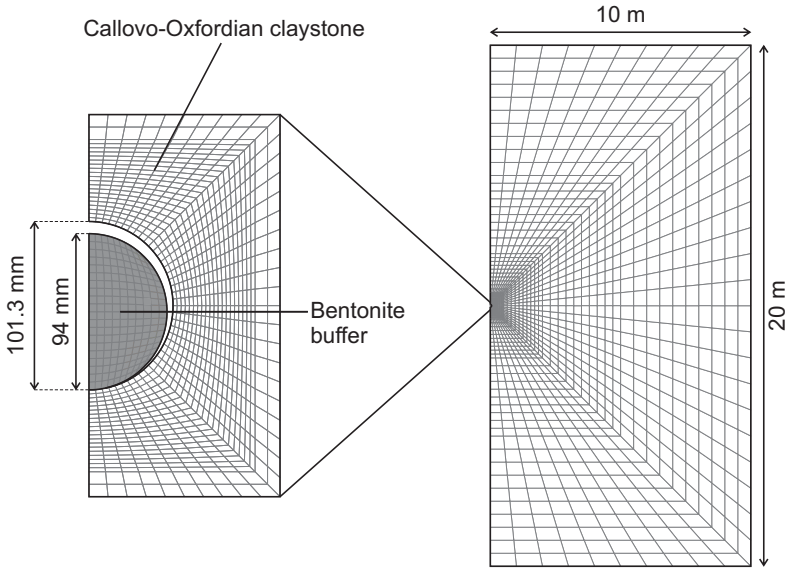

Figure 8.38: Geometry of the two-dimensional problem.

4.4.2 Numerical results

Water transfer between the host rock and the bentonite buffer is controlled by the water pressure drop between both sides of the interface and is proportional to the transversal transmissivity of the gap. As a first step, this transmissivity is assumed constant, regardless the presence or absence of contact, and the volume of the gap. Figure 8.39 presents the evolution with time of the global degree of saturation of the buffer. As can be observed in the figure, the two-dimensional model predicts a hydration kinetics that is similar to the one-dimensional analysis. This result was to be expected since the only direct effect of gravity on the hydraulic problem is the definition of hydrostatic water pressure field, which has negligible effects.

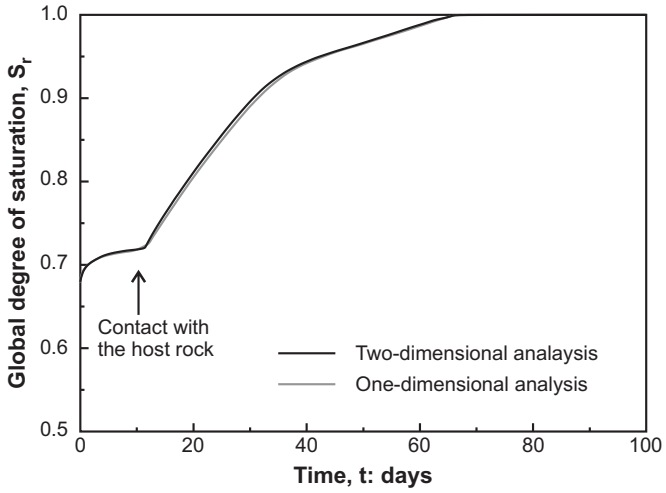

Figure 8.39: Evolution through time of the global degree of saturation of the buffer. Comparison between two-dimensional and one-dimensional analysis.

4.4.3 Influence of the gap and interface properties

As for the one-dimensional problem, different transversal transmissivities are now considered depending whether contact occurs or not. More specifically, the transfer coefficient is chosen equal to 10^{-16} m/Pa·s when contact between the bentonite buffer and the host rock is not achieved, while it is taken equal to 10^{-12} m/Pa·s when contact occurs.

The contact between the materials is reached after 34,5 days of hydration, which is somewhat lower than the 46 days determined by the one-dimensional model with the same assumptions. This difference is justified by the existence of contact (enhancing water flow) since the beginning of the buffer installation (in the one-dimensional model, the buffer and the host rock were not in contact initially). Figure 8.40 illustrates how the contact is reached during the 34th day of hydration. Initially, a contact pressure exists at the bottom of the buffer. This contact pressure corresponds to the reaction of the host rock to the weight of the buffer. Indeed, as long as contact is not reached at the top of the borehole, the vertical component of the contact pressure should counterbalance the weight of the buffer, and only this force. During hydration, the buffer swells towards the top of the borehole. Once the contact reached at the top of the borehole, the contact pressure increases rapidly towards the horizontal direction, as depicted in Figure 8.40. Once that the contact is reached all around the buffer, the pressure increases uniformly around the borehole.

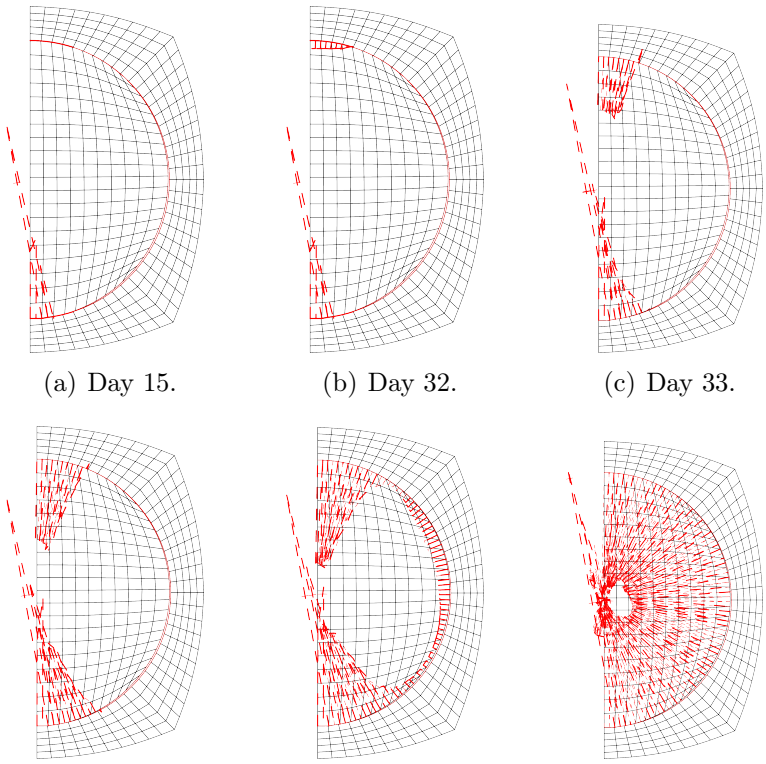

(a) Day 15. (b) Day 32. (c) Day 33.

(d) Day 34. (e) Day 34,5. (f) Day 35.

Figure 8.40: Progressive development of contact pressure between the buffer and the Callovo-Oxfordian claystone. The length of the red lines is a measure of the contact pressure.

Figure 8.41 shows the evolution of the porosity and degree of saturation distributions in the buffer during the first month after its placement. The figure shows that the preferential hydration from the bottom leads to a more significant increase in water saturation at the bottom of the buffer. An increase in porosity is also associated to hydration of the buffer as highlighted on the left part of the figures. The complete saturation of the bentonite buffer is achieved after 82 days, against 94 days for the one-dimensional model. The influence of the initial contact between the materials on the hydration and swelling kinetics is thus significant. Yet, once that contact is completely reached, the heterogeneities in dry density and degree of saturation along the buffer circumference quickly disappear.

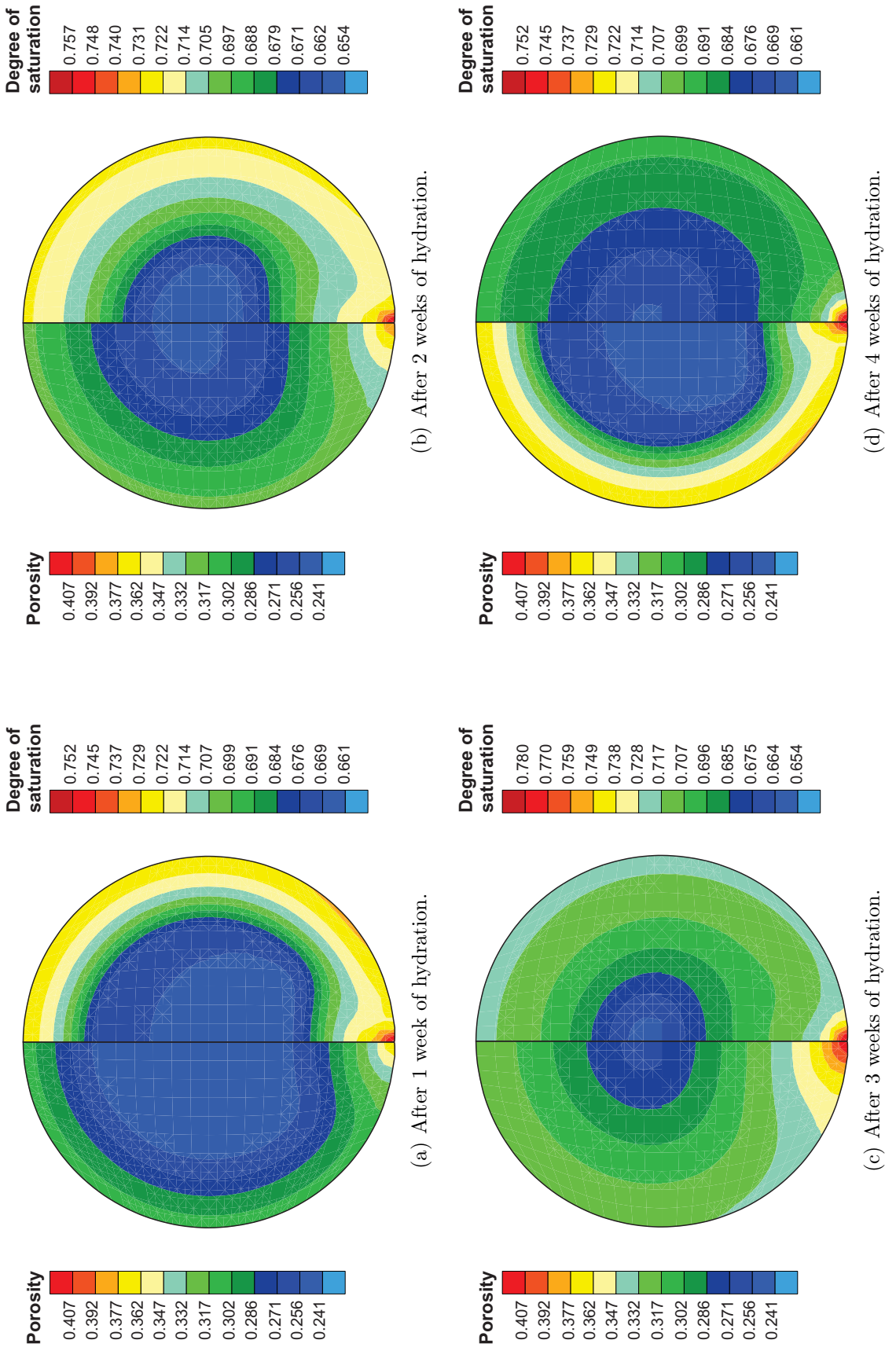

(a) After 1 week of hydration.

(b) After 2 weeks of hydration.

(c) After 3 weeks of hydration.

(d) After 4 weeks of hydration.

Figure 8.41: Evolution through time of porosity and degree of saturation in the buffer.

5 Conclusions

The experimental characterization of the behaviour of bentonite-based materials, whether at the laboratory or under *in situ* conditions, is essential to assess the performance of engineered barriers. These experiments provide fundamental information notably on the hydration and swelling kinetics. However, as modern as it may be, the monitoring generally provides punctual (in time, but mostly in space) data only. In addition, some uncertainties generally come along with the data: what do we exactly measure? For these reasons, a complete and valuable interpretation of the experimental data generally requires performing numerical simulations.

In this chapter, the complete hydromechanical model developed in this PhD work was used to reproduce the behaviour of bentonite upon hydration. Two tests were modelled, namely the Bentogaz 2 experiment and the PGZ2 *in situ* test. Interestingly, these experiments were carried out on the same material, a mixture of MX-80 bentonite and sand, but compacted to two different dry densities of 1.78 Mg/m^3 and 2.06 Mg/m^3 respectively.

The former test was realized at the laboratory scale by the French Atomic Energy Commission. It consisted in the hydration of a bentonite sample under constant volume conditions. The main originality of the test is its extensive instrumentation, making possible the complete monitoring of the hydromechanical state of the sample. However, the complex responses of the sensors made difficult a good and comprehensive understanding of the material. The modelling of the experiment using an advanced constitutive framework supplied new explanations allowing a better understanding of the material behaviour and of the experimental data. In particular, the complex evolution of the total axial and radial pressure sensors with time could be explained by an advancing hydration and swelling front in the bentonite sample. The good agreement between the numerical results and the experimental data, both qualitatively and quantitatively, allowed validating the developed framework.

On the other hand, the PGZ2 test was carried out by the French national radioactive waste management agency (Andra) in the Meuse/Haute-Marne Underground Research Laboratory. It aimed at investigating the hydration kinetics of the buffer under *in situ* conditions. As for any *in situ* test, technological gaps cannot be avoided during installation of the experiment. As a matter of fact, these gaps reached at least 14% of the total volume of the borehole section. In this work, the technological gaps are explicitly considered and modelled using zero-thickness interface elements. These special finite elements allow reproducing the initial absence of contact between the materials and the progressive development of contact pressure. The one-dimensional and two-dimensional modelling of the *in situ* test highlights the influence of these gaps on the hydromechanical behaviour of the barrier, and the importance of using advanced constitutive models to accurately reproduce this behaviour. In particular, the influence of the technological gap is particularly important for the hydration kinetics which is an important stake when designing engineered barriers.

Finally, numerical models are created as idealisations of complex situations, assuming for

instance axisymmetric conditions. That was the case for the one-dimension and partly the two-dimension models analysed in this PhD work. Yet, in practice, the excavation of drifts does not yield perfectly circular sections, but breakouts and debris are observed. In addition, important heterogeneities of the excavation damaged zone are observed (Pardoen, 2015; Salehnia, 2015), not to mention anisotropy of the hydromechanical behaviour. The two-dimension model created in this work offers the possibility of investigating these situations, these deflections from ideal, which are rarely measured nor estimated.

Chapter 9

Conclusions

1 Summary

Deep geological disposal constitutes one of the most promising solutions for the safe isolation of high-level and intermediate-level radioactive wastes. The isolation of the radioactive wastes from the biosphere relies on a multi-barrier concept in which bentonite-based materials play a central role. Under repository conditions, the engineered barrier experiences hydration from the saturated host rock (Figure 9.1). This hydration process yields an important swelling of the material allowing sealing of the existing technological gaps. When contact between the geological formation and the engineered barrier is reached, the global volume constraints imposed to the bentonite buffer are close to constant volume conditions and a swelling pressure develops on the gallery wall, closing at the same time any fracture from the excavation damaged zone. The objective of the bentonite barrier is to form a tight contact with the surrounding geological formation and to create a zone of low permeability able to limit water flow around the excavated galleries, thereby delaying the release of radionuclides to the biosphere.

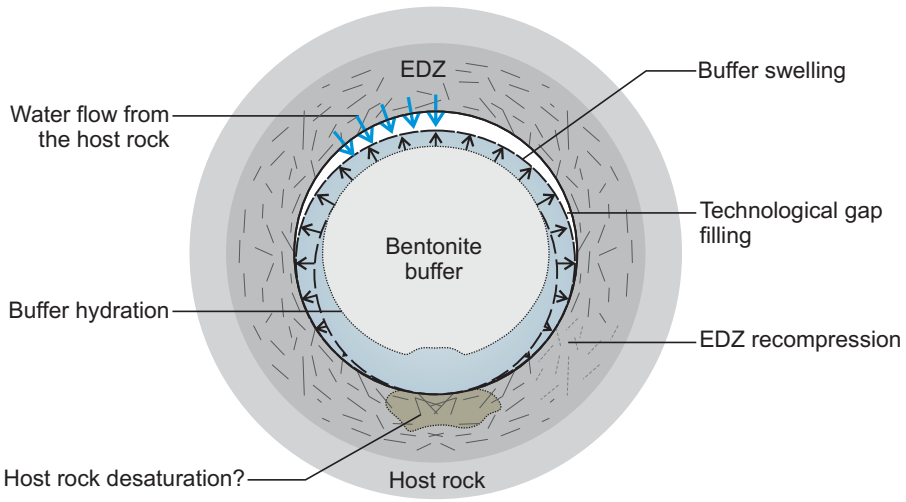

Figure 9.1: Hydromechanical processes affecting bentonite and the near-field of a repository for radioactive waste.

Yet, this macroscopic behaviour of the engineered barrier comes along with important structural changes which significantly affect the hydromechanical properties of the material. Accordingly, classical hydromechanical models for porous media have generally failed in reproducing the coupled behaviour of bentonite-based materials. The present work was motivated by the challenging task of better understanding and modelling the hydromechanical behaviour of compacted bentonites that will be used as engineered barriers in geological disposals of radioactive waste.

To address the issue, the strategy adopted in this work was to start from a clear understanding of the material microstructure behaviour. As a first step, the hydration and swelling mechanisms were addressed at the scale of the compacted material microstructure. The effects of hydraulic and mechanical loading on the microstructure of bentonites were thoroughly analysed. The complex structure of compacted bentonites makes a full quantitative description of the structure almost impossible. Based on the interpretation of experimental data, a new model for the evolution of the micropores volume was proposed. Accordingly, the effects of the microstructure on the overall behaviour of engineered barriers will be quantified through the definition of a microstructural void ratio function.

Experimental data show that the water retention behaviour of compacted bentonites is strongly affected by the material hydration and swelling. Consequently, conventional models are unable to represent the water retention behaviour of bentonite-based materials under both confined and unconfined conditions. To overcome those limitations, a new phenomenological water retention model was developed. The model accounts for the double structure of compacted bentonite-based materials and its evolution along hydromechanical stress paths. It successfully captures the main features of the water retention behaviour of compacted bentonites, including the evolution of the water retention properties upon free swelling.

The constitutive and numerical modelling of bentonite behaviour was then addressed at a macroscopic scale. The Barcelona Basic Model developed by Alonso *et al.* (1990) was extended to better reproduce the mechanical behaviour of bentonites, and especially the development of the swelling pressure. From a hydraulic point of view, experimental data show that the permeability of bentonite-based materials is not only affected by the degree of saturation of the material, but also by the density and microstructure. A Kozeny-Carman type model was thus extended to account for the evolution of the permeability with the macropores volume. Both mechanical and hydraulic models were implemented in the finite element code `LAGAMINE` and validated on different bentonite-based materials in order to highlight their good performance.

Beyond the behaviour of bentonite, another important issue concerns the role and influence of technological gap and interfaces between materials of the disposal. In order to investigate the influence of interfaces on the normal fluid transfer properties and swelling behaviour of bentonites, an experimental study was carried out at the Technical University of Catalonia in Barcelona, Spain. The experimental data evidence a major influence of the interface on the saturation process, which cannot be reproduced with numerical models assuming perfect contact between materials. To get over this limitation, zero-

thickness interface elements were adopted to represent interfaces and technological gaps.

Experimental characterization and large-scale testing provide essential data for the comprehension of the hydromechanical processes involved under repository conditions. On the other hand, constitutive and numerical modelling allows improving our understanding of the system behaviour by accessing information that cannot be obtained experimentally (experimental characterization generally provides information that is discrete in space and time). In addition, it allows evaluating various scenarios and studying very large structures over long time periods. Finally, the developed hydromechanical model was used to analyse two experiments, namely the Bentogaz 2 test and the PGZ2 *in situ* test. Numerical results were not only in good agreement with the experimental data, both qualitatively and quantitatively, but the developed hydromechanical model provided a new understanding of the complex material behaviour. In particular, it highlighted the important effects of multi-physical and multi-scale processes on the state of the bentonite buffer.

2 Original contributions

Dealing with the hydromechanical modelling of compacted bentonites, this PhD work has drawn strength from earlier research from the geomechanics research group of the University of Liege and, in particular, previous PhD thesis of Li (1999), Collin (2003) and Gerard (2011). Accordingly, the aim of the PhD research consisted in the extension of an existing constitutive framework through the development and implementation of new constitutive models in order to better reproduce the hydromechanical behaviour of bentonite-based materials.

The main original contributions of this PhD work include:

- a literature review and in-depth analysis of the material microstructure, the hydration and swelling mechanisms. This analysis thrives on research in clay science to provide a better understanding of bentonite-based materials macroscopic behaviour.

- the extension of a multiphase flow model for partially saturated porous media to account for the material structure. In particular, a new water retention model was developed. This model considers separate water retention mechanisms in the micro- and macropores and is able to reproduce the water retention behaviour of bentonite-based materials compacted to different dry densities and wetted under various confining conditions. To our knowledge, the model is the first proposed model that is able to interpret and model within a unified framework the water retention behaviour of bentonites in such a range of conditions. In addition, the model was implemented in a finite element code and used to model the behaviour of bentonite under *in situ* conditions. Finally, the permeability model was extended to account for the dependency of permeability on the macrostructural void ratio.

- the implementation of the Barcelona Basic Model in `LAGAMINE` using an efficient return-mapping algorithm, and the extension of the model to better represent the swelling behaviour of bentonites under confined conditions. The proposed extension

is strengthened and enriched by the detailed analysis of the swelling mechanisms at the microscopic level.

- the numerical modelling and analysis of a fully instrumented mock-up test, namely the Bentogaz 2 experiment. Thanks an advanced modelling, a new and better understanding of the test and the complex material behaviour is provided.

- the numerical modelling and analysis of an *in situ* experiment, namely the PGZ2 test. In the model, the technological gap between the bentonite buffer and the host rock is explicitly represented using a zero-thickness interface element. The analysis using the developed hydromechanical model provides a new comprehension of the saturation process under *in situ* condition. In addition, the estimation of the saturation kinetics is considerably improved.

3 Outlooks

The research work carried out in this PhD has enabled a better comprehension of the hydromechanical processes taking place in engineered barriers. Yet, several aspects would merit additional investigations in order to further improve our understanding. These investigations should involve fundamental research, deeper experimental characterization, improved constitutive and numerical modelling and finally, continuation of large-scale experiments analysis. The different outlooks are detailed hereafter.

3.1 Fundamental aspects

Bentonites are clay materials in which the solid – water interactions are extremely strong, the smectite particles being highly hydrophilic. The extension of concepts that are commonly accepted in granular materials raises therefore several questions.

An important question concerns the concept of suction, its validity and definition in clay materials. Classically, soils have been assimilated to a bundle of capillary tubes and the internal water potential has been associated to capillary suction (defined as the difference between air and water pressures). Accordingly, upon wetting, water is supposed to be stored in thin pores first, and then in pores of increasing diameters. The water retention mechanisms in clays, and bentonites in particular, are however far more complex. Experimental data have shown that water stored by capillarity represents only a small fraction of the total amount of water and that water is essentially stored by adsorption at the clay surfaces. Yet, in most constitutive frameworks, the total suction is associated to a difference in fluid pressures, so that highly negative water pressures correspond to low relative humidities. One may then ask whether these negative water pressures are physical and realistic. Are the underlying hypothesis not too strong?

These rather fundamental considerations have strong implications on our modelling and the following questions are raised:

- in the water flow model, the movement of water is mainly associated with water pressure gradients. The fact that highly negative water pressures are initially con-

sidered in partially saturated bentonites involves the definition of initially important pressure gradients between the bentonite and the host rock. This gradient acts as an important driving force for water flow.

- in our model, all water is considered mobile. Is it really the case? Shouldn't we consider different mobilities for bulk and adsorbed water?
- what about the equation of state adopted for water? Experimental evidences have shown that the water density in saturated bentonites is higher than the one of bulk water. What about the density in unsaturated conditions? In our model, a constant (and positive) water compressibility is considered in the domain of positive water pressures, but also in the range of highly negative water pressures. This yields values of water density that are significantly lower than for bulk water. Shouldn't the equation of state for water evolve?
- do capillary and adsorbed waters equally affect the mechanical behaviour of compacted bentonites?

Furthermore, in the developed model, thermodynamic equilibrium is implicitly assumed between the two structural levels of bentonites. Accordingly, the microstructure is presumed to develop instantaneously in contact of water, and macropores to be instantly clogged. This strong hypothesis affects *a priori* mainly the short-term behaviour of the material. However, ageing effects accompanied with structural reorganisation have been observed over several weeks at least. The question of the importance of ageing and creeping effects in compacted bentonites should thus be raised, especially as engineered barriers should be designed to perform over very long time periods.

Another direct consequence of the assumed thermodynamic equilibrium is the inability of the constitutive framework to distinguish flow of liquid water from flow of saturated water vapour. There is a certain degree of uncertainty concerning the way water flows from the host rock to bentonite. Some experimental data tends to show that the hydration kinetics could be slower when the material is hydrated under vapour form, although a more homogeneous swelling is observed in this case.

3.2 Experimental characterization

While there is a huge amount of experimental data related to swelling pressure tests, there are limited results of mechanical tests performed along simple stress paths. The experimental characterization is indeed complex and time demanding. In addition, the complexity of bentonite behaviour generally justifies the realisation of oedometer tests, rather than triaxial tests. However, oedometer tests do not provide a full description of the material behaviour, as the lateral stress state is rarely measured. Therefore, the development of constitutive models and the calibration of the model parameters using experimental tests are made more complex. Rather than performing triaxial (which are complex to carry out and whose interpretation raises numerous questions), it would be interesting to use - or develop - oedometer cells allowing the measurement of lateral stress. It is likely that the experimental results would raise other questions, including the question of the stress uniformity or distribution along the sample height, but they would help

to model the material behaviour.

In addition, most of the laboratory tests carried out under controlled suction deal with high suction values. There is a stake in better characterizing the behaviour of bentonite-based materials in the low suction range, i.e. below the air-entry value. It is actually in this suction range that the engineered barrier will spend most of its life in the repository.

Finally, our study has shown the importance of the material microstructure on the overall behaviour. Consequently, a good microstructural characterization of bentonite is fundamental.

3.3 Constitutive modelling

The good capacities of the developed model to reproduce the hydromechanical behaviour of compacted bentonites along various stress paths have been highlighted. However, the model has shown some limitations in representing the behaviour of materials with different initial dry densities. Indeed, the initial dry density of the material is poorly taken into account. Yet, it significantly affects the hydromechanical behaviour of the material:

- from a hydraulic point of view, an increase in dry density yields a decrease of the permeability. This feature has been taken into account in this work by defining the permeability as a function of the macrostructural void ratio, the latest decreasing during wetting under confined conditions.
- from a mechanical point of view, the compaction pressure required for the preparation of a sample is all the more important than the target density is high. Accordingly, the *preconsolidation pressure* of the initial material is all the more high than the density is high. This influence of the dry density on the yield surface can only be taken into account explicitly in the developed model. However, the modelling of the compaction process allows, as a first approximation (there are few experimental data) to reproduce this effect.

The dry density is also likely to affect the mechanical compressibility of the material. Indeed, materials compacted at low dry densities exhibit a more open structure than high-density materials.

Yet the most significant effect in bentonites deals with the increasing swelling potential (and swelling pressure) with increasing dry density. This effect is not considered in the model and the definition of different model parameters is required for materials with different dry densities. This aspect is a major issue and should be further investigated. It is indeed all the more important than granular bentonites or pellet mixtures are considered as sealing and backfilling materials. In this case, there is on one hand a heterogeneity of dry density within the mixture and, on the other hand, a natural gradient of dry density created during the construction (due to material segregation).

Finally, the anisotropy behaviour, depending on the compaction mode, would merit increasing attention. Indeed, in the case of buffers compacted uniaxially, the swelling pressure developed axially and radially could be significantly different. Yet, at the laboratory,

the axial pressure is generally measured and identified to the swelling pressure during swelling pressure tests. When materials are compacted uniaxially, the axial pressure is likely to be higher than the radial swelling pressure, so that the actual swelling pressure could be overestimated. Under repository conditions, the radial pressure has more importance as it allows to limit preferential pathways between the buffer and the host rock.

3.4 Engineered barrier and long-term behaviour

Among other objectives, the design of the engineered barrier involves the selection of a target dry density of the buffer. This target density is generally determined considering requirements in terms of swelling pressure and it is obtained from experimental relationships between the dry density and the swelling pressure at saturation. However, these curves only provide a picture of the stress state of the material at the saturated state. Is this stress always the highest that the material has undergone? Or could it be that the material undergoes higher stress along its wetting path? In small-scale swelling pressure tests, important collapse is sometimes observed, so that the final swelling pressure is lower than the peak pressure. Detailed numerical analysis are therefore essential to better understand the behaviour of engineered barrier under *in situ* conditions.

The concerns and study of the influence of technological voids and interfaces in underground structures are relatively recent. So far, classic approaches have consisted in considering homogeneous either initial or final dry density. Yet, several experimental studies have highlighted the role on technological voids on the hydromechanical behaviour of bentonite-based materials. In addition, the laboratory tests carried out in the framework of this thesis tend to demonstrate the significant effect of interfaces on fluid transfer. This observation will have to be checked. While interfaces could thus significantly affect the behaviour of engineered barriers, their explicit modelling at very large scale is probably not realistic as cumbersome. Accordingly, simpler tools should maybe be developed. Note that this comment is much the same as the modelling issue related to the self-sealing phenomenon.

Regarding the numerical modelling of the PGZ2 test, two-dimensional axisymmetric and three-dimensions modelling would allow better understanding:

- the influence of the boundary conditions imposed to the bentonite buffer during the *in situ* experiments. For instance, in the PGZ2 experiment, bases are present at the ends of the bentonite plug in order to allow monitoring. However, they affect the development of swelling pressures.
- the influence of perpendicular galleries. These galleries significantly influence the distribution of water pressures in the host rock close to the PGZ2 experiment.
- the influence of parallel drifts.

Finally, some uncertainties remain concerning the very long-term behaviour of engineered barriers, including chemo-hydro-mechanical processes and creeping. A better comprehension should probably benefit from natural analogues.

References

Adamson, A. W. (1990). *Physical chemistry of surfaces*. John Wiley & Sons.

Agus, S. S. (2005). *An experimental study on hydro-mechanical characteristics of compacted bentonite-sand mixtures*. Ph.D. thesis, Bauhaus - University Weimar.

Agus, S. S., Arifin, Y. F., Tripathy, S. & Schanz, T. (2013). Swelling pressure – suction relationship of heavily compacted bentonite–sand mixtures. *Acta Geotechnica* **8**, No. 2, 155–165.

Ahn, H. S. & Jo, H. Y. (2009). Influence of exchangeable cations on hydraulic conductivity of compacted bentonite. *Applied Clay Science* **44**, No. 1–2, 144–150.

Aitchison, G. D. (1965). Soil properties, shear strength and consolidation. In *Proceedings of the Sixth International Conference on Soil Mechanics and Foundation Engineering*, Montreal, Canada, pp. 318–321.

Aitchison, G. D. & Martin, R. (1973). A membrane oedometer for complex stress-strain studies in expansive clays. In *Proceedings of the Third International Conference on Expansive Soils*, Haifa, Israel, pp. 83–88.

Akesson, M., Jacinto, A. C., Gatabin, C., Sánchez, M. & Ledesma, A. (2009). Bentonite THM behaviour at high temperatures: experimental and numerical analysis. *Géotechnique* **59**, No. 4, 307–318.

Alonso, E. E., Alcoverro, J., Coste, F., Malinsky, L., Merrien-Soukatchoff, V., Kadiri, I., Nowak, T., Shao, H., Nguyen, T. S., Selvadurai, A. P. S., Armand, G., Sobolik, S. R., Itamura, M., Stone, C. M., Webb, S. W., Rejeb, A., Tijani, M., Maouche, Z., Kobayashi, A., Kurikami, H., Ito, A., Sugita, Y., Chijimatsu, M., Börgesson, L., Hernelind, J., Rutqvist, J., Tsang, C. F. & Jussila, P. (2005a). The FEBEX benchmark test: case definition and comparison of modelling approaches. *International Journal of Rock Mechanics & Mining Sciences* **42**, No. 5–6, 611–638.

Alonso, E. E., Gens, A. & Josa, A. (1990). A constitutive model for partially saturated soils. *Géotechnique* **40**, No. 3, 405–430.

Alonso, E. E., Romero, E. & Hoffmann, C. (2011). Hydromechanical behaviour of compacted granular expansive mixtures: experimental and constitutive study. *Géotechnique* **61**, No. 4, 329–344.

Alonso, E. E., Romero, E., Hoffmann, C. & García-Escudero, E. (2005b). Expansive bentonite–sand mixtures in cyclic controlled-suction drying and wetting. *Engineering Geology* **81**, No. 3, 213–226.

Alonso, E. E., Vaunat, J. & Gens, A. (1999). Modelling the mechanical behaviour of expansive clays. *Engineering Geology* **54**, No. 1–2, 173–183.

Alonso, E. E., Zandarin, M. T. & Olivella, S. (2013). Joints in unsaturated rocks: Thermo-hydro-mechanical formulation and constitutive behaviour. *Journal of Rock Mechanics and Geotechnical Engineering* **5**, No. 3, 200–213.

Anderson, D. M. & Low, P. F. (1958). The density of water adsorbed by Li-, Na-, and K-bentonite. *Soil Science Society of America Proceedings* **22**, 99–103.

Andra (2005). Dossier Argile 2005. Synthèse Argile: Evaluation de la faisabilité du stockage géologique en formation argileuse. *Technical report*, Andra.

Andra (2016). Le laboratoire souterrain. *Technical report*, Andra.

Apted, M. (1995). The scientific and regulatory basis for the geological disposal of radioactive waste. In *Repository and barrier concepts* (Savage, D., Ed.), Wiley.

Armand, G. (2000). *Contribution à la caractérisation en laboratoire et à la modélisation constitutive du comportement mécanique des joints rocheux*. Ph.D. thesis, Université de Grenoble 1.

Armand, G., Noiret, A., Zghondi, J., de La Vaissière, R., Conil, N., Morel, J. & Bumbieler, F. (2014). Rock mechanics of the Callovo-Oxfordian claystone at the Meuse/Haute-Marne Underground Research Laboratory and consequences for CIGEO repository design. In *Symposium on rock mechanics and rock engineering of geological repositories in Opalinus clay and similar claystone*, ETH Zurich, Switzerland.

Bachmat, Y. & Bear, J. (1986). Macroscopic modelling of transport phenomena in porous media. 1: The continuum approach. *Transport in Porous Media* **1**, No. 3, 213–240.

Baker, R. & Frydman, S. (2009). Unsaturated soil mechanics: critical review of physical foundations. *Engineering Geology* **106**, No. 1–2, 26–39.

Bandis, S. C., Lumsden, A. & Barton, N. R. (1983). Fundamentals of rock joint deformation. *International Journal of Rock Mechanics & Mining Sciences & Geomechanics Abstracts* **20**, No. 6, 249–268.

Barnichon, J. D. (1998). *Finite element modelling in structural and petroleum geology*. Ph.D. thesis, Université de Liège.

Barnichon, J. D. & Deleruyelle, F. (2009). Sealing experiments at the Tournemire URL. *Technical report*, IRSN.

Bart, M. (2000). *Contribution à la modélisation du comportement hydromécanique des massifs rocheux avec fracture*. Ph.D. thesis, Université des Sciences et Technologies de Lille.

Bart, M., Shao, J. F., Lydzba, D. & Haji-Sotoudeh, M. (2004). Coupled hydromechanical modeling of rock fractures under normal stress. *Canadian Geotechnical Journal* **41**, No. 4, 686–697.

Barton, N. (1976). The shear strength of rock and rock joints. *International Journal of Rock Mechanics & Mining Sciences & Geomechanics Abstracts* **13**, No. 9, 255–279.

Barton, N. & Choubey, V. (1977). The shear strength of rock joints in theory and practice. *Rock Mechanics* **10**, No. 1, 1–54.

Barton, N. R., Bandis, S. C. & Bakhtar, K. (1985). Strength, deformation and conductivity coupling of rock joints. *International Journal of Rock Mechanics & Mining Sciences & Geomechanics Abstracts* **22**, No. 3, 121–140.

Bastiaens, W., Bernier, F. & Li, X. L. (2007). SELFRAC: experiments and conclusions on fracturing, self-healing and self-sealing processes in clays. *Physics and Chemistry of the Earth* **32**, No. 8–14, 600–615.

Baver, L. D. & Winterkorn, H. W. (1935). Sorption of liquids by soil colloids: II. Surface behaviour in the hydration of clays. *Soil Science* **40**, No. 5, 403–418.

Bear, J. (1972). *Dynamics of fluids in porous media.* Elsevier.

Belgacem, F., Hild, P. & Laborde, P. (1998). The mortar finite element method for contact problems. *Mathematical and Computer Modelling* **193**, No. 6, 601–629.

Biot, M. A. (1941). General theory of three-dimensional consolidation. *Journal of Applied Physics* **12**, No. 2, 155–164.

Biot, M. A. (1956). The theory of propagation of elastic waves in a fluid-saturated porous solid. I. Low-frequency range. *Journal of the Acoustical Society of America* **28**, No. 2, 168–178.

Biot, M. A. (1962). Mechanics of deformation and acoustic propagation in porous media. *Journal of Applied Physics* **33**, No. 4, 1482–1498.

Biot, M. A. (1972). Theory of finite deformations of porous solids. *Indiana University Mathematics Journal* **21**, No. 7, 597–620.

Bishop, A. W. (1959). The principle of effective stress. *Tecnisk Ukeblad* **39**, 859–863.

Bishop, A. W. & Blight, G. E. (1963). Some aspects of effective stress in saturated and partially saturated soils. *Géotechnique* **13**, No. 3, 177–197.

Blatz, J. A., Cui, Y. J. & Oldecop, L. (2009). Vapour equilibrium and osmotic technique for suction control. *Geotechnical and Geological Engineering* **26**, No. 6, 661–673.

Blight, G. E. (1966). Strength characteristics of desiccated clays. *Journal of the Soil Mechanics and Foundations Division* **92**, No. 6, 18–388.

Bolt, G. H. (1956). Physico-chemical analysis of the compressibility of pure clays. *Géotechnique* **6**, No. 2, 86–93.

Bolzon, G., Schrefler, B. A. & Zienkiewicz, O. C. (1996). Elastoplastic soil constitutive laws generalized to partially saturated states. *Géotechnique* **46**, No. 2, 279–289.

Borgesson, L., Johannesson, L. E. & Gunnarssin, D. (2003). Influence of soil structure heterogeneities on the behaviour of backfill materials based on mixtures of bentonite and crushed rock. *Applied Clay Science* **23**, 121–131.

Borja, R. I. (2004). Cam–clay plasticity. Part V: a mathematical framework for three-phase deformation and strain localization analyses of partially saturated porous media. *Computer Methods in Applied Mechanics and Engineering* **193**, 5301–5338.

Borja, R. I. & Alarcón, E. (1995). A mathematical framework for finite strain elasto-plastic consolidation. Part 1: Balance laws, variational formulation, and linearization. *Computer Methods in Applied Mechanics and Engineering* **122**, No. 1-2, 145–171.

Boulin, P. F. (2008). *Expérimentation et modélisation du transfert d'hydrogène à travers des argiles de centre de stockage de déchets radioactifs*. Ph.D. thesis, Institut Polytechnique de Grenoble.

Boulon, M. J., Selvadurai, A. P. S., Benjelloun, H. & Feuga, B. (1993). Influence of rock joint degradation on hydraulic conductivity. *International Journal of Rock Mechanics & Mining Sciences & Geomechanics Abstracts* **30**, No. 7, 1311–1317.

Bourg, I. C., Bourg, A. C. M. & Sposito, G. (2003). Modeling diffusion and adsorption in compacted bentonite: a critical review. *Journal of Contaminant Hydrology* **61**, No. 1–4, 293–302.

Boussinesq, J. (1868). Mémoire sur l'influence des frottements dans les mouvements réguliers des fluides. *Journal de Mathématiques Pures et Appliquées* **13**, 377–424.

Bowen, R. M. (1980). Incompressible porous media models by use of the theory of mixtures. *International Journal of Engineering Science* **18**, No. 9, 1129–1148.

Bowen, R. M. (1982). Compressible porous media models by use of the theory of mixtures. *International Journal of Engineering Science* **20**, No. 6, 697–735.

Bradbury, M. H. & Baeyens, B. (2003). Porewater chemistry in compacted re-saturated MX-80 bentonite. *Journal of Contaminant Hydrology* **61**, No. 1–4, 329–338.

Börgesson, L., Karnland, O. & Johannesson, L. E. (1996). Modelling of the physical behaviour of clay barriers close to water saturation. *Engineering Geology* **41**, No. 1–4, 127–144.

Brooks, R. N. & Corey, A. T. (1964). Hydraulic properties of porous media. *Technical report*, Colorado State University Hydrology Paper No. 3.

Bruno, G. (1993). *Etude expérimentale des mécanismes de reduction et d'oxydation du Fer d'une argile naturelle – Evolution de ses propriétés physiques et chimiques*. Ph.D. thesis, Université de Poitiers.

Buzzi, O., Boulon, M., Deleruyelle, F. & Besnus, F. (2008). Hydromechanical behaviour of rock-bentonite interfaces under compression. *Rock Mechanics and Rock Engineering* **41**, No. 2, 343–371.

Cases, J. M., Berend, I., Besson, G., Francois, M., Uriot, J. P., Thomas, F. & Poirier, J. E. (1995). Mechanism of adsorption and desorption of water vapor by homoionic montmorillonites: 2. The Li^+, Na^+, K^+, Rb^+ and Cs^+- exchanged forms. *Clays and Clay Minerals* **43**, No. 3, 324–336.

Cases, J. M., Berend, I., Delon, J. F., François, M., Grillet, Y., Michot, I., Poirier, J. E. & Yvon, J. (1990). Quelques aspects de l'étude des propriétés texturales des argiles. In *Matériaux argileux: structure, propriétés et applications, Société Française de Minéralogie, Groupe français des argiles* (Decarreau, A., Ed.), pp. 309–342.

Cases, J. M., Berend, I., Francois, M., Uriot, J. P., Michot, L. J. & Thomas, F. (1997). Mechanism of adsorption and desorption of water vapor by homoionic montmorillonite. 3. The Mg^{2+}, Ca^{2+}, and Ba^{2+} exchanged forms. *Clays and Clay Minerals* **45**, No. 1, 8–22.

Cattaneo, F., Della Vecchia, G. & Jommi, C. (2014). Evaluation of numerical stress-point algorithms on elastic – plastic models for unsaturated soils with hardening dependent on the degree of saturation. *Computers and Geotechnics* **55**, 404–415.

Cerfontaine, B., Dieudonné, A. C., Radu, J. P., Collin, F. & Charlier, R. (2015). 3D zero-thickness coupled interface element: Formulation and application. *Computers and Geotechnics* **69**, 124–140.

Chambon, R., Crochepeyre, S. & Charlier, R. (1997). Numerical study of bifurcation of a biaxial test. In *Proceedings of the Fifth International Conference on Computational Plasticity* (Owen, D. R. J., Onate, E. & Hinton, E., Eds.), Barcelona, Spain, pp. 674–681.

Chambon, R., Crochepeyre, S. & Charlier, R. (2001). An algorithm and a method to search bifurcation points in non-linear problems. *International Journal for Numerical Methods in Engineering* **51**, No. 3, 315–332.

Chandler, N., Dixon, D. A., Gray, M. N., Hara, K., Cournut, A. & Tillerson, J. (1998). The tunnel sealing experiment : an in situ demonstration of technologies for vault sealing. In *Proceedings of the 19th Annual Conference of the Canadian Nuclear Society*, Toronto, Canada.

Chapman, D. L. (1913). A contribution to the theory of electro-capillarity. *Physiological Magazine* **25**, No. 6, 475–481.

Chapman, N. A. & McKinley, I. G. (1987). *The geological disposal of nuclear waste*. John Wiley & Sons.

Chapuis, R. P. & Aubertin, M. (2003). On the use of the Kozeny-Carman equation to predict the hydraulic conductivity of soils. *Canadian Geotechnical Journal* **40**, No. 3, 616–628.

Charlier, R. (1987). *Approche unifiée de quelques problèmes non linéaires de mécanique des milieux continus par la méthode des éléments finis (grandes déformations des métaux et des sols, contact unilatéral de solides, conduction thermique et écoulements en milieu poreux)*. Ph.D. thesis, Université de Liège.

Charlier, R. & Cescotto, S. (1988). Modélisation du phénomène de contact unilatéral avec frottement dans un contexte de grandes déformations. *Journal de Mécanique Théorique et Appliquée* **7**, No. 1, 177–192.

Charlier, R., Collin, F., Pardoen, B., Talandier, J., Radu, J. P. & Gerard, P. (2013). An unsaturated hydro-mechanical modelling of two in-situ experiments in Callovo-Oxfordian argillite. *Engineering Geology* **165**, 46–63.

Charlier, R., Li, X. L., Bolle, A., Geiser, F., Laloui, L. & Vulliet, L. (1997). Mechanical behaviour modelling of an unsaturated sandy silt. In *Proceedings of the 14th International Conference on Soil Mechanics and Foundation engineering*, Hamburg, Germany, pp. 41–644.

Chen, G., Verstricht, J. & Li, X. L. (2012). Numerical modeling of the in situ "Praclay Seal Test". Comparison between model and measurement. In *Unsaturated Soils: Research and Applications* (Mancuso, C., Jommi, C. & D'Onza, F., Eds.), Naples, Italy, pp. 333–341.

Chen, Y., Zhou, C. & Jing, L. (2009). Modeling coupled THM processes of geological porous media with multiphase flow: Theory and validation against laboratory and field scale experiments. *Computers and Geotechnics* **36**, No. 8, 1308–1329.

Chen, Y. G., Cui, Y. J., Tang, A. M., Wang, Q. & Ye, W. M. (2014). A preliminary study on hydraulic resistance of bentonite/host-rock seal interface. *Géotechnique* **64**, No. 12, 997–1002.

Coleman, J. D. (1962). Stress strain relations for partially saturated soil. *Géotechnique* **12**, No. 4, 348–350.

Collin, F. (2003). *Couplages thermo-hydro-mécaniques dans les sols et les roches tendres partiellement saturés*. Ph.D. thesis, Université de Liège.

Collin, F., Chambon, R. & Charlier, R. (2006). A finite element method for poro mechanical modelling of geotechnical problems using local second gradient models. *International Journal for Numerical Methods in Engineering* **65**, No. 11, 1749–1772.

Collin, F., Cui, Y. J., Schroeder, C. & Charlier, R. (2002). Mechanical behaviour of Lixhe chalk partly saturated by oil and water: experiment and modelling. *International Journal for Numerical and Analytical Methods in Geomechanics* **26**, No. 9, 897–924.

Conti, R., Tamagnini, C. & DeSimone, A. (2013). Critical softening in Cam-Clay plasticity: adaptive viscous regularisation, dilated time and numerical integration across stress-strain jump discontinuities. *Computer Methods in Applied Mechanics and Engineering* **258**, 118–133.

Coussy, O. (1995). *Mechanics of porous continua*. Wiley-Blackwell.

Cui, Y. J. (1993). *Etude du comportement d'un limon compacté non saturé et da sa modelisation dans un cadre elasto-plastique*. Ph.D. thesis, Ecole Nationale des Ponts et Chaussée.

Cui, Y. J. & Delage, P. (1996). Yielding and plastic behaviour of an unsaturated compacted silt. *Géotechnique* **46**, No. 2, 291–311.

Cui, Y. J., Delage, P. & Sultan, N. (1995). An elasto-plastic model for compacted soils. In *Proceedings of the First International Conference on Unsaturated Soils, UNSAT 1995* (Alonso, E. E. & Delage, P., Eds.), Paris, France, pp. 703–709.

Cui, Y. J., Tang, A. M., Loiseau, C. & Delage, P. (2008). Determining the unsaturated hydraulic conductivity of a compacted sand-bentonite under constant volume and free-swell conditions. *Physics and Chemistry of the Earth* **33**, 462–471.

Cuss, R. J., Milodowski, A. & Harrington, J. F. (2011). Fracture transmissivity as a function of normal and shear stress: First results in Opalinus Clay. *Physics and Chemistry of the Earth* **36**, No. 17–18, 1960–1971.

Dananaj, I., Frankovska, J. & Janotka, I. (2005). The influence of smectite content on microstructure and geotechnical properties of calcium and sodium bentonites. *Applied Clay Science* **28**, 223–232.

Dang, K. D. & Robinet, J. C. (2005). Matériaux à base d'argile gonflante: comportement thermo-hydro-mécanique en conditions non saturée et saturée pour des températures inférieures à 150°. Modèle THM simplifié du comportement da l'argile MX80. *Technical report*, ANDRA, Rapport C.RP.OEUG.05.002.

Daniel, D. E. (1982). Measurement of hydraulic conductivity of unsaturated soils with thermocouple psychrometers. *Soil Science Society of America Journal* **46**, No. 6, 1125–1129.

Day, R. & Potts, D. (1994). Zero-thickness interface elements - numerical stability and application. *International Journal for Numerical and Analytical Methods in Geomechanics* **18**, No. 10, 689–708.

de La Vaissière, R. (2013). Hydration versus gas percolation in bentonite. In-situ experiment PGZ2. Experimental borehole results. *Technical report*, FORGE.

de La Vaissière, R., Armand, G. & Talandier, J. (2014). Excavation damaged zone under imbibition: Evidence of self-sealing in claystone. In *Proceedings of the Sixth International Conference on Unsaturated Soils, UNSAT 2014* (Khalili, N., Russell, A. & Khoshghalb, A., Eds.), Sydney, Australia, pp. 1481–1488.

De Marsily, G. (1986). *Quantitative hydrogeology: Groundwater hydrology for engineers*. Academic Press.

De Wit, C. T. & Arens, P. L. (1950). Moisture content and density of some clay minerals and some remarks on the hydration pattern of clay. In *Proceeding of the Fourth International Congress of Soil Sciences*, pp. 59–62.

Delage, P. (2002). Experimental unsaturated soil mechanics. In *Proceedings of the Third International Conference on Unsaturated Soils, UNSAT 2002* (Juca, J. F. T., de Campos, T. M. P. & Marinho, F. A. M., Eds.), Recife, Brazil, pp. 973–996.

Delage, P., Audiguier, M., Cui, Y. & Howat, M. (1996). Microstructure of a compacted silt. *Canadian Geotechnical Journal* **33**, No. 1, 150–158.

Delage, P. & Cui, Y. J. (2001). L'eau dans les sols non saturés. *Techniques de l'Ingénieur* **C301**.

Delage, P., Howat, M. D. & Cui, Y. J. (1998). The relationship between suction and swelling properties in a heavily compacted unsaturated clay. *Engineering Geology* **50**, No. 1–2, 31–48.

Delage, P. & Lefebvre, G. (1984). Study of the structure of a sensitive Champlain clay and of its evolution during consolidation. *Canadian Geotechnical Journal* **21**, No. 1, 21–35.

Delage, P., Marcial, D., Cui, Y. J. & Ruiz, X. (2006). Ageing effects in a compacted bentonite: a microstructure approach. *Géotechnique* **56**, No. 5, 291–304.

Delage, P. & Pellerin, F. M. (1984). Influence de la lyophilisation sur la structure d'une argile sensible du Québec. *Clay Minerals* **19**, No. 2, 151–160.

Delage, P., Romero, E. & Tarantino, A. (2008). Recent developments in the techniques of controlling and measuring suction in unsaturated soils. In *Unsaturated Soils: Advances in Geo-Engineering. Proceedings of the First European Conference on Unsaturated Soils, E-UNSAT 2008* (Toll, D. G., Augarde, D., Gallipoli, D. & Wheeler, S. J., Eds.), Durham, UK, pp. 33–52.

Delage, P., Tessier, D. & Audiguier, M. M. (1982). Use of the cryoscan apparatus for observation of freez-fractured planes of a sensitive Quebec clay in scanning electron microscopy. *Canadian Geotechnical Journal* **19**, No. 1, 111–114.

Delahaye, C. H. & Alonso, E. E. (2002). Soil heterogeneity and preferential paths for gas migration. *Engineering Geology* **64**, No. 2–3, 251–271.

Delay, J., Vinsot, A., Krieguer, J. M., Rebours, H. & Armand, G. (2007). Making of the underground scientific experimental programme at the Meuse/Haute-Marne underground research laboratory, North Eastern France. *Physics and Chemistry of the Earth* **32**, No. 8–14, 2–18.

Della Vecchia, G. (2009). *Coupled hydro-mechanical behaviour of compacted clayey soils.* Ph.D. thesis, Politecnico di Milano.

Della Vecchia, G., Jommi, C. & Romero, E. (2013). A fully coupled elastic–plastic hydromechanical model for compacted soils accounting for clay activity. *International Journal for Numerical and Analytical Methods in Geomechanics* **37**, No. 5, 503–535.

Denis, J. D. (1991). Compaction and swelling of Ca-smectite in water and in CaCl2 solutions: water activity measurements and matric resistance to compaction. *Clays and Clay Minerals* **39**, No. 1, 35–42.

Derjaguin, B. V., Karasev, V. V. & Khromova, E. N. (1986). Thermal expansion of water in fine pores. *Journal of Colloid and Interface Science* **109**, No. 2, 586–587.

Devineau, K., Bihannic, I., Michot, L., Villiéras, F., Masrouri, F., Cuisinier, O., Fragneto, G. & Michau, N. (2006). In situ neutron diffraction analysis of the influence of geometric confinement on crystalline swelling of montmorillonite. *Applied Clay Science* **31**, No. 1–2, 76–84.

Diamond, S. (1970). Pore size distributions in clays. *Clays and Clay Minerals* **18**, No. 1, 7–23.

Dixon, D. A., Chandler, N., Graham, J. & Gray, M. N. (2002). Two large-scale sealing tests conducted at Atomic Energy of Canada's underground research laboratory: the buffer-container experiment and the isothermal test. *Canadian Geotechnical Journal* **39**, No. 3, 503–518.

Dixon, D. A., Cheung, S. C. G., Gray, M. N. & Davidson, B. C. (1987). The hydraulic conductivity of dense clay soils. In *Proceedings of the 40th Canadian Geotechnical Conference*, Regina, Canada, pp. 389–396.

Dixon, D. A., Gray, M. N. & Graham, J. (1996). Swelling and hydraulic properties of bentonites from Japan, Canada and the USA. *Environmental Geotechnics* **1**, 43–48.

Dixon, D. A., Gray, M. N. & Thomas, A. W. (1985). A study of the compaction properties of potential clay-sand buffer mixtures for use in nuclear fuel waste disposal. *Engineering Geology* **21**, No. 3–4, 247–255.

Dormieux, L., Barboux, P., Coussy, O. & Dangla, P. (1995). A macroscopic model of the swelling phenomenon of a saturated clay. *European Journal of Mechanics. A. Solids* **14**, No. 6, 981–1004.

Dridi, W., Gatabin, C. & Guillot, W. (2013). Etude des transferts de gaz dans la bentonite. FT BENTOGAZ. *Technical report*, Commissariat à l'Energie Atomique (CEA).

Drucker, D. C. & Prager, W. (1952). Soil mechanics and plastic analysis or limit design. *Quaterly of Applied Mathematics* **10**, No. 2, 157–164.

Dubinin, M. M. & Radushkevich, L. V. (1947). Equation of the characteristic curve of activated charcoal. *Proceedings of the Academy of Sciences, Physical Chemistry Section, USSR* **55**, 331–333.

Dupray, F., François, B. & Laloui, L. (2011). Analysis of the FEBEX multi-barrier system including thermoplasticity of unsaturated bentonite. *International Journal for Numerical and Analytical Methods in Geomechanics* **37**, No. 4, 399–422.

Dupray, F., Li, C. & Laloui, L. (2013). THM coupling sensitivity analysis in geological nuclear waste storage. *Engineering Geology* **163**, 113–121.

Escario, V. & Saez, J. (1986). The shear strength of partly saturated soils. *Géotechnique* **36**, No. 13, 453–456.

Escario, V. & Saez, J. (1987). Shear strength of soils under high suction values. written discussion. In *Proceedings of the 9th European Conference on Soil Mechanics and Foundation Engineering*, Dublin, Ireland, p. 1157.

Ewen, J. & Thomas, H. R. (1989). Heating unsaturated medium sand. *Géotechnique* **3**, No. 1, 455–470.

Fernandez, A. M. (2004). *Caracterización y modelización del agua intersticial en materiales arcillosos: estudio de la bentonita de Cortijo de Archidona*. Ph.D. thesis, CIEMAT.

Fernandez, A. M., Baeyens, B., M., B. & Rivas, P. (2004). Analysis of the pore water chemical composition of a spanish compacted bentonite used in an engineered barrier. *Physics and Chemistry of the Earth* **29**, No. 1, 105–118.

Fernández, A. M. & Rivas, P. (2005). Analysis and distribution of waters in the compacted FEBEX bentonite: pore water chemistry and adsorbed water properties. In *Proceedings of International Symposium on large scale field tests in granite: Advances in understanding engineered clay barriers* (Alonso, E. E. & Ledesma, A., Eds.), Sitges, Spain, pp. 257–276.

Fischer, K. & Wriggers, P. (2004). Mortar based frictional contact formulation for higher order interpolations using the moving friction cone. *Computer Methods in Applied Mechanics and Engineering* **195**, No. 37–40, 5020–5036.

Fredlund, D. G. & Morgenstern, N. R. (1976). Constitutive relations for volume change in unsaturated soils. *Canadian Geotechnical Journal* **13**, No. 3, 261–276.

Fredlund, D. G. & Morgenstern, N. R. (1977). Stress state variables for unsaturated soils. *Journal of the Geotechnical Engineering Division* **103**, No. GT5, 447–466.

Fredlund, D. G. & Rahardjo, H. (1993). *Soil mechanics for unsaturated soils*. Wiley.

Fredlund, D. G., Rahardjo, H. & Gan, J. K. M. (1987). Nonlinearity of strength enveloppe for unsaturated soils. In *Proceedings of the Sixth International Conference on Expansive Soils*, New Delhi, India, pp. 49–54.

Frydman, S. (2012). Shear strength and negative water potential in unsaturated, compacted clays. In *Unsaturated Soils: Research and Applications* (Mancuso, C., Jommi, C. & D'Onza, F., Eds.), Naples, Italy, pp. 31–37.

Gallipoli, D. (2012). A hysteretic soil-water retention model accounting for cyclic variations of suction and void ratio. *Géotechnique* **62**, No. 7, 605–616.

Gallipoli, D., Wheeler, S. J. & Karstunen, M. (2003). Modelling the variation of degree of saturation in a deformable unsaturated soil. *Géotechnique* **53**, No. 1, 105–112.

Garcia-Siñeriz, J. L., Villar, M. V., Rey, M. & Palacios, B. (2015). Engineered barrier of bentonite pellets and compacted blocks: state after reaching saturation. *Engineering Geology* **192**, 33–45.

Garrels, R. M. & Christ, C. L. (1965). *Solutions, minerals, and equilibra*. Harper & Row.

Gatabin, C. & Guillot, W. (2008). Etude des transferts de gaz dans la bentonite MX80 compactée (FT Bentogaz). Rapport d'avancement 2008. *Technical report*, Commissariat à l'Energie Atomique (CEA).

Gatabin, C., Guillot, W. & Dridi, W. (2011). Etude des transferts de gaz dans la bentonite MX80 compactée (FT Bentogaz). Rapport d'avancement 2011. *Technical report*, Commissariat à l'Energie Atomique (CEA).

Gatabin, C., Talandier, J., Collin, F., Charlier, R. & Dieudonné, A. C. (2016). Competing effects of volume change and water uptake on the water retention behaviour of a compacted mx-80 bentonite/sand mixture. *Applied Clay Science* **121–122**, 57–62.

Gatabin, C., Touze, G., Billaud, P., Imbert, C. & Guillot, W. (2006). ESDRED Project – Module 1. Selection and THM characterisation of the buffer material. *Technical report*, Commissariat à l'Energie Atomique (CEA).

Gatmiri, B. & Delage, P. (1995). A new void ratio state surface formulation for the nonlinear elastic constitutive modeling of unsaturated soil — Code UDAM. In *Proceedings of the First International Conference on Unsaturated Soils, UNSAT 1995* (Alonso, E. E. & Delage, P., Eds.), Paris, France, pp. 1049–1056.

Gaucher, E., Robelin, C., Matray, J. M., Négrel, G., Gros, Y., Heitz, J. F., Vinsot, A., Rebours, H., Cassagnabère, A. & Bouchet, A. (2004). Andra Underground Research Laboratory: interpretation of the mineralogical and geochemical data acquired in the Callovian– Oxfordian formation by investigative drilling. *Physics and Chemistry of the Earth* **29**, 55–77.

Geiser, F., Laloui, L. & Vulliet, L. (2006). Elasto-plasticity of unsaturated soils: laboratory test results on a remoulded silt. *Soils and Foundations* **46**, No. 5, 545–556.

Gens, A. (1996). Constitutive modelling: application to compacted soils. In *Proceedings of the First International Conference on Unsaturated Soils, UNSAT 1996* (Alonso, E. E. & Delage, P., Eds.), Paris, France, pp. 1179–1200.

Gens, A. (2010). Soil–environment interactions in geotechnical engineering. *Géotechnique* **60**, No. 1, 3–74.

Gens, A. & Alonso, E. E. (1992). A framework for the behaviour of unsaturated expansive clays. *Canadian Geotechnical Journal* **29**, No. 6, 1013–1032.

Gens, A., Carol, I. & Alonso, E. E. (1990). A constitutive model for rock joints. Formulation and numerical implementation. *Computers and Geotechnics* **9**, No. 1–2, 3–20.

Gens, A. & Sánchez, M. (2014). Formulation of a model suitable for long term predictions. *Technical report*, PEBS Deliverable D3.5-2.

Gens, A., Sánchez, M., Guimarães, L., Alonso, E. E., Lloret, A., Olivella, S., Villar, M. V. & Huertas, F. (2009). A full-scale in situ heating test for high-level nuclear waste disposal: observations, analysis and interpretation. *Géotechnique* **59**, No. 4, 377–399.

Gens, A., Sánchez, M. & Sheng, D. (2006). On constitutive modelling of unsaturated soils. *Acta Geotechnica* **1**, No. 3, 137–147.

Gens, A., Vallejan, B., Sánchez, M., Imbert, C., Villar, M. V. & Van Geet, M. (2011). Hydromechanical behaviour of a heterogeneous compacted soil: experimental observations and modelling. *Géotechnique* **61**, No. 5, 367–386.

Gentier, S. (1986). *Morphology and hydromechanical behavior of a natural fracture in granite under normal stress*. Ph.D. thesis, Université d'Orléans.

Gerard, P. (2011). *Impact des transferts de gaz sur le comportement poro-mécanique des matériaux argileux*. Ph.D. thesis, Université de Liège.

Gerard, P., Charlier, R., Chambon, R. & Collin, F. (2008). Influence of evaporation on the convergence of a ventilated cavity. *Water Resources Research* **44**, W00C02.

Ghayaza, M., Skoczylas, F., Robinet, J. C. & Talandier, J. (2013). Self-sealing capacity of macro-cracked argillite under confinement. In *Poromechanics V - Proceedings of the Fifth Biot Conference on Poromechanics* (Hellmich, C., Pichler, B. & Adam, D., Eds.), Vienna, Austria, pp. 1580–1589.

Goodman, R. E., Taylor, R. L. & Brekke, T. L. (1968). A model for the mechanics of jointed rock. *Journal of the Soil Mechanics and Foundations Division* **94**, No. 3, 637–659.

Gouy, M. (1910). Sur la constitution de la charge électrique à la surface d'un électrolyte. *Journal de Physique Théorique et Appliquée* **9**, No. 1, 457–468.

Graham, J., Oswell, J. M. & Gray, M. N. (1992). The effective stress concept in saturated sand–clay buffer. *Canadian Geotechnical Journal* **29**, No. 6, 1033–1043.

Grim, R. E. (1968). *Clay mineralogy*. New-York, USA: McGraw-Hill.

Grunberger, D. (1995). *Etude expérimentale de l'évolution des microstructures et des propriétés physiques et mécaniques des argiles au cours de la compaction*. Ph.D. thesis, Université de Montpellier II.

Habraken, A. M., Cescotto, S. & Banning, Q. (1998). Contact between deformable solids: the fully coupled approach. *Mathematical and Computer Modelling* **28**, No. 4, 153–169.

Hall, M. R., Mooney, S. J., Sturrock, C., Matelloni, P. & Rigby, S. (2013). An approach to characterisation of multi-scale pore geometry and correlation with moisture storage and transport coefficients in cement-stabilised soils. *Acta Geotechnica* **8**, No. 1, 67–79.

Hassanizadeh, M. & Gray, W. G. (1979a). General conservation equations for multi-phase systems: 1. Averaging procedure. *Advances in Water Resources* **2**, 131–144.

Hassanizadeh, M. & Gray, W. G. (1979b). General conservation equations for multi-phase systems: 2. Mass, momenta, energy, and entropy equations. *Advances in Water Resources* **2**, 191–203.

Hassanizadeh, M. & Gray, W. G. (1980). General conservation equations for multi-phase systems: 3. Constitutive theory for porous media flow. *Advances in Water Resources* **3**, No. 1, 25–40.

Hattab, M. & Fleureau, J. M. (2011). Experimental analysis of kaolinite particle orientation during triaxial path. *International Journal for Numerical and Analytical Methods in Geomechanics* **35**, No. 8, 947–968.

Haug, M. D. & Wong, L. C. (1992). Impact of molding water content on hydraulic conductivity of compacted sand-bentonite. *Canadian Geotechnical Journal* **29**, No. 2, 253–262.

Hawkins, R. K. & Egelstaff, P. A. (1980). Interfacial water structure in montmorillonite from neutron diffraction experiments. *Clays and Clay Minerals* **28**, No. 1, 19–28.

Hewitt, D. F. (1917). The origin of bentonites. *Washington Academy of Sciences Journal* **7**, 196–198.

Hicher, P. Y., Wahyudi, H. & Tessier, D. (2000). Microstructural analysis of inherent and induced anisotropy in clay. *Mechanics of Cohesive-Frictional Materials* **5**, No. 5, 341–371.

Hilf, J. W. (1956). An investigation of pore-water pressure in compacted cohesive soils. *Technical report*, Denver: US Bureau of Reclamation.

Hoffmann, C. (2005). *Caracterización hidromecánica de mezclas de pellets de bentonita. estudio experimental y constitutivo*. Ph.D. thesis, Universitat Politecnica de Catalunya.

Homand, F., Belem, T. & Souley, M. (2001). Friction and degradation of rock joint surfaces under shear loads. *International Journal for Numerical and Analytical Methods in Geomechanics* **25**, No. 10, 973–999.

Homand, F., Giraud, A., Escoffier, S. & Koriche, D., A. nd Hoxha (2004). Permeability determination of a deep argilite in saturated and partially saturated conditions. *International Journal of Heat and Mass Transfer* **47**, 3517–3531.

Horseman, S. T., Harrington, J. F. & Sellin, P. (1999). Gas migration in clay barriers. *Engineering Geology* **54**, No. 1–2, 139–149.

Hoxha, D. & Auvray, C. (2005). Résultats des essais sur échantillons pour le développement des modèles rhéologiques HM et THM des argiles. *Technical report*, Andra C.RP0.ENG.03.0380/D.

Hueckel, T. (1992a). On effective stress concepts and deformation in clays subjected to environmental loads: discussion. *Canadian Geotechnical Journal* **29**, No. 6, 1120–1125.

Hueckel, T. (1992b). Water-mineral interaction in hygromechanics of clays exposed to environmental loads: a mixture-theory approach. *Canadian Geotechnical Journal* **29**, No. 6, 1071–1086.

Hueckel, T. & Pellegrini, R. (1989). Modeling of thermal failure of saturated clays. In *International Symposium on Numerical Models in Geomechanics – NUMOG* (Pietruszczak, S. & Pande, G. N., Eds.), pp. 81–90.

IAEA (2009). Classification of radioactive waste. General safety guide. *IAEA Safety Standards* **GSG-1**, 68.

Imbert, C., Billaud, P., Touzé, G. & Dang, K. D. (2004). Acquisition des paramètres de comportement hydraulique et hydromécanique de base de l'argile MX80 à l'état saturé. *Technical report*, Commissariat à l'Energie Atomique (CEA).

Imbert, C., Olchitzky, E., Lassabatère, T., Dangla, P. & Courtois, A. (2005). Evaluation of a thermal criterion for an engineered barrier system. *Engineering Geology* **81**, No. 3, 269–283.

Iwai, K. (1976). *Fundamental of fluid flow through a single interface*. Ph.D. thesis, University of California.

Jacinto, A. C., Villar, M. V. & Ledesma, A. (2012). Influence of water density on the water-retention curve of expansive clays. *Géotechnique* **62**, No. 8, 657–667.

Jaime, M., Guiras, H. & Olivella, S. (2015). Analysis of slope movement initiation induced by rainfall using the elastoplastic barcelona basic model. *European Journal of Civil Engineering* **19**, No. 9, 1–26.

Jennings, J. E. B. & Burland, J. B. (1962). Limitations to the use of effectives stresses in partially saturated soils. *Géotechnique* **12**, No. 2, 125–144.

JNC (2000). H12 project to establish technical basis for HLW disposal in Japan. Supporting report 3: safety assessment of the geological disposal system. *Technical report*, Japan Nuclear Cycle Developement Institute.

Jommi, C. & di Prisco, C. (1994). Un semplice approccio teorico per la modellazione del comportamento meccanico dei terreni granulari parzialmente saturi. In *Atto Convegno sul Tema: il ruolo dei fluidi nei problemi di ingegneria geotecnica*, Mondovi, Italy, pp. 167–188.

Juang, C. H. & Holtz, R. D. (1986). A probabilistic permeability model and the pore size density function. *International Journal for Numerical and Analytical Methods in Geomechanics* **10**, No. 5, 543–553.

Karnland, O., Nilsson, U., Weber, H. & Wersin, P. (2008). Sealing ability of Wyoming bentonite pellets foreseen as buffer material – Laboratory results. *Physics and Chemistry of the Earth* **33**, 472–475.

Karnland, O., Olsson, S. & Nilsson, U. (2006). Mineralogy and sealing properties of various bentonites and smectite-rich clay materials. *Technical report*, Clay Technology AB.

Keller, L. M., Seiphoori, A., Gasser, P., Lucas, F., Holzer, L. & Ferrari, A. (2014). The pore structure of compacted and partly saturated MX-80 bentonite at different dry densities. *Clays and Clay Minerals* **62**, No. 3, 174–187.

Kezdi, A. (1974). *Handbook of soil mechanics. Soil physics*. Elsevier Scientific.

Khalili, N., Geiser, F. & Blight, G. E. (2004). Effective stress in unsaturated soils: review with new evidence. *International Journal of Geomechanics* **4**, No. 2, 115–126.

Kloubek, J. (1981). Hysteresis in porosimetry. *Powder Technology* **29**, No. 1, 63–73.

Knight, W. C. (1898). Bentonite. *Engineering and Mining Journal* **66**, 491.

Koliji, A. (2008). *Mechanical behaviour of unsaturated aggregated soils*. Ph.D. thesis, Ecole Polytechnique Fédérale de Lausanne.

Komine, H. (2004). Simplified evaluation on hydraulic conductivities of sand–bentonite mixture backfill. *Applied Clay Science* **26**, No. 1–4, 13–19.

Komine, H. (2010). Predicting hydraulic conductivity of sand-bentonite backfill before and after swelling deformation for underground disposal of radioactive waste. *Engineering Geology* **114**, No. 3–4, 123–134.

Komine, H. & Ogata, N. (1992). Experimental study on swelling characteristics of compacted bentonite. *Canadian Geotechnical Journal* **31**, No. 4, 478–490.

Komine, H. & Ogata, N. (1996). Prediction for swelling characteristics of compacted bentonite. *Canadian Geotechnical Journal* **33**, No. 1, 11–22.

Komine, H., Ogata, N., Takao, H., Nakashima, A., Osada, T. & Ueda, H. (2001). Self-sealing ability of buffer materials containing bentonite for HLW disposal. In *Clay Science for Engineering* (Adachi, K. & Fukue, M., Eds.), Shizuoka, Japan, pp. 571–576.

Kraehenbuehl, F., Stoeckli, H. F., Brunner, F., Kahr, G. & Mueller-Vonmoos, M. (1987). Study of the water - bentonite system by vapour adsorption, immersion calorimetry and X-ray techniques: I. Micropore volumes and internal surface areas, following Dubinin's theory. *Clay Minerals* **22**, No. 1, 1–9.

Kulatilake, P. H. S., He, W., Um, J. & Wang, H. (1997). A physical model study of jointed rock mass strength under uniaxial compressive loading. *International Journal of Rock Mechanics & Mining Sciences* **34**, No. 3–4, 692–693.

Labalette, T., Harman, A., Dupuis, M. C. & Ouzounian, G. (2009). Cigeo, the $\frac{1}{2}$French geological repository project. In *Proceedings of the Waste Management Conference, WM2013*, Phoenix, USA, p. 9.

Lade, P. V. & Duncan, J. M. (1977). Elasto-plastic stress-strain theory for cohesionless soil. *International Journal of Solids and Structures* **13**, No. 11, 1037–1053.

Lajudie, A., Raynal, J., Petit, J. C. & Toulhoat, P. (1994). Clay-based materials for engineered barriers: a review. *Materials Research Society Symposium Proceedings* **353**, 221–229.

Laloui, L. & Nuth, M. (2005). An introduction to the constitutive modelling of unsaturated soils. *European Journal of Civil Engineering* **9**, No. 5–6, 651–670.

Langmuir, I. (1917). The constitution and fundamental properties of solids and liquids. *Journal of the American Chemical Society* **39**, 1848–1906.

Lanyon, G. W., Marschall, P., Trick, T., de La Vaissière, R., Shao, H. & Leung, H. (2014). Self-sealing experiments and gas injection tests in a backfilled microtunnel of the Mont Terri URL. In *Natural and Engineered Barriers for Radioactive Waste Confinement* (Norris, S., Bruno, J., Cathelineau, M., Delage, P., Fairhurst, C., Gaucher, E. C., Hohn, E. H., Kalinichev, A., Lalieux, P. & Sellin, P., Eds.), pp. 93–106.

Lee, J. & Shackelford, C. D. (2005). Impact of bentonite quality on hydraulic conductivity of geosynthetic clay liners. *Journal of Geophysical Research: Solid Earth* **131**, No. 1, 64–77.

Lewis, R. W. & Schrefler, B. A. (1998). *The finite element method in the static and dynamic deformation and consolidation of porous media*. John Wiley & Sons.

Li, X. L. (1999). *Comportement hydromécanique des sols fins: de l'état saturé à l'état non saturé*. Ph.D. thesis, Université de Liège.

Likos, W. J. & Lu, N. (2006). Pore-scale analysis of bulk volume change from crystalline interlayer swelling in Na^{+}- and Ca^{2+}-smectite. *Clays and Clay Minerals* **54**, No. 4, 515–528.

Liu, J. F. (2013). *Etanchéité de l'interface argilite-bentonite re-saturée et soumise à une pression de gaz, dans le contexte du stockage profond de déchets radioactifs*. Ph.D. thesis, Ecole Centrale de Lille.

Liu, J. F., Davy, C. A., Talandier, J. & Skoczylas, F. (2014). Effect of gas pressure on the sealing efficiency of compacted bentonite – sand plugs. *Journal of Contaminant Hydrology* **170**, 10–27.

Lloret, A. & Alonso, E. E. (1985). State surfaces for partially saturated soils. In *Proceedings of the 11th International Conference on Soil Mechanics and Foundation Engineering*, San Francisco, USA, pp. 557–562.

Lloret, A., Romero, E. & Villar, M. V. (2005). FEBEX II Project. Final report on thermo-hydro-mechanical laboratory tests. *Technical report*, ENRESA.

Lloret, A. & Villar, M. V. (2007). Advances on the knowledge of the thermo-hydro-mechanical behaviour of heavily compacted FEBEX bentonite. *Physics and Chemistry of the Earth* **32**, No. 8–14, 701–715.

Lloret, A., Villar, M. V., Sánchez, M., Gens, A., Pintado, X. & Alonso, E. E. (2003). Mechanical behaviour of heavily compacted bentonite under high suction changes. *Géotechnique* **53**, No. 1, 27–40.

Loiseau, C. (2001). *Transferts d'eau et couplages hydromécaniques dans les barrières ouvragées*. Ph.D. thesis, Ecole Nationale des Ponts et Chaussées.

Loiseau, C., Cui, Y. J. & Delage, P. (2002). The gradient effect on the water flow through a compacted swelling soil. In *Proceedings of the Third International Conference on Unsaturated Soils, UNSAT 2002* (Juca, J., de Campos, T. & Marinho, F., Eds.), Recife, Brazil, pp. 395–400.

Loret, B. & Khalili, N. (2000). A three-phase model for unsaturated soils. *International Journal for Numerical and Analytical Methods in Geomechanics* **24**, No. 11, 893–927.

Low, P. F. (1979). Nature and properties of water in montmorillonite-water systems. *Soil Science Society of America Journal* **43**, No. 4, 651–658.

Lu, N. & Likos, W. J. (2004). *Unsaturated soil mechanics*. Wiley.

Mackenzie, R. C. (1958). Density of water sorbed on montmorillonite. *Nature* **181**, 334.

Madsen, F. T. (1998). Clay mineralogical investigations related to nuclear waste disposal. *Clay Minerals* **33**, No. 1, 109–129.

Mainka, J., Murad, M. A., Moyne, C. & Lima, S. A. (2014). A modified effective stress principle for unsaturated swelling clays derived from microstructure. *Vadose Zone Journal* **13**, 5.

Marcial, D. (2003). *Comportement hydromécanique et microstructural des matériaux de barrière ouvragée*. Ph.D. thesis, Ecole Nationale des Ponts et Chaussées.

Marcial, D., Delage, P. & Cui, Y. J. (2002). On the high stress compression of bentonites. *Canadian Geotechnical Journal* **39**, No. 4, 812–820.

Marcial, D., Delage, P. & Cui, Y. J. (2006). A laboratory study of the self sealing behaviour of a compacted sand–bentonite mixture. *Geomechanics and Geoengineering: An International Journal* **1**, No. 1, 73–85.

Martin, P. L., Barcala, J. M. & Huertas, F. (2006). Large-scale and long-term coupled thermo-hydro-mechanic experiments with bentonite: the FEBEX mock-up test. *Journal of Iberian Geology* **32**, No. 2, 259–282.

Martin, T. R. (1960). Adsorbed water on clay: a review. *Clays and Clay Minerals* **9**, No. 1, 28–70.

Masin, D. & Khalili, N. (2016). Swelling phenomena and effective stress in compacted expansive clays. *Canadian Geotechnical Journal* **53**, 134–147.

Mata, C., Romero, E. & Ledesma, A. (2002). Hydro-chemical effects on water retention in bentonite-sand mixtures. In *Proceedings of the Third International Conference on Unsaturated Soils, UNSAT 2002* (Juca, J. F. T., de Campos, T. M. P. & Marinho, F. A. M., Eds.), Recife, Brazil, pp. 283–288.

Matsuoka, H. & Nakai, T. (1974). Stress deformation and strength characteristics of soil under three different principal stresses. *Proceedings of Japanese Society of Civil Engineering* **232**, 59–70.

Matyas, E. L. & Radhakrishna, H. S. (1968). Volume change characteristics of partially saturated soils. *Géotechnique* **18**, No. 4, 432–448.

Mayor, J. C. & Velasco, M. (2014). EB dismantling. Synthesis report. *Technical report*, Long-term Performance of Engineered Barrier Systems PEBS.

Meunier, A. (2005). *Clays*. Springer.

Millington, R. J. & Quirk, J. P. (1961). Permeability of porous media. *Nature* **1983**, 387–388.

Mitchell, J. K. & Soga, K. (2005). *Fundamentals of soil behaviour*. Wiley.

Mokni, N. & Barnichon, J. D. (2016). Hydro-mechanical analysis of SEALEX in-situ tests — Impact of technological gaps on long term performance of repository seals. *Engineering Geology* **205**, 81–92.

Montes-H, G. (2002). *Etude expérimentale de la sorption d'eau et du gonflement des argiles par microscopie électronique à balayage environnementale (ESEM)*. Ph.D. thesis, Université Louis Pasteur.

Mooney, R. W., Keenan, A. G. & Wood, L. A. (1952). Adsorption of water vapor by montmorillonite. II. Effect of exchangeable ions and lattice swelling as measured by X-ray diffraction. *Journal of the American Chemical Society* **74**, No. 6, 1371–1374.

Moore, D. M. & Reynolds, R. C. (1997). *X-ray diffraction and the identification and analysis of clay minerals*. Oxford University Press.

Mualem, Y. (1976). A new model for predicting the hydraulic conductivity of unsaturated porous media. *Water Resources Research* **12**, No. 3, 513–522.

Nakashima, Y. (2004). Nuclear magnetic resonance properties of water-rich gels of Kunigel-V1 bentonite. *Journal of Nuclear Science and Technology* **41**, No. 10, 981–992.

NEA (2008). Moving forward with geological disposal of radioactive waste, a collective statement by the NEA Radioactive Waste Management Commitee (RWMC). *Technical report*, OECD – Nuclear Energy Agency.

Nguyen, T. A. & Selvadurai, A. P. S. (1998). A model for coupled mechanical and hydraulic behaviour of a rock joint. *International Journal for Numerical and Analytical Methods in Geomechanics* **22**, No. 1, 29–48.

Norrish, K. (1954). The swelling of montmorillonite. *Discussions of the Faraday Society* **18**, 120–134.

Nuth, M. & Laloui, L. (2008a). Advances in modelling hysteretic water retention curve in deformable soils. *Computers and Geotechnics* **35**, No. 6, 835–844.

Nuth, M. & Laloui, L. (2008b). Effective stress concept in unsaturated soils: clarification and validation of a unified framework. *International Journal for Numerical and Analytical Methods in Geomechanics* **32**, No. 7, 771–801.

OECD/NEA (1995). The environmental and ethical basis of geological disposal of long-lived radioactive wastes. ïA collective opinion of the Radioactive Waste Management Committee of the OECD Nuclear Energy Agency. *Technical report*, OECD – Nuclear Energy Agency.

Olchitzky, E. (2002). *Couplage hydromécanique et perméabilité d'une argile gonflante non saturée sous sollicitations hydriques et thermiques. courbe de sorption et perméabilité à l'eau*. Ph.D. thesis, Ecole Nationale des Ponts et Chaussée.

Olivella, S., Carrera, J., Gens, A. & Alonso, E. E. (1994). Nonisothermal multiphase flow of brine and gas through saline media. *Transport in Porous Media* **15**, No. 3, 271–293.

Olsson, R. & Barton, N. (2001). An improved model for hydromechanical coupling during shearing of rock joints. *International Journal for Numerical and Analytical Methods in Geomechanics* **32**, 317–329.

Oron, A. & Berkowitz, B. (1998). Flow in rock fractures: the local cubic law assumption reexamined. *Water Resources Research* **34**, No. 11, 2811–2825.

Ortiz, M. & Simo, J. C. (1986). An analysis of a new class of integration algorithms for elastoplastic constitutive relations. *International Journal for Numerical Methods in Engineering* **23**, No. 3, 353–366.

Panday, S. & Corapcioglu, M. Y. (1989). Reservoir transport equations by compositional approach. *Transport in Porous Media* **4**, No. 4, 369–393.

Pardoen, B. (2015). *Hydro-mechanical analysis of the fracturing induced by the excavation of nuclear waste repository galleries using shear banding*. Ph.D. thesis, Université de Liège.

Pellet, F. L., Keshavarz, M. & Boulon, M. (2013). Influence of humidity conditions on shear strength of clay rock discontinuities. *Engineering Geology* **157**, 33–38.

Pham, Q. T. (2006). *Effet de la désaturation et de la resaturation sur l'argilite dans les ouvrages souterrains*. Ph.D. thesis, Ecole Polytechnique.

Philip, J. R. & de Vries, D. A. (1957). Moisture movement in porous materials under temperature gradients. *Eos, Transactions American Geophysical Union* **38**, No. 2, 222–232.

Plesha, M. E. (1987). Constitutive models for rock discontinuities with dilatancy and surface degradation. *International Journal for Numerical and Analytical Methods in Geomechanics* **11**, No. 4, 345–362.

Plesha, M. E. (1995). Rock joints: Theory, constitutive equations **42**, 375–393.

Prager, W. (1949). Recent developments in mathematical theory of plasticity. *Journal of Applied Physics* **20**, 235–241.

Prikryl, R., Ryndova, T., Bohac, J. & Weishauptova, Z. (2003). Microstructures and physical properties of 'backfill' clays: comparison of residual and sedimentary montmorillonite clays. *Applied Clay Science* **23**, 149–156.

Proust, D., Lechelle, J., Lajudie, A. & Meunier, A. (1990). Hydrothermal reactivity of mixed-layer kaolinite/smectite: experimental transformation of high-charge to low-charge smectite **38**, No. 4, 415–425.

Pusch, R. (1982). Mineral-water interactions and their influence on the physical behavior of highly compacted Na bentonite. *Canadian Geotechnical Journal* **19**, No. 3, 381–387.

Pusch, R. (2001). The buffer and backfill handbook. Part 2: Materials and techniques. *Technical report*, SKB.

Pusch, R., Karnland, O. & Hokmark, H. (1990). GMM - a general microstructural model for qualitative and quantitative studies of smectite clays. *Technical report*, SKB.

Puso, M. & Laursen, T. A. (2004). A mortar segment-to-segment contact method for large deformation solid mechanics. *Computer Methods in Applied Mechanics and Engineering* **193**, No. 6, 601–629.

Pyrak-Nolte, L. J. & Morris, J. P. (2000). Single fractures under normal stress: The relation between fracture specific stiffness and fluid flow. *International Journal of Rock Mechanics & Mining Sciences* **37**, No. 1–2, 245–262.

Rao, N. S. & Mathew, P. K. (1995). Effect of exchangeable cations on hydraulic conductivity of marine clay. *Clays and Clay Minerals* **43**, No. 4, 433–437.

Raven, K. G. & Gale, J. E. (1985). Water flow in a natural rock fracture as a function of stress and sample size. *International Journal of Rock Mechanics & Mining Sciences & Geomechanics Abstracts* **22**, No. 4, 251–261.

Richards, L. A. (1941). A pressure-membrane extraction apparatus for soil suction. *Soil Science* **51**, No. 5, 377–386.

Rigby, S. P. (2002). New methodologies in mercury porosimetry. *Studies in Surface Science and Catalysis* **144**, 185–192.

Rodwell, W. (1999). Gas migration and two-phase flow through engineered and geological barriers for a deep repository for radioactive waste. *Technical report*, Joint EC/NEA, EUR19112 EN.

Romero, E. (1999). *Characterisation and thermo-hydro-mechanical behaviour of unsaturated Boom Clay: an experimental study*. Ph.D. thesis, Universitat Politecnica de Catalunya.

Romero, E. (2011). Controlled-suction triaxial tests on low-density Kunigel V1. *Technical report*, Universitat Politecnica de Catalunya.

Romero, E. (2012). Complementary triaxial compression and direct shear tests under high matric suctions on low-density Kunigel V1. *Technical report*, Universitat Politecnica de Catalunya.

Romero, E. (2013). A microstructural insight into compacted clayey soils and their hydraulic properties. *Engineering Geology* **165**, 3–19.

Romero, E. (2014). Water retention tests on Kunigel V1 bentonite: sand mixture (70% bentonite dry mass ratio). *Technical report*, Universitat Politecnica de Catalunya.

Romero, E., Della Vecchia, G. & Jommi, C. (2011). An insight into the water retention properties of compacted clayey soils. *Géotechnique* **61**, No. 4, 313–328.

Romero, E., Gens, A. & Lloret, A. (1999). Water permeability, water retention and microstructure of unsaturated compacted Boom clay. *Engineering Geology* **54**, No. 1–2, 117–127.

Romero, E. & Jommi, C. (2008). An insight into the role of hydraulic history on the volume changes of anisotropic clayey soils. *Water Resources Research* **44**.

Romero, E. & Simms, P. H. (2008). Microstructure investigation in unsaturated soils: a review with special attention to contribution of mercury intrusion pororismetry and environmental scanning electron microscopy. *Geotechnical and Geological Engineering* **26**, No. 6, 705–727.

Roscoe, K. H. & Burland, J. B. (1968). On the generalized stress–strain behaviour of he "wet" clay. In *Engineering plasticity* (Heyman, J. & Leckic, F., Eds.), Cambridge, UK, pp. 535–609.

Ross, C. S. & Shannon, E. V. (1926). The minerals of bentonite and related clays and their physical properties. *Journal of the American Ceramic Society* **9**, No. 2, 77–96.

Rothfuchs, T., Jockwer, N. & Zhang, C. L. (2007). Self-sealing barriers of clay/mineral mixtures – The SB project at the Mont Terri Rock Laboratory. *Physics and Chemistry of the Earth* **32**, No. 1–7, 108–115.

Rutqvist, J., Ijiri, Y. & Yamamoto, H. (2011). Implementation of the Barcelona Basic Model into TOUGH–FLAC for simulations of the geomechanical behavior of unsaturated soils. *Computers and Geosciences* **37**, No. 6, 751–762.

Saba, S. (2013). *Comportement hydromécanique diféré es barrières ouvragées argileuses gonflantes*. Ph.D. thesis, Université Paris-Est.

Saba, S., Delage, P., Lenoir, N., Cui, Y. J., Tang, A. M. & Barnichon, J. D. (2014). Further insight into the microstructure of compacted bentonite-sand mixture. *Engineering Geology* **168**, 141–148.

Saiyouri, N., Hicher, P. Y. & Tessier, D. (2000). Microstructural approach and transfer water modelling in highly compacted unsaturated swelling clays. *Mechanics of Cohesive-Frictional Materials* **5**, 41–60.

Saiyouri, N., Tessier, D. & Hicher, P. Y. (2004). Experimental study of swelling in unsaturated compacted clays. *Clay Minerals* **39**, 469–479.

Salehnia, F. (2015). *From some obscurity to clarity in Boom clay behavior: analysis of its coupled hydro-mechanical response in the presence of strain localization*. Ph.D. thesis, Université de Liège.

Salles, F., Douillard, J. M., Denoyel, R., Bildstein, O., Jullien, M., Beurroies, I. & Van Damme, H. (2009). Hydration sequence of swelling clays: evolutions of specific surface area and hydration energy. *Journal of Colloid and Interface Science* **333**, No. 2, 510–522.

Sanden, T. & Börgesson, L. (2008). Deep repository-engineered barrier system. piping and erosion in tunnel backfill. laboratory tests to understand processes during early water uptake. *Technical report*, SKB R-06-72.

Sane, P., Laurila, T., Olin, M. & Koskinen, K. (2013). Current status of mechanical erosion studies of bentonite buffer. *Technical report*, POSIVA 2012-45.

Santamarina, J. C., Klein, W. Y. H., K. A. & Prencke, E. (2002). Specific surface: determination and relevance. *Canadian Geotechnical Journal* **39**, No. 1, 233–241.

Schanz, T. & Al-Badran, Y. (2014). Swelling pressure characteristics of compacted Chinese Gaomiaozi bentonite GMZ01. *Soils and Foundations* **54**, No. 4, 748–759.

Schreyer Bennethum, L., Murad, M. A. & Cushman, J. H. (1997). Modified Darcy's law, Terzaghi's effective stress principle and Fick's law for swelling clay soils. *Computers and Geotechnics* **20**, No. 3–4, 245–266.

Segad, M., Jönsson, B., Akesson, T. & Cabane, B. (2010). Ca/Na montmorillonite: structure, forces and swelling properties. *Langmuir* **26**, No. 8, 5782–5790.

Seidel, J. P. & Haberfield, C. M. (2002). A theoretical model for rock joints subjected to constant normal stiffness direct shear. *International Journal of Rock Mechanics & Mining Sciences* **39**, No. 5, 539–553.

Seiphoori, A., Ferrari, A. & Laloui, L. (2014). Water retention behaviour and microstructural evolution of MX-80 bentonite during wetting and drying cycles. *Géotechnique* **64**, No. 9, 721–734.

Sellin, P. & Leupin, O. X. (2013). The use of clay as an engineered barrier in radioactive-waste management – a review. *Clays and Clay Minerals* **61**, No. 6, 477–498.

Semete, P., Imbert, C., Desgree, P., Février, B., Courtois, A. & Touzé, G. (2008). Experimental study of the water permeability of a partially saturated argilite. In *Proceedings of the Third International Symposium GeoProc'2008. Thermo-Hydromechanical and Chemical Coupling in Geomaterials and Applications*, pp. 219–230.

Shackelford, C. D., Daniel, D. E. & Liljestrand, H. M. (1989). Diffusion of inorganic chemical species in compacted clay soil. *Journal of Contaminant Hydrology* **4**, No. 3, 441–473.

Sharma, K. & Desai, C. (1993). Analysis and implementation of thin-layer element for interfaces and joints. *Journal of Engineering Mechanics* **118**, No. 27005, 2442–2462.

Sheng, D. (2011). Review of fundamental principles in modelling unsaturated soil behaviour. *Computers and Geotechnics* **38**, No. 6, 757–776.

Sheng, D., Fredlund, D. G. & Gens, A. (2008a). A new modelling approach for unsaturated soils using independent stress variables. *Canadian Geotechnical Journal* **345**, No. 4, 511–534.

Sheng, D., Gens, A., Fredlund, D. G. & Sloan, S. W. (2008b). Unsaturated soils: From constitutive modelling to numerical algorithms. *Computers and Geotechnics* **35**, No. 6, 810–824.

Sheng, D., Sloan, S. W. & Gens, A. (2004). A constitutive model for unsaturated soils: thermomechanical and computational aspects. *Computational Mechanics* **33**, 453–465.

Sheng, D., Sloan, S. W., Gens, A. & Smith, D. W. (2003). Finite element formulation and algorithms for unsaturated soils. Part I: Theory. *International Journal for Numerical and Analytical Methods in Geomechanics* **27**, No. 9, 745–765.

Sheng, D., Sloan, S. W. & Yu, H. S. (2000). Aspects of finite element implementation of critical state models. *Computational Mechanics* **26**, No. 2, 185–196.

Simms, P. H. & Yanful, E. K. (2002). Predicting soil-water retention characteristic curves of compacted plastic soils from measured pore-size distributions. *Géotechnique* **52**, No. 4, 269–278.

Simms, P. H. & Yanful, E. K. (2004). A discussion of the application of mercury intrusion porosimetry for the investigation of soils, including an evaluation of its use to estimate volume change in compacted clayey soils. *Géotechnique* **54**, No. 6, 421–426.

Simo, J. C. & Taylor, R. L. (1985). Consistent tangent operators for rate-independent elastoplasticity. *Computer Methods in Applied Mechanics and Engineering* **48**, No. 1, 101–118.

Sinnathamby, G., Korkiala-Tanttu, L. & Salvador, L. T. (2015). Shear resistance of bentonite backfill materials and their interfaces under varying hydraulic conditions in a deep rock nuclear waste repository. *Applied Clay Science* **104**, 211–220.

Sánchez, M., Gens, A. & Guimarães, L. (2005). A double structure generalised plasticity model for expansive materials. *International Journal for Numerical and Analytical Methods in Geomechanics* **29**, No. 8, 751–787.

Sánchez, M., Gens, A. & Guimarães, L. (2012a). Thermal-hydraulic-mechanical (THM) behaviour of a large-scale in situ heating experiment during cooling and dismantling. *Canadian Geotechnical Journal* **49**, No. 10, 1169–1195.

Sánchez, M., Gens, A., Guimarães, L. & Olivella, S. (2008). Implementation algorithm of a generalised plasticity model for swelling clays. *Computers and Geotechnics* **35**, No. 6, 860–871.

Sánchez, M., Gens, A. & Olivella, S. (2010). Effect of thermo-coupled processes on the behaviour of a clay barrier submitted to heating and hydration. *Anais da Academia Brasileira de Ciências (Annals of the Brazilian Academy of Sciences)* **82**, No. 1, 153–168.

Sánchez, M., Gens, A. & Olivella, S. (2012b). THM analysis of a large-scale heating test incorporating material fabric changes. *International Journal for Numerical and Analytical Methods in Geomechanics* **36**, No. 4, 391–421.

Solowski, W. T. & Gallipoli, D. (2010). Explicit stress integration with error control for the Barcelona Basic Model. Part I: Algorithms formulations. *Computers and Geotechnics* **37**, No. 1–2, 59–67.

Solowski, W. T., Hofmann, M., Hofstetter, G., Sheng, D. & Sloan, S. W. (2012). A comparative study of stress integration methods for the Barcelona Basic Model. *Computers and Geotechnics* **44**, 22–33.

Sposito, G., Skipper, N. T., Sutton, R., Park, S. H., Soper, A. K. & Greathouse, J. A. (1984). Surface geochemistry of the clay minerals. *Proceedings of the National Academy of Sciences* **96**, No. 7, 3358–3364.

Sridharan, A., Rao, A. S. & Sivapullaiah, P. V. (1986). Swelling pressure of clays. *Geotechnical Testing Journal* **9**, No. 1, 24–33.

Sridharan, A. & Venkatappa, R. G. (1973). Mechanisms controlling volume change of saturated clays and the role of the effective stress concept. *Géotechnique* **23**, No. 3, 359–382.

Stçepkowska, E. T. (1990). Aspects of the clay/electrolyte/water system with special reference to the geotechnical properties of clays. *Engineering Geology* **28**, No. 3–4, 249–267.

Stern, O. (1924). Zur Theorie der elektrolytischen Doppelschicht (The theory of the electrolytic double-layer). *Zeitschrift für Elektrochemie und Angewandte Physikalische Chemie* **30**, 508–516.

Sulem, J. & Vardoulakis, I. G. (1995). *Bifurcation analysis in geomechanics*. CRC Press.

Sun, A., Cui, H. B. & Sun, W. J. (2009). Swelling of compacted sand bentonite mixtures. *Applied Clay Science* **43**, 485–492.

Sun, W. J., Liu, S. Q., Sun, D. A. & Fang, L. (2014). Swelling characteristics and permeability of bentonite. In *Proceedings of the Sixth International Conference on Unsaturated Soils, UNSAT 2014* (Khalili, N., Russell, A. & Khoshghalb, A., Eds.), Sydney, Australia, pp. 1211–1217.

Suzuki, K., Asano, H., Yahagi, R., Kobayashi, I., Sellin, P., Svemar, C. & Holmqvist, M. (2013). Experimental investigations of piping phenomena in bentonite-based buffer materials for an HLW repository. *Clay Minerals* **48**, No. 2, 363–382.

Swenson, J., Bergman, R. & Howells, W. S. (2000). Quasielastic neutron scattering of two-dimensional water in vermiculite clay. *Journal of Chemical Physics* **113**, No. 7, 2873–2879.

Tang, A. M. & Cui, Y. J. (2005). Controlling suction by the vapour equilibrium technique at different temperatures and its application in determining the water retention properties of MX80 clay. *Canadian Geotechnical Journal* **42**, No. 1, 287–296.

Tarantino, A. (2009). A water retention model for deformable soils. *Géotechnique* **59**, No. 9, 751–762.

Tarantino, A. & De Col, E. (2008). Compaction behaviour of clay. *Géotechnique* **58**, No. 3, 199–213.

Tarantino, A., Romero, E. & Cui, Y. J. (2008). *Laboratory and field testing of unsaturated soils*. Springer.

Terzaghi, K. (1936). The shearing resistance of saturated soils and the angle between the planes of shear. In *Proceedings of the First International Conference on Soil Mechanics and Foundation Engineering*, Cambridge, UK, pp. 54–56.

Terzaghi, K. (1943). *Theoretical soil mechanics*. John Wiley & Sons.

Tessier, D. (1978). Etude de l'organisation des argiles calciques. Evolution au cours de la dessication. *Annales d'Agronomie* **29**, No. 4, 319–355.

Thomas, H. R., Vardon, P. J. & Cleall, P. J. (2013). Three-dimensional behaviour of a prototype radioactive waste repository in fractured granitic rock. *Canadian Geotechnical Journal* **51**, No. 3, 246–259.

Toprak, E., Mokni, N., Olivella, S. & Pintado, X. (2013). Thermo-hydro-mechanical modelling of buffer. Synthesis report. *Technical report*, POSIVA 2012-47.

Tripathy, S., Sridharan, A. & Schanz, T. (2004). Swelling pressures of compacted bentonites from diffuse double layer theory. *Canadian Geotechnical Journal* **41**, No. 3, 437–450.

Tsang, Y. & Witherspoon, P. (1981). Hydromechanical behavior of a deformable rock fracture subject to normal stress. *Journal of Geophysical Research: Solid Earth* **86**, No. B10, 9287–9298.

Tuller, M. & Or, D. (2005). Water films and scaling of soil characteristic curves at low water contents. *Water Resources Research* **41**, No. W09403, 1–6.

van Brakel, J., Modry, S. & Svata, M. (1981). Mercury porosimetry: state of the art. *Powder Technology* **29**, No. 1, 1–12.

van Eekelen, H. A. M. (1980). Isotropic yield surfaces in three dimensions for use in soil mechanics. *International Journal for Numerical and Analytical Methods in Geomechanics* **4**, No. 1, 89–101.

Van Geet, M., Bastiaens, W. & Ortiz, L. (2008). Self-sealing capacity of argillaceous rocks: Review of laboratory results obtained from the SELFRAC project. *Physics and Chemistry of the Earth* **33**, S396–S406.

van Genuchten, M. T. (1980). A closed-form equation for predicting the hydraulic conductivity of unsaturated soils. *Soil Science Society of America Journal* **44**, No. 5, 892–898.

Van Olphen, H. (1963). *An introduction to clay colloid chemistry.* John Wiley & Sons.

Van Olphen, H. (1977). *An introduction to clay colloid chemistry: for clay technologists, geologists and soil scientists.* Wiley-Interscience.

Vaunat, J., Cante, J. C., Ledesma, A. & Gens, A. (2000). A stress point algorithm for an elastoplastic model in unsaturated soils. *International Journal of Plasticity* **16**, No. 2, 121–141.

Vaunat, J. & Gens, A. (2005). Analysis of the hydration of a bentonite seal in a deep radioactive waste repository. *Engineering Geology* **81**, 317–328.

Villar, M. V. (2000). *Caracterizacion thermo-hidro-mecanica de una bentonita de Cabo de Gata.* Ph.D. thesis, Universidad Complutense de Madrid.

Villar, M. V. (2002). Thermo-hydro-mechanical characterisation of a bentonite from Cabo de Gata. *Technical report*, CIEMAT.

Villar, M. V. (2004a). MX-80 bentonite. Thermo-hydro-mechanical characterization performed at CIEMAT in the context of the Prototype Project. *Technical report*, CIEMAT.

Villar, M. V. (2004b). Thermo-hydro-mechanical characteristics and processes in the clay barrier of a high level radioactive waste repository. State of the art report. *Technical report*, CIEMAT.

Villar, M. V. (2005). Infiltration tests on a granite/bentonite mixture: Influence of water salinity. *Applied Clay Science* **31**, 96–109.

Villar, M. V. (2007). Water retention of two natural compacted bentonites. *Clays and Clay Minerals* **55**, No. 3, 311–322.

Villar, M. V., Garcia-Siñeriz, J. L., Barcena, I. & Lloret, A. (2005). State of the bentonite barrier after five years operation of an in situ test simulating a high level radioactive waste repository. *Engineering Geology* **80**, 175–198.

Villar, M. V., Gómez-Espina, R. & Guitiérrez-Nebot, L. (2012). Basal spacings of smectite in compacted bentonite. *Applied Clay Science* **65–66**, 95–105.

Villar, M. V. & Lloret, A. (2001). Variation of intrinsic permeability of expansive clays upon saturation. In *Clay Science for Engineering* (Adachi, K. & Fukue, M., Eds.), Shizuoka, Japan, pp. 259–266.

Wang, Q. (2012). *Hydro-mechanical behaviour of bentonite-based materials used for high-level radioactive waste disposal*. Ph.D. thesis, Université Paris-Est.

Wang, Q., Cui, Y. J., Tang, A. M., Barnichon, J. D., Saba, S. & Ye, W. M. (2013a). Hydraulic conductivity and microstructure changes of compacted bentonite/sand mixture during hydration. *Engineering Geology* **164**, 67–76.

Wang, Q., Cui, Y. J., Tang, A. M., Li, X. L. & Ye, W. M. (2014). Time- and density-dependent microstructure features of compacted bentonite. *Soils and Foundations* **54**, No. 4, 657–666.

Wang, Q., Tang, A. M., Cui, Y. J., Barnichon, J. D. & Ye, W. M. (2013b). A comparative study on the hydro-mechanical behavior of compacted bentonite/sand plug based on laboratory and field infiltration tests. *Engineering Geology* **162**, 79–87.

Wang, Q., Tang, A. M., Cui, Y. J., Delage, P., Barnichon, J. D. & Ye, W. M. (2013c). The effects of technological voids on the hydro-mechanical behaviour of compacted bentonite–sand mixture. *Soils and Foundations* **53**, No. 2, 232–245.

Wang, Q., Tang, A. M., Cui, Y. J., Delage, P. & Gatmiri, B. (2012). Experimental study on the swelling behaviour of bentonite/claystone mixture. *Engineering Geology* **124**, 59–66.

Wang, X. & Wang, L. (2006). Continuous interface elements subject to large shear deformations. *International Journal of Geomechanics* **6**, No. 2, 97–107.

Washburn, E. W. (1921). Note on a method of determining the distribution of pore sizes in a porous material. In *Proceedings of the National Academy of Science*, vol. 7, pp. 115–116.

Wen, Z. J. (2006). Physical property of China's buffer material for high-level radioactive waste repositories. *Chinese Journal of Rock Mechanics and Engineering* **25**, 794–800.

Wheeler, S. J. & Karube, D. (1995). Constitutive modelling. In *Proceedings of the First International Conference on Unsaturated Soils, UNSAT 1995* (Alonso, E. E. & Delage, P., Eds.), Paris, France, pp. 1323–1356.

Wheeler, S. J., Sharma, R. S. & Buisson, M. S. R. (2003). Coupling of hydraulic hysteresis and stress–strain behaviour in unsaturated soils. *Géotechnique* **53**, No. 1, 41–54.

Wheeler, S. J. & Sivakumar, V. (1995). An elasto-plastic critical state framework for unsaturated soil. *Géotechnique* **45**, No. 1, 35–53.

Wherry, E. T. (1917). Clay derived from volcanic dust in the Pierre of South Dakota. *Washington Academy of Sciences Journal* **7**, 576–583.

Winterkorn, H. F. (1943). The condition of water in porous systems. *Soil Science* **56**, 109–115.

Witherspoon, P., Wang, J., Iwai, K. & Gale, J. (1980). Validity of cubic law for fluid flow in a deformable rock fracture. *Water Resources Research* **16**, No. 6, 1016–1024.

Wriggers, P. (2006). *Computational contact mechanics*. Wiley.

Wriggers, P., Schroder, J. & Schwarz, A. (2013). A finite element method for contact using a third medium. *Computational Mechanics* **52**, No. 4, 837–847.

Ye, W. M., Cui, Y. J., Qian, L. X. & Chen, B. (2009). An experimental study of the water transfer through confined compacted GMZ bentonite. *Engineering Geology* **108**, No. 3–4, 169–176.

Ye, W. M., Zhang, Y. W., Chen, B., Zheng, Z. J., Chen, Y. G. & Cui, Y. J. (2012). Investigation on compression behaviour of highly compacted GMZ01 bentonite with suction and temperature control. *Nuclear Engineering and Design* **252**, 11–18.

Yong, R. N., Pusch, R. & Nakano, M. (2009). *Containment of high-level radioactive and hazardous solid wastes with clay barriers*. CRC Press.

Yu, L., Gedeon, M., Wemaere, I., Marivoet, J. & De Craen, M. (2011). Comm clay hydraulic conductivity. A synthesis of 30 years of research. *Technical report*, SCK-CEN.

Zandarin, M. T., Alonso, E. E. & Olivella, S. (2013). A constitutive law for rock joints considering the effects of suction and roughness on strength parameters. *International Journal of Rock Mechanics & Mining Sciences* **60**, 333–344.

Zandarin, M. T., Gens, A., Olivella, S. & Alonso, E. E. (2011). Thermo-hydro-mechanical model of the Canister Retrivial Test. *Physics and Chemistry of the Earth* **36**, 1806–1816.

Zhang, C. L. (2011). Experimental evidence for the self-sealing of fractures in claystone. *Physics and Chemistry of the Earth* **36**, 1972–1980.

Zhang, C. L. (2013). Sealing of fractures in claystone. *Journal of Rock Mechanics and Geotechnical Engineering* **5**, No. 3, 214–220.

Zienkiewicz, O. & Taylor, R. (2000). *The finite element method*. Butterworth-Heinemann.

Appendices

Appendix A

Interpretation of MIP data

Mercury intrusion porosimetry (MIP) provides cumulative intrusion and extrusion volumes normalized by sample dry weight as a function of the applied mercury pressure u_{Hg}. Under the assumption of cylindrical-shaped pores, Washburn equation (Washburn, 1921) links u_{Hg} to the apparent pore diameter x (also called entrance pore diameter)

$$u_{Hg} = -\frac{4\sigma_{Hg}\cos\theta_{Hg}}{x} \tag{A.1}$$

where σ_{Hg} is the surface tension of mercury and θ_{Hg} is the contact angle between mercury and the pore wall. In the present study, values of $\sigma_{Hg} = 0.484$ N/m (surface tension of mercury at 25°C) and $\theta_{Hg} = 140°$ are adopted. Accordingly normalized cumulative volumes may be expressed as a function of the apparent pore size x in order to obtain the pore size distribution (PSD) of the porous sample. Due to the wide range of pore sizes, semi-logarithmic plots are generally used. An example is provided in Figure A.1 for a compacted sample of Kunigel V1 bentonite.

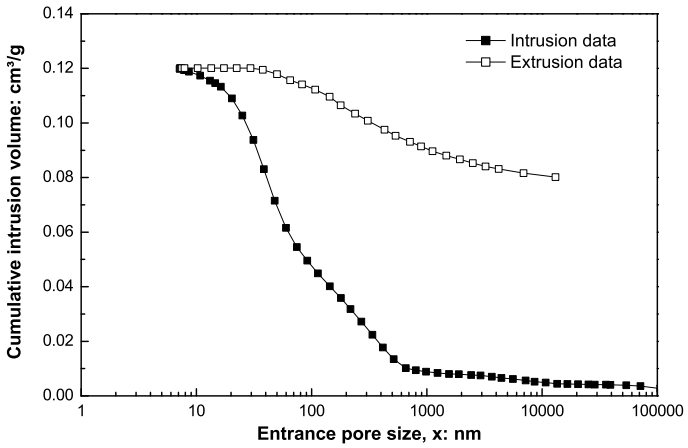

Figure A.1: Cumulative intrusion volume normalized by sample dry weight (MIP raw data). Experimental data on compacted Kunigel V1 bentonite ($\rho_d = 1.85$ Mg/m^3).

In soil mechanics, cumulative curves are often presented in terms of intruded mercury void ratio e_{Hg}, defined as the ratio between the intruded (or extruded) mercury volume and the volume of solid particles (Figure A.2). Such a representation evidences the amount of

non-intruded porosity[1], which is generally assumed to reflect the volume of porosity with an apparent size below 6 – 8 nm, i.e. the minimum value detected by MIP[2].

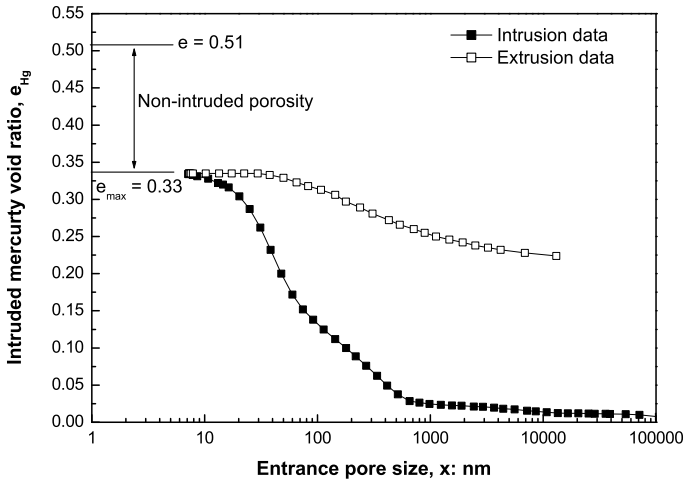

Figure A.2: Intruded mercury void ratio. Experimental data on compacted Kunigel V1 bentonite ($\rho_d = 1.85$ Mg/m^3).

Eventually, the information obtained from mercury intrusion porosimetry may also be presented in terms of pore size density function (Juang & Holtz, 1986) and used to derive a water retention curve. The corresponding mathematical developments are presented in the next two sections. Further details and discussion on mercury intrusion porosimetry can be found in Diamond (1970), Delage & Lefebvre (1984), Delage & Pellerin (1984), Simms & Yanful (2002), Simms & Yanful (2004) and Romero & Simms (2008), among others.

1 Derivation of the pore size density function

The pore size density function $f(x)$ is another possible representation of the pore size distribution of a porous sample. It is defined as the derivative of the cumulative function $F(x) = e_{Hg}(x)$, representing the amount of pores whose size ranges between x and ∞. Accordingly, the quantity $f(x)\mathrm{d}x$ represents the relative frequency of pores whose size ranges between x and $x + \mathrm{d}x$ so that

$$f(x) = -\frac{\mathrm{d}e_{Hg}}{\mathrm{d}x} \tag{A.2}$$

and

$$F(x) = \int_x^\infty f(x)\mathrm{d}x = e_{Hg}(x). \tag{A.3}$$

[1]The non-intruded porosity corresponds to the difference between the total void ratio e, obtained by macroscopic measurement, and the final value of intruded mercury void ratio e_{max}.

[2]Generally speaking, the difference $(e - e_{max})$ arises not only from the porosity with an apparent size below the MIP resolution, but also from the enclosed porosity. However, according to Simms & Yanful (2004), the effect of enclosed porosity is believed to be negligible in compacted soils.

Under the assumption of constant surface tension and contact angle[3], the following expression is obtained from Washburn equation

$$\mathrm{d}x = -\frac{x}{u_{Hg}}\mathrm{d}u_{Hg} \tag{A.4}$$

so that the pore size density function may be expressed as

$$f(x) = \frac{u_{Hg}}{x}\frac{\mathrm{d}e_{Hg}}{\mathrm{d}u_{Hg}} \tag{A.5}$$

or

$$f(\log x) = -\frac{\mathrm{d}e_{Hg}}{\mathrm{d}(\log x)} = \frac{\mathrm{d}e_{Hg}}{\mathrm{d}(\log u_{Hg})} = \frac{u_{Hg}}{\log \mathrm{e}}\frac{\mathrm{d}e_{Hg}}{\mathrm{d}u_{Hg}}. \tag{A.6}$$

In practice, the intruded mercury void ratio is known for discrete values of mercury pressure, so that the pore size density function takes the form

$$f(\log x_m) = \frac{\Delta e_{Hg}}{\Delta(\log u_{Hg})} \tag{A.7}$$

where $\log x_m$ is the midpoint of each subclass of width $-\Delta(\log u_{Hg})$ (Figure A.3).

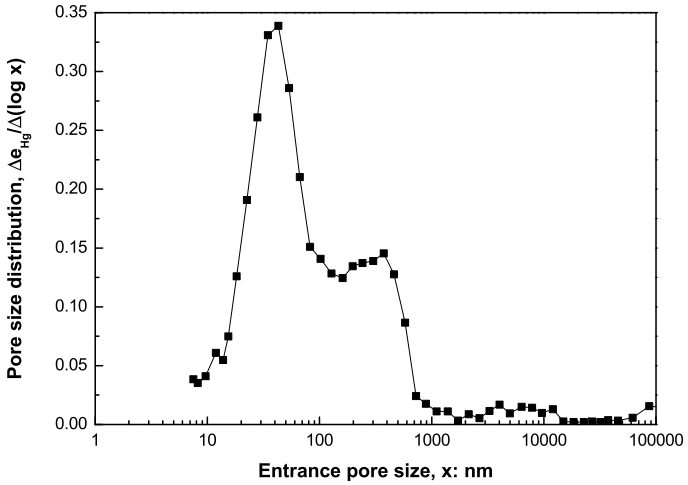

Figure A.3: Pore size density function. Experimental data on compacted Kunigel V1 bentonite ($\rho_d = 1.85$ Mg/m^3).

2 Derivation of the water retention curve

The intrusion of non-wetting mercury into a initially dry sample may be assimilated to the injection of air in an initially water saturated sample. Therefore mercury intrusion porosimetry data may be used to derive the water retention curve of the porous sample (Romero, 1999).

[3]Refer to van Brakel *et al.* (1981), Kloubek (1981), Rigby (2002) and Hall *et al.* (2013), among others, for a discussion on the validity of this hypothesis.

The relationship between the mercury intrusion pressure u_{Hg} and matrix suction $(u_a - u_w)$ is obtained applying Washburn equation for the same size x of pores being intruded

$$u_{Hg} = -\frac{4\sigma_{Hg}\cos\theta_{Hg}}{x} \tag{A.8}$$

and

$$u_a - u_w = \frac{4\sigma_w \cos\theta_w}{x} \tag{A.9}$$

so that

$$u_a - u_w = -\frac{\sigma_w \cos\theta_w}{\sigma_{Hg}\cos\theta_{Hg}} u_{Hg} \simeq 0.196 u_{Hg} \tag{A.10}$$

where $\sigma_w = 0.07275$ N/m is the water surface tension and $\theta_w = 0°$ is the contact angle between water and the pore wall.

The corresponding water degree of saturation S_r is given by

$$S_r = 1 - S_{rHg} = 1 - \frac{e_{Hg}}{e} \tag{A.11}$$

where S_{rHg} is the degree of saturation of the non-wetting mercury, defined as the ratio between the intruded mercury void ratio e_{Hg} and the total void ratio e.

Romero (1999) suggested to correct equation (A.11) to account for the non-intruded porosity (Figure A.4), which may be assimilated to a residual water content (Figure A.4). Equation (A.11) becomes

$$S_r = (1 - S_{rHg}) + \frac{(e - e_{max})}{e} S_{rHg}. \tag{A.12}$$

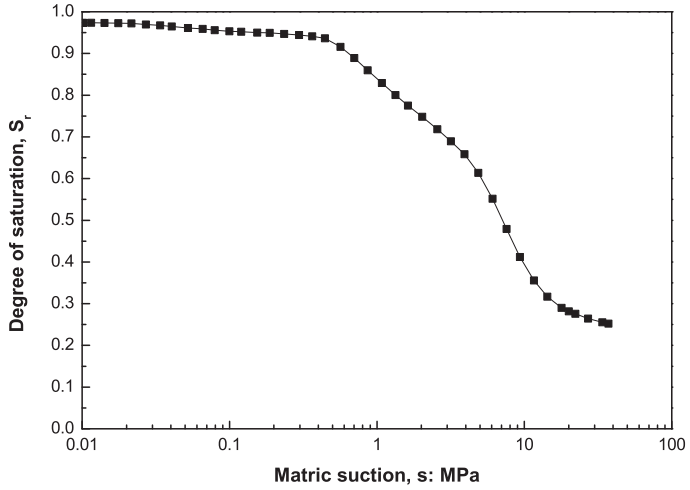

Figure A.4: Water retention curve derived from mercury intrusion porosimetry. Experimental data on compacted Kunigel V1 bentonite ($\rho_d = 1.85$ Mg/m^3).

The water retention curve derived in this way is a theoretical curve lying on several assumptions (Simms & Yanful, 2002; Romero & Simms, 2008). In particular, the method disregards pore size density changes along hydraulic paths and assumes that water is stored only by capillary, water adsorption on the clay surface being ignored.

Appendix B

Elastoplastic framework

Elastoplasticity is based on the decomposition of the total strain increment $\mathrm{d}\boldsymbol{\varepsilon}$ into a reversible elastic part $\mathrm{d}\boldsymbol{\varepsilon}^e$ and a plastic irreversible part $\mathrm{d}\boldsymbol{\varepsilon}^p$. It yields

$$\mathrm{d}\boldsymbol{\varepsilon} = \mathrm{d}\boldsymbol{\varepsilon}^e + \mathrm{d}\boldsymbol{\varepsilon}^p \tag{B.1}$$

in the small strain framework[1]. The elastic deformation produced upon loading is recoverable upon unloading while plastic deformation is irrecoverable, meaning that energy is dissipated during loading. Accordingly, Equation (B.1) writes in rate form

$$\dot{\boldsymbol{\varepsilon}} = \dot{\boldsymbol{\varepsilon}}^e + \dot{\boldsymbol{\varepsilon}}^p. \tag{B.2}$$

The formulation of an elastoplastic constitutive model requires the definition of four elements:

- A **stress − strain relation**, expressed as

$$\dot{\boldsymbol{\sigma}} = \boldsymbol{D}^e : (\dot{\boldsymbol{\varepsilon}} - \dot{\boldsymbol{\varepsilon}}^p) \tag{B.3}$$

  where $\boldsymbol{D}^e$ is a fourth-order elastic stiffness tensor.

- A **yield surface** f bounding the elastic domain. Mathematically, it is expressed as

$$f(\boldsymbol{\sigma}, \boldsymbol{\kappa}) = 0 \tag{B.4}$$

  where $\boldsymbol{\sigma}$ represents any generalized stress tensor[2] and $\boldsymbol{\kappa}$ is a vector of internal variables characterizing the state of the material. The function f takes negative values in the elastic domain and is equal to zero on the surface (Figure B.1). In elastoplasticity, stress state outside the yield surface, corresponding to positive values of f, are not admissible.

[1] In the large strain framework, a multiplicative formulation should be adopted.

[2] In this appendix, the elastoplastic formalism is presented in a general fashion, regardless the definition of stress that is adopted.

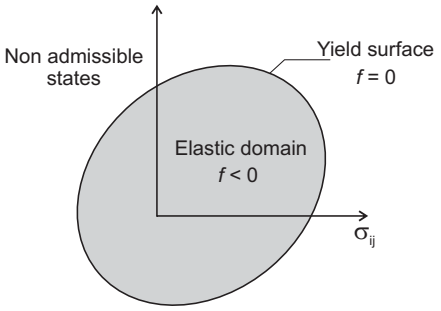

Figure B.1: Definition of a yield surface in the stress space.

- The **consistency condition** and a **hardening law**. During plastic loading, the stress state should always lie on the yield surface f. This condition is known as the consistency conditions (Prager, 1949) and is expressed as

$$\dot{f} = \frac{\partial f}{\partial \boldsymbol{\sigma}} : \dot{\boldsymbol{\sigma}} + \frac{\partial f}{\partial \boldsymbol{\kappa}} : \dot{\boldsymbol{\kappa}} = 0. \tag{B.5}$$

  During plastic loading, the term $\frac{\partial f}{\partial \boldsymbol{\sigma}}\dot{\boldsymbol{\sigma}}$ is positive. Therefore, it should be counterbalanced by an evolution of the yield function f in order to satisfy Equation (B.5).

  The evolution of the yield surface during loading is called hardening and is governed by a hardening law. It leads to expansion, translation or rotation of the yield surface in the stress space, or a combination of these mechanisms. In particular, if during plastic loading, the yield surface expands without any change of its shape, hardening is said to be isotropic. The hardening law is defined as the relation between the material hardening parameter and plastic strains undergone by the material upon yielding. It reads

$$\dot{\boldsymbol{\kappa}} = \dot{\lambda}^p \boldsymbol{h}\left(\boldsymbol{\sigma}, \boldsymbol{\kappa}\right) \tag{B.6}$$

  where λ^p is called the plastic multiplier and $\boldsymbol{h}$ is a vector or functions describing the evolution of internal variables.

  Finally, note that in the case of perfect plasticity or neutral loading, the term $\frac{\partial f}{\partial \boldsymbol{\sigma}}\dot{\boldsymbol{\sigma}}$ is equal to zero and $\dot{\boldsymbol{\kappa}} = 0$.

- A **flow rule**. The rate of plastic deformation $\dot{\boldsymbol{\varepsilon}}^p$ is characterized by an amplitude and a direction. Accordingly, it may be expressed as

$$\dot{\boldsymbol{\varepsilon}}^p = \dot{\lambda}^p \boldsymbol{n}_{\mathrm{d}\boldsymbol{\varepsilon}^p} \tag{B.7}$$

  where λ^p is called the plastic multiplier and is a measure of the amount of plastic strain developed by the material. $\dot{\boldsymbol{\varepsilon}}^p$ is positive if the stress state is plastic and null if it is elastic. $\boldsymbol{n}_{\mathrm{d}\boldsymbol{\varepsilon}^p}$ is the direction of plastic strain rates in the stress space. It is given by the flow rule, such that

$$\boldsymbol{n}_{\mathrm{d}\boldsymbol{\varepsilon}^p} = \frac{\partial g}{\partial \boldsymbol{\sigma}}. \tag{B.8}$$

The function g is called the plastic potential. If $g = f$, the plasticity is said to be associated, otherwise it non-associated.

The plastic multiplier is determined from the consistency condition. Introducing Equations (B.3), (B.6), (B.7) and (B.8) in Equation (B.5), it yields

$$\dot{f} = \frac{\partial f}{\partial \boldsymbol{\sigma}} : \boldsymbol{D^e} : \left(\dot{\boldsymbol{\varepsilon}} - \dot{\lambda}^p \frac{\partial g}{\partial \boldsymbol{\sigma}} \right) + \frac{\partial f}{\partial \boldsymbol{\kappa}} : \dot{\lambda}^p \boldsymbol{h} \left(\boldsymbol{\sigma}, \boldsymbol{\kappa} \right) = 0 \tag{B.9}$$

which can be rearranged to isolate $\dot{\lambda}^p$

$$\dot{\lambda}^p = \frac{\frac{\partial f}{\partial \boldsymbol{\sigma}} : \boldsymbol{D^e} : \dot{\boldsymbol{\varepsilon}}}{\frac{\partial f}{\partial \boldsymbol{\sigma}} : \boldsymbol{D^e} : \frac{\partial g}{\partial \boldsymbol{\sigma}} - \frac{\partial f}{\partial \boldsymbol{\kappa}} : \boldsymbol{h} \left(\boldsymbol{\sigma}, \boldsymbol{\kappa} \right)}. \tag{B.10}$$

Appendix C

General conventions and definition

In this work, the geomechanics sign convention is adopted, i.e. stresses and strains are positive in compression.

In three dimensions, the stress state is represented by a 3×3 tensor with 6 independent components

$$\boldsymbol{\sigma} = \begin{bmatrix} \sigma_{11} & \sigma_{12} & \sigma_{13} \\ \sigma_{12} & \sigma_{22} & \sigma_{23} \\ \sigma_{13} & \sigma_{23} & \sigma_{33} \end{bmatrix}. \tag{C.1}$$

The following stress invariants are defined

$$I_1 = \sigma_{ii} = \sigma_{11} + \sigma_{22} + \sigma_{33} \tag{C.2}$$

$$J_2 = \sqrt{\frac{1}{2} s_{ij} s_{ij}} \tag{C.3}$$

$$J_3 = \frac{1}{3} s_{ij} s_{jk} s_{ki} \tag{C.4}$$

where s_{ij} is the deviatoric stress defined as

$$s_{ij} = \sigma_{ij} - \frac{I_1}{3} \delta_{ij}. \tag{C.5}$$

The Lode's angle θ is defined from the third invariant. It is given by

$$\theta = -\frac{1}{3} \sin^{-1} \left(\frac{3\sqrt{3}}{2} \frac{J_3}{J_2^2} \right). \tag{C.6}$$

In oedometer and triaxial laboratory tests, σ_1 is the axial stress and $\sigma_3 = \sigma_2$ is the lateral stress. Accordingly, stress state is defined by the mean net stress p such as

$$p = \frac{\sigma_1 + 2\sigma_3}{3} = \frac{I_1}{3} \tag{C.7}$$

and the deviatoric stress q defined as

$$q = \sigma_1 - \sigma_3 = \sqrt{3} J_2. \tag{C.8}$$

Appendix D

Analytical derivatives for the implementation of the BBM in LAGAMINE

1 Loading-Collapse mechanism

The Loading-Collapse yield surface f_{LC} reads

$$f_{LC} \equiv 3J_2^2 + M_\theta^2 \left(p + p_s\right)\left(p - p_0\right) = 0 \tag{D.1}$$

where p is the mean net stress, J_2 is the second invariant of the deviatoric stress, M_θ is the slope of the critical state line, p_s is the left intercept of the yield surface and p_0 the preconsolidation pressure. The dependency on the Lode's angle θ is introduced in the slope of the critical state line M_θ through

$$M_\theta = a\left(1 + b\sin 3\theta\right)^n \tag{D.2}$$

with

$$\sin 3\theta = -\left(\frac{3\sqrt{3}}{2}\frac{J_3}{J_2^2}\right) \tag{D.3}$$

and a, b and n model parameters.

The consistency equation reads

$$\dot{f}_{LC} = \frac{\partial f_{LC}}{\partial \boldsymbol{\sigma}}\dot{\boldsymbol{\sigma}} + \frac{\partial f_{LC}}{\partial s}\dot{s} + \frac{\partial f_{LC}}{\partial p_0^*}\dot{p}_0^* = 0 \tag{D.4}$$

where s is the suction and p_0^* is the preconsolidation pressure for saturated conditions and is a hardening variable. In order to implement the Barcelona Basic Model in LAGAMINE, the different derivatives of the yield surface should be defined. Note that, in the integration routine, the suction is considered fixed at its final value and there is no return mapping on the suction axis (Borja, 2004). Accordingly, ds is equal to 0 in Equation (D.4).

1.1 Derivatives with respect to stress

The derivatives of the yield surface with respect to net stress are obtained by the chain rule

$$\frac{\partial f_{LC}}{\partial \sigma_{ij}} = \frac{\partial f_{LC}}{\partial p}\frac{\partial p}{\partial \sigma_{ij}} + \frac{\partial f_{LC}}{\partial J_2}\frac{\partial J_2}{\partial \sigma_{ij}} + \frac{\partial f_{LC}}{\partial \sin 3\theta}\frac{\partial \sin 3\theta}{\partial \sigma_{ij}} \tag{D.5}$$

with

$$\frac{\partial f_{LC}}{\partial p} = M_\theta^2 \left(p - p_0\right) + M_\theta^2 \left(p + p_s\right) \tag{D.6}$$

$$\frac{\partial f_{LC}}{\partial J_2} = 6J_2 \tag{D.7}$$

$$\frac{\partial f_{LC}}{\partial \sin 3\theta} = abn \left(1 + b \sin 3\theta\right)^{n-1} 2M_\theta \left(p + p_s\right) \left(p - p_0\right) \tag{D.8}$$

and

$$\frac{\partial p}{\partial \sigma_{ij}} = \frac{1}{3}\delta_{ij} \tag{D.9}$$

$$\frac{\partial J_2}{\partial \sigma_{ij}} = \frac{s_{ij}}{2J_2} \tag{D.10}$$

$$\frac{\partial \sin 3\theta}{\partial \sigma_{ij}} = -\frac{3\sqrt{3}}{2J_2^3}\left(s_{ik}s_{kj} - \frac{2}{3}J_2^2\delta_{ij} - \frac{3J_3}{2J_2^2}s_{ij}\right). \tag{D.11}$$

1.2 Derivative with respect to suction

The derivative of the yield surface with respect to suction is given by

$$\frac{\partial f_{LC}}{\partial s} = M_\theta^2 \frac{k}{\tan\varphi}\left(p - p_0\right) - M_\theta^2 \frac{\partial p_0}{\partial s}\left(p + p_s\right) \tag{D.12}$$

where k is a parameter controlling the increase of cohesion with suction and φ is the friction angle. In the previous equation, the following derivatives hold

$$\frac{\partial p_0}{\partial s} = -p_c \left(\frac{p_0^*}{p_c}\right)^{\frac{\lambda(0)-\kappa}{\lambda(s)-\kappa}} \ln\left(\frac{p_0^*}{p_c}\right) \frac{\lambda\left(0\right) - \kappa}{\left[\lambda\left(s\right) - \kappa\right]^2} \frac{\partial \lambda\left(s\right)}{\partial s} \tag{D.13}$$

and

$$\frac{\partial \lambda\left(s\right)}{\partial s} = -\omega\lambda\left(0\right)\left(1 - r\right)\exp\left(-\omega s\right) \tag{D.14}$$

with $\lambda\left(0\right)$ the slope of the saturated virgin consolidation line, κ the slope of the unloading–reloading line for changes in mean net stress, p_0^* the preconsolidation pressure in saturated conditions, p_c a reference pressure, and r and ω parameters controlling the shape of the LC curve in the $(p - s)$ plane.

1.3 Derivative with respect to p_0^*

The derivative of the yield surface with respect to the preconsolidation pressure p_0^* is given by

$$\frac{\partial f_{LC}}{\partial p_0^*} = -M_\theta^2 \left(p + p_s\right) \frac{\partial p_0}{\partial p_0^*}. \tag{D.15}$$

Given the hardening law

$$\mathrm{d}p_0^* = p_0^* \frac{1 + e}{\lambda(0) - \kappa} \mathrm{d}\varepsilon_v^p \tag{D.16}$$

where e is the void ratio and ε_v^p is the volumetric plastic deformation, the consistency equation (D.4) becomes

$$\dot{f}_{LC} = \frac{\partial f_{LC}}{\partial \boldsymbol{\sigma}} \dot{\boldsymbol{\sigma}} + \frac{\partial f_{LC}}{\partial s} \dot{s} + \frac{\partial f_{LC}}{\partial p_0^*} \frac{\mathrm{d}p_0^*}{\mathrm{d}\varepsilon_v^p} \dot{\varepsilon}_v^p = 0 \tag{D.17}$$

with

$$\frac{\partial p_0}{\partial p_0^*} = \frac{\lambda(0) - \kappa}{\lambda(s) - \kappa} \left(\frac{p_0^*}{p_c} \right)^{\frac{\lambda(0)-\kappa}{\lambda(s)-\kappa}-1} \tag{D.18}$$

$$\frac{\mathrm{d}p_0^*}{\mathrm{d}\varepsilon_v^p} = p_0^* \frac{1+e}{\lambda(0) - \kappa} \tag{D.19}$$

$$\dot{\varepsilon}_v^p = \dot{\lambda}^p \frac{\partial g_{LC}}{\partial \sigma_{ii}} \tag{D.20}$$

and g_{LC} the flow surface related to the Loading-Collapse mechanism, given by

$$g_{LC} \equiv \alpha 3 J_2^2 - M_\theta^2 (p + p_s)(p_0 - p) = 0 \tag{D.21}$$

and α chosen in such a way that the flow rule predicts zero lateral strain for stress states corresponding to Jacky's K_0 values. It yields

$$\frac{\partial g_{LC}}{\partial \sigma_{ii}} = \frac{\partial f_{LC}}{\partial p} \frac{\partial p}{\partial \sigma_{ii}} + \frac{\partial g_{LC}}{\partial J_2} \frac{\partial J_2}{\partial \sigma_{ii}} + \frac{\partial f_{LC}}{\partial \sin 3\theta} \frac{\partial \sin 3\theta}{\partial \sigma_{ii}} \tag{D.22}$$

with

$$\frac{\partial g_{LC}}{\partial J_2} = \alpha 6 J_2. \tag{D.23}$$

2 Suction Increase mechanism

The Suction Increase yield surface f_{SI} reads

$$f_{SI} \equiv s - s_0 = 0 \tag{D.24}$$

where s_0 is a threshold suction suction beyond which irreversible plastic strain are created and is the hardening variable of the SI yield surface. The related consistency equation reads

$$\dot{f}_{SI} = \frac{\partial f_{SI}}{\partial \boldsymbol{\sigma}} \dot{\boldsymbol{\sigma}} + \frac{\partial f_{SI}}{\partial s} \dot{s} + \frac{\partial f_{SI}}{\partial s_0} \dot{s}_0 = 0 \tag{D.25}$$

with

$$\frac{\partial f_{SI}}{\partial \boldsymbol{\sigma}} = 0 \tag{D.26}$$

$$\frac{\partial f_{SI}}{\partial s} = 1 \tag{D.27}$$

$$\frac{\partial f_{SI}}{\partial s_0} = -1. \tag{D.28}$$

The hardening law related to s_0 reads

$$\mathrm{d}s_0 = \frac{1+e}{\lambda_s - \kappa_s}\left(s_0 + u_{atm}\right)\mathrm{d}\varepsilon_v^p \tag{D.29}$$

where λ_s the lope of the virgin drying line and u_{atm} the atmospheric pressure. Accordingly, the consistency equation (D.25) becomes

$$\dot{f}_{SI} = \frac{\partial f_{SI}}{\partial \boldsymbol{\sigma}}\dot{\boldsymbol{\sigma}} + \frac{\partial f_{SI}}{\partial s}\dot{s} + \frac{\partial f_{SI}}{\partial s_0}\frac{\mathrm{d}s_0}{\mathrm{d}\varepsilon_v^p}\dot{\varepsilon}_v^p = 0 \tag{D.30}$$

with

$$\frac{\mathrm{d}s_0}{\mathrm{d}\varepsilon_v^p} = \frac{1+e}{\lambda_s - \kappa_s}\left(s_0 + u_{atm}\right) \tag{D.31}$$

and

$$\dot{\varepsilon}_v^p = \dot{\lambda}^p\frac{\partial g_{SI}}{\partial s} = \dot{\lambda}^p\frac{\partial f_{SI}}{\partial s} \tag{D.32}$$

considering an associated flow rule.